Nanosecond pulsed power technology for transient plasma generation

Document status and date:
Published: 01/01/2015

Document Version:
Publisher's PDF, also known as Version of Record (includes final page, issue and volume numbers)

Please check the document version of this publication:

• A submitted manuscript is the version of the article upon submission and before peer-review. There can be important differences between the submitted version and the official published version of record. People interested in the research are advised to contact the author for the final version of the publication, or visit the DOI to the publisher's website.
• The final author version and the galley proof are versions of the publication after peer review.
• The final published version features the final layout of the paper including the volume, issue and page numbers.

Link to publication

Nanosecond Pulsed Power Technology for Transient Plasma Generation

PROEFSCHRIFT

ter verkrijging van de graad van doctor aan de
Technische Universiteit Eindhoven, op gezag van de
rector magnificus prof.dr.ir. F.P.T. Baaijens, voor een
commissie aangewezen door het College voor
Promoties, in het openbaar te verdedigen
op dinsdag 29 september 2015 om 16.00 uur

door

Tom Huiskamp

geboren te De Bilt

Dit proefschrift is goedgekeurd door de promotoren en de samenstelling van de promotiecommissie is als volgt:

voorzitter:	prof.dr.ir. A.C.P.M. Backx
1^e promotor:	prof.ir. W.L. Kling †
2^e promotor:	prof.dr. U.M. Ebert
copromotor:	dr.ing. A.J.M. Pemen
leden:	prof.dr. B.M. Novac (Loughborough University)
	prof.dr. L.M. Redondo (Instituto Superior de Enghenharia de Lisboa)
	prof.dr.ir. G.M.W. Kroesen
	prof.dr.ir. A.B. Smolders
adviseur:	dr.ir. E.J.M. van Heesch

prof.dr. U.M. Ebert neemt tijdens de promotiezitting de taken van wijlen prof.ir. W.L. Kling over

Contents

Summary

This thesis focuses on the use of nanosecond pulsed power technology to generate a corona streamer plasma with the purpose of air purification. A streamer plasma is a non-thermal, transient plasma that is widely studied for its effect on such applications as plasma medicine, material surface engineering, water purification, and the removal of pollutants from gases. Recent studies have indicated that using very short (nanosecond) high-voltage pulses to generate a corona streamer plasma is a very efficient method for a number of air purification applications. However, due to the complexities involved in generating such short pulses, the underlying mechanisms of these high efficiencies are not very well studied or understood, and the existing studies were not conducted over a broad range of pulse parameters. The study in the present thesis seeks to address this discrepancy by exploring the effects on the streamer plasma when even shorter pulses are used than in previous studies. It also seeks to investigate and (re)solve several issues and interesting phenomena that arise when using these very short high-voltage pulses for corona streamer plasma generation. Furthermore, a significant part of this thesis focuses on the development of the nanosecond pulsed power technology that we used for the plasma investigations.

The thesis can be divided into three main parts — from the technology to the application. The first part covers the development of repetitive, adjustable-parameter, nanosecond pulse technology. The second part is the study of the interaction between the nanosecond pulse technology and the plasma. The third part deals with the application of the nanosecond pulse technology to air-purification applications.

In the first part, we designed and implemented a variable voltage (± 0–$50\,\mathrm{kV}$), variable pulse duration (0.5–$10\,\mathrm{ns}$), variable pulse repetition rate (up to several kHz), sub-nanosecond rise time (several hundred picoseconds), high-voltage pulse source (Chapters 2 and 3). The operating principle of the nanosecond pulse source is straightforward: a pulse-forming line (PFL) is charged and consequently discharged by a spark gap switch into a coaxial cable (or transmission line), which is connected to the load: the corona plasma reactor. The advantages of this type of pulse source are that the output voltage can be varied flexibly and the output pulses are square-shaped. A

thorough design was necessary in order to obtain a practical implementation of the nanosecond pulse source. We designed the nanosecond pulse source from theory and with the aid of 3D time-domain electromagnetic simulations, because the geometry of the pulse source is a determining feature for the very short pulse regimes in which the pulse source will operate. The practical implementation of the nanosecond pulse source successfully reached the design goals and features a variable length PFL to change the pulse duration. For the first time at Eindhoven University of Technology we implemented an oil spark gap to obtain fast switching (120 kV in several hundreds of picoseconds). We also verified the operation of the spark gap extensively and showed that it is a suitable switch for our pulse source.

As part of the nanosecond pulse technology, we developed two auxiliary systems: a microsecond pulse charger (Chapter 4) and a high-frequency sensor system (Chapter 5). The microsecond pulse charger is used to charge the PFL of the nanosecond pulse source. The PFL must be charged quickly, because this increases the hold-off voltage of the oil spark gap. However, it should not be charged so quickly that the charging pulses can capacitively couple to the load. The microsecond pulse charger consists of two pulse charger modules connected in series. Each of these modules is a short-circuit-proof, solid-state, microsecond pulse source comprising a pulse transformer and a printed circuit board with the solid-state switches and auxiliary devices. We used them to generate ±0–120 kV charging pulses for the PFL of the nanosecond pulse source, but they can also be operated as stand-alone pulse sources for other applications, such as DBD plasmas and in high-voltage trigger circuits.

The second auxiliary system is the high-frequency sensor system and consists of D-dot and B-dot sensors to measure the voltage and the current of the high-voltage pulses, respectively, in order to be able to calculate the energy supplied by the pulse source and the energy that is dissipated by the transient plasma. We developed this system because there are no readily available solutions to measure the very fast high-voltage and high-current pulses from our nanosecond pulse source. The sensors have a bandwidth of over 4 GHz and we integrated them on the coaxial cable connecting the pulse source to the load. The advantage of this method is that the sensors can be calibrated using a time-domain method and a frequency-domain method before the cable is installed in the nanosecond pulse source setup. An advantage of this calibration method is that the sensors are not limited to working only in the differentiating regime or only in the self-integrating regime; we can calibrate both regimes simultaneously. Furthermore, due to the installation of the sensors on a cable, our developed sensors are very versatile and can be used in any pulsed-power system in which a cable connects a pulse source to its load.

In the second part of this thesis we studied the interaction between the nanosecond pulse source and the plasma. We did this by studying the electrical energy transfer efficiency (or 'matching') of the pulse source to the transient plasma (Chapter 6) and by optically observing the generated streamer plasma with time-resolved and space-resolved ICCD imaging (Chapter 7).

A transient plasma is a highly dynamic load, which makes matching the nanosecond

pulse source with a fixed output impedance to the plasma reactor and the plasma a challenge. Furthermore, the high-frequency nature of the pulses causes pulse reflections at the plasma-reactor interface to complicate the matching even further. Through an extensive study of various pulse-source parameters and reactor geometries, we have investigated the matching with energy measurements. We showed that pulse reflections on the cable coupler significantly influence the matching; the impedance of the plasma reactor should be as close as possible to that of the nanosecond pulse source. We made use of these reflections by calculating time-dependent reflection coefficients and transmission coefficients to determine the time-dependent reactor impedance. This reactor impedance shows good agreement with calculated values and decreases in time and with an increased applied voltage due to plasma development. Thus, good matching is achieved for long pulses with a high voltage. By systematically varying parameters of the reactor, we obtained a wire-cylinder reactor with which matching of over 80 percent is possible. This finding shows that, even with the short pulses we work with, we are able to obtain good matching. Furthermore, we developed and implemented two new types of wire-cylinder reactor to significantly improve the matching: a multiple-wire reactor and a reactor with a DC bias voltage. First, the multiple-wire reactor significantly decreases the vacuum impedance of the plasma reactor, while maintaining a high electric field on the high-voltage electrode for streamer generation by using multiple thin wires as the high-voltage electrode. We showed that we could achieve matching of over 90 percent with this reactor. Second, during a visit to Kumamoto University in Japan we developed a plasma reactor with integrated bias electrodes that eliminates the issue of pulse deterioration by a coupling network for the DC voltage that a traditional implementation has. We used this reactor on a nanosecond pulse source and showed an initial matching that improved by a factor of 1.2–2.

To investigate the streamer development in the plasma reactor, we developed a fully automated ICCD-imaging setup for time-resolved and space-resolved imaging of the plasma for various pulse source settings. We found that the development and propagation of the streamers in the plasma reactor depends on the voltage profiles in the reactor. These voltages — as a function of time and position — result from a complex interaction of the pulse propagation, the pulse reflections and the energy the streamers dissipate. Consequently, when the pulse is short with respect to the reactor length, the voltage profiles in the reactor are far from homogenous, which causes the coverage of the streamers in the reactor to be non-homogenous due to the fact that a higher voltage at a position in the reactor results in a higher streamer velocity at that position (and, consequently, a longer streamer). Furthermore, the streamer width increases slightly with the voltage. To support the analysis of the experimental results, we developed a SPICE model of the plasma reactor to simulate the voltage inside the reactor as a function of time and position in the reactor. Comparison with experimental results shows good agreement, but also shows that a more extensive model would be required in order to correctly model the pulse dispersion that is caused by the plasma. Furthermore, the rise time of the pulses has a significant influence on the streamer properties: the streamer velocity, streamer length and streamer width are all lower for a longer rise time. We showed with the simulated voltage profiles that at least

part of the explanation can be found in the lower voltages in the reactor due to longer rise times, but it is likely that other effects, such as inception at a lower voltage, also play an important role. Finally, positive and negative pulses result in similar streamer properties, such as the streamer width, streamer length and streamer velocity. Only the streamer coverage was less homogeneous for negative pulses due to unexpectedly thick streamers originating from a triple point on a reactor feature.

In the final part of this thesis, we investigated the effect of the short pulses on plasma-processing applications (Chapter 8). We chose three applications: ozone generation, NO removal and CO_2 conversion. The results show that the ozone yields for our nanosecond pulsed transient plasma are very high and change only slightly with different pulse parameters. The plasma volume and the consequent streamer phase (primary/secondary) influence the ozone yield slightly. When the pulse duration and/or the applied voltage increase, the plasma volume increases until streamers start to cross the gap in the reactor. As long as the plasma volume can increase, the ozone yield increases. However, when streamers start to cross the gap, secondary streamer effects can become important and the ozone yields start to decrease. Furthermore, the ozone yield is lower for negative pulses. The effects of the thick streamers for negative pulses decrease the plasma volume and are a likely cause of the lower ozone yield. The optimal settings for ozone generation (high yield and high throughput) are the longest, positive pulses we used at the highest positive voltages we used due to the very high matching at these settings, combined with the higher ozone yields for positive pulses. The maximum obtained ozone yields were approximately $170\text{--}190\,\text{g}\cdot\text{kWh}^{-1}$ in synthetic air, which is very high compared to other pulsed corona plasmas.

NO can be removed very efficiently with our nanosecond transient plasma, with yields as high as $2.5\,\text{mol}\cdot\text{kWh}^{-1}$, which are among the highest reported in literature. At high energy densities and high initial NO concentrations, the production of NO by the plasma becomes important due to the presence of nitrogen radicals that the plasma produces. Just like ozone production, the optimal settings for NO removal are long pulses and high voltages due to the high matching and yields at these settings. However, unlike ozone generation, the polarity is less important. Furthermore, for ozone generation and NO removal, the rise time of the pulses has a significant influence on the process yields: using a longer rise time results in a lower process yield. Finally, the high yields we achieve for ozone production and NO removal are a result of the high electric field at the streamer heads in our plasma due to the sort rise time of the pulses, generating electrons with high energies and therefore producing radicals very effectively.

The results of the CO_2-conversion experiments show that the CO_2 plasma is significantly different from the plasma in synthetic air. Comparing our results with those of other non-thermal plasmas, such as DBDs, leads to the main conclusion that a nanosecond transient plasma should not be used for CO_2 conversion due to the higher complexity of the technology and the low yields. These low yields are a result of the electron energies in the nanosecond transient plasma, which are too high for efficient CO_2 conversion.

Samenvatting

Dit proefschrift focust zich op het gebruik van nanoseconde pulsed power techniek om een corona streamer plasma te genereren met het doel om luchtreiniging te bewerkstelligen. Een streamer plasma is een niet-thermisch, transiënt plasma dat op veel plekken bestudeerd wordt voor het effect dat het heeft op toepassingen als plasma medicine, oppervlaktebehandeling van materialen, waterreiniging en het verwijderen van verontreinigingen uit gassen. Recente studies hebben aangetoond dat het gebruik van zeer korte (nanoseconden) hoogspanningspulsen om het corona streamer plasma te genereren, zeer efficiënt is voor verschillende luchtreinigingstoepassingen. Echter, door de hoge complexiteit van het genereren van zulke korte pulsen, zijn de onderliggende mechanismen van de goede prestaties nog niet zeer uitgebreid bestudeerd en begrepen. Verder zijn de bestaande studies niet uitgevoerd over een uitgebreid bereik van pulsparameters. Het onderzoek in dit proefschrift probeert dit gemis op te lossen door het effect op het streamer plasma te bestuderen van nog kortere pulsen dan voorheen gebruikt werden. Het onderzoek is daarnaast gericht op het bestuderen van verschillende problemen en interessante fenomenen die ontstaan wanneer zulke korte hoogspanningspulsen worden gebruikt voor het genereren van een corona streamer plasma. Tevens focust een significant deel van dit proefschrift zich op de nanoseconde pulstechnologie die we ontwikkeld hebben voor het plasmaonderzoek.

Het proefschrift kent drie delen — van de technologie tot de toepassing. Het eerste deel gaat over de ontwikkeling van de repeterende, variabele-parameter, nanoseconde pulstechnologie. Het tweede deel beschrijft het onderzoek naar de interactie tussen de nanoseconde puls technologie en het plasma. Het derde deel gaat over het gebruik van de nanoseconde pulstechnologie voor luchtreinigingstoepassingen.

In het eerste deel hebben we een variabele spanning (± 0–$50\,\mathrm{kV}$), variabele pulsduur (0.5–$10\,\mathrm{ns}$), variabele puls herhalingsfrequentie (tot enkele kHz), sub-nanoseconde stijgtijd (honderden picoseconden), hoogspanningspulsbron ontworpen en geïmplementeerd (Hoofdstuk 2 en 3). Het principe van de nanoseconde pulsbron is eenvoudig: een pulsvormende lijn (PFL) wordt opgeladen en wordt vervolgens door een spark-gap schakelaar ontladen in een coaxiale kabel (of transmissielijn) die verbonden is met de corona plasmareactor. Het voordeel van dit type pulsbron is dat de uitgangsspanning

flexibel gevarieerd kan worden en dat de pulsen aan de uitgang een rechthoekige vorm hebben. Een zorgvuldig ontwerp was noodzakelijk om tot een praktische uitvoering van de pulsbron te komen. Het ontwerp van de pulsbron kwam tot stand vanuit theorie en met behulp van 3D elektromagnetische simulaties, omdat de geometrie van de pulsbron een bepalende factor is voor het zeer korte pulsregime waarin de pulsbron bedreven wordt. De praktische uitvoering van de nanoseconde pulsbron voldoet aan alle doelstellingen en heeft een PFL met instelbare lengte. We hebben voor het eerst op de Technische Universiteit Eindhoven een olie spark gap geïmplementeerd om tot zeer hoge schakelsnelheden te komen (120 kV in enkele honderden picoseconden).

Als onderdeel van de nanoseconde pulstechniek hebben we twee ondersteunende systemen ontworpen: een microseconde pulslader (Hoofdstuk 4) en een hoogfrequent sensorsysteem (Hoofdstuk 5). De microseconde pulslader wordt gebruikt om de PFL van de nanoseconde pulsbron op te laden. De PFL moet snel worden geladen, want dit verhoogt de schakelspanning van de spark gap. Hij moet echter niet té snel geladen worden, want dan kunnen de laadpulsen capacitief koppelen naar de load. De microseconde pulslader bestaat uit twee pulsladermodules die in serie geschakeld zijn. Ieder van deze modules is een kortsluitvaste, solid-state, microseconde pulsbron bestaande uit een pulstransformator en een printplaat met de semiconductor schakelaars en aanvullende systemen. We hebben ze gebruikt om in totaal $\pm$0–120 kV laadpulsen te genereren voor de nanoseconde pulsbron, maar ze kunnen ook functioneren als losse pulsbronnen voor andere applicaties, zoals DBD plasma's en in hoogspannings trigger circuits.

Het tweede ondersteunende systeem is het hoogfrequente sensor systeem dat bestaat uit D-dot en B-dot sensoren om respectievelijk de spanning en de stroom van de hoogspanningspulsen te meten die we gebruiken om de pulsenergie en de plasmaenergie te bepalen. We hebben dit systeem ontwikkeld omdat er geen beschikbare oplossingen waren om de zeer snelle hoge spanningen en hoge stromen van de nanoseconde pulsbron te meten. De sensoren hebben een bandbreedte van op z'n minst 4 GHz en zijn gemonteerd op de coaxiale kabel die de pulsbron met de belasting verbindt. Het voordeel van deze methode is dat de sensoren zo gekalibreerd kunnen worden in zowel het tijddomein als in het frequentiedomein voordat de kabel geïnstalleerd wordt in de nanoseconde pulsbron opstelling. Een voordeel van deze kalibratiemethode is dat de sensors niet gelimiteerd zijn tot alleen het differentiërende domein of alleen het integrerende domein; we kunnen beide domeinen tegelijkertijd kalibreren om tot één overdracht te komen. Daarnaast zijn onze sensors door de montage op een coaxiale kabel zeer veelzijdig en kunnen daardoor in ieder pulsed power systeem worden gebruikt waar een coaxiale kabel wordt gebruikt om de pulsbron met de load te verbinden.

In het tweede deel van dit proefschrift hebben we de interactie tussen de nanoseconde pulsbron en het plasma bestudeerd. We deden dit door de elektrische energieoverdracht ('matching') van de pulsbron naar het transiënte plasma te onderzoeken (Hoofdstuk 6) en door het gegenereerde streamer plasma optisch te observeren met tijd- en plaatsopgeloste ICCD fotografie (Hoofdstuk 7).

Een transiënt plasma is een zeer dynamische belasting, wat het matchen van de pulsbron met de plasmareactor een uitdaging maakt. Tevens zorgt het hoogfrequente

gedrag van de pulsen voor reflecties op de koppeling van de plasmareactor, wat het matchen verder bemoeilijkt. We hebben de matching onderzocht met energiemetingen door de pulsparameters over een uitgebreide range te variëren. Daarbij hebben we laten zien dat de pulsreflecties op de kabelkoppeling een significante invloed hebben op de matching; de impedantie van de plasmareactor moet zo dicht mogelijk bij dat van de nanoseconde pulsbron liggen. We hebben deze reflecties gebruikt om tijdafhankelijke reflectie- en transmissiecoëfficiënten te bepalen om daarmee de tijdafhankelijke reactorimpedantie te bepalen. Deze reactorimpedantie laat een goede overeenkomst zien met berekende waardes en neemt door plasmaontwikkeling af in de tijd en met een toenemende spanning. Oftewel, goede matching wordt bereikt met lange pulsen met een hoge spanning. We behaalden een matching van boven de 80 procent met een draad-cilinder reactor door systematisch reactorparameters te veranderen. Dit laat zien dat zelfs met zeer korte pulsen een goede matching bereikt kan worden. Verder ontwikkelden we twee nieuwe type draad-cilinder reactors om de matching nog verder te verhogen: een meerdraads reactor en een reactor met een DC bias spanning. De meerdraads reactor heeft meerder dunne draden als hoogspanningselektrode en zorgt voor een significante afname van de vacumimpedantie van de plasmareactor, terwijl het elektrisch veld op de draad — dat benodigd is voor streameropwekking — hoog blijft. Met deze reactor is matching van boven de 90 procent mogelijk. De tweede nieuwe reactor ontwikkelden we tijdens een bezoek aan de Kumamoto Universiteit in Japan. Het is een reactor met geïntegreerde bias elektrodes dat het probleem van pulsverslechtering oplost dat traditionele technieken met een koppelnetwerk om de DC spanning toe te voegen kenmerkt. We hebben deze reactor gebruikt met een nanoseconde pulsbron en lieten zien dat de initiële matching met een factor 1.2–2 toeneemt.

Om de streamerontwikkeling in de plasmareactor te onderzoeken, hebben we een volledig geautomatiseerde ICCD-fotografie opstelling ontwikkeld om tijd- en plaats-opgeloste foto's te maken van het plasma voor verschillende pulsbroninstellingen. We hebben ontdekt dat de ontwikkeling en voortplanting van de streamers afhangt van de spanningsprofielen in de reactor. Deze spanningen — as een functie van de tijd en positie — zijn het resultaat van een complexe interactie tussen de pulsvoortplanting, de pulsreflecties en de energie die de streamers verbruiken. Zodoende zijn de spanningsprofielen in de reactor niet homogeen wanneer de puls kort is in vergelijking met de reactorlengte. Daardoor is de dekkingsgraad van de streamers in de reactor ook niet homogeen, omdat een hoge spanning op een bepaalde plaats in de reactor voor een hogere streamersnelheid op die positie zorgt. Verder neemt de streamerbreedte iets toe met de spanning. We hebben een SPICE model ontwikkeld van de plasmareactor om de spanningen in de reactor te simuleren om daarmee de analyse van de experimentele resultaten te ondersteunen. Een vergelijking tussen de simulaties en de experimenten toonde goede overeenkomst, maar liet ook zien dat een uitgebreider model nodig is om de pulsdispersie — die veroorzaakt wordt door het plasma — correct te modelleren. Verder heeft de stijgtijd van de pulsen een significante invloed op de streamereigenschappen: de streamersnelheid, streamerlengte en streamerbreedte zijn allemaal lager voor een langere stijgtijd. De gesimuleerde spanningsprofielen lieten zien dat op z'n minst een gedeelte van de verklaring hiervoor is dat de spanning in de reactor lager

is voor langere stijgtijden, maar het is waarschijnlijk dat ook andere effecten zoals de aanvang van de streamers bij een lagere spanning een belangrijke rol spelen. Als laatste bleek dat positieve en negatiever streamers vergelijkbare eigenschappen hebben, zoals breedte, lengte en snelheid. Alleen de streamer dekkingsgraad was minder homogeen voor negatieve streamers vanwege onverwachte dikke streamers die ontstaan op een triple point in de reactor.

In het laatste deel van dit proefschrift hebben we het effect van de korte pulsen op plasmatoepassingen onderzocht (Hoofdstuk 8). We kozen drie toepassingen: ozonproductie, NO verwijdering en CO_2 conversie. De resultaten laten zien dat de ozonproductie efficiëntie van ons transiënte plasma erg hoog is en dat deze slechts in lichte mate afhangt van verschillende pulsparameters. Het plasmavolume en de bijbehorende streamerfase (primair/secundair) beïnvloeden het plasma enigszins. Zolang de pulsduur en/of de spanning toenemen kan het plasmavolume toenemen totdat de streamers de reactor overbruggen. Zolang het plasmavolume kan toenemen neemt de ozonproductie efficiëntie toe, maar wanneer streamers de reactor overbruggen neemt de efficiëntie weer af. Daarnaast is de efficiëntie lager voor negatieve pulsen. Het effect van de dikke streamers voor negatieve pulsen is dat het plasma volume afneemt. Daarom zijn ze een waarschijnlijke oorzaak voor de lagere ozonproductie efficiëntie. De optimale instellingen voor ozonproductie (hoge efficiëntie en hoge productie) zijn de langste positieve pulsen die we gebruikten, in combinatie met de hoogste spanning, omdat voor deze instellingen de matching het hoogst was en voor positieve pulsen de ozonproductie efficiëntie het hoogst was. De maximale ozonproductie efficiëntie die we behaald hebben was zo'n 170–190 g·kWh^{-1} in synthetische lucht, wat erg hoog is in vergelijking met andere gepulste corona plasma's.

NO kan zeer efficiënt worden verwijderd met ons nanoseconde transiënte plasma, met een efficiëntie tot wel 2.5 mol·kWh^{-1}, wat onder de hoogste gerapporteerde waardes in de literatuur behoort. Bij hoge energiedichtheden en hoge initiële NO concentraties, wordt het NO dat het plasma zelf produceert belangrijk. Net zoals bij ozonproductie zijn de optimale instellingen voor NO verwijdering lange pulsen en hoge spanningen door de hoge matching en de hoge efficiëntie voor deze instellingen. Echter, de polariteit is in dit geval minder belangrijk. Verder heeft de stijgtijd een significante invloed op de efficiëntie voor zowel ozonproductie als NO verwijdering: een langere stijgtijd zorgt voor een lagere efficiëntie. De hoge efficiëntie van ozonproductie en NO verwijdering zijn het resultaat van een hoog elektrisch veld bij de streamerkop door de korte stijgtijd van de pulsen. Daardoor worden elektronen met een hoge energie geproduceerd, die op hun beurt zeer effectief radicalen produceren.

De resultaten van de CO_2-conversie experimenten laten zien dat het CO_2 plasma significant anders is dan het plasma in synthetische lucht. Als we onze resultaten vergelijken met andere niet-thermische plasma's, zoals DBD's, dan kunnen we concluderen dat een nanoseconde transiënt plasma niet gebruikt moet worden voor CO_2 conversie vanwege de hogere complexiteit van de techniek en de lage efficiëntie. Deze lage efficiëntie is het resultaat van de elektronenenergieën in nanoseconde transiënte plasma, die te hoog zijn voor efficiënte CO_2 conversie.

One

Introduction

Transient plasmas generated by high-voltage pulses have been widely studied and used for industrial and environmental applications for more than 100 years [1,2]. Due to the fast electrons that are generated by these non-thermal plasmas, they are very efficient in producing highly reactive radical species and energetic photons [1,3]. These products can consequently react with, for instance, particles in gas streams (for example, pollutants, odour and dust), contamination in water, biological tissue, and material surfaces [1,4]. In this thesis, we mainly consider transient plasma for air-purification applications.

Regulations concerning air pollution by industry and the transportation sector are continuously increasing in number and stringency to work towards a cleaner environment. Conventional, proven air-purification techniques such as filters, catalysts, and scrubbers have significant disadvantages, such as a limited range of pollutants they can handle, high maintenance costs, a high pressure drop over the system, and high operating costs for low-concentration pollutant removal. Therefore, there is an urgent need for alternative pollution abatement technologies, in particular for technologies that perform efficiently at lower concentrations and/or for mixtures of polluting compounds.

The main advantage of using transient plasma for air purification — besides the high efficiency — is that it simultaneously targets a wide variety of pollutants, which makes it very versatile. Furthermore, it can be turned on and off on demand, can be easily controlled, has low maintenance and operating costs, and can be operated at a wide range of conditions (concerning temperature, pressure, moisture, etc.). However, for successful utilisation of transient-plasma technology for air purification, a better understanding and an increased energy efficiency of the technology would be very beneficial. This observation is the **main motivation** for the research in this thesis.

Recent research has shown that transient plasmas generated by very short nanosecond high-voltage pulses are very efficient for a variety of applications [5–12]. More specifically, some researches have noted that the pulse duration of the applied high-voltage pulse has a significant influence on the radical yield of the transient plasmas generated with these pulses; shorter pulses result in higher yields [5–7, 11]. However, the pulses that have been used for plasma generation so far are either still relatively long

1

($>10\,$ns), have a long rise time (several nanoseconds), and/or are not square-shaped. Furthermore, a parametric study to investigate the effect of the pulse duration, rise time, and voltage (amplitude and polarity) is lacking (but strongly needed) for these short pulses.

Our aim is to develop adjustable, nanosecond pulse technology with sub-nanosecond rise-time pulses that can deliver this wide variety of pulses for transient-plasma generation. The use of these very fast-rising and short pulses is accompanied by many new challenges such as the measurement of these fast pulses and the interaction of such short pulses with the plasma reactor and the transient plasma. Moreover, we will investigate what the effect of the short pulses is on several air-purification applications.

Before we present the goals of the project, we will discuss the mechanism by which plasma processing is achieved through the application of high-voltage pulses and shortly introduce nanosecond pulsed corona plasmas for air purification.

1.1   From high-voltage pulses to plasma processing

Electrical discharges can take many forms, from natural phenomena such as lightning during thunderstorms and St. Elmo's fire, to man-made discharges such as plasmas for welding and cutting, sparks in a petrol-engine spark plug, discharges in lamps for lighting, corona around high-voltage transmission lines, and many more. Furthermore, discharges are applied in many industrial applications such as plasma etching, plasma deposition, material surface engineering, air purification, and water decontamination [4]. As previously mentioned, our research will focus on electrical discharges for the purpose of air purification. This leads to the following question: How can electrical discharges effectively perform air purification?

When a transient voltage is applied between two electrodes, an electric field is present in the gap between these electrodes. Free electrons that are always present due to, for example, cosmic radiation, are accelerated by this electric field. These electrons can subsequently collide with gas molecules or atoms. Upon this collision, the gas molecule or atom can be ionised or excited if the energy of the electron is sufficiently high. In the case of ionisation, there are now two electrons instead of the original one. These again gain energy from the electric field, and can initiate new ionisation and again multiply. Meanwhile, when a gas atom or molecule is excited by electron impact, it can fall back to its ground state by emitting radiation. As long as more electrons are generated, the discharge is sustained. This type of discharge is called an avalanche discharge, and is illustrated by Fig. 1.1a [3].

When an avalanche discharge propagates, it leaves behind charged molecules or atoms. If this space charge becomes high enough (when more than 10^8–10^9 free electrons exist in the discharge, according to the classical Raether-Meek criterion [13,14]), the electric field that this charge generates starts to influence the discharge. At this point, streamers can form. Figure 1.1b shows a negative and a positive streamer.

A streamer is an ionised channel with a space charge layer at its head. The streamer can propagate under the influence of the applied electric field, as well as under the
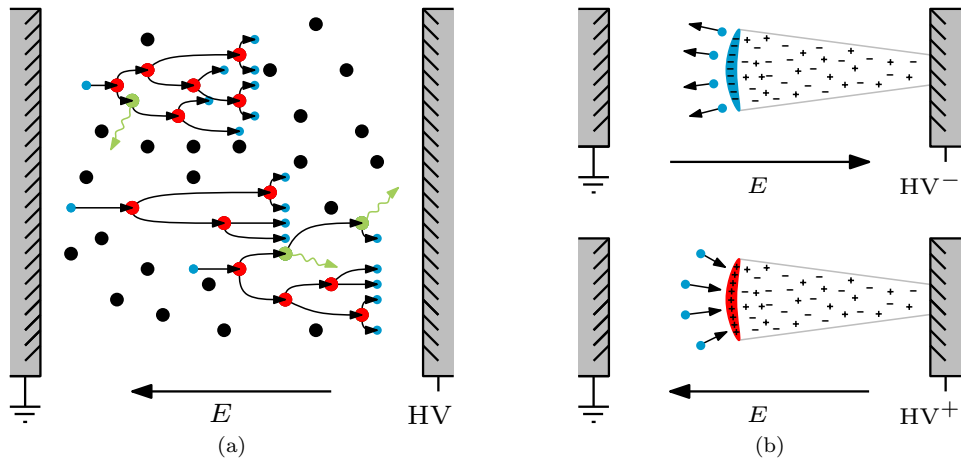
Figure 1.1: (a) A simple representation of an avalanche discharge. Free electrons (●) are accelerated in the electric field E that is generated by the applied high voltage (HV) between two electrodes. The electrons can collide with neutral particles (●), leaving behind ionised particles (●) (if the energy of the electron is high enough) and generating an additional electron. An electron collision can also generate an excited particle (●), which does not produce a new electron. When the excited particle returns to its ground state, it emits a photon (⤳). The black arrows indicate the path of the electrons. (b) A negative streamer (top) and a positive streamer (bottom). The streamers consist of a thin space charge region (coloured blue and red for the negative and positive streamer in the figure respectively), or the streamer head, and an ionised channel behind it. Each type of streamer needs new free electrons in front of its head to propagate. Where the negative streamer can gain these electrons by electron drift from the ionised channel, the positive streamer needs mechanisms such as photoionisation to receive new electrons.

influence of its own electric field due to the space charge layer. A sufficient number of free electrons has to be available in front of the streamer head to generate new ionisation, thereby allowing the streamer to propagate. In the negative streamer, these electrons can drift from the ionised channel, but this is not possible for the positive streamer due to the direction of the electric field. For positive streamers, photoionisation is the dominant mechanism for the generation of new electrons [15,16]. In this process, an excited nitrogen molecule emits a UV photon, which is then able to ionise an oxygen molecule some distance away (including the region in front of the streamer head).

When a streamer propagates between two electrodes, it constantly accelerates electrons to high energy levels (up to around $10\,\mathrm{eV}$). We already explained that these electrons play an important role in sustaining the discharge by ionising molecules and atoms, but even more crucial is that these electrons (and excited molecules) are also able to dissociate molecules upon collision. As a result of this dissociation, highly reactive species are formed. These reactive species, or radicals, such as atomic oxygen,
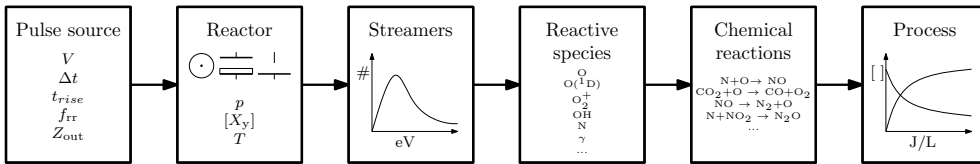
Figure 1.2: From high-voltage pulses to plasma processing. From the left to the right: a high-voltage pulse is generated by a pulse source and applied to a plasma reactor, where the voltage pulse has parameters such as the voltage magnitude V, pulse duration Δt, rise time t_{rise}, pulse repetition rate f_{rr} and output impedance Z_{out}. The plasma reactor can have different geometries (coaxial corona reactor, DBD reactor, point-plate reactor, etc.) and the gas in the reactor has a pressure p, a temperature T and can contain pollutants with concentration $[X_{\text{y}}]$. The pulse-source and reactor parameters determine whether streamers can develop and what parameters these streamers have (electron energy distribution, velocity, width, etc.). The electrons generated by the streamers subsequently generate reactive species, which then initiate chemical reactions with the particles in the gas, changing the concentrations of these particles.

atomic nitrogen, and hydroxyl radicals are then able to react with other molecules, such as pollutants. As a result, these pollutants can be converted into less harmful substances. In summary, a transient plasma is an effective source of radicals that can be efficiently utilised for a range of air-purification applications.

If a streamer crosses the gap between the electrodes, it leaves behind an ionised channel. At this point, a large current can flow through this channel if the high-voltage source that generates the external electric field is powerful enough. As a result, the channel heats up, and eventually, a full breakdown can occur. The period in which the streamer is crossing the inter-electrode gap is called the primary streamer phase, whereas the period after crossing — but before a full breakdown — is called the secondary streamer phase. When short duration high-voltage pulses are used to generate the electric field, the electric field is only applied to the electrodes during the first phases (primary and/or early secondary streamer phase) of plasma generation, which prevents spark breakdown and significant heating of the discharge channel and the background gas. Consequently, the loss of energy due to these thermal processes is avoided, which is why these plasmas are called 'non-thermal' or 'cold', and also why they are so efficient in the production of reactive species [3]. This is the primary reason a pulsed voltage is used to generate streamer plasmas for air purification instead of a continuous voltage. For a continuous voltage, the applied voltage has to be much lower to prevent spark breakdown, and as a result the streamers propagate less far and produce electrons with a lower energy. Both effects reduce the effectiveness of streamers for air purification.

We started our explanation with how electrical discharges can effect air purification, finally explaining why high-voltage pulses are used rather than a continuous voltage. Figure 1.2 sums up this process in a clear overview of the necessary steps to initiate chemical reactions with high-voltage pulses — from the high-voltage pulse source to the
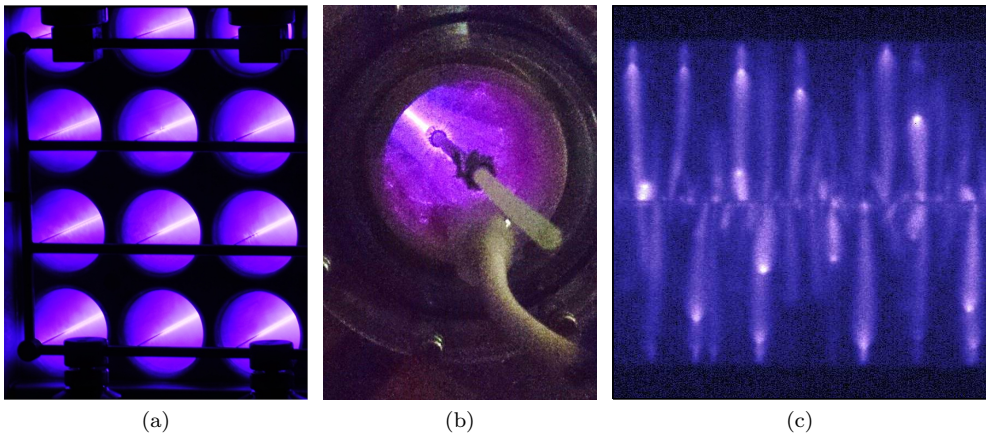
Figure 1.3: Examples of pulsed corona plasmas. The purple colour of the plasma is caused by photon emission from exited nitrogen. (a) The multiple-cylinder corona-plasma reactor that is used in the demonstrator developed at Eindhoven University of Technology in collaboration with HMVT-Antea Group [19, 20] (image reproduced with permission from [21]). A high-power, high-voltage pulse source powers 16 parallel corona reactors to treat large polluted air streams. (b) The corona plasma generated with the nanosecond pulse source of Kumamoto University in Japan, with the DC-bias reactor we developed in Appendix A. (c) The corona plasma generated (side view) with the nanosecond pulse source we developed in this thesis. In this 100-ns exposure image, the streamers can be clearly seen as bright heads. The image (with a colour map applied) was taken with the ICCD-imaging setup of Chapter 7.

plasma-processing application. From this figure, it is clear that the main parameters that we have available to optimise the entire process chain are the properties of the applied high-voltage pulse. Clarifying the importance of the pulse parameters is one of the main objectives of this thesis.

In this section, we briefly introduced streamer discharges. A much more comprehensive overview of streamers, their initiation, development and propagation can, for instance, be found in the PhD thesis of Sander Nijdam [17]. Furthermore, a very detailed explanation on how streamer discharges can be used for chemical processing was presented in the PhD thesis of Hans Winands in [18, Chapter 2]. Finally, while we have commented on the avalanche and streamer discharges here, there are other types of non-thermal discharges, such as the Townsend and the glow discharge. A detailed description of all types of non-thermal discharges was composed by Fridman *et al.* in [3].

1.2   Nanosecond pulsed corona plasmas

The radicals that a streamer generates and that are needed for air purification typically only exist for hundreds of nanoseconds to hundreds of microseconds before they react

with other particles in the gas [22]. On that time scale, the gas that has to be treated practically stands still. Therefore, a large number of distributed streamers is necessary to effectively treat a polluted airflow. A typical streamer plasma which exhibits a large number of distributed streamers is the pulsed corona plasma.

A corona plasma is generated by applying high voltage to a two-electrode reactor such as a wire-cylinder reactor or a wire-plate reactor, where high voltage is applied to the wire electrode and the outer electrode is grounded. In this way, a very high electric field is generated around the wire electrode and a large number of streamer discharges per meter length will occur. If a pulsed voltage is applied to the electrode, multiple streamer discharges are generated that can reach the outer electrode if the voltage is sufficiently high, thereby generating a large homogeneous plasma. The use of short pulses then prevents the development into a full breakdown and results in high-yield radical generation, as was already discussed in the previous section. Figure 1.3 shows some examples of corona plasmas in wire-cylinder reactors. In this thesis, we will also use a corona plasma.

Pulsed corona plasmas are often used for air-purification research because of their large volume and chemical efficiency. For instance, pulsed corona plasmas for air purification have already been studied for a long time not only at Eindhoven University of Technology [18, 19, 21, 23–27], but also at other research institutes and universities around the world, both as small-scale laboratory research (e.g. [6, 7, 11, 28–31]), and as industrial scale operation (e.g. [19, 32–35]). Most studies reported high efficiencies in removing pollutants such as nitrous oxides, sulphur oxides and the production of ozone. In addition, recent research has shown that very short high-voltage pulses achieve the highest efficiencies [5–12]. Figure 1.4 shows some examples of this research.

It appears that short duration, high rise rate pulses produce very efficient streamers for air purification purposes. However, the pulses other researchers used are still relatively long, or have a relatively long rise time. An extensive parametric study with subnanosecond rise time, nanosecond pulse duration pulses investigating the effect of pulse rise time, pulse duration, voltage polarity, and voltage amplitude was never performed. In this thesis we aim to address this shortcoming.

In most studies, pulsed corona plasmas are operated at atmospheric pressure and temperature, because these are representative conditions for the actual applications. In this thesis we will also operate our corona plasma at atmospheric pressure and room temperature (except for the study in Appendix B, which has the specific aim to investigate the dependencies of these parameters on the plasma).

1.3 Project goals

In this thesis we investigate the effect of very fast nanosecond pulses on transient-plasma generation with the purpose of air purification. The goals of this work are inspired by Fig. 1.2 and can subsequently be divided into three categories:

- development of repetitive, adjustable-parameter, nanosecond pulse technology;
- study of the interaction between the nanosecond pulse technology and the plasma;
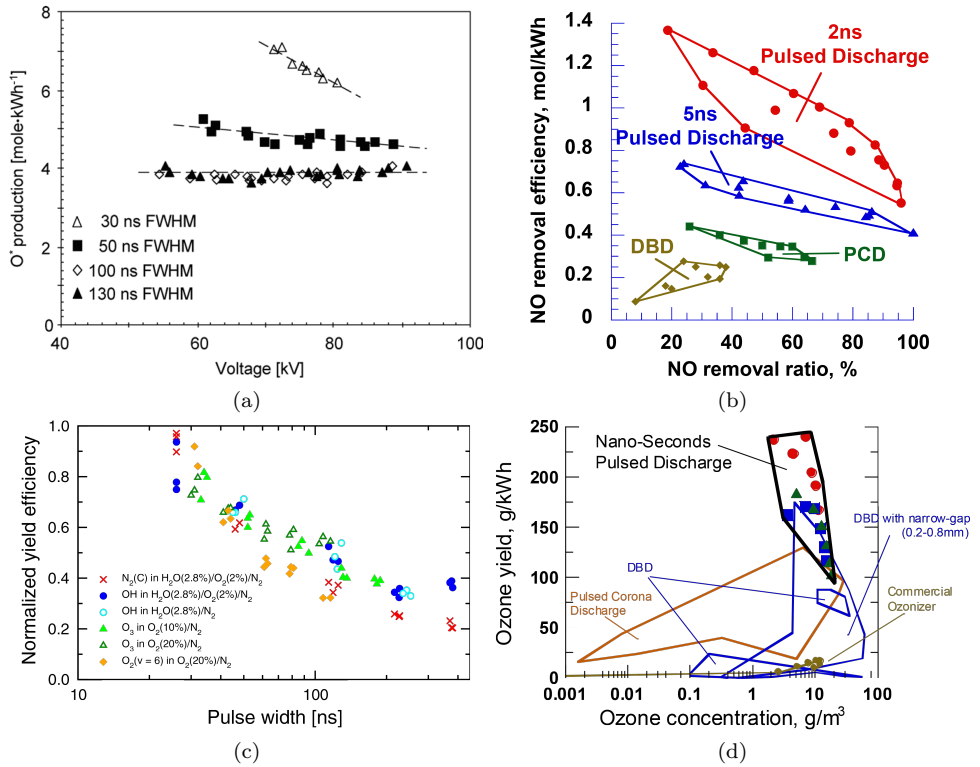
Figure 1.4: This figure shows the effect the pulse duration has on radical generation and plasma processing applications such as NO removal and ozone generation. (a) The oxygen radical yield as a function of the applied voltage and pulse duration in a large corona-plasma reactor [5]. The results indicate that a shorter pulse is more efficient at oxygen radical production than longer pulses. (b) This figure shows the NO-removal yield for different discharge types, such as dielectric barrier discharge plasmas (DBD), pulsed corona discharges (PCD), and nanosecond pulsed discharges [6, 8, combined results]. The nanosecond pulsed discharges are generated by the nanosecond pulse source (at higher than 50-kV positive voltages) of the Kumamoto University, Japan. (c) The yield efficiencies of different types of radicals as a function of the duration of the applied pulses [11]. 20-kV positive voltage pulses of different durations were applied to a point-plane gap. The results show a clear dependency of the obtained yields on the pulse duration: shorter pulses are more efficient. (d) A map of the ozone yield for different discharge types as composed by Wang *et al.* in [36], which again indicates the superiority of very short pulses. All figures are reproduced with permission.

- application of the nanosecond pulse technology to air-purification applications to study the effect of the high-voltage pulse parameters on the process yield.

The first goal is achieved by developing a nanosecond pulse source, a microsecond pulse charger to charge the nanosecond pulse source and high-frequency sensors to

measure the high-voltage pulses from the nanosecond pulse source. Each separate system is designed with the aid of theory and models, after which they are successfully implemented in the total system.

We study the interaction between the nanosecond pulse technology and the plasma by considering the electrical energy transfer from the nanosecond pulse source to the plasma and by optically observing the development of the streamers in the corona reactor as a function of time and position in the reactor. This last study is aided by simulations with an electrical plasma reactor model. The two separate studies provide a method to understand the development and propagation of the streamers as a function of the pulse parameters, as well as giving meaningful information to analyse the results of the plasma-processing experiments.

The last goal is obtained by extensively investigating plasma-processing applications with the wire-cylinder corona-plasma reactor that is energised by the developed nanosecond pulse source for a wide variety of pulse parameters. We study three different air-purification applications to analyse the performance of the nanosecond pulsed plasma: ozone generation, NO removal, and CO_2 dissociation. Combined with the results from the second goal, we are able to comment on the observed results in detail and to establish recommendations on how to apply the developed technologies.

1.4   Organisation of the thesis

The chapters in this thesis are organised in the same way as the project goals: from the technology to the application, just as in Fig. 1.2. Due to the wide variety of topics in this thesis, we omitted a general chapter that explores the state of the art of each topic. Rather, comparative studies and technologies are presented in the introduction of each chapter (and throughout the chapters).

A brief description of the chapters is listed below.

- **Chapter 2** — In this chapter we describe the design of the nanosecond pulse source and present flexible pulse variation ideas. A first implementation is proposed.
- **Chapter 3** — This chapter describes the implementation of the design of the nanosecond pulse source. Two versions are presented: a first 5-ns implementation to verify the pulse duration variation methods we designed, and the final 0.5–10-ns, ± 0–50-kV, subnanosecond rise time pulse source.
- **Chapter 4** — For the operation of the nanosecond pulse source, we developed two auxiliary systems to complete the nanosecond pulse technology. The first is a solid-state, ± 0–120-kV microsecond pulse charger, which is presented in this chapter.
- **Chapter 5** — The second auxiliary system is the high-frequency sensor system, consisting of D-dot and B-dot sensors. This chapter presents the development of these sensors.
- **Chapter 6** — This is the first of two chapters in which we consider the interaction of the nanosecond pulse technology with the transient plasma. In this chapter

we investigate the electrical energy transfer ('matching') of the pulse source to the corona-plasma reactor.

- **Chapter 7** — In this chapter we use ICCD-imaging and a SPICE model to visualise and analyse the streamer development and propagation as a function of time and position in the reactor.
- **Chapter 8** — This chapter describes the results of the plasma-processing experiments with the nanosecond pulse technology. We investigated three different plasma-processing applications: ozone generation, NO removal, and CO_2 conversion.
- **Chapter 9** — In this final chapter we present the conclusions of this thesis, recommendations for future work, and a general outlook.

We added three appendices to this thesis which present the work of transient-plasma studies we performed in parallel with the main study of this thesis. They are highly recommended for the interested reader.

- **Appendix A** — This appendix describes matching experiments on a nanosecond pulse source with a novel DC-bias reactor that was developed during a visit to Kumamoto University, Japan.
- **Appendix B** — In this appendix we show an experimental investigation on how the properties of a streamer plasma depend on temperature and pressure, and the differences between the effects of these two process parameters.
- **Appendix C** — This final short appendix presents the first transient-plasma results that we obtained with the nanosecond pulse technology.

Two

Nanosecond Pulse Technology: Theory and Design

Abstract

In this chapter we present a design approach of a high-voltage single-line nanosecond pulse source by using a thorough analytical investigation and by verification with 3D EM simulations in CST Microwave Studio. Through detailed analysis and simulation we arrive at a design for a fast rise time, variable pulse duration pulse source which is able to produce 1–10-nanosecond pulses with tens of kilovolt amplitude and less than hundreds of picosecond rise time. The variable pulse duration is achieved in two ways: i) by varying the length of the pulse forming line of the pulse source by using telescopic antennas, and ii) by realising a high-ohmic termination of the pulse forming line by means of magnetic material in the pulse forming line. Finally, we present the design of a first implementation of a 5-nanosecond pulse source with an oil spark gap for very fast switching.

2.1   Introduction

In this thesis we will investigate what effect pulse parameters such as pulse duration (1–10 ns), pulse polarity and pulse amplitude (up to 60 kV) have on different transient plasma air-purification applications. Therefore, we need a high-voltage pulse source that is able to generate this variety of pulses.

To achieve a high degree of comparability between the different plasma experiments in this thesis, we chose to build one pulse source with output pulses of variable pulse duration and variable output voltage (both polarity and amplitude) rather than to

---

The content of this chapter has been published previously as [37]:

- T. Huiskamp, S. J. Voeten, E. J. M. van Heesch and A. J. M. Pemen, "Design of a Subnanosecond Rise Time, Variable Pulse Duration, Variable Amplitude, Repetitive, High-Voltage Pulse Source," *Plasma Science, IEEE Transactions on*, vol. 42, no. 1, pp. 127–137, 2014.

build several pulse sources to vary these parameters. The design of this pulse source is the main focus of this chapter.

In Section 2.2 we choose, describe and analyse the type of pulse source for our application. The design of the pulse source will be further refined in Section 2.3 with the aid of time-domain 3D-EM simulations. Subsequently, we present a first implementation of the pulse source in Section 2.4 and finally the conclusions in Section 2.5.

2.2 Pulse source

The requirements for the pulse source for the corona plasma generation in this project are:

- variable output voltage (up to $60\,kV$);
- positive and negative output voltage;
- variable pulse duration (1–10 ns);
- short rise time ($< 250\,ps$);
- square-shaped pulses;
- 50-Ω coaxial output impedance.

The first, second and third requirement are needed to achieve a high degree of flexibility in our plasma experiments and to compare the results of plasmas generated at different pulse-source parameter settings. We chose an upper voltage limit of $60\,kV$ because at this voltage, at the longest pulse setting, we can be sure to have a significant secondary streamer phase in the size of the plasma reactor that we will use. For instance, Wang *et al.* uses a 2-ns rise time, 5-ns pulse duration, 100-kV pulse and imaged the plasma that was generated with this pulse in a larger plasma reactor than we intend to use and observed a strong secondary streamer phase [38].

The rise time-requirement originates from the idea that we want our pulses to rise "as fast as possible" and faster than pulses other researchers used, while remaining within the physical possibilities.

The fifth requirement is needed to ensure that the comparisons between plasma experiments with different pulse source parameter settings can be compared as directly as possible. For instance, if we look at the study performed by Matsumoto *et al.* in [8], we see that a 2-ns pulsed plasma outperforms a 5-ns pulsed plasma for NO removal. However, besides changing the pulse duration, the pulse rise time also changes between these experiments. Therefore, to be able to change only the pulse duration we require the output pulses from our source to be square-shaped.

With the last requirement it will be possible to connect a coaxial cable to the pulse source with minimal insertion losses. The ability to connect a coaxial cable is useful to generate a time delay between the pulse generation and the pulse arrival at the load. This delay is necessary for the triggering of plasma diagnostics such as an ICCD (Intensified Charge Coupled Device) camera.

The incorporation of all our requirements in one pulse source will be challenging. Careful attention to detail and a thorough design and analysis will be required to

achieve these requirements. The end result will be a pulse source that is very flexible and will be useful for various applications and experiments; not only for air purification, but also for water-purification applications and pulsed electric field (PEF) treatment of biological cells [39, 40].

2.2.1 Pulse source selection

Two options can be used to generate fast nanosecond pulses: a semiconductor pulse source or a transmission-line based pulse source [41]. A third option is the magnetic pulse compression (MPC) pulse source [42–45]. This type of pulse source exists in many different topologies and has some advantages over the semiconductor pulse source and the transmission line pulse source. However, the output pulses generated by a MPC pulse source are generally not fast enough to be of real interest for our application.

Semiconductor based nanosecond pulse sources typically make use of the recovery process of specially constructed semiconductor devices [46–48]. Such pulse sources are able to produce sub-nanosecond (hundreds of picoseconds) to nanosecond rise time pulses with pulse durations from several hundred picoseconds to several tens of nanoseconds and amplitudes up to hundreds of kilovolt. However, pulse sources that make use of these devices are not always easy (if not impossible) to adjust in output voltage (amplitude and polarity) and pulse duration and their output voltage is not square-shaped. Also, these semiconductor devices are not commonly available.

A very versatile type of pulse source is the transmission line based pulse source [6–8, 41, 49–51]. Two commonly used variations are the triaxial Blumlein-line pulse source and the single-line pulse source [44]. The advantage of these pulse sources is that they are flexible in output voltage amplitude, polarity and pulse duration. Furthermore they produce square pulses. The advantage of the Blumlein-line pulse source is that the output voltage amplitude is equal to the charging voltage. With the single-line pulse source the output voltage is only half that of the charging voltage, but the spark-gap load is lower (as compared to the Blumlein-line pulse source). Here we have chosen for a single-line pulse source due to its simple design, ease of charging, and because the integration of the spark gap is better suited (lower inductance) for fast rise time pulses.

2.2.2 Principle of operation

Fig. 2.1 shows the proposed single-line pulse source.

A pulse charger charges a pulse forming line (PFL) to voltage V_0. The PFL is then discharged by a self-breakdown spark gap into a matched coaxial cable that is connected to a load (a corona-plasma reactor in our case). The cable acts as a delay line for synchronisation of measuring equipment with the breaking of the spark gap. We chose here for a spark-gap switch instead of an alternative method (e.g. a thyratron or semiconductor switch) because other methods are either to slow, can not handle the high voltage and/or high current, or are unable to switch very fast [41]. We will use an untriggered, self-breakdown spark gap for uncomplicated switching; integrating
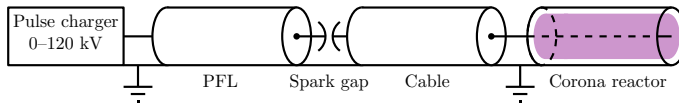
Figure 2.1: Schematic of the single-line pulse source. The pulse charger charges the pulse forming line (PFL) which is then discharged by the spark gap in a matched coaxial cable. When the voltage pulse reaches the corona-plasma reactor it generates a streamer plasma.

a trigger electrode into the spark gap, and still obtaining a fast-rise time design is extremely challenging and might be implemented in the future.

When the spark gap breaks down at t_0, a wave with amplitude $-V_0/2$ propagates from the PFL output (spark-gap side) towards the PFL input (pulse-charger side), where it is reflected back (open end) towards the PFL output and the cable. At the same time (t_0), a wave with amplitude $V_0/2$ propagates through the cable towards the corona-plasma reactor. Together, these waves form the output pulse of the single-line pulse source. The pulse duration Δt is determined by the PFL according to

$$\Delta t = \frac{2l_{\mathrm{PFL}}}{c}\sqrt{\mu_{\mathrm{r,PFL}}\epsilon_{\mathrm{r,PFL}}}, \tag{2.1}$$

where l_{PFL} is the length of the PFL, c is the speed of light in vacuum and $\mu_{\mathrm{r,PFL}}$ and $\epsilon_{\mathrm{r,PFL}}$ are the relative permeability and relative permittivity of the insulating material of the PFL respectively.

Similarly the pulse delay t_{d} that is achieved by the coaxial cable is determined by

$$t_{\mathrm{d}} = \frac{l_{\mathrm{c}}}{c}\sqrt{\mu_{\mathrm{r,c}}\epsilon_{\mathrm{r,c}}}, \tag{2.2}$$

where l_{c} is the length of the cable and $\mu_{\mathrm{r,c}}$ and $\epsilon_{\mathrm{r,c}}$ are the relative permeability and relative permittivity of the insulating material of the cable respectively.

Fig. 2.2 shows a sketch of the waveforms in the pulse source.

The output voltage and the polarity of the pulse source can be controlled by the pulse charger since the output voltage is half that of the PFL charge voltage. The rise time of the output voltage is mainly determined by the geometry of the spark gap and its connection between the PFL and the cable. The pulse duration can be adjusted by modifying the length of the PFL.

A 50-Ω coaxial output impedance is ensured by making the PFL of a coaxial structure. Furthermore, we should choose the inner diameter of the outer conductor d_{o} and the outer diameter of the inner conductor d_{i} such that the transmission-line impedance Z_0 of the PFL is $50\,\Omega$. This impedance is calculated with

$$Z_0 = \frac{1}{2\pi}\sqrt{\frac{\mu_0\mu_{\mathrm{r,PFL}}}{\epsilon_0\epsilon_{\mathrm{r,PFL}}}}\ln\frac{d_{\mathrm{o}}}{d_{\mathrm{i}}}, \tag{2.3}$$

where μ_0 and ϵ_0 are the permeability and permittivity of vacuum respectively.
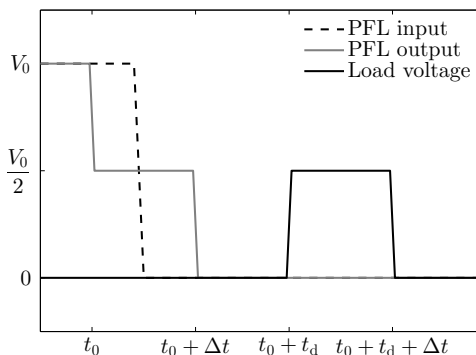
Figure 2.2: A sketch of the waveforms in the pulse source. The output pulse has a duration of Δt (determined by the length and the properties of the insulating material of the PFL) and is delayed by t_d (determined by the length and the properties of the insulating material of the transmission line) seconds. The output voltage is half the charging voltage V_0.

2.2.3 High-voltage insulation

In order to achieve a 60-kV output voltage the PFL has to be charged to $120\,\mathrm{kV}$ (see Fig. 2.2). Also, the diameter of the PFL and other pulse source components must be small to avoid higher-order propagating modes (see Section 2.2.5). These two requirements necessitate a good insulating material to prevent a high-voltage breakdown in the pulse source.

Solid insulators offer good insulating properties, but require very careful construction to avoid air gaps, triple points and surface discharges. Furthermore, they will be irreparably damaged in case of a breakdown.

As a gaseous insulator, SF_6 would be suitable. However, toxic components can be formed in the presence of moisture in the event of a breakdown. It would also need to be pressurised to hold off high voltages, which would lead to a complex and inflexible design. Nitrogen or air could also be used in order to avoid the toxic compounds in the event of a breakdown, but then the pressure would need to be even higher to hold off high voltages [52].

As a liquid insulator, transformer oil has very good high-voltage insulating properties and has the added advantage over a gaseous insulator that it has a relative permittivity of 2.1. Therefore the PFL can be a factor of $\sqrt{2.1}$ shorter (as compared to a gaseous insulator with $\epsilon_\mathrm{r} = 1$) to achieve the required pulse durations (see Eq. 2.1). Moreover, the pulse source will not only be filled with transformer oil, but also needs solid material for mechanical support. Making these mechanical supports from a good high-voltage insulating material like PTFE (Teflon, $\epsilon_\mathrm{r} = 2.1$) ensures that the relative permittivity in the entire pulse source is constant. This will minimise reflections of the voltage pulse within the pulse source. The high-voltage design of the mechanical supports will be made easier because triple points can be avoided (because the dielec-

tric constant of transformer oil and PTFE is the same) and because the breakdown strength of transformer oil and PTFE is roughly equal (around $65\,\text{kV·mm}^{-1}$ for the PFTE we used [53] and $>60\,\text{kV·mm}^{-1}$ for the transformer oil we used [54]). Furthermore, transformer oil has excellent heat transfer properties (especially when compared to a solid or gaseous insulator). For all these advantages we chose transformer oil (Shell Diala S3 ZX-I Dried [54]) as the insulating material for the pulse source.

2.2.4 Oil spark gap

The spark gap that will be used to discharge the PFL in the transmission line needs to be able to switch in a very short time. This requires a compact connection (low inductance) of the spark gap to the PFL and the transmission line and that the impedance of the arc in the spark gap is very low. The first requirement can be met by integrating the spark gap in a coaxial structure with the PFL and the transmission line. The second requirement can be met by making the gap of the spark gap very small ($<1\,\text{mm}$), which could be achieved by creating a spark gap in SF_6 or air at a high pressure (around 2 and $6\,\text{MPa}$ respectively). However, to ensure high-voltage insulation the design of such a gap would be complicated and not very compact. Furthermore, a 50-Ω impedance along the length of the spark gap would be hard to achieve due to the low dielectric constant of the gas, which would result in unwanted reflections of the voltage pulse.

Another way to construct a very compact spark gap is by using an oil gap [49,55–58]. The advantage is the possibility to switch very high voltages across small gaps and it can ensure a 50-Ω impedance along the length of the gap more easily. In addition, the dielectric constant of the insulation will be similar along the entire pulse source. The disadvantage is that oil gaps require a moderate oil pressure to operate properly ($>0.5\,\text{MPa}$) and flushing and filtering to keep the oil clean. However, these conditions can be easily provided for in the design of the gap and by using hydraulic equipment that is commonly available.

Initial experiments with a simple oil gap showed very promising results. We tested an atmospheric pressure oil gap in a simple setup. The results showed high breakdown voltages at low gap distances. The performance is only expected to improve at higher pressures. Therefore, for the proposed pulse source an oil gap will be implemented using the same transformer oil that will be used for the insulation of the PFL.

The hold-off voltage of an oil spark gap is much higher for a pulsed voltage as compared to a DC-voltage [59]. Therefore, we need to charge the PFL of the nanosecond pulse source with a high-voltage pulse with a duration of several microseconds. Shorter pulses would be able to cross the spark gap through capacitive coupling and longer pulses would result in a lower hold-off voltage. The required microsecond pulse charger we developed for this purpose is described in Chapter 4.

2.2.5 Higher-order propagating modes

The electromagnetic waves that are generated by the pulse source should only propagate in the TEM-mode. If part of the pulse can propagate in higher-order modes, these parts can propagate at different velocities, thereby distorting the output pulse shape.

The cut-off frequency f_c above which higher-order modes can propagate is determined by the geometry of the PFL and the transmission line. For a coaxial structure the first higher order mode which can propagate is the TE_{11} mode [60, 61]. Its cut-off wavelength λ_c is given by

$$\lambda_c \approx \pi \left[\frac{d_o + d_i}{2} \right],$$ (2.4)

and the corresponding cut-off frequency by

$$f_c = \frac{c}{\lambda_c \sqrt{\epsilon_{r,PFL}}}.$$ (2.5)

From Eq. 2.4 and 2.5 we see that to increase f_c the coaxial lines must be as small as possible. However a smaller coaxial line also has a higher electric field at the inner conductor as compared to a larger coaxial line.

We apply Gauss' Law to the coaxial line and integrate and rearrange the result to find the electric field at the inner conductor (which is the maximum electric field) as

$$E_{max} = \frac{2V_0}{d_i \ln \frac{d_o}{d_i}}.$$ (2.6)

For the minimum required pulse duration of 1 ns a rise time in the order of 100–200 ps is acceptable. This corresponds to a signal bandwidth of around 3.5–1.75 GHz respectively. If we set this frequency range as f_c we find from Eq. 2.5 (with Z_0 as $50\,\Omega$ and ϵ_r as 2.1) that d_o should be approximately 29–58 mm respectively and d_i 8.7–17.4 mm respectively. This would result in an E_{max} (with $V_0 = 120$ kV) of 23–11.5 kV·mm^{-1} respectively. The DC-breakdown strength of transformer oil and of PTFE is roughly 60 kV·mm^{-1}. This breakdown strength will be higher for a pulsed electric field, but as a safe margin we will take E_{max} at least four times lower than the DC-breakdown strength of the insulating materials. This safe margin might be too conservative, but we have to allow for the high repetition rate of the pulse source and the fact that the oil might become contaminated during the extensive experimental program with the nanosecond pulse source.

From all the trade-offs we choose d_o as 50 mm. This results in an acceptable minimum rise time of 173 ps ($f_c = 2.03$ GHz) and an acceptable E_{max} of 13.3 kV·mm^{-1}.

Another source of signal degradation that was not taken into account in this discussion is dispersion due to the skin effect. However, for a coaxial line of this short length and with these large conductor diameters there will be little dispersion effects. In Section 2.2.6 it will be shown that for a longer coaxial structure dispersion effects due to skin effect will start to be important.

2.2.6 Delay cable

We will use ICCD imaging to study the plasma that is generated by the pulse source (Chapter 7 and in Appendix C). The minimum time delay that is necessary to synchronise the arrival of the pulse at the corona-plasma reactor with the shutter action of the ICCD camera is 60 ns. A long coaxial cable will be connected between the pulse source and the corona-plasma reactor to achieve this delay. The skin effect in the cable at high frequencies will be a source of dispersion and attenuation.

If we consider a coaxial line with length l then the relation between the input voltage V_{in} and the output voltage V_{out} is

$$V_{out} = V_{in}e^{-l\gamma}, \tag{2.7}$$

$$\gamma = \sqrt{(R + j\omega L)(G + j\omega C)}, \tag{2.8}$$

where R is the distributed resistance of the cable, L is the sum of the distributed internal inductance L_i and the distributed external inductance L_e of the cable, G is the distributed conductance of the cable and C is the distributed capacitance of the cable [62].

For high frequencies the skin depth becomes small with respect to the conductor diameters and we get

$$R = \omega L_i = \sqrt{\omega}\lambda, \tag{2.9}$$

$$\lambda = \frac{1}{\pi}\left[\frac{1}{d_i} + \frac{1}{d_o}\right]\sqrt{\frac{\mu}{2\sigma}}, \tag{2.10}$$

where μ is the permeability and σ is the conductivity of the conductor respectively [60].

With these expressions the transfer function of the cable becomes (with G neglected)

$$\frac{V_{out}}{V_{in}} = e^{-l\gamma} = e^{-l\sqrt{[(1+j)\lambda\sqrt{\omega}+j\omega L_e]j\omega C}}. \tag{2.11}$$

From Eq. 2.9 and 2.10 it follows that to minimise dispersion, the diameter of the delay cable in the pulse source should be as large as possible. This is also beneficial from a high-voltage insulation perspective. However, the cable diameter should not be so large as to allow the TE_{11} mode to propagate. Two cables that are worthwhile to investigate are the RG218 cable and the SA24272 cable*. Both are large diameter coaxial cables. Some key characteristics of these cables are listed in Table 2.1. RG58 is also added as a reference. All of these cables have a higher cut-off frequency than the PFL of the pulse source ($f_c = 2.03$ GHz), so they would all suffice with regards to preventing higher-order propagating modes.

---

*The SA24272 cable was manufactured by Suhner (later Huber-Suhner). It was used at Eindhoven University of Technology at the end of the 1980s and the beginning of the 1990s for low-loss signal transport [63, 64]. A technical data sheet of the SA24272 cable is included as an appendix in [63]. A comparable cable in today's market would be for instance the LMR-1700 cable from Times Microwave [65].

Table 2.1: Key characteristics of three types of coaxial cable

	d_o (mm)	d_i (mm)	ϵ_r	f_c (GHz)
RG58	3.5	1	2.3	28
RG218	17.3	4.9	2.3	5.7
SA24272	23.5	8.5	1.5	4.9
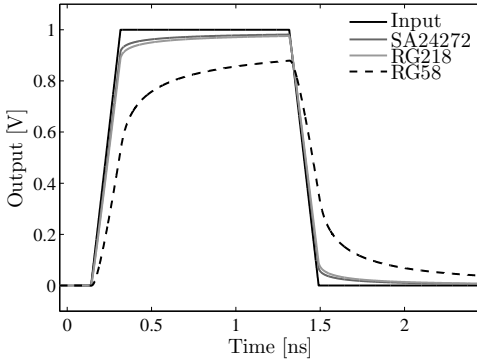
Figure 2.3: Output voltage (normalised to the input) after the input pulse has travelled 60 ns through three types of cable: SA24272, RG218, and RG58.
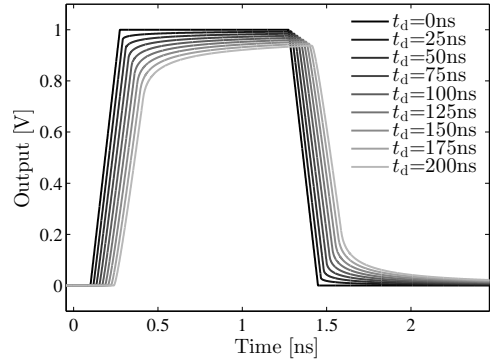
Figure 2.4: Output voltage (normalised to the input) for several delays for the SA24272 cable. For display purposes the waveforms have been shifted with respect to each other.

Fig. 2.3 shows the calculated response (using Eq. 2.11) of the three cables when they are used to achieve a 60 ns delay of a pulse of 173-ps rise and fall time and 1-ns pulse duration (which is the pulse with the highest frequency content that is expected out of the pulse source).

The RG218 and SA24272 cables show less dispersion than the RG58 and of these two the SA24272 is slightly better. If the SA24272 and RG218 would be of the same length the dispersion in the SA24272 cable would be significantly less than in the RG218 cable, but because the dielectric constant of the SA24272 cable is lower than that of the RG218 cable, a longer length of SA24272 cable is needed to achieve a 60-ns delay. We chose the SA24272 cable as a delay cable for the pulse source, because it shows slightly less dispersion than the RG218 cable and because it has a solid outer conductor, which will be important for the application of D-dot and B-dot sensors on the cable (Chapter 5). Fig. 2.4 shows the result of a variety of lengths of SA24272 cable to achieve a variety of delays. It shows that the delay should be kept as short as possible to maintain signal integrity.

The SA24272 cable is not a high-voltage cable by design and has a voltage rating of only 7 kV. However, under pulsed conditions cables can withstand much higher voltages than their rated voltages. For instance, the RG218 cable has an official withstand voltage of 11 kV, yet this cable can operate repetitively at much higher pulsed
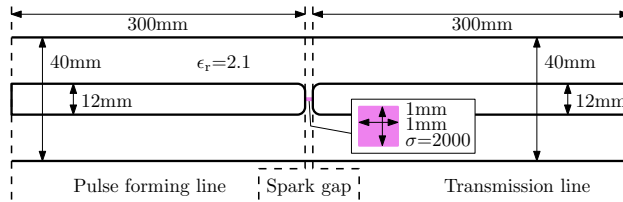
Figure 2.5: Sketch of the basic coaxial geometry of the pulse source (not to scale) that was used in the CST MWS simulations. The PFL is located on the left part and the transmission line with the 50-Ω load (not shown) is to the right. The small section in the middle represents the spark gap.

voltages [25, 66]. With the very short pulses we will generate, cables might be stressed even further without breakdown. Before we built the pulse source with the SA24272 cable, extensive testing showed that the cable can withstand repetitive pulsed voltages (hundreds of nanoseconds pulse duration) of over 80 kV. The final proof that this cable is suitable for our pulse source is that after all the experiments of this thesis ($> 5 \cdot 10^7$ pulses at varying voltage amplitude) there have been no breakdowns.

2.3 CST MWS simulations

With the fundamental basis of the previous section, we will design our pulse source to the specifications proposed at the beginning of that section. For the pulse durations in which we are interested and for our chosen pulse source type, each component acts as a transmission line. Therefore, a transmission-line model of the pulse source can be used to model the behaviour of the nanosecond pulse source. However, (non-symmetrical) small geometry features of the design will influence the properties of the output pulse and will have to be taken into account. Furthermore, the geometry of the spark gap significantly influences the rise time of the output pulse. For these reasons, it is more appropriate to use a 3D electromagnetic solver software package like CST Microwave Studio (CST MWS) to simulate the pulse source [67].

We will use CST MWS to refine and verify and update our pulse source design. Several key problems are solved using the transient (time-domain) solver.

2.3.1 Simulation geometry

Fig. 2.5 shows the basic geometry that we started from. It consists of two coaxial lines connected by the spark gap. The left line is the PFL and the right line is the transmission line that is connected to four evenly spaced 200-Ω resistors (not shown) that make up the 50-Ω load of the pulse source.

In Section 2.2.5 we chose an inner diameter of the outer conductor of 50 mm, whereas the initial pulse source of Fig. 2.5 uses a diameter of 40 mm. This smaller diameter was used in the initial "proof of principle" simulations of this section. The
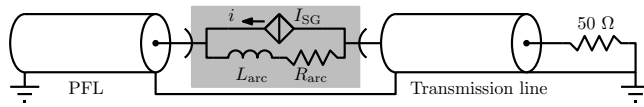
Figure 2.6: Schematic of the spark-gap simulation method. The spark gap is simulated by circulating a current through a ground referenced impedance that simulates the arc impedance of the spark gap. This process charges the PFL and when the current source is switched off the switching of the spark gap is simulated.

50-mm diameter was later chosen after the thorough analytical investigation of Section 2.2. The effect of the difference in diameter on the simulation results appeared to be so small that the results are also representative for a 50-mm outer diameter. Naturally, the later simulations of the actual pulse source design use the correct dimensions (Section 2.4).

2.3.2 Spark gap simulation

The spark gap is simulated by a current source (discrete edge port in CST MWS) inside a piece of conducting material. This simulation method was first described in [68]. The schematic of the configuration is shown in Fig. 2.6.

The current source circulates a predetermined current through the loop $I_{\mathrm{SG}} - L_{\mathrm{arc}} - R_{\mathrm{arc}}$, generating a voltage drop across the spark gap arc impedance $L_{\mathrm{arc}} - R_{\mathrm{arc}}$ (the conducting material between the line inner conductors in Fig. 2.5). Since the arc impedance is ground-referenced via the 50-Ω output impedance at the end of the transmission line, the PFL is charged with respect to ground by the current source-arc impedance combination. After a while a steady-state is reached ($V_{\mathrm{PFL}} = V_0 = I_{\mathrm{SG}} R_{\mathrm{arc}}$) where the PFL is charged and the current ceases to flow in the 50-Ω load. Once this steady-state is reached, the actual simulation of the closure of the spark gap and the pulse formation starts as soon as the current source is turned off, be it instantaneously or gradually. Once the current source is fully turned off it has an infinite impedance and thus has no effect on the simulation. With the fall-time of the current from the current source we can control the rise time of the spark gap current.

Figure 2.7a shows simulation results of the pulse source from Section 2.3.1 simulated in CST MWS with the described spark gap. Figure 2.7b shows a close-up of the same results and corresponds well with the sketch in Fig. 2.2. Here $\Delta t = 3\,\mathrm{ns}$ and $t_{\mathrm{d}} = 1.5\,\mathrm{ns}$. Note that the results are normalised with respect to the amplitude of the output voltage pulse. This convention will be kept throughout the remainder of this chapter.

There are still some small reflections in the load voltage. To reduce these reflections we could replace the four evenly spaced load resistors by a coaxially distributed resistor.

2.3.3 Higher-order propagating modes

In Section 2.2.5 we analysed higher-order propagating modes in the pulse source and found that d_{o} should be 50 mm to achieve a satisfactory minimum rise time and still
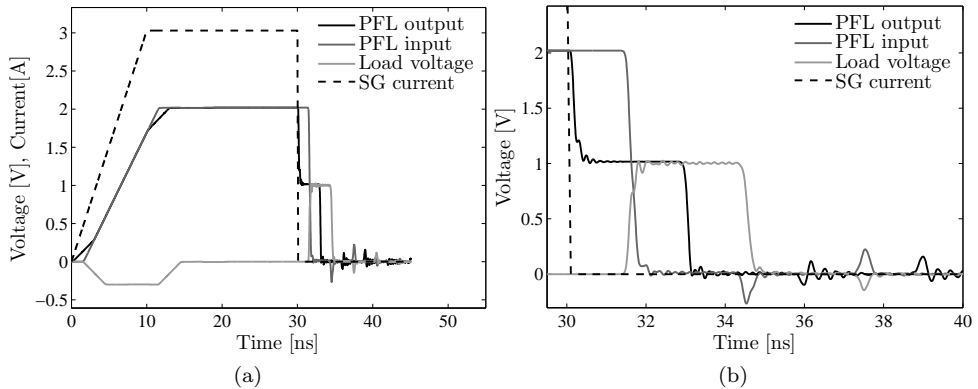
Figure 2.7: (a) A CST MWS simulation of the pulse source represented in Fig. 2.5 (normalised). (b) A close-up of the results.
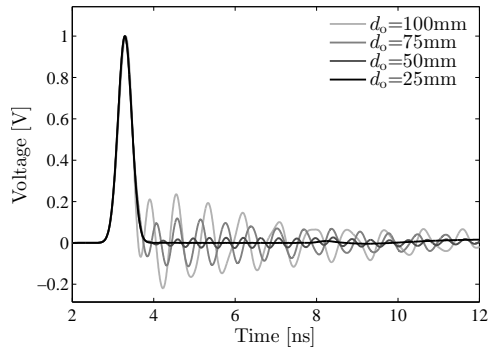
Figure 2.8: CST MWS simulation results to verify the propagation of higher-order modes (normalised). The figure shows the voltage waveforms after a Gaussian pulse with $f_{\max} = 2.03\,\mathrm{GHz}$ has passed through $0.5\,\mathrm{m}$ of a $50\,\Omega$ coaxial structure with four different outer diameters.

maintain a proper HV-design. We simulated a coaxial structure in CST MWS with different values of d_{o} to verify this analysis. We inserted a Gaussian pulse into the 50-Ω coaxial structure with a maximum frequency $f_{\max}$ of $2.03\,\mathrm{GHz}$ (which is the maximum expected signal bandwidth of our pulse) through a waveguide port. Fig. 2.8 shows the waveforms after the pulse passed $0.5\,\mathrm{m}$ through the coaxial structure.

The results show that oscillations in the waveform start from $d_{\mathrm{o}} = 50\,\mathrm{mm}$ and that they are small and acceptable at this diameter. The results also show that for higher values of d_{o} the oscillations become unacceptable. These oscillations are due to part of the pulse propagating in a higher-order mode. Therefore for high values of d_{o} the large diameter can become a serious source of degradation for the pulse waveform. Therefore, the simulations confirm the analysis of Section 2.2.5.

Figure 2.9: The four types of outer conductors used in the simulation results of Fig. 2.10 are: a solid cylinder and a cylindrical outer conductor made up of 12, 8 and 4 rods respectively.
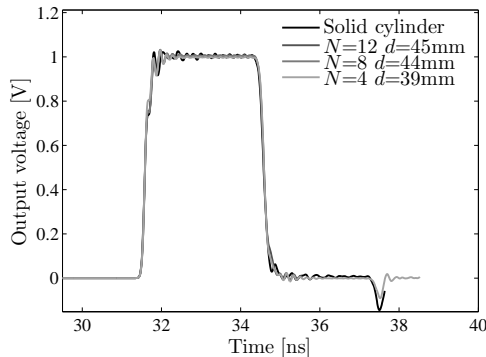
Figure 2.10: CST MWS simulation results (normalised) with different conductor shapes of the PFL outer conductor (see Fig. 2.9).

2.3.4 Variable pulse duration: antennas

In order to achieve a variable duration of the output pulses of the nanosecond pulse source we need to be able to change the length of the PFL, as can be seen in Eq. 2.1. Obviously, we can change the entire line every time we require a different pulse duration, but this is not practical. The first proposed solution to flexibly change the pulse duration is to make the outer conductor of the PFL out of multiple telescopic antennas. Such antennas are commonly found on transmitters of radio controlled cars or old radios. Now the entire outer conductor can change length just by pulling on the antennas. The question that arises is: can the outer conductor be made up of rods (thereby forming a 'squirrel cage') instead of a solid cylindrical conductor? And if so, how many rods are required?

We used the four configurations shown in Fig. 2.9 to answer this question. Fig. 2.10 shows the results of simulations where the outer conductors were made out of $N = 4$, 8 and 12 rods with a diameter of $7\,\mathrm{mm}$. The diameter d of the outer conductor (see Fig. 2.9) was changed on a case by case basis to achieve the best results. When N is low, the impedance of the PFL will be slightly higher as compared to when N is higher, but at the same value of d. This means that when N reduces, d also has to reduce to maintain an impedance of $50\,\Omega$. When the impedance of the PFL is not $50\,\Omega$ the lines will be mismatched and the amplitude of the pulse is incorrect and consequently there is a reflection after the pulse is finished. However, when the impedance is $50\,\Omega$
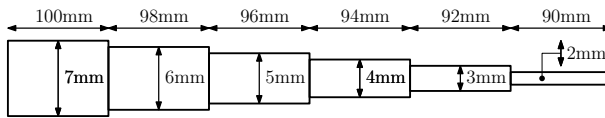
Figure 2.11: Telescopic antenna of which eight are used in the CST MWS simulations. It has six sections.
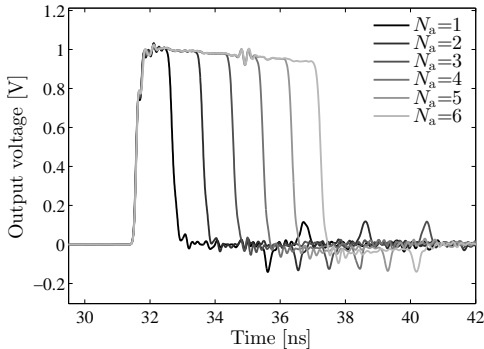
Figure 2.12: CST MWS Simulation results (normalised) with eight antennas, which increase in length as N_a increases.
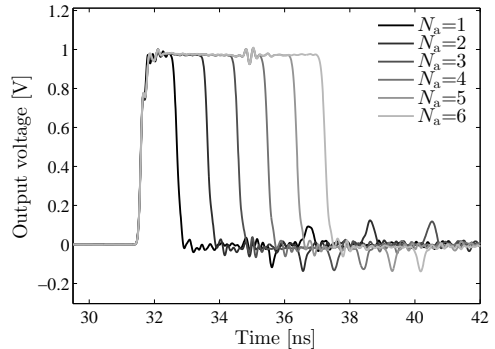
Figure 2.13: CST MWS Simulation results (normalised) with the new antenna configuration of Fig. 2.14.

the results in Fig. 2.10 indicate that even a PFL made up of only four rods still works well as a PFL.

Eight telescopic antennas replace the fixed rods in the next simulations to achieve a variable pulse duration. Fig. 2.11 shows one of the telescopic antennas that was used in the simulation. Each pulse was simulated with a number N_a sections of the antennas extended. For each simulation the length of the inner conductor of the PFL was matched to the length of the antennas (at the end of this section we will show what happens when we keep the inner conductor a constant length). Fig. 2.12 shows the results of the simulations.

The results show that telescopic antennas can indeed be used to create a variable pulse duration pulse source. However, because the sections of the antennas become thinner at the end, the effective impedance of the PFL increases towards the end. This results in a droop of the voltage as the pulse duration increases and a dip in the voltage when the pulse finishes, which is common behaviour for a non-uniform transmission line [69]. Also, there is a small disturbance around 35 ns due to the reflection of the load resistors, which is irrelevant because in a practical implementation we would use a longer transmission line (and a better distributed load).

From the eight antennas we flip the even-numbered antennas such that their thin end is near the spark gap instead of their thick end. The odd-numbered antennas remain in place. Fig. 2.14 illustrates this change in configuration. Now the impedance
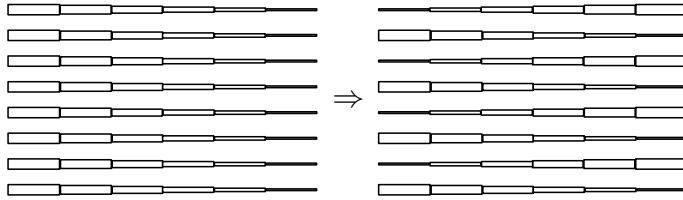
Figure 2.14: Left: all the antennas in the same direction (simulation results of Fig. 2.12). Right: after flipping over the even-numbered antennas (simulation results of Fig. 2.13).
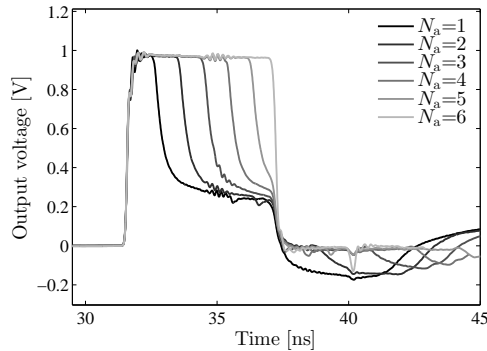
Figure 2.15: Same CST MWS simulations as in Fig. 2.13 but now the inner conductor is 575 mm long in all simulations, as it would be in a real situation.

of the PFL will be more or less constant along its length when it is fully extended. Fig. 2.13 shows the results.

In this case the pulse remains almost flat along the entire pulse duration variation. A slight dip in the middle indicates that the impedance is still not entirely constant along the PFL, but it is significantly better when compared with Fig. 2.12. The results of the simulations show a pulse duration variation of 1–6 ns. The length of the antennas can be adjusted proportionally to achieve the required 1–10-ns pulse duration.

In the first design of the real pulse source the inner conductor will be hollow and will be used as an entry point for the high-pressure oil-flushing system of the spark gap (see Section 2.4). Therefore, changing the length of the inner conductor to match the length of the PFL becomes very impractical. Fig. 2.15 shows the result of simulations where the inner conductor remains 575 mm for all the simulations. The results show that the waveform is not a near-perfect square anymore. This is caused by the wave that originates from the spark gap. This wave now does not reflect entirely on an open end anymore as it did in the simulations of Fig. 2.13. It partly travels along the inner conductor where there is no outer conductor, finally reflecting on the open end.

The results of the simulations show that it is possible to create a variable pulse
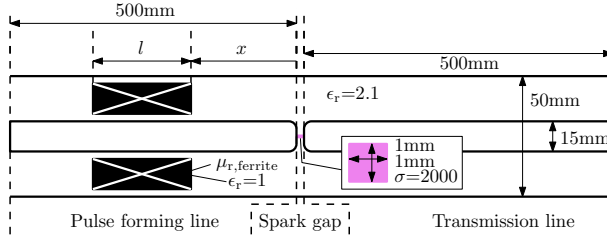
Figure 2.16: Sketch of the basic coaxial geometry of the pulse source with the added ferrite cores that artificially change the length of the PFL (not to scale).
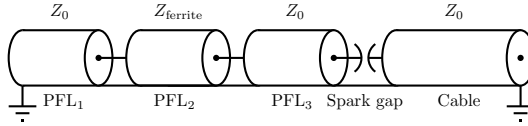
Figure 2.17: Schematic of the single-line pulse source of Fig. 2.16. PFL_1 and PFL_3 are the sections of the PFL without ferrites and PFL_2 is the section with the ferrites.

duration pulse source by using antennas as the outer conductor of the PFL. However, the inner conductor should also change length for the best results, which is difficult in a practical situation.

2.3.5   Variable pulse duration: ferrites

The second proposed solution to create a variable pulse duration pulse source is by using ferrites (or other magnetic material). The pulse formation process to generate a perfect square pulse in the single-line pulse source requires an infinite impedance (open end) at the end of the PFL. This can be easily seen from the reflection coefficient R, which is given by

$$R = \frac{Z_{\text{end}} - Z_0}{Z_{\text{end}} + Z_0},\tag{2.12}$$

where Z_{end} is the impedance that is connected to the end of the PFL. In the case of an ideal open end $Z_{\text{end}} = \infty$, $R = 1$ and the wave is reflected back completely.

It is possible to artificially change the length of the PFL by inserting ferrite cores around the inner conductor of the PFL. This is illustrated by Fig. 2.16 and the resulting schematic in Fig. 2.17. At the position of the ferrites the characteristic impedance of that part of the PFL Z_{ferrite} is given by

$$Z_{\text{ferrite}} = Z_0\sqrt{\mu_{\text{r,ferrite}}\epsilon_{\text{r,PFL}}},\tag{2.13}$$

where $\mu_{\text{r,ferrite}}$ is the relative permeability of the ferrite.
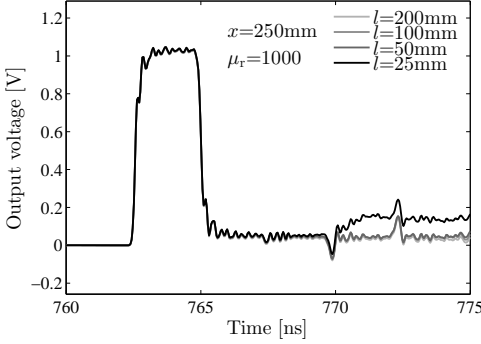
Figure 2.18: CST MWS simulation results (normalised) for when the geometry of Fig. 2.16 is simulated for different values of l.
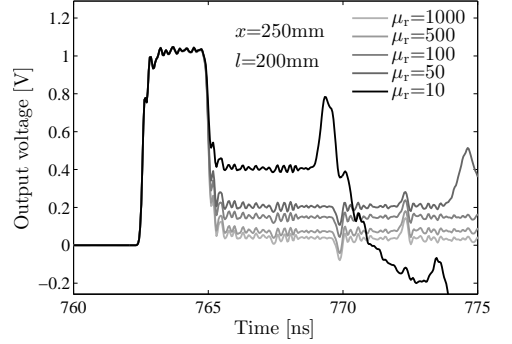
Figure 2.19: CST MWS simulation results (normalised) for when the geometry of Fig. 2.16 is simulated for different values of $\mu_{\mathrm{r,ferrite}}$.
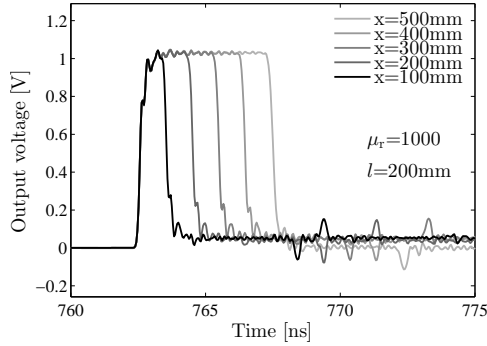
Figure 2.20: CST MWS simulation results (normalised) for when the geometry of Fig. 2.16 is simulated for different values of x.

If we make Z_{ferrite} high enough R approaches 1 and the output waveform of the pulse source will still be roughly square. Now changing the position of the ferrites will change the pulse duration. The disadvantage of this solution is that at $t = 0$, PFL_1 and PFL_2 (see Fig. 2.17) are also charged and will eventually discharge into the load as well.

We simulate the geometry of Fig. 2.16 in CST MWS where we change the length of the ferrite cores l, $\mu_{\mathrm{r,ferrite}}$ and the position of the ferrite cores x. The results are presented in Figs. 2.18–2.20.

Fig. 2.18 shows that the length of the ferrite is not very critical when μ_{r} is very high. This was expected, because in this case Z_{ferrite} is very high (2291) and R is almost 1 (0.96). Fig. 2.19 shows that the effectiveness of the ferrite as an "open end" predictably deteriorates as μ_{ferrite} decreases. When μ_{ferrite} decreases, R decreases and

Table 2.2: Reflection coefficient R for different values of $\mu_{\text{r,ferrite}}$

$\mu_{\text{r,ferrite}}$	Z_{ferrite} (Ω)	R
1000	2291	0.96
500	1620	0.94
100	725	0.87
50	512	0.82
10	229	0.64

the wave is able to partly travel into PFL_2 and consequently into PFL_1. This results in a complicated waveform after the main pulse has finished. Table 2.2 shows how R decreases with $\mu_{\text{r,ferrite}}$. It shows that to keep R high (> 0.9), $\mu_{\text{r,ferrite}}$ must be high as well ($>$ several hundred). Commercially available high-frequency ferrite or magnetic material normally does not have a very high μ_{r} and is non-linear, so this might be challenging in a practical implementation. However, Fig. 2.20 shows that if $\mu_{\text{r,ferrite}}$ is 1000 and is therefore high enough to mimic an "open end", sliding a long ferrite core up and down the PFL indeed achieves a variable pulse duration output pulse. Generating a 1–10-ns pulse is now possible if the PFL is changed to a length of 1 m.

The only concern is that in a practical situation a significant amount of energy will still be stored in PFL_1 and PFL_2 when PFL_3 is discharged. This energy might then start to oscillate in the system.

2.3.6 Variable pulse duration: combination of antennas and ferrites

The disadvantage of creating a pulse source with a variable pulse duration by using an outer conductor of the PFL made out of antennas was that the inner conductor has to change length as well when the length of the outer conductor changes. Using ferrites in the PFL to create a high impedance section in the PFL does not have this disadvantage, but has the problem that there is still energy stored in the parts of the PFL that are not used for the pulse forming process. This energy will start to oscillate after the main pulse. By combining these two options for a variable pulse duration we can obtain a configuration that has neither disadvantages.

Fig. 2.21 shows the combined geometry. It is the same geometry as was used for the simulations of Fig. 2.15 in Section 2.3.4, but now we place a ferrite core at the end of the outer conductor. This prevents the reflected wave from the spark gap travelling along the inner conductor, as it did in the simulations of Fig. 2.15. Furthermore, we now have no extra sections of PFL that are also charged as was the case in Section 2.3.5, which will prevent unwanted oscillations.

In the CST MWS simulations of this section we keep l at 200 mm and change x by extending the antennas as was done previously.

Fig. 2.22 shows the first simulation results with the combined geometry. Here we change $\mu_{\text{r,ferrite}}$ and extend three parts of the antennas ($N_{\text{a}} = 3$) to show the influence of
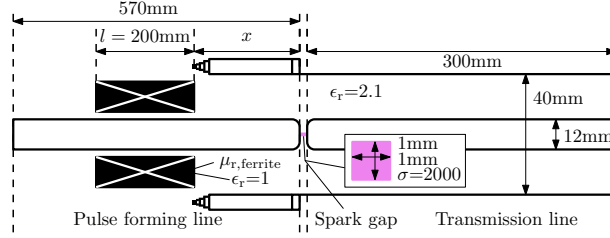
Figure 2.21: Sketch of the basic coaxial geometry of the pulse source that uses a ring of antennas as an outer conductor of the PFL and ferrites to mimic an "open end" (not to scale).
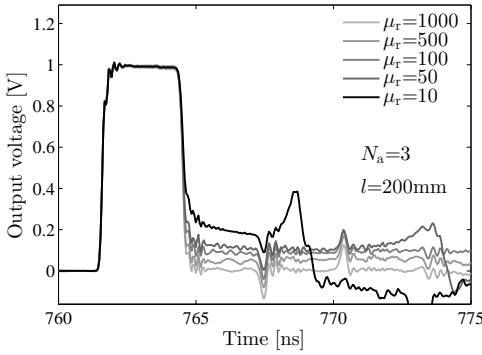
Figure 2.22: CST MWS simulation results (normalised) for when the geometry of Fig. 2.21 is simulated for different values of $\mu_{r,\text{ferrite}}$.
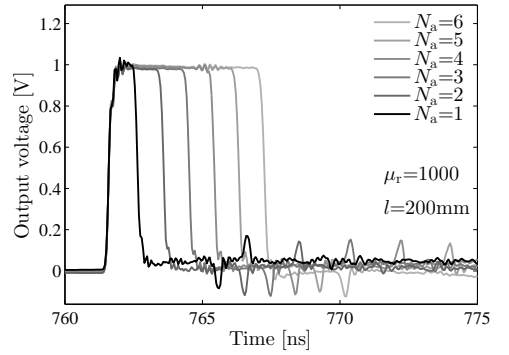
Figure 2.23: CST MWS simulation results (normalised) for when the geometry of Fig. 2.21 is simulated for different values of N_a.

the ferrite material. Compared to Fig. 2.15 the new results show a great improvement in the waveform. Also, comparing Fig. 2.22 with Fig. 2.19 reveals that for the combined geometry the value of $\mu_{r,\text{ferrite}}$ can be lower to achieve an acceptable pulse.

Fig. 2.23 shows the simulation results for when N_a is changed (the ferrites move together with the end of the antennas). The results show that the combination of the two previously discussed options for a variable pulse duration is indeed a new possibility.

2.4 First implementation of the pulse source

We designed a first 5-ns implementation of the pulse source. This pulse source has a fixed-length PFL and has the function to test out the ideas presented in the previous sections before we commit to one of them. Furthermore, the first implementation serves to investigate the performance of an oil spark gap and verify the validity of the CST
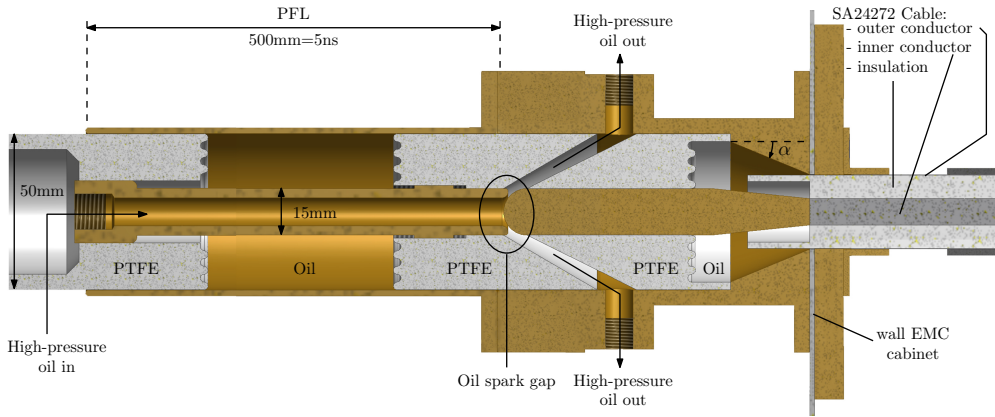
Figure 2.24: Cut-away sketch of the first implementation of the nanosecond pulse source (for display purposes the length and thickness of various parts have been modified). It is a coaxial structure. The left side is a 500-mm long oil-filled 50-Ω structure that comprises the PFL. The inner conductor of the PFL is hollow to allow high-pressure oil to flow to the radial spark gap. The leftmost PTFE section can be rotated to adjust the spark gap distance. After the spark gap, the pulse source is connected to the SA24272 cable that will transmit the output pulses towards the load. A close-up of the spark gap is shown in Fig. 2.25.

MWS simulations.

Fig. 2.24 shows a drawing of the first actual implementation of the pulse source we have built. The inner diameter of the outer conductor is 50 mm and the outer diameter of the inner conductor is 15 mm to obtain a 50-Ω impedance in the transformer oil. The PFL of the pulse source is 500 mm long to obtain pulses with a duration of 5 ns. Furthermore, it has a radial oil spark gap fed by a high pressure oil system, like the spark gap in [57]. A close-up of the radial spark gap is shown in Fig. 2.25. The gap distance in the spark gap can be adjusted by turning the leftmost PTFE part because the inner connector and the middle PTFE part have a screw thread.

The high-voltage insulation of the pulse source is achieved by PTFE and oil for the advantages described in Section 2.2.3. Unlike the high-pressure, flowing oil in the spark gap, the oil used in the insulation will be static and at atmospheric pressure.

The pulse source is connected to the SA24272 cable that was described in Section 2.2.6. The connection of the pulse source to the cable is a tapered connection to avoid sharp edges that result in electric-field enhancement. The angle α (indicated in Fig. 2.24) should be as small as possible to avoid a high field enhancement. However, because the dielectric constant of the cable is unequal to the dielectric constant of the transformer oil, the tapered connection should be as short as possible to avoid a mismatch over a long length. We use oil between the PTFE and the cable connection to fill all the voids at this complicated interface.

The cable connection is simulated in CST MWS with the basic geometry of Fig. 2.5. We increased the length of the PFL to 500 mm and shortened the transmission line
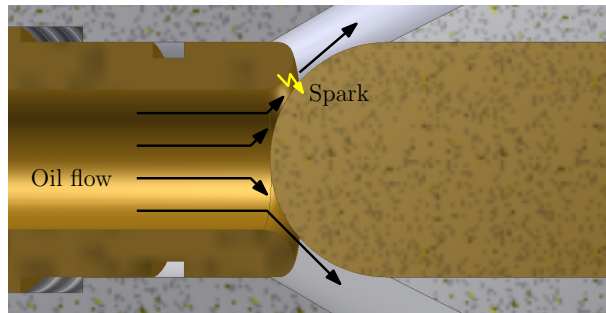
Figure 2.25: Close-up of the spark gap of the first implementation of the pulse source. The spark gap is a radial spark gap with oil flowing from the inner conductor of the PFL towards the oil exhausts in the outer conductor.
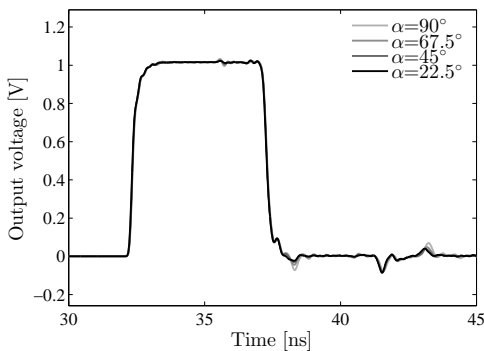
Figure 2.26: CST MWS simulation results (normalised) for different values of α in the cable connection in the first implementation of the pulse source.
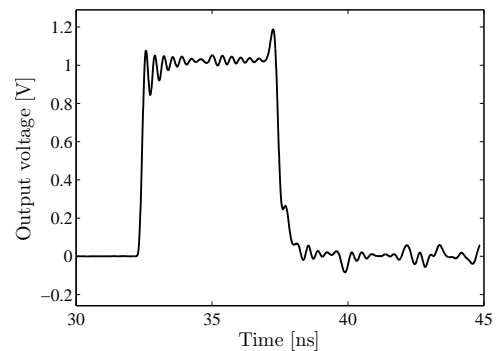
Figure 2.27: CST MWS simulation result (normalised) for the first 5-ns implementation of the pulse source (geometry of Fig. 2.24).

to 100 mm and inserted the cable connection at the end and simulated the geometry for different values of α. The simulation results, shown in Fig. 2.26, indicate that the influence of α is insignificant. We chose α as 22.5 degrees in the first implementation to minimise the electric field enhancement at sharp edges. The next chapter will give more details on the entire experimental setup of the pulse source.

Fig. 2.27 shows the results of the CST MWS simulation of the geometry of Fig. 2.24. The first observation is the high-frequency oscillation in the waveform. This oscillation is introduced by the radial spark gap. The current source used to simulate the spark gap (see Fig. 2.6) now has to be placed under an angle, which is not ideal, because the 3D mesh of the CST MWS simulations is rectangular. By decreasing the mesh size the oscillations become less pronounced. It is difficult to determine whether the oscillations are an inherent property of the geometry or are solely caused by the simulation settings.

In any case, the oscillations are not severe and are acceptable if kept small, because they are not likely to influence the propagation of streamers in the corona-plasma reactor when this pulse is used for transient plasma generation.

The second observation is the peak in the waveform just before it falls back to zero (at $t = 37.5$ ns). This peak is caused by the thicker end of the inner conductor where the high-pressure oil is inserted. This thicker end is necessary to hold the plug for the flexible hose through which the oil flows. The peak is acceptable, because it is small and lasts for such a short time that it will hardly influence the propagation of the streamers in the corona-plasma reactor.

With these last simulations, the design of the first implementation is finished. In the next chapter we describe the implementation and verification of this pulse source and also design and implement the final version of the nanosecond pulse source that will be used for the plasma experiments described in this thesis.

2.5   Summary and conclusions

To investigate what effect pulse parameters such as pulse duration, pulse polarity and pulse amplitude have on different air-purification applications (using a pulsed streamer plasma), we require a pulse source that can provide this variety of pulses. One of the most important requirements for the pulse source is that it can generate very short (1–10 ns) variable pulse duration pulses. Other requirements for the pulse source are a variable output voltage (up to 60 kV and both negative and positive polarity), a 50-Ω output impedance to connect it to a cable (useful for inserting delays for synchronisation purposes), a square-shaped output pulse and a very short rise time (< 250 ps). A transmission-line based single-line pulse source was proposed to meet these requirements, using an oil spark gap for very fast switching.

The single-line pulse source was thoroughly analysed, considering the spark gap, the dispersion in the delay line and possible signal degradation due to higher-order propagating modes in the pulse source. With the basic design finished, the pulse source was then verified and refined with the time-domain 3D EM solver of CST MWS.

The charging of the pulse forming line and the spark gap were modelled with a current source inside a piece of conducting material (which formed the spark gap arc). Furthermore, we investigated how the pulse forming line of the pulse source could be constructed such that the pulse duration could be easily varied.

The first option we proposed replaces the outer conductor of the PFL by telescopic antennas. We used CST MWS to verify that the outer conductor could indeed be made up of only rods (and how to do this). Next we performed simulations with the telescopic antennas. The results show that it is indeed possible to generate variable pulse duration pulses with this configuration. However, the inner conductor of the PFL should also change length for the best results. In a practical situation this would be very difficult because high-pressure oil flows through this conductor.

A second option was proposed that uses sliding ferrites inside the PFL to mimic an "open end". This solution works well for ferrites with a high μ_r, but these might

prove difficult to find in practice. Also, the energy still stored in the PFL behind the ferrites after the discharge will start to oscillate in the system.

A final solution combines both options and uses an outer conductor made out of antennas and a ferrite at the end of this conductor. Now the inner conductor can be of a fixed length and there is no unnecessary energy stored in the system that might oscillate. Furthermore, ferrites with a lower μ_r suffice for this solution.

A first 5-ns implementation of the pulse source was designed to test the various options to vary the pulse duration, to verify the spark-gap performance and to verify the CST MWS simulation methods. In the next chapter we describe the implementation and verification of this pulse source and also design and implement the final version of the nanosecond pulse source that will be used for the plasma experiments described in this thesis.

Three

Nanosecond Pulse Technology: Implementation and Verification

Abstract

In this chapter we present the first and the final implementation of the 0–50-kV picosecond rise time 0.5–10-nanosecond pulse source. The first results with the first implementation show a very sharp 5-ns pulse with a rise time of around 200 ps. Furthermore, the pulse charger connection to the PFL of the nanosecond pulse source has to be made to mimic an open end to avoid a plateau in the waveform after the 5-ns pulse duration. Subsequently, we test the various methods of generating variable pulse duration pulses. The results are good, but show a small plateau after the pulse. This plateau must be avoided for our application — it can sustain the plasma — so a new version is designed.

In the final design the inner conductor and outer conductor both change length to vary the pulse duration. A variation in pulse duration from 0.5–10 ns is possible and the output pulses are square-shaped without the plateau behind the main pulse that was present in the pulses from the first implementation of the nanosecond pulse source.

Last, we investigate the performance of the oil spark gap. We measure breakdown voltages of the oil spark gap as a function of oil pressure, gap distance, charging voltage, and repetition rates, and studied the erosion of the spark gap. The results show that the oil spark gap is a feasible switch for our pulse source and that its lifetime is 10^7–10^8 shots.

The content of this chapter has been published previously in parts as [70, 71]:

- T. Huiskamp, F. J. C. M. Beckers, E. J. M. van Heesch and A. J. M. Pemen, "First Implementation of a Subnanosecond Rise Time, Variable Pulse Duration, Variable Amplitude, Repetitive, High-Voltage Pulse Source," *Plasma Science, IEEE Transactions on*, vol. 42, no. 3, pp. 859–867, 2014.

- T. Huiskamp, E. J. M. van Heesch and A. J. M. Pemen, "Final Implementation of a Subnanosecond Rise Time, Variable Pulse Duration, Variable Amplitude, Repetitive, High-Voltage Pulse Source," *Plasma Science, IEEE Transactions on*, vol. 43, no. 1, pp. 444–451, 2015.
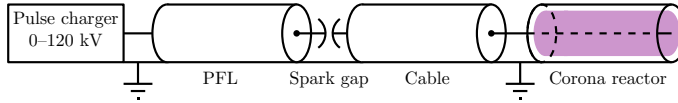
Figure 3.1: Schematic of the single-line pulse source. The pulse charger charges the pulse forming line (PFL) which is then discharged by the spark gap in a matched cable. When the voltage pulse reaches the corona-plasma reactor it generates a streamer plasma.

3.1 Chapter organisation

In Chapter 2 we designed and presented the first 5-nanosecond implementation of the pulse source. It is a single-line pulse source which simplified schematic is shown in Fig. 3.1. In Section 3.2 we will show the experimental details of the first implementation and the results of the experiments. With the results from the first implementation we then present the final implementation of the pulse source in Section 3.3. In Section 3.4 we evaluate the switching behaviour and the erosion of the oil spark gap, followed by the conclusions in Section 3.5.

3.2 First implementation

In this section we describe the experimental setup of the first implementation of the nanosecond pulse source and the subsequent experimental results. Besides the nanosecond pulse source there are two auxiliary systems that are vital for the experiments with (and operation of) the pulse source: D-dot and B-dot sensors and a microsecond pulse charger to charge the PFL of the nanosecond pulse source.

The D-dot and B-dot sensors will be presented in Chapter 5. Together with numerical techniques these sensors enable us to measure the very fast pulses generated by the nanosecond pulse source. A first implementation of the D-dot sensor was used to measure the output pulses in the experiments of the first implementation of the nanosecond pulse source (this section). It is described in detail in Section 5.2. The D-dot sensor is mounted on the SA24272 cable at the output of the pulse source and allows us to measure the output voltage of the pulse source.

A second vital component of the nanosecond pulse source setup is the microsecond pulse charger. As was already stated in Chapter 2, the hold-off voltage of an oil spark gap is much higher for a pulsed voltage as compared to a DC-voltage [59]. Therefore, we need to charge the PFL of the nanosecond pulse source with a high-voltage pulse with a duration of several microseconds. Shorter pulses would be able to cross the spark gap through capacitive coupling and longer pulses would result in a lower hold-off voltage. The required microsecond pulse charger we developed for this purpose is described in Chapter 4 and will be used in the current chapter. As an example, the output voltage of the microsecond pulse charger is shown in Fig. 3.2 for different moments of the spark-gap switch time t_{sg}.
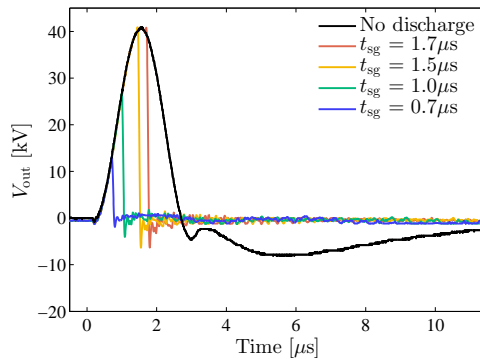
Figure 3.2: The measured output voltage of one pulse charger module connected to the PFL of the nanosecond pulse source for different moments of the spark gap switch time. When the spark gap switches, the PFL is quickly discharged and the output of the pulse charger becomes zero. Chapter 4 gives more information.

3.2.1 Nanosecond pulse source

Fig. 3.3 shows the first implementation of our nanosecond pulse source. It is a 5-ns pulse source, as determined by the length of its PFL. The design of the pulse source was described in detail in the previous chapter.

The load of the pulse source is connected to the SA24272 cable. The load is a 50-Ω resistive load made up of carbon-composite resistors inside a small, seperate EMC cabinet. This load will most likely only be $50\,\Omega$ for low frequencies and is thus not a perfectly matched load. However, for now we are only interested in the initial waveform. Reflections of the pulse are not an issue because the pulse will already have passed the D-dot sensor by the time reflections from the load could appear back at the sensor. The cable is $3\,\mathrm{m}$ long, has the D-dot sensor situated at about $2.25\,\mathrm{m}$ from the load and its insulating material has a dielectric constant ϵ_r of 1.5. Therefore we can measure the first $18.5\,\mathrm{ns}$ of the waveform before the first reflection passes the D-dot sensor.

In the final application the SA24272 cable will be connected to a corona-plasma reactor. Also, the cable will be much longer to facilitate synchronisation between the pulses and diagnostics such as ICCD imaging.

3.2.2 Variable pulse duration testing

Fig. 3.4 shows the four different PFL configurations we used for the experiments in this section. Configuration 1 is the configuration without any modification from Fig. 3.3. It is the fixed 5-ns implementation of the PFL.

In Chapter 2 we proposed three different methods of flexibly varying the pulse duration.
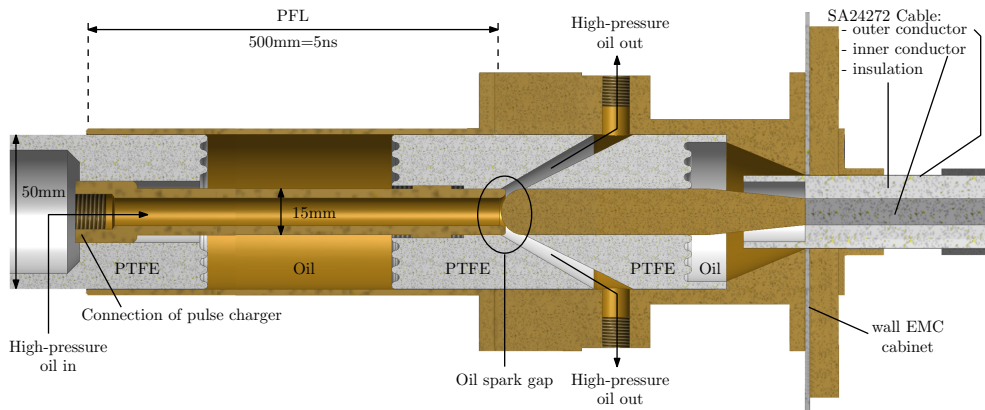
Figure 3.3: Cut-away sketch of the first implementation of the nanosecond pulse source. Not to scale (for display purposes the length and thickness of various parts have been modified). It is a coaxial structure. The left side is a 500 mm-long oil-filled 50-Ω structure that comprises the PFL. The inner conductor of the PFL is hollow to allow high-pressure oil to flow to the radial spark gap. The leftmost PTFE section can be rotated to adjust the spark gap distance. After the spark gap, the pulse source is connected to the SA24272 cable that will transmit the output pulses towards the load. A close-up of the spark gap is shown in Fig. 2.25. The wall of the EMC cabinet in the figure is the wall of the container in which the nanosecond pulse source is placed (see Fig. 3.5).

The first method is to change the length of the outer conductor of the PFL by constructing it out of telescopic antennas. 3D EM simulations showed that the inner conductor should also change length to retain a proper rectangular waveform. Unfortunately this is very impractical in the pulse source due to the oil flushing of the spark gap. To test this method we used a (solid) outer conductor of the PFL that is shorter than the inner conductor (configuration 3 in Fig. 3.4).

The second proposed method to vary the pulse duration was to insert ferrites (or other magnetic material) into the PFL. These ferrites increase the transmission line impedance of the PFL at the position at which they are inserted and therefore reflect the wave that originates from the spark gap when the spark gap switches. This should result in a pulse duration depending on the position of the ferrites. The downside of this method is that the energy stored in the part of the PFL behind the ferrites at the pulse charger side can oscillate, which might be detrimental to the output waveform. Configuration 2 in Fig. 3.4 shows the PFL configuration we used to test this method. Simulations showed that this method works, but only if the permeability μ_{r} of the ferrite is high enough.

The last method combines both previous methods. To prevent unnecessary stored energy in the PFL oscillating in the system we use the first method, but now with the ferrites at the end of the antennas to create a high transmission line impedance to reflect the wave from the spark gap. Configuration 4 in Fig. 3.4 shows the PFL
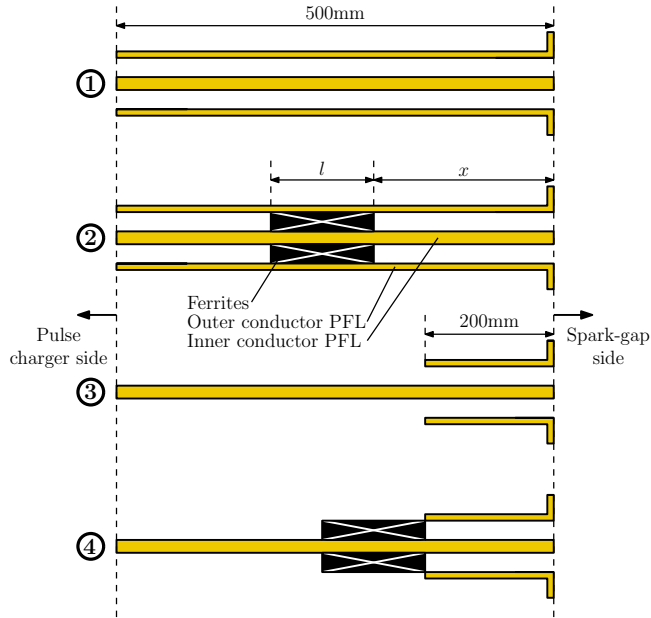
Figure 3.4: The four PFL configurations used in the experiments of this chapter (use Fig. 3.3 as a reference). The first configuration is the unmodified 5-ns implementation of the PFL. Configuration 2 is the PFL with ferrites in the interior to create a high impedance region. Configuration 3 is used to simulate a PFL made out of antennas and configuration 4 is the same as configuration 3 but with ferrites at the end of the outer connector to block the incident wave travelling towards the pulse charger.

configuration we used to test this final method.

3.2.3 Oil setup

The nanosecond pulse source is submerged in a $1.3 \times 0.35 \times 0.3$-m (length×width×height) stainless-steel container filled up to 0.15 m with transformer oil (Shell Diala S3-ZX-I Dried). The container has a lid and acts as an EMC cabinet to shield the outside from the fast electromagnetic phenomena inside the container. Aside from the oil in the container, a second oil system feeds high-pressure oil into the spark gap. Fig. 3.5 shows a schematic of this system. The oil is pumped into a filter and through the spark gap of the nanosecond pulse source. After passing the spark gap, the oil flows back into an oil reservoir. We can set the oil pressure by adjusting the speed of the pump and measure the pressure with a sensor.

The ground of the pulse-charger modules is connected to the container. Therefore, the charger and the nanosecond pulse source share the same ground.
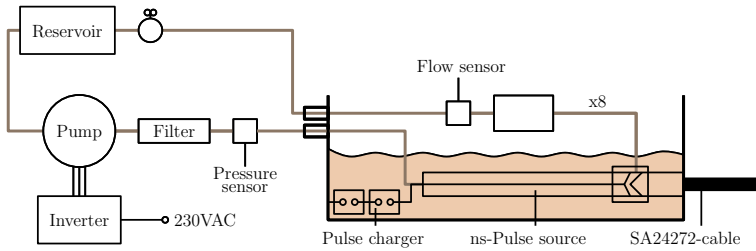
Figure 3.5: The oil system for the spark gap flushing. An oil pump pumps the oil via a filter to the spark gap of the nanosecond pulse source and back into a reservoir. The rest of the nanosecond pulse source system (including the charger of Chapter 4) is submerged in static oil.
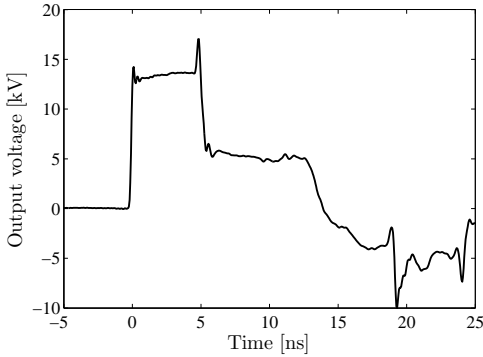
Figure 3.6: The first measured output from the pulse source with the D-dot sensor. Noticeable is the plateau behind the pulse.
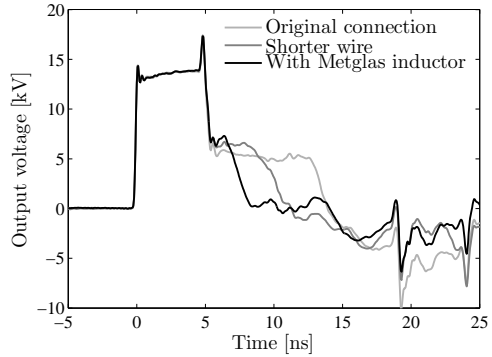
Figure 3.7: Influence of the pulse charger connection to the PFL of the nanosecond pulse source.

3.2.4   Results: connection of the pulse charger

The first result of the first implementation of the nanosecond pulse source is shown in Fig. 3.6.

The pulse is square-shaped, has a rise time of 175 ps and has a duration of 5 ns, just as designed. However, there is a long plateau at the end of the pulse. This plateau results from the connection of the PFL to the pulse charger. As stated in Section 2.2.2, when the spark gap switches a wave propagates back into the PFL towards the charger. Ideally, here it reflects back on a perfect open end at the PFL input. In practice, this is where the pulse charger is connected, which is not an ideal open end. Instead of reflecting perfectly, a part of the wave propagates over the wire that connects the PFL to the pulse charger.

Another observation is the reflected pulse shape that starts from around 19 ns. This is the expected reflection from the load and will be ignored here.
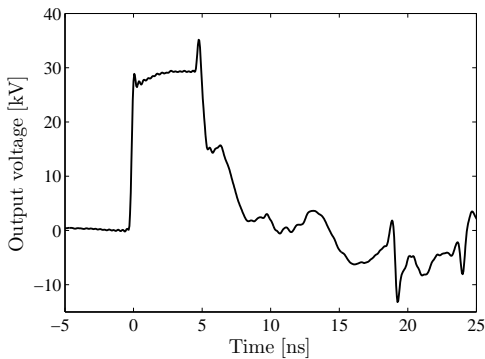
Figure 3.8: The final obtainable output pulse with one pulse charger module.
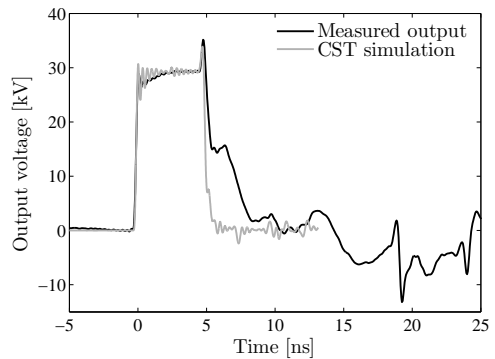
Figure 3.9: Comparison of the simulated waveform in CST MWS and the actual measured waveform.

The plateau that is evident in the pulse shape after the 5-ns pulse duration is unwanted, because when the pulse is used to generate a transient plasma, it could sustain the plasma after the main pulse has ended. We decreased the length of the wire that connects the PFL to the pulse charger as much as possible to minimise the length over which the pulse has to travel towards the chargers before reflecting, which should result in a shorter plateau. This helped, but a plateau was still there, as shown in Fig. 3.7. Then, to mimic the high impedance of an open end, we wound the wire a couple of times around a Metglas magnetic core. This produced a satisfying initial result.

In configurations 2 and 4 of the variable pulse duration tests we will introduce ferrites at the end of the PFL to change the pulse duration of the pulse source. In this situation the connection of the pulse charger is less important. However, if we eventually build a pulse source without these ferrites, extra care should be taken with the connection of the pulse charger.

With one pulse charger module at 60 kV the best obtainable result is shown in Fig. 3.8. These 5-ns pulses were used (with a longer SA24272 cable) for the first plasma experiments with the pulse source in Appendix C and in [72].

3.2.5 Results: comparison with 3D EM simulations

In Section 2.4 we simulated the geometry of Fig. 3.3 in the time-domain solver of CST MWS. Now we can compare the simulated results with the actual measured results. This comparison is shown in Fig. 3.9. The measured pulse and the simulated pulse are a very good match, but there are two discrepancies.

The first discrepancy are the high-frequency oscillations in the waveforms. These are much more severe in the simulated waveform as compared with the real, measured waveform. The severity of the oscillations in the simulations are partly a simulation

artifact of the spark gap due to the mesh properties in CST MWS. A finer mesh reduces the oscillations, but remain present. Since they are also present in the measured waveform, they have a physical origin, which was also observed by Hendriks *et al.* in [73]. They showed that the origin of these oscillations is the way the electromagnetic field propagates from the spark gap towards the cable after the spark gap switches; first the field propagates radially from the spark gap, before being directed towards the output and the PFL. In this process, oscillations occur, which are dependent on the shape of the spark-gap electrodes.

A second discrepancy is the plateau that is still present after the 5-ns pulse duration in the measured waveform, but we already showed that this is due to the connection of the pulse charger and will have to be taken care of in the eventual 1–10-ns pulse source.

A nice similarity between the simulations and the experimental result is the peak at the end of the pulse due to the thicker part of the inner conductor at the end of the PFL. If we want to remove this peak we have to remove the thicker part of the inner conductor and find another method of adjusting the spark gap distance. However, for now this is not deemed necessary, as we suspect it does not influence the streamer propagation in the corona-plasma reactor (much).

3.2.6 Results: variable pulse duration

In Fig. 3.4 we showed three configurations (configuration 2–4) to test the feasibility of the variable pulse duration generation methods put forth in Section 2.3. In the first of these configurations we placed a magnetic material in the PFL and varied the position of this material. We used a stack of Metglas MP4510LDGC magnetic material (initial $\mu_r = 245$). The stack was 100 mm long ($l = 100$ mm in Fig. 3.4). The part of the PFL with the Metglas now has a (theoretical) transmission line impedance of around $1130\,\Omega$ (Section 2.3). The results are shown in Fig. 3.10. The variable x denotes the position of the magnetic material (see Fig. 3.4).

In the results the pulse duration variation is apparent, but far from ideal. A more appropriate magnetic material might improve the results, but when the spark gap switches, the energy stored in the PFL behind the ferrites is still present and starts to oscillate. This can be seen in Fig. 3.10 after the intended pulse duration. When x decreases, the part of the PFL behind the magnetic material contains more energy because the capacitance of this part is higher. Therefore, the oscillation period is longer, which can also be observed in the results. It is doubtful whether this oscillation can be prevented by additional measures and therefore configuration 2 seems implausible for variable pulse duration generation.

In configurations 3 and 4 we shortened the outer conductor of the PFL to 200 mm and used stacks of different types of magnetic material around the inner conductor at $x = 200$ mm. Each stack of magnetic material was 100 mm long. Figure 3.11 shows the results of the experiments.

We started with no magnetic material and the results show a pulse which is initially 2 ns (as desired) but has a high plateau behind it. This is not surprising, because now
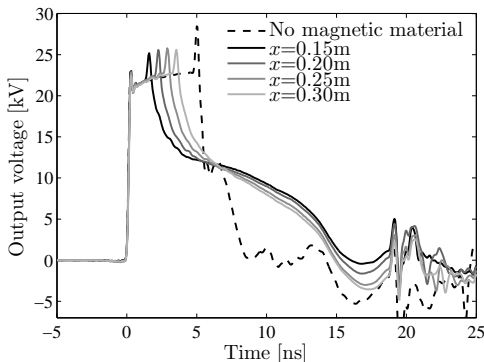
Figure 3.10: The results of experiments with configuration 2 of Fig. 3.4. The ferrites are a stack of Metglas MP4510LDGC cores with $l = 100$ mm.
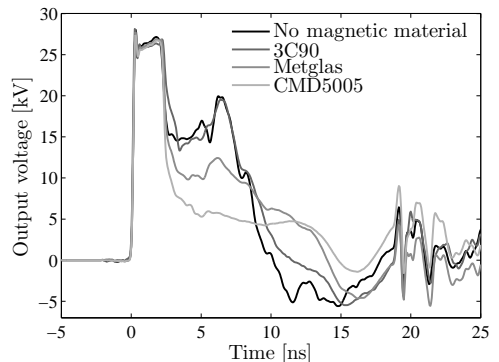
Figure 3.11: The results of experiments with configuration 3 and 4 of Fig. 3.4. The ferrites are a stack of different magnetic materials with $l = 100$ mm at $x = 200$ mm.

the wave from the spark gap can propagate unhindered over the inner conductor to the pulse charger before reflecting. A stack of 3C90 ferrites does not improve the pulse much. Again, this is no surprise, because 3C90 ferrite is standard power-electronics ferrite that can only be used efficiently up to frequencies far below (up to several hundreds of kHz) the frequencies in the nanosecond pulse source. The last two magnetic materials we used are pulsed power cores from Metglas (MP4510LDGC material) and National Magnetics Group (CMD5005 material). These magnetic materials both give improved results, where the CMD5005 material is best. A more appropriate magnetic material might improve the results, but it is clear that with a magnetic material at the end of the outer conductor of the PFL a 2-ns pulse can be created. However, there is still a plateau at the end of the pulse. A test with a longer stack of CMD5005 material shows that more material does not improve the pulse by much. This is shown in Fig. 3.12.

The experiments with configurations 3 and 4 show that it is possible to generate a pulse with a variable pulse duration by changing the length of the outer conductor of the PFL and adding magnetic material at the end of this conductor. This suggests that the solution with an outer conductor made of telescopic antennas with magnetic material at the end is feasible.

It depends on the application whether the plateau at the end of the pulse is an issue. For a plasma application it might mean that more energy is added to the plasma when the main pulse has already finished. Therefore, for our plasma application the first implementation of the pulse source with the variable pulse duration methods we proposed is deemed insufficient. To remove the plateau behind the pulse, the PFL should be made of an adjustable-length outer conductor as well as an adjustable-length inner conductor, coupled to a PFL-charging method that mimics an open end. We will use this method in the final implementation of the pulse source in the next section.
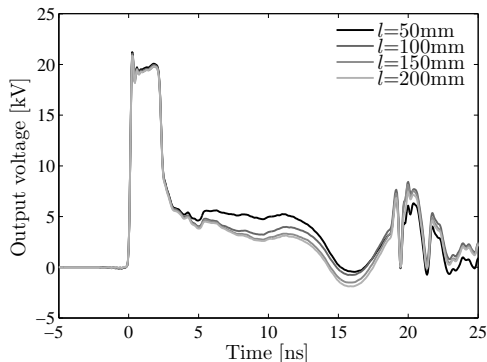
Figure 3.12: The results of experiments with configuration 4 of Fig. 3.4 where we used CM5005 magnetic materials at $x = 200\,\mathrm{mm}$ with different values of l.
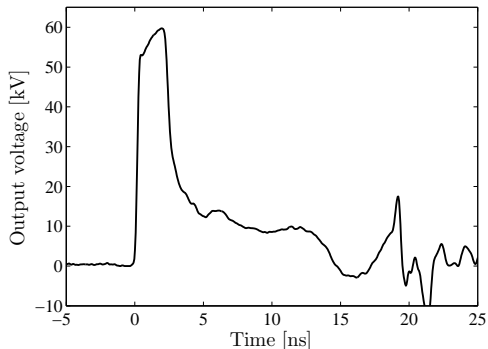
Figure 3.13: The maximum obtainable output voltage of the pulse source. Here we used configuration 4 of Fig. 3.4 with CMD5005 material at $x = 200\,\mathrm{mm}$ and with $l = 200\,\mathrm{mm}$.

If we compare the variable pulse duration results of this section with the CST MWS simulations of Section 2.3 we observe that there are some similarities between the simulations and the measured waveforms (e.g. Fig. 2.22 and Fig. 3.11). However, mostly the results are very different. Two reasons the results differ are the connection to the pulse charger (which is absent in the simulation) and the reflection of the load in the measured results, but the main reason for the difference are the magnetic properties of the used materials. In the CST MWS simulations these materials are ideal and have a high and constant permeability, whereas the real materials have more complex properties such as non-linearity, saturation and losses. Furthermore, at the high frequencies that occur in the pulse source, the permeability of the materials will likely be very low.

As a final experiment, we used the maximum voltage of the pulse chargers to generate a 60-kV pulse. Figure 3.13 shows the resulting output pulse. this confirms that our targeted voltage level can be reached with the present design.

3.3 Final implementation

In the previous section we showed a method to vary the pulse duration in the nanosecond pulse source that worked, but caused a plateau behind the main pulse which was regarded as a problem for plasma generation. In this section we present the final implementation of the nanosecond pulse source that provides a solution for this issue.

3.3.1 Nanosecond pulse source

In the new design of the pulse source the inner and outer PFL conductor both have to change length in order to obtain a variable pulse duration without a plateau at the end of the pulse. We re-designed the oil input of the spark gap in such a way that the
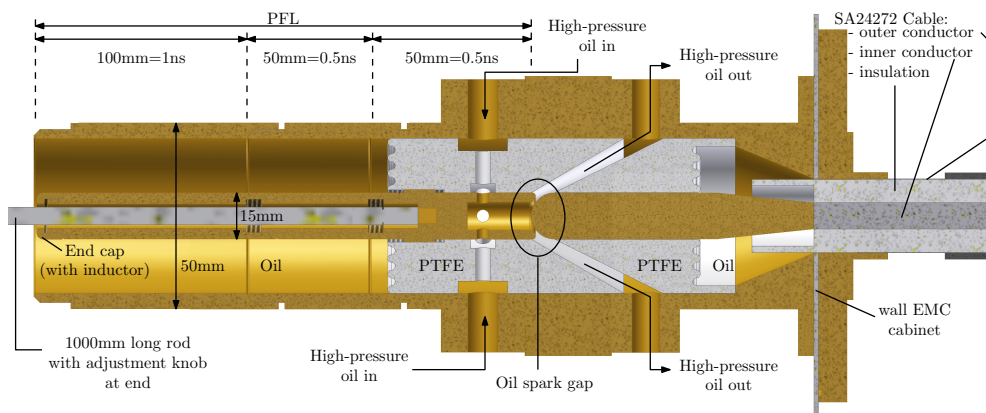
Figure 3.14: Cut-away sketch of the final implementation of the nanosecond pulse source. Not to scale (for display purposes the length and thickness of various parts have been modified). The oil is now fed into the spark gap through the PTFE support between the PFL and the spark gap. The duration of the output pulse can be varied by adding or removing sections of the inner and outer conductor of the PFL. Each large section of 100 mm represents a 1-ns pulse duration and the smaller sections of 50 mm represent a pulse duration of 0.5 ns. Both the inner and outer conductor sections of the PFL are threaded so that they can be easily connected together. A 1000-mm long rod inserted into the inner conductors of the PFL has an adjustment knob on the end to rotate the inner conductors and thereby change the gap distance in the spark gap. A close-up of the spark gap is shown in Fig. 3.29. The end cap can be replaced with an end cap with an attached inductor (see Section 3.3.2).

inner conductor can be removed and changed (in the first implementation of the pulse source the inner conductor served as the oil input). Now the oil is fed through the PTFE support between the PFL and the spark gap. Furthermore, the length of the PFL can be changed by adding or removing sections of the inner and outer conductor. Figure 3.14 shows the design of the new pulse source.

Sections of 100 mm and 50 mm of inner and outer conductor represent 1-ns and 0.5-ns pulse durations respectively. They can be added up to a total length of 1000 mm (10 ns). This results in a pulse duration variability of 0.5–10 ns in steps of 0.5 ns. The spark-gap distance can still be adjusted by rotating the inner conductor, but in the new version of the pulse source this is implemented with a long rod in the centre of the inner conductors at the end of which an adjustment knob (not shown in the figure) is attached. This adjustment knob is removed during operation of the pulse source.

The oil system for the final implementation of the nanosecond pulse source is slightly adapted from the previous version and is shown in Fig. 3.15. Also a longer SA24272 cable is connected to the pulse source to enable ICCD imaging. New D-dot and B-dot sensors were installed on this cable. These sensors are described in Section 5.3.

Previously, we simulated the pulse source with CST MWS. We use the same simulation technique to simulate the new design of the nanosecond pulse source. Figure 3.16
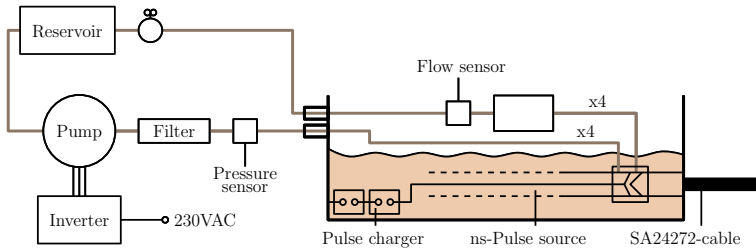
Figure 3.15: The adapted oil-system for the spark gap flushing. Now the spark-gap oil is fed into the PFL at a different position.
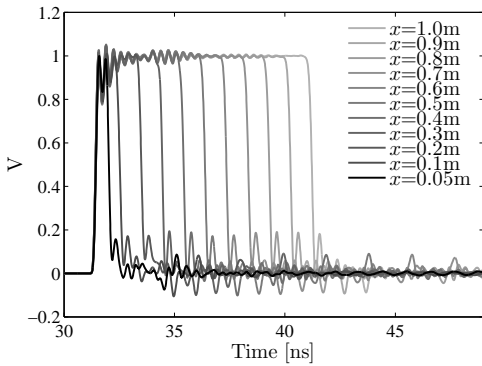
Figure 3.16: CST MWS simulation results of the new pulse source design (normalised). Various numbers of PFL sections were attached to the pulse source to vary the total length x of the PFL.
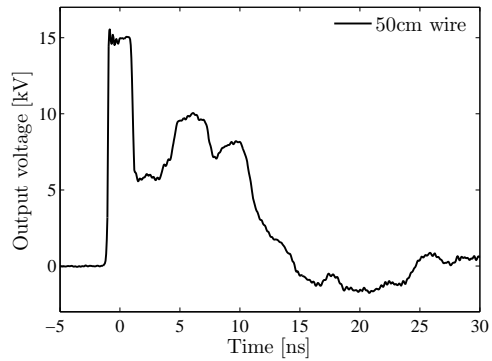
Figure 3.17: The 2-ns output pulse of the pulse source when the pulse charger is connected to the PFL of the nanosecond pulse source by a 0.5-m wire.

shows the results for various number of sections of PFL attached to the pulse source. In the figure, x is the total length of the PFL.

The results show that the pulse duration can be varied from 0.5–10 ns without any deterioration of the pulse shape.

3.3.2 Connection of the pulse charger

During our experiments with the first implementation of the pulse source we noticed that the connection of the pulse charger to the nanosecond pulse source is an important consideration. Ideally, the wave that travels from the spark gap to the end of the PFL should reflect on a perfect open end to generate a perfect square-shaped output pulse. In reality the end of the PFL is the position where the pulse charger is connected to charge the PFL. Therefore, the wave is partially transmitted over the wire that connects the PFL to the pulse charger. It will reflect on the pulse charger and add
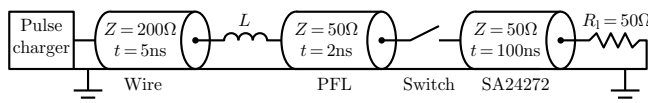
Figure 3.18: The simulation circuit in LTspice we used to simulate the connection of the pulse charger to the PFL of the nanosecond pulse source. The wire connecting the pulse charger to the PFL, the PFL and the SA24272 cable are represented by lossless transmission lines. The spark gap is represented by an ideal switch. The inductor under investigation is placed between the wire and the PFL.

to the output pulse at a later point in time. This causes a plateau after the pulse. Figure 3.17 illustrates this problem: it is the 2-ns output of the new pulse source with a 0.5-m-long wire connecting it to the pulse charger.

We require a high impedance between the pulse charger and the PFL of the nanosecond pulse source to decouple the two systems for high frequencies. This ensures that the nanosecond pulses can not travel over the connecting wire. However, the microsecond pulses from the pulse charger should still be able to charge the PFL. An inductor with the right value L would be a good choice for the decoupling impedance, because its impedance increases linearly with frequency: $j\omega L$.

Adding an inductor (a wire wrapped around a Metglas core) between the PFL and the pulse charger achieved moderate success with the first implementation of the nanosecond pulse source in decoupling the two systems. However, the inductor should be placed as close to the PFL and be as compact as possible.

In order to obtain a good indication on how big the inductor should be, we used the circuit of Fig. 3.18 to simulate the pulse charger connection in LTspice, a SPICE (Simulation Program with Integrated Circuit Emphasis) program [74]. The pulse charger block represents the simulation circuit for the microsecond pulse charger that will be described in Chapter 4. All the transmission line components in the circuit are lossless and ideal. The first of these transmission lines represents the wire connecting the pulse charger to the PFL of the nanosecond pulse source, followed by the inductor under investigation and the transmission line representing the PFL itself. An ideal switch represents the oil spark gap and a the third transmission line represents the SA24272 cable. This last transmission line is terminated with a resistor R_l which is equal to the characteristic impedance of the line. This simulation model is very simplistic and ideal, but should give a good impression on the behaviour of the proposed inductor between the pulse charger and the nanosecond pulse source.

Figure 3.19 shows the simulated voltage over R_l for a number of values of L. The results show that for $L = 1000\,\mu\mathrm{H}$ the pulse charger is properly decoupled. However, the practical implementation of such a very large inductor value is difficult to realise. Furthermore, the voltage drop across this inductor while charging the PFL becomes quite large for this inductor value. This indicates that the PFL also starts to become decoupled for the microsecond charging pulse. As a compromise, and after experimental verification, we chose a value for L of $200\,\mu\mathrm{H}$.
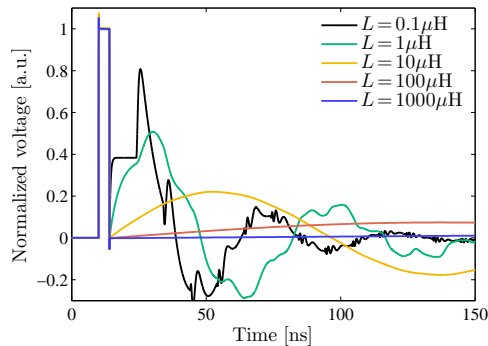
Figure 3.19: The LTspice simulation results of the circuit of Fig. 3.18 for different values of the inductance of L.
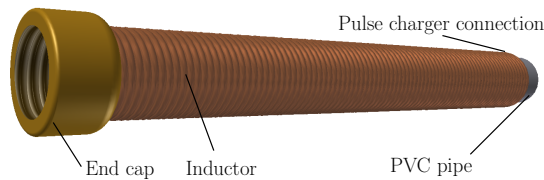
Figure 3.20: Sketch of the decoupling inductor. It is compactly connected to the end cap of the inner conductor of the PFL (see Fig. 3.14).

We designed and built a compact air-cored inductor of around $200\,\mu H$ which is connected to the end cap of the inner conductor of the PFL (see Fig. 3.14) and therefore completely submerged in the transformer oil. This value for the inductor ensures an impedance of only several hundreds of Ohms for the microsecond pulses, but hundreds of kilo Ohms for the nanosecond pulses. Figure 3.20 shows a sketch of the practical implementation of this decoupling inductor and Fig. 3.21 shows the impact it has on the output of the nanosecond pulse source: it is successfully able to remove the plateau from the pulse.

3.3.3 Flexible pulse generation

With the decoupling inductor in place we varied the length of the PFL of the nanosecond pulse source in steps of 1 ns and measured the output pulse. Figure 3.22 shows the results.

The figure shows that the new pulse variation method works very well with square-shaped output pulses as a result. The slight rise towards the end of the pulse for longer pulse durations will be addressed further on in the text. Apart from this issue, the results show very good agreement with the CST MWS simulations of Section 3.3.1. The pulses have a rise time of around 200 ps. This very short rise time is realised by the
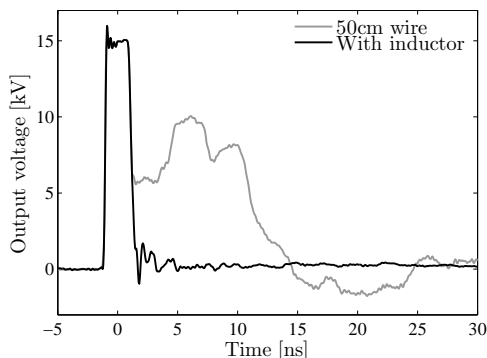
Figure 3.21: These measurements show that the connection of the pulse charger to the PFL with an inductor instead of a 0.5 m wire eliminates the plateau behind the 2-ns pulse.
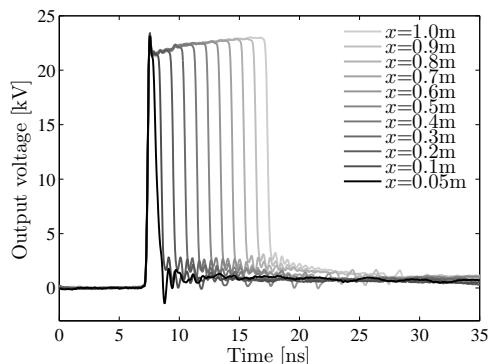
Figure 3.22: The measured output voltage of the pulse source for different lengths of PFL. The pulse duration can be successfully varied between 0.5–10 ns.

compact design of the spark gap. If we would want to decrease this rise time further, we would have to design the spark gap in such a way to mould the electromagnetic wave that is generated in the spark gap [73].

We can vary the output voltage of the nanosecond pulse source by changing the gap distance (in the range 0.2–1 mm) of the spark gap and the charge voltage of the PFL. Figure 3.23 shows the result of such an experiment. The figure shows that a variation in output voltage is possible. The lowest voltage for which the spark gap still performs well is around 3 kV. For the moment, we limit the output voltage of the nanosecond pulse source to 40 kV because there is no load at the end of the SA24272 cable. This results in a doubling of the voltage at the end of the cable, which might damage the cable for higher voltages. This brings the practical output voltage range at the moment to 3–40 kV, which can be extended to at least 3–50 kV on a matched load.

In Fig. 3.22 we already noticed that the pulse rises towards the end of the pulse duration. The results of Fig. 3.23 shows that this effect becomes more pronounced at higher voltages. At low voltages the pulse top is very flat, but at high voltages it takes some time before the pulse reaches its end value. There is no noticeable difference between positive and negative output voltages.

The explanation for the non-flat pulse top at high voltages is an impedance mismatch at the spark gap in the pulse source. When the spark gap switches, one wave travels towards the end of the PFL and another propagates towards the SA24272 cable. However, when there is a slight mismatch at the spark gap, a small part of the wave that should propagate towards the cable is reflected towards the PFL. It then travels the entire length of the PFL, reflects at the end and then adds at the end of the pulse.

The reason that the spark gap is mismatched at high voltages is twofold. First, the gap distance is larger at high voltages and therefore the discontinuity in the 50-Ω
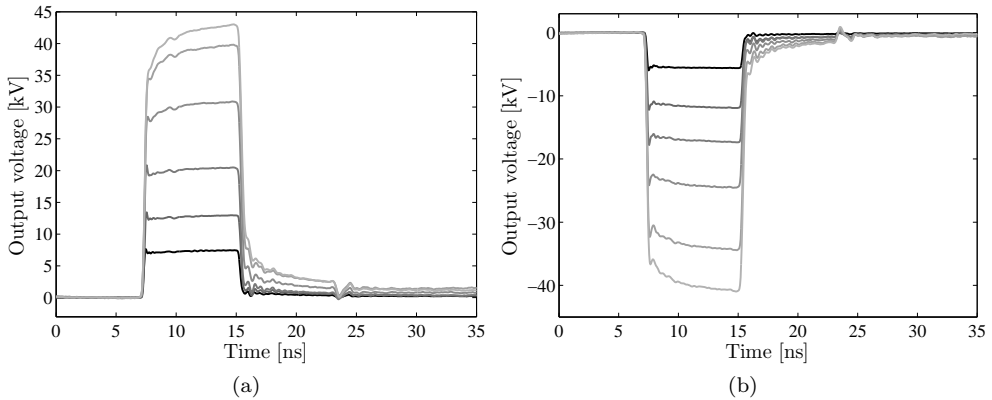
Figure 3.23: The output voltage of the pulse source for different amplitudes at a pulse duration of 8 ns for (a) positive voltages and (b) negative voltages.

structure around the spark gap is bigger. This in itself causes more mismatch than at low voltages. Second, when the spark gap has just switched on the spark channel is very thin. It then heats up and expands. This decreases the resistance of the spark and simultaneously lowers the transmission line impedance of the spark gap. So in time, the mismatch reduces and the wave propagating towards the SA24272 cable is reflected to a lesser extent. Therefore, the voltage rises in time. When the main pulse has passed the spark gap, the original reflected wave arrives at the spark gap, is now not reflected and propagates towards the load. This is the tail that is apparent after the main pulse has finished. The mismatch caused by the expanding spark channel is less pronounced at low voltages because it has less effect at smaller gap distances.

Figure. 3.24 shows a more detailed figure. At t_1 the pulse begins, but its amplitude is lower than when it finishes at t_2 because of the time-dependent mismatch. Between t_2 and t_3 we see the tail caused by the reflected initial wave. To show that this tail is indeed the reflected initial wave, we add this tail (t_2–t_3) to the period t_1–t_2. The result is a square-shaped pulse as it was intended (dashed line).

The tail of the pulse is not nearly as pronounced as the plateau that we had previously with the first implementation of the pulse source (see Fig. 3.13) and is not expected to influence the plasma in the corona-plasma reactor much.

The most straight-forward method to improve the pulse shape at high voltages is to keep the gap distance small. However, the oil pressure would have to be increased significantly (by a factor of at least 10) to be able to switch the very high voltages required for a high output voltage [57]. This is currently not possible in our nanosecond pulse source, but would be an option for the future. For our plasma experiments, the final implementation of our nanosecond pulse source is deemed sufficient.
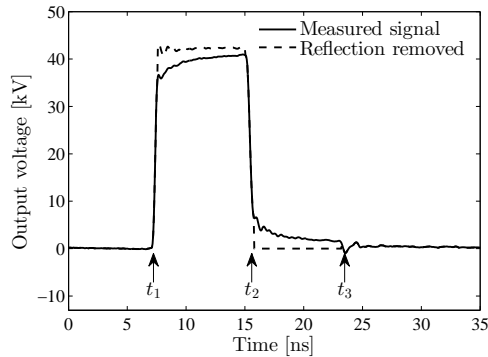
Figure 3.24: The measured output pulse at a high voltage setting. Due to a time-dependent mismatch in the spark gap the pulse only reaches its end value after some time and exhibits a tail behind the main pulse. When the tail (t_2–t_3) is added to the main pulse (t_1–t_2) the result is a square-shaped pulse as it was intended (dashed line).

3.4 Oil spark gap performance

There are important previous studies on oil spark gaps [49, 55–58, 75]. However, at Eindhoven University of Technology we have no previous experience with oil spark gaps. It is therefore essential to investigate some key characteristics of the oil spark gap in the nanosecond pulse source to evaluate its usefulness as a switch. In this section we investigate the switching characteristics and the erosion of the oil spark gap.

3.4.1 Switching performance

We tested the oil spark gap under various conditions to evaluate its performance and to find operating points for the pulse source for certain desired output voltages and repetition rates. Specifically we measured the breakdown voltage V_{HV} of the spark gap at various charging voltages V_{ch}, repetition rates f_r, oil pressures P and gap distances d. For each operating condition we measured hundreds of breakdowns. The resulting data can be represented by a Weibull distribution [57]. Fig. 3.25 shows typical results of one measurement. The breakdown voltage results in this section are calculated using the Weibull distribution.

The results show that there is a significant deviation on the output voltage, which is not unexpected, because it was also reported by other researchers (e.g. in [57]). Therefore, the oil spark gap shows normal behaviour for this type of switch. Later, we will comment on possible improvements to decrease the deviation on the output voltage.

In [57] it was found that the mean breakdown voltage of an oil spark gap increased with increased operating pressure. In our spark gap we can increase the oil pressure only up to 0.5 MPa, an order of magnitude lower than in [57]. Still, it is worth investigating

51
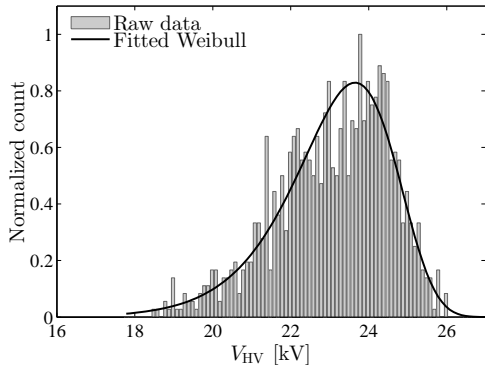
Figure 3.25: Breakdown voltage distribution for hundreds of breakdowns at one spark-gap distance setting for $V_{ch} = 30\,kV$ and $f_r = 10\,Hz$.
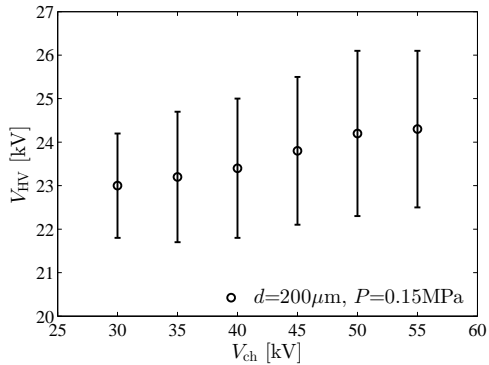
Figure 3.26: Breakdown voltage as a function of the charging voltage of the spark gap.
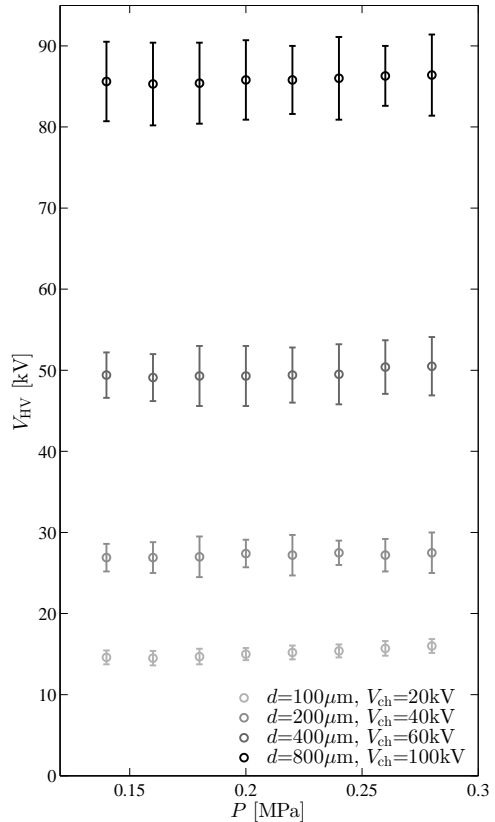
Figure 3.27: Breakdown voltage as a function of the oil pressure in the spark gap for different gap distances for $f_r = 10\,Hz$.

what effect the oil pressure has on the spark gap in our nanosecond pulse source. We tested this at four different gap distances at a repetition rate of 10 Hz. Fig. 3.27 shows the results. The error bars indicate the standard deviation on the breakdown voltage.

From the results it appears that the breakdown voltage increases only slightly with pressure, but the increase is insignificant. Likely, the pressure has to increase much further to show any effect in breakdown voltage.

As a second test, we measured the breakdown voltage as a function of the charging voltage. Fig. 3.26 shows the results. The breakdown voltage increases when the charging voltage increases. At a higher charging voltage the voltage across the spark gap increases faster (higher dV/dt) as compared to low charging voltages. Therefore the spark gap can hold off a higher voltage.

Last, and most important, we tested the breakdown voltage as a function of the
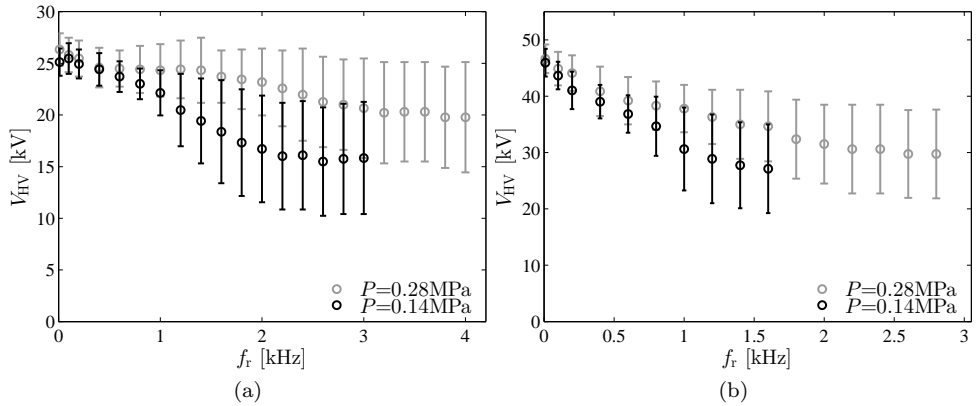
Figure 3.28: Breakdown voltage as a function of the pulse repetition rate and at two different oil pressures with (a) $d = 200\,\mu m$ and (b) $d = 400\,\mu m$

pulse repetition rate f_r. At higher repetition rates the oil gap has less time to recover after a breakdown as compared to low repetition rates. A higher oil pressure (and therefore a higher oil flow) will replenish the oil in the gap faster. Therefore it is expected that the breakdown voltage will remain stable at higher repetition rates when the oil pressure is higher. The results of these experiments are presented in Figs. 3.28a and 3.28b.

The results show that at higher oil pressures the oil gap retains its breakdown voltage longer at higher repetition rates. Also, for a shorter gap distance and therefore a lower breakdown voltage, the oil gap operates more stable at higher repetition rates as compared to a larger gap distance. In the case of a large gap distance more energy is deposited in the gap and a larger volume of oil is influenced by the discharge, which will then take longer to recover under similar oil-flushing conditions. This means that for a higher output voltage of the nanosecond pulse source, the maximum pulse repetition rate is lower. However, from the results it can be concluded that the oil gap performs very well in the nanosecond pulse source and that high repetition rates can be achieved.

3.4.2 Erosion

When the oil spark gap switches, a thin channel of plasma is created between the electrodes of the spark gap. This channel heats up rapidly as the current density through the channel increases. It locally heats the electrodes to very high temperatures, causing melting and evaporation of electrode material. The molten metal at the base of the arc may furthermore be removed from the surface when the surface is rapidly cooled by the oil. A second mechanism of erosion is the formation of liquid jets as vapour bubbles inside the oil collapse [75].

The erosion processes limit the lifetime of the spark gap. Furthermore, debris from the electrodes ends up in the oil, which further limits the lifetime of the oil and the oil
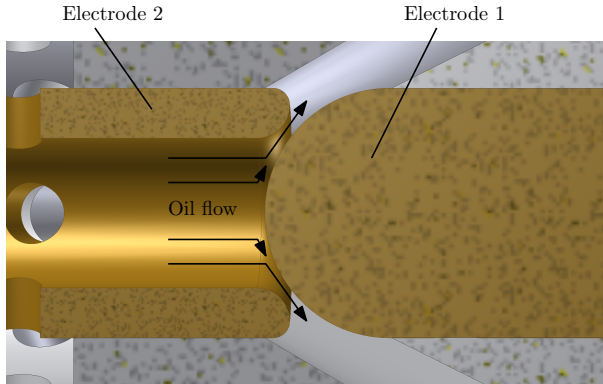
Figure 3.29: Close up cut-away drawing of the oil spark gap in the nanosecond pulse source. Refer to Fig. 3.14 for the drawing of the entire nanosecond pulse source.

filter.

Numerous studies on erosion of electrode materials in gas spark gaps have been carried out previously [76–81]. Unfortunately, there have been little studies on electrode erosion of liquid spark gaps [75, 82]. While electrode erosion is not a key research interest for our nanosecond pulse source, it is worthwhile investigating because of the influence on the life time of the spark gap.

After around $4 \cdot 10^7$ shots of the oil spark gap we removed the electrodes to investigate the amount of electrode erosion the oil spark gap suffered. At this point the spark gap still performed well for high output voltages (>20 kV) — albeit with a higher statistical deviation on the amplitude of the output voltage — but performed poorly at lower output voltages (frequent pre-fires). The output voltage waveform did not change significantly from the situation with new electrodes to the situation after $4 \cdot 10^7$ shots.

Figure 3.29 shows a close up drawing of the spark gap for reference.

Figure 3.30a shows a brass electrode 1 after $4 \cdot 10^7$ shots. An estimated $2 \cdot 10^{-8}$ m^3 of material has been removed from the brass electrode by the discharges. During its lifetime an estimated 35-100 C of charge has been switched by this electrode, which brings the erosion rate of electrode 1 of the oil spark gap in the range of 200–600 μcm$^3 \cdot$C^{-1}. In comparison, brass electrodes in gas spark gaps have erosion rates in the range of 1–100 μcm$^3 \cdot$C^{-1}, with most in the lower part of this range [76, 78, 81]. Therefore, the electrode erosion rate of the brass electrode 1 in the oil spark gap is on average almost an order higher than the brass electrode erosion rates of gas spark gaps. This difference can be readily explained by the role the liquid jets play in the erosion of oil spark gaps [75]. These cavitation effects due to collapsing bubbles are for instance also a major source of propeller erosion on ships [83]. The higher erosion rate of the oil spark gap as compared to a gas spark gap indicates that a future improvement of

(a)

(b)
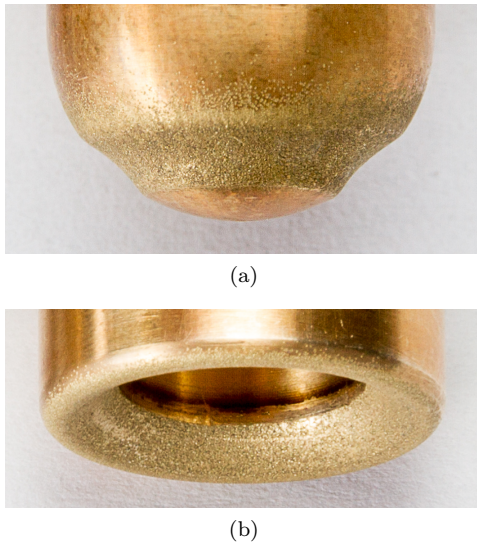
Figure 3.30: Electrode erosion of the electrodes in the oil spark gap of the nanosecond pulse source after $4 \cdot 10^7$ shots. (a) Electrode 1. (b) Electrode 2.

(a)

(b)
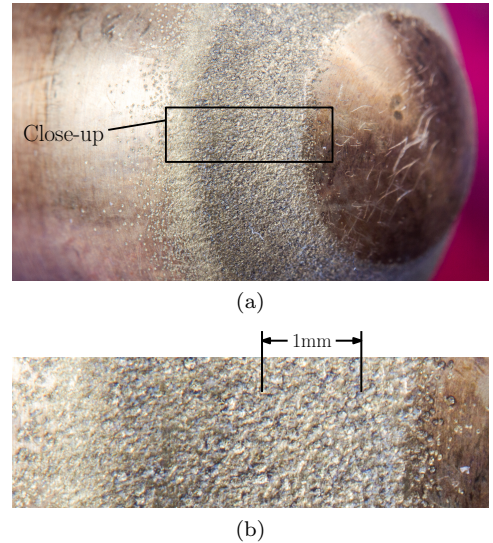
Figure 3.31: A more detailed image of the erosion on the surface of brass electrode 1. (a) Overview. (b) Close-up view, taken from (a), with indicated scale.

the lifetime of the spark gap could be to use a gas spark gap. However, with a gas spark gap we would lose the constant 50-Ω impedance across the length of the pulse source and we would have to operate it at very high pressures to be able to switch high voltages across small gap distances. Using a gas spark gap is therefore deemed unfeasible at the moment.

The erosion of electrode 2 of the oil spark gap shows similar erosion as electrode 1. It is shown in Fig. 3.30b. During about 70 percent of the experiments electrode 2 served as the anode of the spark gap (positive output voltage). An estimated $1 \cdot 10^{-8} \, \mathrm{m}^3$ of material has been removed from the brass electrode 2 by the discharges, which results in an erosion rate of electrode 2 of the oil spark gap in the range of 100–300 $\mu\mathrm{cm}^3 \cdot \mathrm{C}^{-1}$. Therefore, the erosion rate of electrode 2 is only half that of electrode 1. If we consider that electrode 2 was mainly the anode, the result that the cathode erosion rate is higher than the anode erosion rate is consistent with gas spark gap studies, but is also highly dependent on repetition rate and electrode material [78, 81, 84].

Another possible explanation for the higher erosion rate of electrode 1 is that the oil in the spark gap flows from electrode 2 to electrode 1, therefore carrying any debris from the electrodes past electrode 1. This might result in extra intense discharges on the surface of electrode 1. Proof of the latter statement is also evident in Fig. 3.30. There are no erosion pits in the interior of electrode 2 (where the oil flow originates), while there is a significant amount of pits "upstream" on electrode 1. The position of
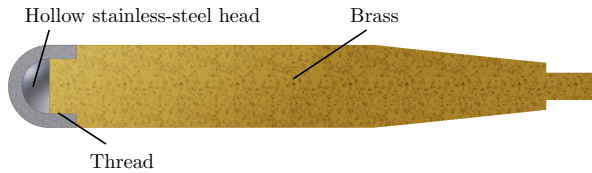
Figure 3.32: Cut-away drawing of the improved electrode 1. Its head can be exchanged while the body remains in place.

these pits on electrode 1 are located away from the highest electric-field region (where the electrodes are closest to each other) and are therefore not likely positions for a self-breakdown discharge of the spark gap.

In gas spark gap studies different electrode materials show different electrode erosion rates. For instance, stainless steel and copper-tungsten alloys seem to outperform brass [78, 80, 81]. Therefore our new electrodes will be made of stainless steel. In our pulse source, electrode 2 is relatively easily exchanged, whereas changing electrode 1 requires the disassembly of the entire pulse source. With this in mind we designed a new electrode 1 for our spark gap. It has a threaded head which can be exchanged without the complete disassembly of the entire pulse source. Furthermore, the head can be made up of a different material than the body allowing for a high-conductivity material body and a hard-material head. A drawing of the new electrode is shown in Fig. 3.32 and will be used in a future implementation of the nanosecond pulse source. The implementation of our nanosecond pulse source with this improved electrode will be the actual final implementation of our pulse source.

Another future improvement of the spark gap electrodes could center around preventing turbulent oil flow around the electrodes and ensuring this flow is laminar by techniques used in [75]. This could decrease the standard deviation on the output pulse amplitude of the nanosecond pulse source that occurs due to a jitter on the moment the spark gap switches. Another method of decreasing this standard deviation is by generating turbulent flow on purpose at certain predefined sites. In this way we might force the discharge to take place there and stabilise it [85].

Currently, we use the spark gap as a self-breakdown switch. Using a triggered spark gap instead of a self-breakdown spark gap might also decrease the standard deviation on the spark-gap switching time. However, to obtain a spark-gap design with integrated trigger electrodes that still has a fast rise time will be challenging. Furthermore, the signal to trigger the spark gap must be a high-voltage pulse as well, so a second pulse source is required with at most a rise time of 10–50 ns.

At the moment, we use the standard deviation on the amplitude of the output voltage to our advantage in our experiments, because it allows us to perform a high number of experiments at different output voltages without having to adjust the spark gap distance constantly. For example, we can investigate the matching of our nanosecond pulse source to a corona-plasma reactor for voltages from 5 to 40 kV with just five spark-gap distances.

A final observation on the electrode erosion of the oil spark gap is the size of the deformations on the electrodes. These appear to be roughly 25–75 μm in diameter, which is consistent with previous studies in gas spark gaps [81]. Figure 3.31 shows a detailed view of the erosion on brass electrode 1.

Considering all the results of this section the oil spark gap is a feasible switch for the nanosecond pulse source and has a lifetime that is sufficient for 10^7–10^8 shots before the electrodes have to be exchanged or repolished.

3.5 Summary and conclusions

In this chapter we presented the first and final implementation of the 0–50-kV picosecond rise time 0.5–10-nanosecond pulse source. The pulse source will be used in the plasma experiments described in this thesis. The first implementation of the pulse source is a single-line pulse source with an oil spark gap which generates 5-nanosecond pulses with a 200-picosecond rise time and can operate at a repetition rate of 1 kHz into a 50-Ω load.

The first results show a very sharp 5-ns pulse with a rise time of around 200 ps. Furthermore, the pulse charger connection to the PFL of the nanosecond pulse source has to be made to mimic an open end to avoid a plateau in the waveform after the 5-ns pulse duration. We then showed that time-domain 3D EM simulations in CST MWS show good agreement with the actual measured waveform.

Subsequently, we tested the various methods of generating variable pulse-duration pulses and discovered that the method to insert magnetic material in the PFL of the nanosecond pulse source is not feasible. However, when we change the length of the outer conductor of the PFL and place magnetic material at the end of the outer conductor, we get the desired result if we choose the right magnetic material. CMD5005 magnetic material gave satisfactory results, but the output pulse still showed a small plateau after the pulse. This is not desirable for our plasma application, so the inner conductor of the PFL has to change length as well when varying the pulse duration.

We then evaluated the performance of the final design, in which the inner conductor and outer conductor both change length to vary the pulse duration. Furthermore, we presented 3D EM simulations of the nanosecond pulse source and showed that the simulations are in good agreement with the measurements. A variation in pulse duration from 0.5–10 ns is possible and the output pulses are square-shaped without the large plateau behind the main pulse that was present in the pulses from the first implementation of the nanosecond pulse source. At high voltages the pulse top becomes less flat due to a time-dependent mismatch in the spark gap, but this is not expected to influence the plasma in our corona-plasma reactor. The lowest voltage for which the spark gap still performs well is around 3 kV. This brings the practical output voltage range to 3–50 kV.

Last, we investigated the performance of the oil spark gap. We measured breakdown voltages of the oil spark gap as a function of oil pressure, gap distance, charging voltage and repetition rates and found that an increase in oil pressure has almost no

effect on the breakdown voltage at low repetition rates. A higher gap distance and charging voltage increase the breakdown voltage and at high repetition rates we need to increase the oil pressure or decrease the gap distance to maintain a stable breakdown. Furthermore, we investigated the electrode erosion of the oil spark gap in the nanosecond pulse source. The erosion rate of the electrodes were in the range of 200–600 μcm$^3 \cdot$C^{-1} for the electrode that was mainly the cathode and 100–300 μcm$^3 \cdot$C^{-1} for the electrode that was mainly the anode. This is almost an order of magnitude higher than most gas spark gap studies show for brass electrodes. Therefore, electrode erosion in the oil spark gap will be a limiting factor on the life time of the system. We designed a new electrode with a stainless-steel head to increase this life time.

What the results of this chapter showed above all was that a pulse source of this kind is suitable to generate ultrashort picosecond rise time pulses and that the final implementation is ready to be used for the plasma experiments.

Four

Auxiliary Systems: Microsecond Pulse Charger

Abstract

In this chapter we present the solid-state 0–120-kV microsecond pulse charger for the nanosecond pulse source of Chapter 3. The pulse forming line of the nanosecond pulse source must be charged with microsecond pulses to prevent the pre-firing of its oil spark gap. The pulse charger consists of two identical compact pulse-charger modules with integrated electronics. The electronics are mounted on a compact PCB and consist mainly of a number of parallel-connected IGBTs that switch a primary capacitor bank into a pulse transformer. Each pulse-charger module can generate 60-kV microsecond pulses at several kHz repetition rate. Connected in series, they are able to deliver up to $120\,\text{kV}$ into a 100-pF load. This 100-pF load is the pulse forming line of our nanosecond pulse source at its maximum length of $1\,\text{m}$. The pulse charger is able to operate in an EMI-unfriendly environment due to its compact layout and optical triggering of the IGBTs.

4.1 Introduction

The first auxiliary system for the nanosecond pulse source is the solid-state pulse 0–120-kV microsecond pulse charger. This chapter introduces this pulse charger.

An oil spark gap is used in the nanosecond pulse source to obtain very fast switching. The hold-off voltage of an oil spark gap is much higher for a pulsed voltage as compared to a DC-voltage [59]. Therefore, we need to charge the PFL of the nanosecond pulse source with a high-voltage pulse with a duration of several microseconds. Shorter pulses would be able to cross the spark gap through capacitive coupling and longer

---

The content of this chapter has been published previously as [86]:

- T. Huiskamp, F. J. C. M. Beckers, E. J. M. van Heesch and A. J. M. Pemen, "A Solid State, 0–120 kV, Microsecond Pulse Charger for a Nanosecond Pulse Source," *Plasma Science, IEEE Transactions on*, vol. 41, no. 12, pp. 3666–3674, 2013.

pulses would result in a lower hold-off voltage. In this chapter we describe the required microsecond pulse charger.

After this introduction the selection, design, simulation and realisation of the pulse charger are presented in Section 4.2. In Section 4.3 we describe and analyse the experimental results, followed by the conclusion in Section 4.4.

4.2   Design of the pulse charger

4.2.1   Requirements

Besides the several-microsecond pulse duration of the pulses, the requirements for the pulse charger are:

- 0–120-kV output voltage;
- positive and negative output voltage;
- able to drive a capacitive load up to 100 pF;
- low jitter in output voltage amplitude;
- able to handle a near short-circuit load;
- pulse repetition rate up to 1 kHz.

The first requirement results from the property that in a single-line pulse source the output voltage is only half the charging voltage [44]. In the previous chapters we defined the output voltage of the nanosecond pulse source as variable up to 60 kV. Therefore the output voltage of the pulse charger has to be variable up to 120 kV.

Second, in our project we are interested in both positive and negative polarity pulses, which results in the second requirement for the pulse charger.

The capacitive load stated in the third requirement is the maximum capacitance of the PFL of the nanosecond pulse source when it is set to 10 ns.

Fourth, using an oil spark gap inherently results in some variance on the amplitude of the output voltage of the nanosecond pulse source. To minimise this variance we require the output of the pulse charger to be stable. The oil spark gap also necessitates the fifth requirement, because when it switches, the output of the pulse charger will see the very low impedance of the transmission line.

Finally, the sixth requirement is needed to generate a larger plasma energy density as compared to when we use a lower repetition rate*.

4.2.2   Pulse source selection

A usual choice for the charging stage of a nanosecond pulsed power system is either a Marx source or a pulse transformer based solution [59, 87]. In our case, the low jitter

---

*At the moment the pulse charger was designed it was still unclear whether the oil spark gap could handle this high repetition rate, but a-priori we needed to incorporate this requirement into the pulse charger. In Chapter 3 we already demonstrated that the spark gap was indeed able to function at very high repetition rates.
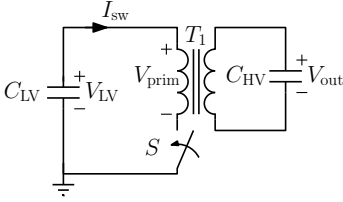
Figure 4.1: A basic pulse charger circuit utilising a pulse transformer. Switch S switches the energy from C_{LV} into the high voltage capacitor via the pulse transformer.
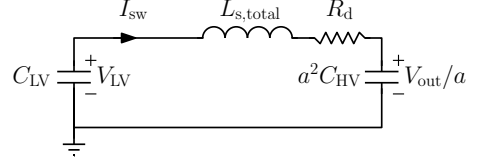
Figure 4.2: The equivalent circuit (transformed to the primary side) of Fig. 4.1 during the resonant charging of C_{HV}.

requirement combined with the high-repetition rate requirement invalidates a spark-gap based Marx source pulse charger. A solid-state Marx source is also a possibility [88–91]. However, it would require a significant amount of capacitor stages and complex engineering to operate one at 120 kV.

A solid state circuit in combination with a pulse transformer would meet all the requirements. It will be this type of pulse charger that we will further analyse and design.

4.2.3 Pulse transformer design

A basic pulse charger circuit utilising a pulse transformer is shown in Fig. 4.1. A primary capacitor C_{LV} is charged by a DC voltage V_{DC}. Then the switch S switches and C_{LV} resonantly discharges into the high-voltage capacitor C_{HV} via the total stray inductance of the transformer $L_{\mathrm{s,total}}$. The equivalent circuit — transformed to the primary side — during the switching period is shown in Fig. 4.2. Here I_{sw} is the current through the primary winding of the transformer (and thus through S), a is the transformer turns ratio ($a = N_2/N_1$, where N_2 and N_1 are the number of turns on the secondary and primary winding respectively) and R_{d} represents the lumped losses in the primary circuit, the secondary circuit and the core of the transformer.

We choose $C_{\mathrm{LV}} = a^2 C_{\mathrm{HV}}$. A lower value for C_{LV} would result in a lower output voltage V_{out} over C_{HV}. A higher value would result in a higher output voltage, but in the event of a sudden impedance drop at the output — e.g. when the spark gap in the nanosecond pulse source switches too early (pre-firing) — I_{sw} would increase beyond the current limit of the switch. This will be illustrated in Section 4.2.4.

Fig. 4.3 shows the waveforms in the circuit of Fig. 4.2 with $C_{\mathrm{LV}} = a^2 C_{\mathrm{HV}}$, $L_{\mathrm{s,total}} \neq 0$ and $R_{\mathrm{d}} = 0$. The oscillation frequency f is given by

$$f = \frac{1}{T} = \frac{1}{2\pi}\sqrt{\frac{2}{C_{\mathrm{LV}}L_{\mathrm{s,total}}}}, \tag{4.1}$$

where T is the time period of the oscillation. If $R_{\mathrm{d}} \neq 0$ then the oscillation will damp. During the analysis of the pulse transformer this damping was neglected.
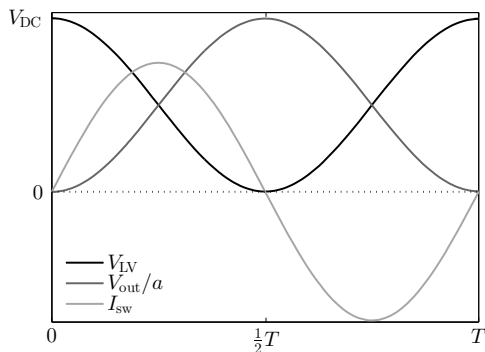
Figure 4.3: LTSpice simulation results of the circuit of Fig. 4.2.

The maximum output voltage $V_{\text{out,max}}$ to which C_{HV} is charged (for $C_{\text{LV}} = a^2 C_{\text{HV}}$) when an ideal transformer is used, is given by

$$V_{\text{out,max}} = a V_{\text{LV}}. \tag{4.2}$$

In reality, the pulse transformer is not ideal and the leakage inductance and losses in the transformer core and windings will cause the voltage to be lower.

We choose a ferrite material for the transformer core instead of air because we require a high coupling factor k between the primary and secondary windings of the transformer. Furthermore, we want to obtain a low electromagnetic-interference (EMI) design, which is improved by a ferrite material that confines the magnetic flux to the pulse-charger core.

We obtain the inductance L_1 of the primary winding and L_2 of the secondary winding with

$$L_x = \frac{N_x^2 \mu_0 A}{\frac{l_c}{\mu_r} + l_g}, \qquad x \in \{1, 2\}, \tag{4.3}$$

where μ_0 is the permeability of vacuum, A is the core cross-section, l_c and l_g are the core length and air-gap length respectively and μ_r is the relative permeability of the core material [92].

The mutual inductance between the windings M is given by

$$M = k\sqrt{L_1 L_2}, \tag{4.4}$$

and the consequent total stray inductance by

$$L_{\text{s,total}} = L_{\text{s,1}} + \frac{L_{\text{s,2}}}{a^2} = \left[L_1 - \frac{M}{a} \right] + \left[\frac{L_2 - Ma}{a^2} \right]. \tag{4.5}$$

There are three important limiting mechanisms in the design of the pulse transformer:

- the maximum practical magnetic flux density $B_{\max}$ of the ferrite material;
- losses in the ferrite material;
- the maximum current through the switch.

First, the flux density in the core of the transformer is given by

$$B = \frac{\phi}{A} = \frac{\int_0^T V_{\mathrm{prim}} dt}{N_1 A} \approx \frac{V_{\mathrm{DC}} T}{2 N_1 A}, \tag{4.6}$$

where ϕ is the flux through the core, V_{prim} is the voltage across the primary winding. The integral over V_{prim} is taken over T because when the spark gap in the nanosecond pulse source fails to fire, a positive voltage is applied to the primary winding throughout the entire period T.

Second, the losses in the ferrite material increase with f. This results in an upper limit of f dictated by the chosen ferrite material.

Third, the maximum current through the primary circuit is determined by the switch type that is used for S. In our application a maximum switch current I_{sw} of $1.5\,\mathrm{kA}$ is acceptable. This value results from a trade-off between a high complexity and a high current (multiple semiconductor switches connected in parallel) and a low complexity and a low current (a small number of parallel-connected semiconductor switches).

The maximum switch current $I_{\mathrm{sw,max}}$ is given by

$$I_{\mathrm{sw,max}} = \frac{V_{\mathrm{LV}}}{2\pi f L_{\mathrm{s,total}}}. \tag{4.7}$$

With 4.1–4.7 it is possible to select a ferrite core and design the pulse transformer. We added an extra requirement that the output voltage of the pulse charger should be $150\,\mathrm{kV}$, because we neglected R_{d} and in a practical implementation there will always be losses.

Unfortunately, within the limits we set ourselves and those that are set by the commercially available ferrite materials, a solution with just a single ferrite-core pair was not feasible. Instead we used two identical pulse-charger modules and connected them in series.

The series connection of the pulse-charger modules is illustrated by Fig. 4.4. This configuration means that each pulse-charger module should be able to charge twice the total load. For instance, if two modules in series have to charge $100\,\mathrm{pF}$, then each module on its own should be able to charge $200\,\mathrm{pF}$, since the total capacitive load can be seen as twice the total capacitive load in a series connection (as illustrated by Fig. 4.4).

An added advantage of multiple pulse-charger modules is that they can also serve as stand-alone pulse sources for other applications, such as pulsed DBD-plasmas [93–95].

The specifications of the final pulse transformers are listed in Table 4.1. In Section 4.2.5 we describe how the pulse transformers are built.
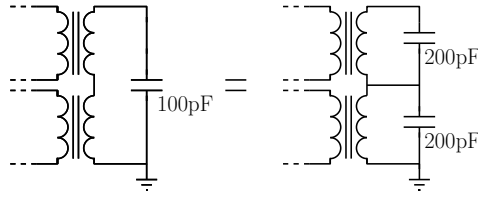
Figure 4.4: Schematic representation of how the transformers of the two identical pulse-charger modules can be connected in series. The load each pulse-charger module sees doubles when they are connected in series.

Table 4.1: Key (measured) characteristics of each pulse transformer.

Description	Value
Ferrite	4 x E100/60/28 3C92
l_{g}	0.8 mm
N_1	2
N_2	180
k	0.99
L_1	7.6 μH
L_2	61 mH
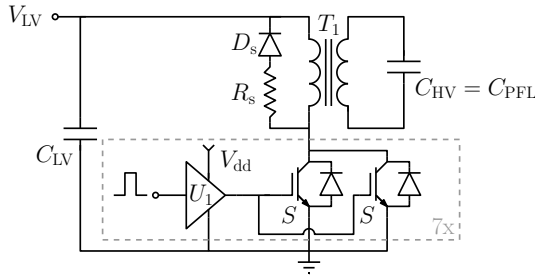
Figure 4.5: Schematic representation of one of the two identical pulse-charger modules of the pulse charger. The switch is implemented with IGBTs.

4.2.4 Circuit design and simulation

The most important component in the circuit that energises the pulse transformer is the solid-state switch. MOSFETs and IGBTs are both good candidates for the switch. We chose IGBTs because the high switching speed of MOSFETs is not needed and IGBTs are available with excellent high-current conducting capabilities and high voltage ratings. To handle the maximum allowed current of 1.5 kA we placed fourteen 1200V-IRGP30B120KD IGBTs in parallel. The complete circuit schematic of one of the pulse-charger modules is shown in Fig. 4.5.
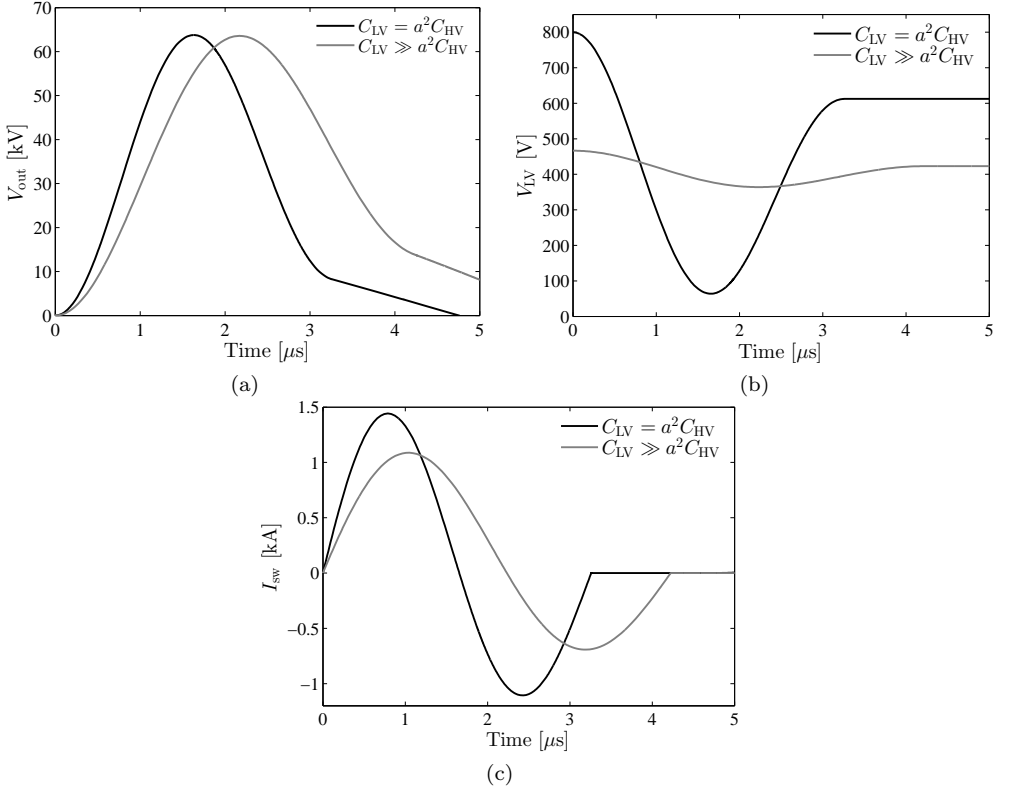
Figure 4.6: LTSpice simulation results of the circuit in Fig. 4.5. The output voltage (a), the primary capacitor voltage (b) and the switch current (c) for a matched and a mismatched C_{LV}.

The diode D_s and resistor R_s constitute a snubber over the primary winding of the transformer. When the spark gap of the nanosecond pulse source fails to switch, the snubber will dissipate the energy stored in C_{HV}. Therefore, the snubber prevents the energy from oscillating between C_{LV} and C_{HV}, while dissipating in the pulse transformer.

Capacitor matching

Fig. 4.6 shows LTSpice simulation results of one pulse-charger module for $C_{LV} = a^2 C_{HV}$ and $C_{LV} \gg a^2 C_{HV}$ when the spark gap of the nanosecond pulse source does not switch. In this simulation we assumed $R_d = 0.05\,\Omega$, which we implemented as a resistance in the primary winding of the pulse transformer. We varied the initial voltage on C_{LV} to obtain the same maximum output voltage on C_{HV}.

The results show that for $C_{LV} \gg a^2 C_{HV}$ the DC charging voltage can be lower,
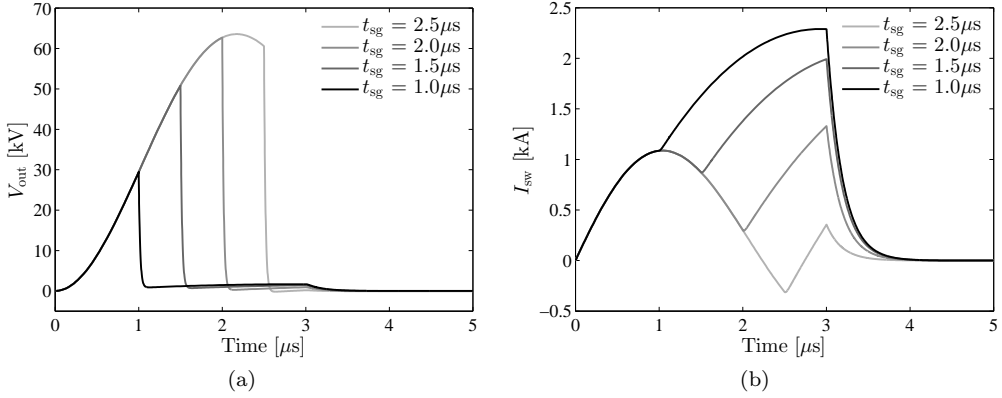
Figure 4.7: The output voltage (a) and the switch current (b) for different spark gap switch moments when $C_{LV} \gg a^2 C_{HV}$.
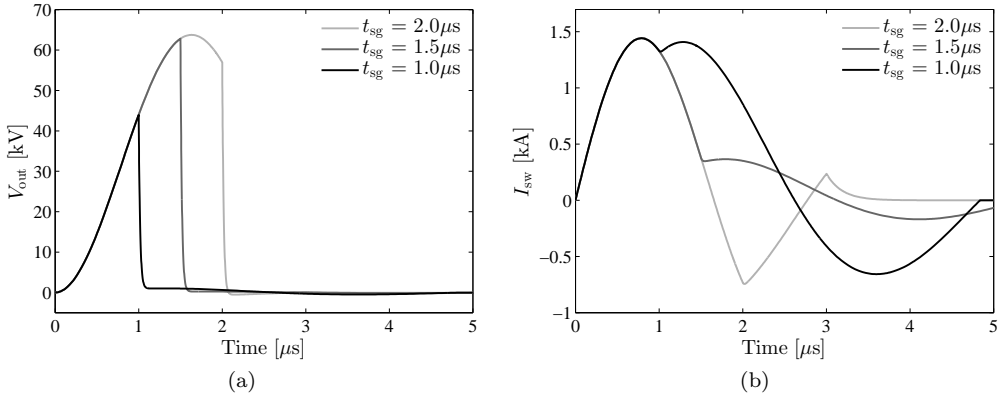
Figure 4.8: The output voltage (a) and the switch current (b) for different spark gap switch moments when $C_{LV} = a^2 C_{HV}$.

the maximum current through the switch is lower and that the oscillation frequency is lower when compared to the case for which $C_{LV} = a^2 C_{HV}$. Only the contribution of $\int_0^T V_{prim} dt$ in Eq. 4.6 is about 34 percent higher for $C_{LV} \gg a^2 C_{HV}$, which means that the flux density in the ferrite core is higher. However, the choice for a matched C_{LV} becomes truly apparent when the spark gap in the nanosecond pulse source switches. This situation is presented in the simulation results of Fig. 4.7 for $C_{LV} \gg a^2 C_{HV}$ and in Fig. 4.8 for $C_{LV} = a^2 C_{HV}$.

When the spark gap switches at $t = t_{sg}$, this results in the complete discharge of C_{LV}. When $C_{LV} \gg a^2 C_{HV}$, I_{sw} becomes very high and the oscillation frequency of the discharge becomes very low. This is illustrated in Fig. 4.7. At $t = 3\,\mu s$ the IGBT control signal switches off, because when the spark gap does not switch, this is the
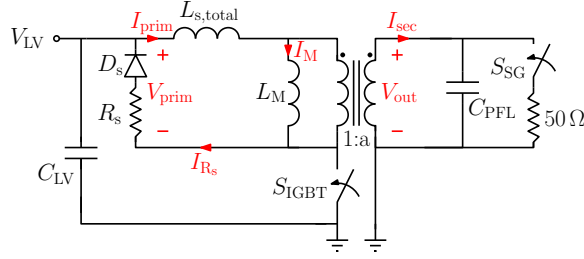
Figure 4.9: The circuit that we used to obtain the simulated waveforms of Fig. 4.10. The IGBTs are represented by an ideal switch S_{IGBT}- and the transformer is replaced by an ideal transformer, where the magnetising inductance and the total stray inductance are placed at the primary side of the transformer. The currents and voltages that Fig. 4.10 shows are coloured red in the circuit. The load of the transformer is the capacitance of the PFL, which is discharged in a 50-Ω load when the spark gap of the nanosecond pulse source (represented by an ideal switch S_{SG}) switches.

time where the diodes of the IGBTs are already conducting. Consequently, the IGBTs switch off a large current and the inductance in the circuit will result in a voltage spike across the IGBTs which could destroy them. This will not happen when $C_{\text{LV}} = a^2 C_{\text{HV}}$ because C_{LV} is already discharging fully when the spark gap switches.

A zero-current detection with feedback to the IGBT-control circuit could prevent the IGBTs switching off while conducting a large current when $C_{\text{LV}} \gg a^2 C_{\text{HV}}$, but besides adding complexity to the control this does not prevent the large peak current through the IGBTs and a very long oscillation period.

Transformer circuit simulation

We replace the transformer in Fig. 4.5 with a model of a transformer to get a better insight into the currents and voltages involved in the switching of the transformer and obtain the circuit in Fig. 4.9. The model of the transformer consists of an ideal transformer with turns ration 1:a, the total stray inductance (transformed to the primary side) and the magnetising inductance (placed on the primary side) L_{M} which is given by [92]

$$L_{\text{M}} = \frac{M}{a}. \tag{4.8}$$

Figure 4.10 shows the primary winding current I_{prim}, the secondary winding current I_{sec}, the primary winding voltage V_{prim}, the secondary winding voltage V_{HV}, the magnetising current I_{M} and the snubber current $I_{\text{R}_{\text{s}}}$ for two operating conditions. Figure 4.10a shows the waveforms for a capacitive load and Fig. 4.10b shows the waveforms for when the spark gap (S_{SG}) of the nanosecond pulse source switches. In both operating conditions, C_{LV} is charged to 600 V and C_{PFL} is 300 pF.
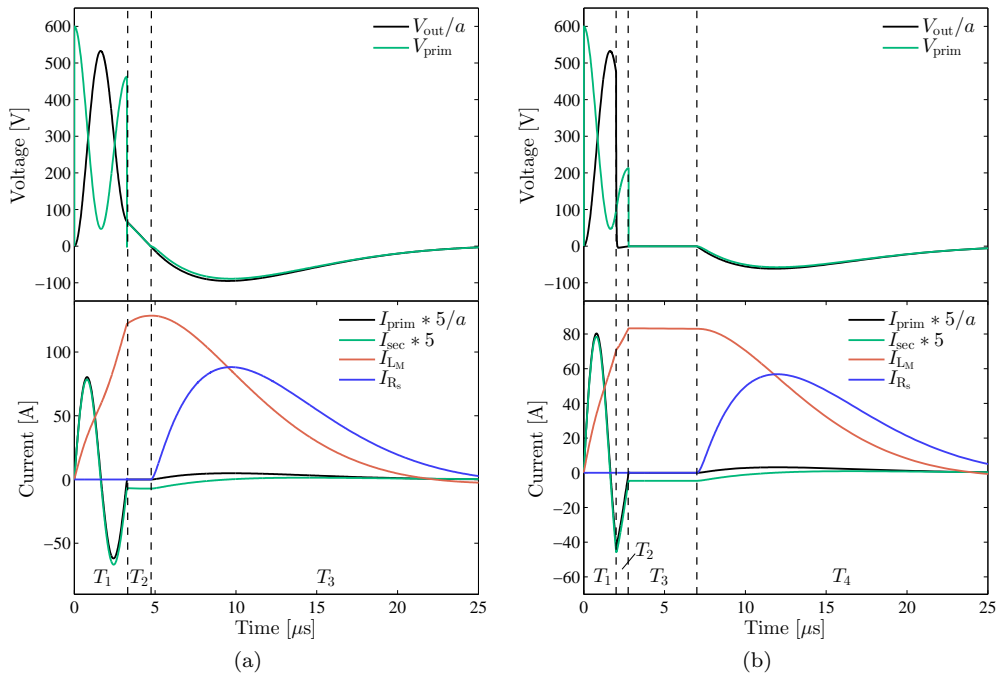
Figure 4.10: Simulated waveforms in the transformer circuit for (a) no spark-gap switching and (b) when the spark gap in the nanosecond pulse source switches. In both operating conditions, C_{LV} is charged to 600 V and C_{PFL} is 300 pF. A detailed explanation of the events during the different time periods is given in the main text.

In the situation when the spark gap does not switch (Fig. 4.10a), three time periods can be distinguished:

T_1 In this time period the IGBTs (S_{IGBTs}) are conducting, either in forward operation, or via their body diodes. During this period the transformer is magnetised and the flux density in the core increases. The low voltage capacitor C_{LV} is discharged and the PFL of the nanosecond pulse source C_{PFL} is charged. If the spark gap does not switch, the output voltage drops again until the primary winding current becomes zero and the body diodes of the IGBTs switch off.

T_2 When the IGBTs switch off, the primary winding is decoupled from the primary capacitor. During this time period, V_{sec} is determined by the resonance between C_{PFL} and the secondary winding inductance. The voltage on the primary side is now determined by V_{sec} and is small, but positive and therefore, the magnetising current increases slightly.

T_3 As soon as V_{sec} becomes negative, V_{prim} also becomes negative and the diode in the snubber starts to conduct. A current flows through the snubber circuit. Consequently, the magnetising current of the transformer drops and all energy is

dissipated in the snubber resistor. At the end of this time period, the flux density in the core has gone back to zero (in a practical transformer, it goes back to the remanent field value).

When the spark gap switches (Fig. 4.10b), the behaviour is slightly different and four time periods can be distinguished:

T_1 This time period is similar to when the spark gap does not switch (Fig. 4.10a), up until the moment the spark gap switches.

T_2 At the beginning of this time period, the spark gap switches. All the energy from the PFL is dissipated by the load. In this period, the body diodes of the IGBTs are still conducting. The resonance in the circuit is now determined by C_{LV} and $L_{s,total}$. During this time, a voltage is still applied to the primary side of the transformer, and the magnetising current increases. Once the switch current reaches zero, the body diodes of the IGBTs stop conducting and V_{prim} becomes zero.

T_3 In this period the voltage over the primary winding is zero and the magnetising current remains constant. The spark gap is still closed and the magnetising current flows trough the load. After several microseconds, the spark gap stops conducting.

T_4 Once the spark gap stops conducting, the diode in the snubber circuit switches and the remainder of this time period is similar as T_3 in the case when the spark gap does not switch (Fig. 4.10a).

4.2.5 Realisation

Fig. 4.11 shows the practical implementation of one of the pulse-charger modules. The pulse transformer is made on a PTFE coil former to ensure high-voltage insulation from the secondary winding to the earth screen. This earth screen is placed around the primary winding to prevent capacitive coupling between the primary and secondary winding. The earth screen is connected to the grounded EMC-cabinet in which the pulse-charger modules are placed (together with the nanosecond pulse source). The primary winding of the pulse transformer is made of two parallel copper strips to ensure a low R_d.

When it is operated, the entire pulse transformer is submerged in transformer oil to complete the high-voltage insulation. Like the insulation of the PFL of the nanosecond pulse source, the advantage of using PTFE in transformer oil is that the relative permittivity of the oil and the PTFE is the same and therefore the effects of field-enhancing triple points are severely reduced.

A printed circuit board (PCB) with all the circuit components is placed on top of the pulse transformer. It connects to the primary winding through two connectors. An advantage of this method of connection is that to obtain a negative V_{out} we just disconnect the primary winding, rotate the PCB by 180 degrees and connect it to the primary winding such that the IGBTs switch the current in the opposite direction through the winding.
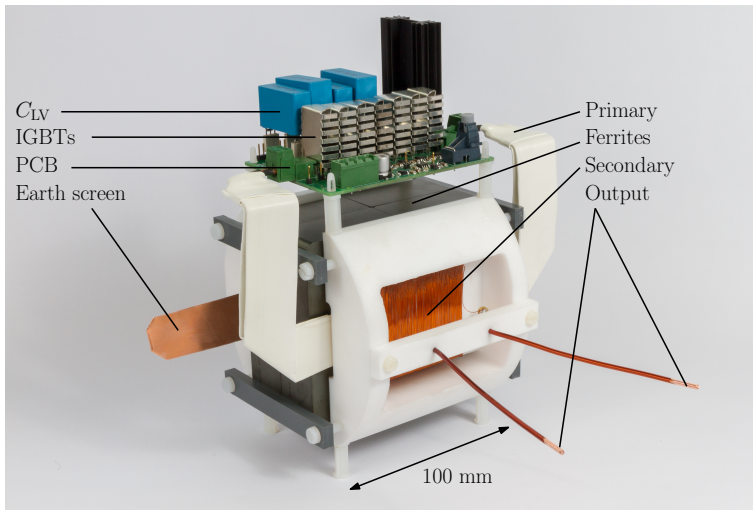
Figure 4.11: Photo of the realisation of one of the pulse-charger modules. Several key components are indicated in the photo.

The capacitors of the capacitor bank that comprise C_{LV} are placed on PCB headers. Now it is possible to adjust the value of C_{LV} flexibly by removing or adding capacitors.

To control the IGBTs we use optic fibres to ensure that the control signals are not distorted due to electromagnetic interference. The IGBT-control circuit that drives the optic fibres is situated in the EMC cabinet that also houses the oscilloscope. Furthermore, we use a 0–800-V DC-voltage source to charge C_{LV} via charging resistors.

4.3 Experimental results

4.3.1 Experimental setup

The experiments for this chapter were performed in the setup of the nanosecond pulse source that was described in Section 3.2.3. It consists of a 1.3×0.35×0.3-m (length× width×height) stainless-steel container filled up to 0.15 m with transformer oil (Shell Diala S3-ZX-I Dried). The pulse-charger modules are submerged in the transformer oil such that the PCBs of the pulse-charger modules remain just above the surface of the oil.

The steel container acts as an EMC shielding cabinet and all the power lines are fed into the container through filters. Furthermore, the fibers that control the pulse-charger modules run through a waveguide through the wall of the container. This waveguide has a lower cut-off frequency of several GHz. The fibers, plus coaxial measuring cables are connected to a separate EMC cabinet [96]. This EMC cabinet is used to house the oscilloscope and the control circuit of the pulse-charger modules.
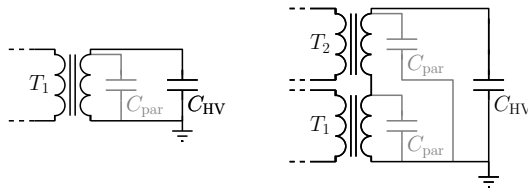
Figure 4.12: Schematic representation of the parasitic capacitances from the HV side of the pulse transformers to the earth screen. Left: situation for one pulse transformer. Right: situation for two pulse transformers connected in series.

The currents through the primary windings of the pulse transformers were measured using Pearson model 110 current transformers. The output voltage of the pulse chargers was measured with a capacitive high-voltage probe that we developed for this purposes and was calibrated with a Northstar PVM-5 high-voltage-probe.

4.3.2 Results on a capacitive load

The first experiments were performed with the pulse-charger modules on a capacitive load C_{HV}. We used loads of 50 pF, 100 pF and 200 pF and started with one pulse-charger module. On the primary side we matched C_{LV} using

$$C_{\text{LV}} \approx a^2[C_{\text{HV}} + C_{\text{par}}], \tag{4.9}$$

where C_{par} is the parasitic capacitance from the HV-winding of the pulse transformer to the earth screen. Fig. 4.12 illustrates this parasitic capacitance. Resonance frequency calculations from no-load experiments suggest that this parasitic capacitance can be as large as several tens of pF, which is not negligible, but also unavoidable. A static capacitance measurement confirmed a value for C_{par} of 30–40 pF.

Fig. 4.13 shows the results with one pulse-charger module. The results show that an output voltage of almost 64 kV can be reached with one pulse-charger module on different loads. The maximum switch current at the maximum load of 200 pF is 1060 A and well within the limits of the combined IGBT switch.

A comparison between the experimental results in Fig. 4.13 and the simulations of Fig. 4.6 shows very similar results. Only the amplitude of the switch current is higher in the LTSpice simulation. The source of this discrepancy can be found in the resistance that was added to the primary side (R_{d}) and the secondary side of the pulse transformer in the simulations. These resistances simulate the losses in the circuit. We chose the resistance on the primary side too low and the resistance on the secondary side too high. Therefore, the primary switch current will be higher in the simulation as compared to the experimental results. However, as long as the total losses in the simulation remain similar to the actual circuit, the simulation will show the same output voltage as the experimental results. The reason we intentionally chose a low resistance on the primary side of the transformer is to have an upper bound in the maximum switch current in order to choose the right IGBTs.

71
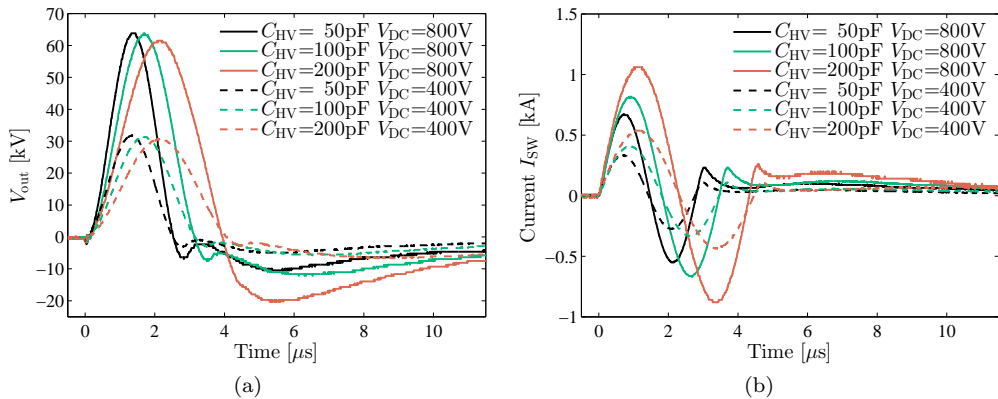
Figure 4.13: Experimental results with different capacitive loads on one pulse-charger module. The output voltage (a) and the current through the primary winding of the pulse transformer (b) are shown.

With two pulse chargers modules in series the capacitive loads are halved and are now representing the capacitance of the PFL in the nanosecond pulse source. The matching of C_{LV} is now done with

$$C_{\text{LV}} \approx a^2[2C_{\text{HV}} + C_{\text{par}}], \tag{4.10}$$

where we take $2C_{\text{HV}}$ because we have two pulse-charger modules in series (see Fig. 4.4). Fig. 4.14 shows the results.

The pulse charger is able to reach an output voltage of $119\,\text{kV}$, which is a good result, because we stated in Section 4.2.3 that we designed the pulse charger to output $150\,\text{kV}$ to allow for some damping and still obtain a 120-kV output voltage.

The currents through the primary windings of the pulse-charger modules are not identical. This is the result of the parasitic capacitances in the transformers of the pulse-charger modules. Especially C_{par} is important because it contains a significant amount of energy when fully charged. Furthermore, C_{par} of the pulse transformer connected to the HV side (T_2, see Fig. 4.12) is charged to double the voltage as compared to its counterpart in the pulse transformer connected to ground (T_1) and therefore contains four times more energy.

The pulse-charger modules were tested at a repetition rate of $1\,\text{kHz}$ at a voltage of $50\,\text{kV}$ each and were found to perform well at this setting. For prolonged periods of operation at this high repetition rate additional cooling of the snubber of the pulse transformer is required, but in reality the energy this snubber has to dissipate will be used in the nanosecond pulse source. Therefore this additional cooling might not be necessary. We did not measure the losses in the IGBTs at the 1-kHz repetition rate directly, but the small heatsinks on the IGBTs were sufficient to dissipate the heat from the IGBTs.
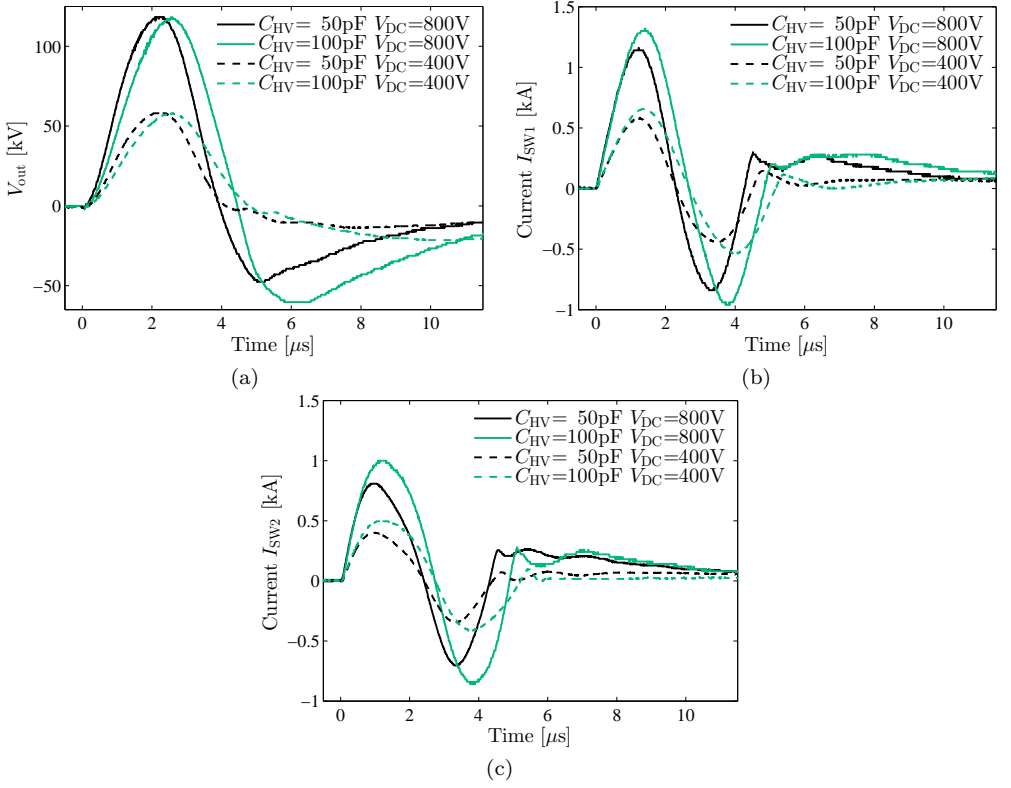
Figure 4.14: Experimental results with different capacitive loads on two pulse-charger modules connected in series. The output voltage (a), the current through the primary winding of the pulse transformer connected to earth (b) and the current through the primary winding of the pulse transformer connected to the HV-side (c) are shown.

The pulse charger was also tested with reversed output voltage polarity. The PCBs were rotated 180 degrees (see Fig. 4.11) and connected to produce negative polarity pulses. This method worked as expected.

4.3.3 Results on the PFL of the nanosecond pulse source

The second set of experiments were performed with the pulse-charger modules connected to its actual load: the PFL of the nanosecond pulse source. The PFL was $0.5\,\mathrm{m}$ long in the experiments (the first implementation of the nanosecond pulse source). This corresponds to a load of $50\,\mathrm{pF}$. We again used one pulse-charger module initially. Fig. 4.15 shows the results.

The results are very similar to Fig. 4.8 and show that the current through the primary winding never increases far beyond the maximum current that is reached
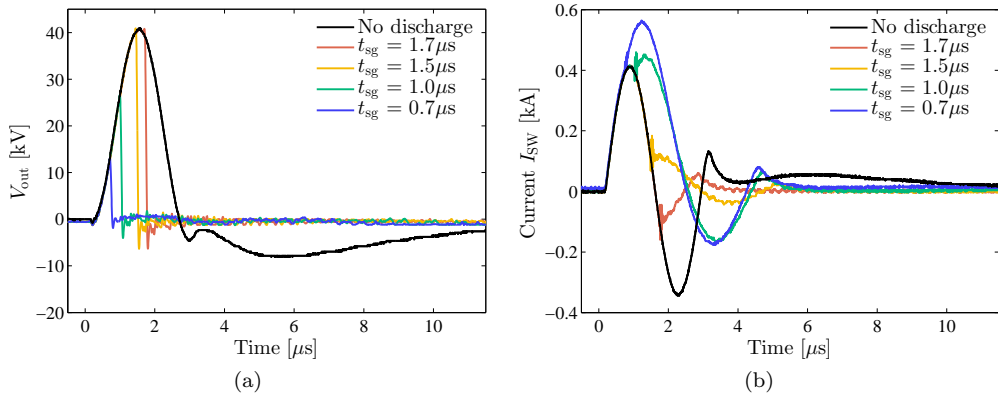
Figure 4.15: Experimental results with one pulse-charger module connected to the PFL of the nanosecond pulse source ($V_{DC} = 500$ V). The output voltage (a) and the current through the primary winding of the pulse transformer (b) are shown.

when no discharge of the spark gap occurs in the nanosecond pulse source. The primary switch current is again lower in the experimental results as compared to the simulations, even when allowing for a difference in output voltage between the simulations of Fig. 4.8 and the experimental results in Fig. 4.15. An explanation for this discrepancy was given in Section 4.3.2. The high-frequency oscillations in the experimental results at the time of switching can have a number of origins, such as parasitic inductances and capacitances in the measuring circuit or the actual pulse-charger module.

Fig. 4.16 shows the results when both pulse-charger modules are connected in series and connected to the nanosecond pulse source. The currents through the primary windings of the pulse transformers are again unequal and also show other oscillations present. These oscillations result from the complex interaction of parasitic capacitances and their stored energies. However, the currents remain within reasonable limits and are no danger for the IGBTs when they switch off.

4.3.4 Efficiency

A high efficiency was not a requirement for the pulse charger. Nevertheless it is a parameter worthwhile investigating. On average the voltage across C_{LV} drops to 10 percent of its charging voltage when the voltage across C_{HV} reaches a maximum. The efficiency η of the pulse charger can then be calculated with

$$\eta = \frac{E_{out}}{E_{in}} = \frac{\frac{1}{2}C_{HV}V_{out}^2}{C_{LV}[V_{LV}^2 - (0.1V_{LV})^2]},\tag{4.11}$$

where E_{out} is the energy the pulse charger charges C_{HV} to and E_{in} is the energy that it takes from C_{LV} of both pulse-charger modules.
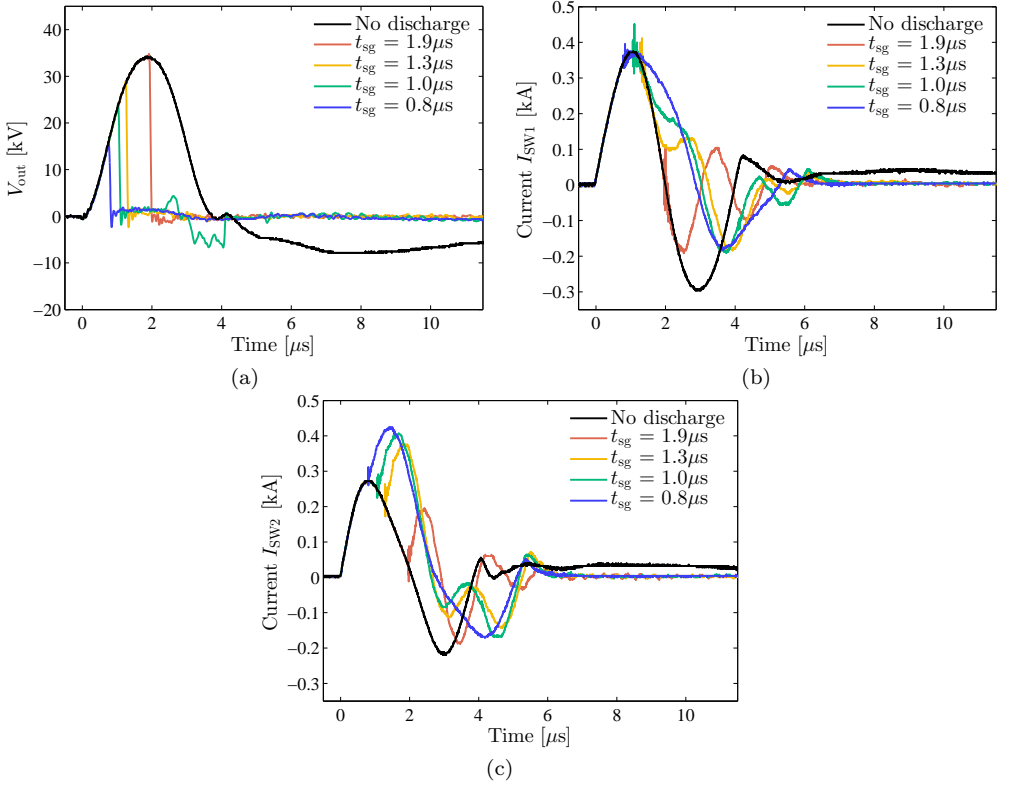
Figure 4.16: Experimental results with two pulse chargers modules connected in series and connected to the PFL of the nanosecond pulse source ($V_{\mathrm{DC}} = 300\,\mathrm{V}$). The output voltage (a), the current through the primary winding of the pulse transformer connected to earth (b) and the current through the primary winding of the pulse transformer connected to the HV-side (c) are shown.

With two pulse-charger modules connected in series η is calculated as 0.58 for a 100-pF load and 0.48 for a 50-pF load. These results are low mainly because of the relatively large value of C_{par}. A large portion of the energy is stored in this parasitic capacitance of each pulse-charger module.

In a future implementation, the energy efficiency could be improved by reusing energy in the transformer that would otherwise be lost [97].

4.4   Summary and conclusions

In this chapter we presented the design and implementation of the 0–120-kV solid-state pulse charger to charge the PFL in our nanosecond pulse source. Its output pulses have a duration of several microseconds, which is short enough to prevent pre-firing of the

oil spark gap in the nanosecond pulse source, but is long enough to prevent the pulse capacitively coupling through the spark gap to the output of the nanosecond pulse source.

The pulse charger consists of two pulse-charger modules. Each module is a pulse transformer with a PCB on top of it. The PCB contains parallel-connected IGBTs that switch the energy of a primary capacitor bank via the pulse transformer into the PFL of the nanosecond pulse source (which forms a capacitive load). The maximum switch current should not exceed 1.5 kA and simulations and experimental results show that the current stays well within this limit. Experimental results further showed that the output voltage of one pulse-charger module exceeds 60 kV and that connected in series they are able to produce almost 120 kV on a 100-pF load. Also, at a repetition rate of 1 kHz the pulse charger worked well and it was shown that changing the direction of the PCBs inverts the polarity of the output pulses.

The pulse charger worked well on its actual load: the PFL of the nanosecond pulse source. As with the tests on a capacitive loads, the currents through the pulse transformers were not identical due to parasitic capacitances in the pulse transformers, but in no way prevented correct operation of the pulse charger.

Five

Auxiliary Systems: D-dot and B-dot sensors

Abstract

In this chapter we present high-frequency voltage and current sensors that we can use to measure the output pulses of our nanosecond pulse source. The type of sensors we use are D-dot and B-dot sensors that are able to measure the voltage and current through capacitive coupling and inductive coupling, respectively. For implementing these sensors we can take advantage of the option to compactly mount them on the SA24272 cable that connects the nanosecond pulse source to its load. This enables us to measure the characteristics of each sensor very precisely with a vector network analyser. With these characteristics we can numerically reconstruct the voltage and current waveforms that passed the sensor positions. Our calibration approach, the mounting on the SA24272 cable, and the post-processing of the results make these sensors very useful.

5.1 Introduction

We require a very high bandwidth measuring system to measure the output pulses of our nanosecond pulse source, because we expect pulses with a bandwidth of up to 2 GHz (Chapter 2). Also, the sensors must be able to accurately measure very high voltage and current levels. In this chapter we will describe the sensors that we developed to measure the current and voltage of the output pulses.

In pulsed-power technology a number of different types of sensors are generally used. For pulsed-power measurements, high-voltage probes and current sensors are commercially available [98–101]. However, these components are expensive and often

---

Part of the first D-dot sensor described in this chapter has been published previously in [70]:

- T. Huiskamp, F. J. C. M. Beckers, E. J. M. van Heesch and A. J. M. Pemen, "First Implementation of a Subnanosecond Rise Time, Variable Pulse Duration, Variable Amplitude, Repetitive, High-Voltage Pulse Source," *Plasma Science, IEEE Transactions on*, vol. 42, no. 3, pp. 859–867, 2014.

not suitable for higher frequencies. Commercial current monitors are available up to several GHz bandwidth, but the disadvantage of these systems is that they can only measure a low current (up to several ampere). Furthermore, most of the commercially available components are bulky and cannot easily be implemented in compact setups. Therefore, homemade systems such as D-I (Differentiating-Integrating) systems, capacitive voltage probes, Rogowski coils [32, 36, 102–106] or even electro-optic probes are often employed [107, 108].

Fast types of capacitive and inductive sensors are D-dot and B-dot sensors respectively [68, 109–111]. They are simple in design, can be made very compact and can measure large signals up to very high frequencies. It is these type of sensors that we will employ to measure the pulses from our nanosecond pulse source. The design of the D-dot and B-dot sensors that we present in this chapter were motivated by the excellent results that were achieved with these type of designs in [110] and [68].

We will integrate the results of the sensor signals numerically rather than passively in hardware because passive integrators at the high frequencies are very difficult to construct [112, 113]. Furthermore, using such a high-frequency passive integrator also requires the sensors to be perfectly differentiating up to a high-frequency. We will see in Section 5.3 that this is not the case for our sensors.

In Section 5.2 we implement a first version of a D-dot sensor. This is the sensor that was used for the measurements of Section 3.2. In Section 5.3 we introduce the B-dot sensor and design the final versions of these sensors for the measurements of Chapters 6, 7 and 8. Finally, Section 5.4 presents the conclusions.

5.2   D-dot sensor

5.2.1   Principle of operation

The D-dot sensor is a capacitively coupled electrode that measures the voltage created by the displacement current through the capacitance between the high-voltage electrode and the D-dot sensor electrode [68, 109]. This current is the derivative of the voltage on the high-voltage electrode.

We use a very small electrode in the D-dot sensor to obtain a very high bandwidth (low parasitic effects). Therefore we measure purely the derivative of the voltage and do not have to worry about non-linear effects that occur at higher frequencies that are beyond our interest. The D-dot sensor we used is shown in Fig. 5.1a. The electrode that picks up the capacitive current from the high-voltage electrode is the tip of an SMA-bulkhead connector (shown clearly in Fig. 5.1b). The body of the sensor is made from aluminium. The nanosecond pulse source is connected to its load by a SA24272 cable (Chapter 3). Fig. 5.1c shows the hole we made in the solid outer conductor of the SA24272 cable for the capacitive coupling between the inner conductor of the cable and the D-dot sensor electrode. Finally, Fig. 5.1d shows how the D-dot sensor is clamped onto the SA24272 cable.

Fig. 5.2 shows the electrical equivalent circuit of the D-dot sensor system. Here V_{Ddot} is the voltage from the D-dot sensor, V_{HV} is the voltage on the inner conductor

(a)

(b)

(c)

(d)
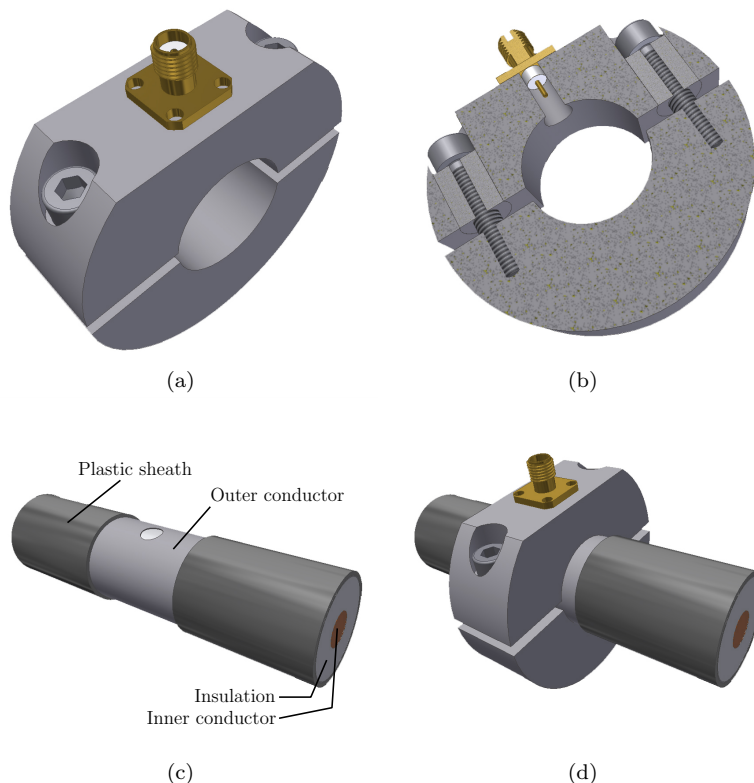
Figure 5.1: (a) A drawing of the D-dot sensor. (b) A cut-away drawing of the D-dot sensor. The tip of the SMA-bulkhead connector is the electrode of the D-dot sensor. (c) Drawing of the SA24272 cable with a hole in the outer conductor. (d) The D-dot sensor mounted on the SA24272 cable.

of the SA24272 cable, Z_{cable} is the impedance of the measuring cable, C_{par} is the parasitic capacitance from the D-dot sensor electrode to ground, and C_{Ddot} is the capacitance from the D-dot sensor electrode to the inner conductor of the SA24272 cable. This system is a voltage divider of which the impedance of the high-voltage part is

$$\frac{1}{j\omega C_{\text{Ddot}}} \tag{5.1}$$

and the impedance of the low-voltage part is

$$\frac{Z_{\text{cable}}}{j\omega Z_{\text{cable}} C_{\text{par}} + 1}. \tag{5.2}$$

79
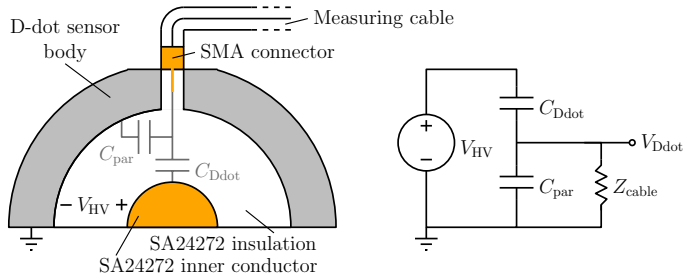
Figure 5.2: A cut-away drawing of the D-dot sensor (compare with Fig. 5.1b) showing the equivalent electrical circuit. The circuit has a high-voltage part (C_{Ddot}) and a low-voltage part (C_{par} in parallel with Z_{cable}) which form a voltage divider.

The transfer function of the system $H_{\mathrm{Ddot}}(j\omega)$ then becomes

$$H_{\mathrm{Ddot}}(j\omega) = \frac{V_{\mathrm{Ddot}}}{V_{\mathrm{HV}}} = \frac{j\omega Z_{\mathrm{cable}} C_{\mathrm{Ddot}}}{j\omega Z_{\mathrm{cable}}(C_{\mathrm{Ddot}} + C_{\mathrm{par}}) + 1}. \tag{5.3}$$

Usually, D-dot sensors are operated either in a regime where $j\omega Z_{\mathrm{cable}}(C_{\mathrm{Ddot}} + C_{\mathrm{par}}) \gg 1$ or in a regime where $j\omega Z_{\mathrm{cable}}(C_{\mathrm{Ddot}} + C_{\mathrm{par}}) \ll 1$. In the first regime (high frequency) the output voltage of the D-dot sensor is proportional to V_{HV}. This regime is generally called the self-integrating regime [114, 115]. In the second regime (low frequency) the output voltage of the D-dot sensor is proportional to $\frac{dV_{\mathrm{HV}}}{dt}$. This regime is called the differentiating regime. In most cases, D-dot sensors are designed in such a way that they operate in one of these two regimes because then the measurements can be easily converted to the high-voltage signal with either a passive integrator and a calibration factor for the differentiating sensor, or just a calibration factor for the self-integrating sensor. However, this puts design constraints on the sensors and requires thorough calculation, calibration and/or 3D EM simulations to design and operate the sensors. However, the advantage of our D-dot sensor is that it is mounted on a cable for which N-connectors are available. This allows us to precisely measure the transfer function. This greatly simplifies the calibration of the sensors and ensures a very good calibration result, as we will show in the next part.

5.2.2 Calibration

We used two methods to calibrate the D-dot sensor: a vector network analyser (VNA) for frequency-domain calibration and a reed-relay pulse source for time-domain calibration. We calibrated the D-dot sensor before the SA24272 cable was installed into the nanosecond pulse source. We connected N-connectors to both sides of the SA24272 cable and connected them and the SMA connector of the D-dot sensor to a Rohde&Schwarz ZVB20 VNA. Fig. 5.3 shows to which ports of the VNA the cable assembly was connected. The transfer function of the D-dot sensor is now determined

Figure 5.3: Drawing of the calibration setup. The SA24272 cable is fitted with N-connectors so that it can be connected to the vector network analyser.
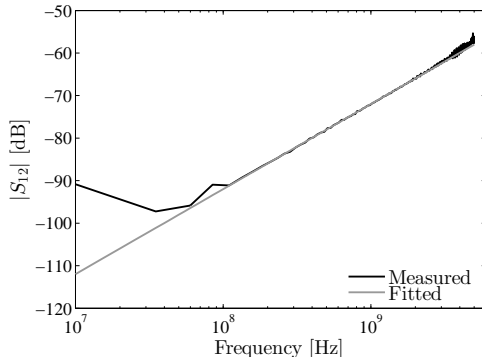
Figure 5.4: Magnitude of S_{12} of the D-dot sensor measurement and the fitted values. The deviation at low frequencies is because of the usable SNR of the VNA.
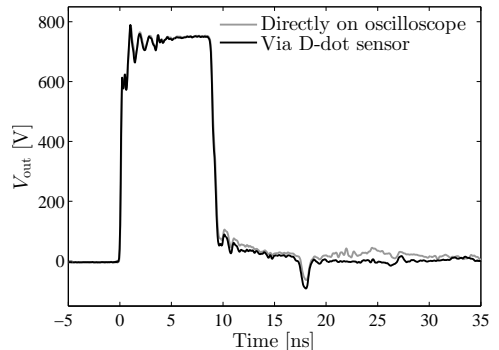
Figure 5.5: D-dot voltage when the reed-relay pulse source is connected to the oscilloscope (at a lower voltage) and when the same pulse is measured by the D-dot sensor.

by measuring the S_{12}-parameters of the setup. Since the D-dot sensor is only 0.5 m from Port 1 the dispersion in the cable can be neglected (Section 2.2.5).

Fig. 5.4 shows the results of the measurement. We measured the S-parameters of the D-dot sensor up to 4 GHz. The result shows that the D-dot sensor operates in the differentiating regime up to this frequency. The lower frequency limit of the VNA is 10 MHz and it has a usable SNR (Signal to Noise Ratio) of about 90 dB. This explains the results below 100 MHz in Fig. 5.4.

The parasitic capacitance C_{par} is typically much larger than C_{Ddot} and will cause the sensor to operate in the self-integrating regime at higher frequencies. However, for the frequency range we are interested in (up to 4 GHz) the term $j\omega Z_{cable}(C_{Ddot} + C_{par})$ is small and can therefore be neglected in the denominator in Eq. 5.3. We are then left with an ideal differentiator

$$H_{Ddot}(j\omega) = j\omega Z_{cable}C_{Ddot}. \qquad (5.4)$$

From this simplified transfer function we fitted a transfer function, which is shown in Fig. 5.4. With Z_{cable} as 50 Ω we found a value of around 0.8 fF for C_{Ddot}. Because of the lower frequency limit and the SNR of the VNA we will use the fitted transfer function in our measurements.

81
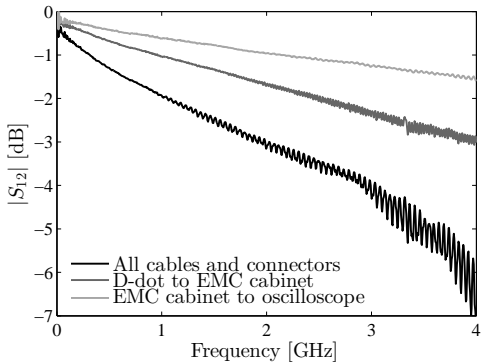
Figure 5.6: Attenuation of the cables and connectors between the D-dot sensor and the oscilloscope, part of which are in the EMC cabinet
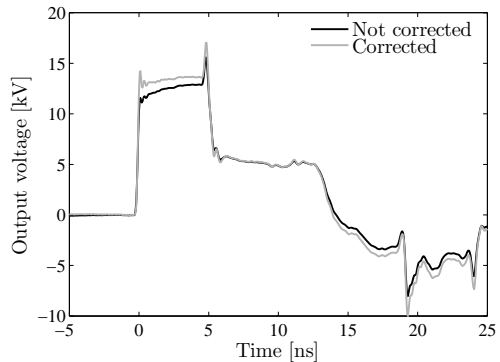
Figure 5.7: Output voltage of the 5-ns pulse source as measured by the D-dot sensor when it is corrected and not corrected for the attenuation of the measuring cable assembly.

To verify the fitted transfer function we tested the D-dot sensor with a reed-relay pulse source. This is a Blumlein pulse source which is switched by a mercury wetted reed-relay [44]. This pulse source is able to generate very fast pulses with a rise-time of several hundreds of picoseconds and a voltage amplitude of up to around 750 V. We performed one measurement at a charging voltage of 5 V with the output of the reed-relay pulse source connected directly to an oscilloscope. Then we generated the same pulse at a higher voltage, but now connected to the N-connector of Port 1 in Fig. 5.3. A 0–4 GHz 50 Ω load was connected at Port 3. The output of the D-dot sensor was captured by the oscilloscope and integrated using the inverse of the fitted transfer function from Fig. 5.4. Fig. 5.5 shows the result together with the scaled result of the 5 V measurement directly on the oscilloscope. The figure shows that we can measure correctly with the D-dot sensor.

5.2.3   Cable response

When the nanosecond pulse source is operated, all measuring equipment will be situated in an EMC cabinet [96]. Therefore, the D-dot sensor has to be connected by a long cable to the EMC cabinet. With the VNA, we measured the S_{12}-parameters of the entire cable assembly from the D-dot sensor to the oscilloscope, including the cable inside the EMC cabinet and all the adapters and connectors. Fig. 5.6 shows the results. It is clear that we have to correct for this attenuation.

Fig. 5.7 shows the result of the measuring cable attenuation on a measured 5-ns pulse from the first implementation of the nanosecond pulse source and what happens when we correct for it. Especially the high frequencies in the pulse are influenced, which results in a change of measured rise-time from 200 ps to 175 ps and a higher pulse amplitude when we correct for the attenuation. Clearly, we need to correct for
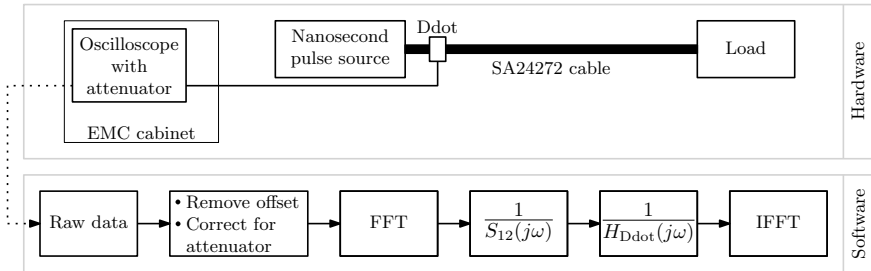
Figure 5.8: The total experimental setup. In the hardware part the voltage pulse is measured by the D-dot sensor with the oscilloscope. The raw waveform is then processed in software and corrected for the measuring cable attenuation ($S_{12}(j\omega)$) and the sensor transfer function of the sensor ($H_{\text{Ddot}}(j\omega)$) in the frequency domain.
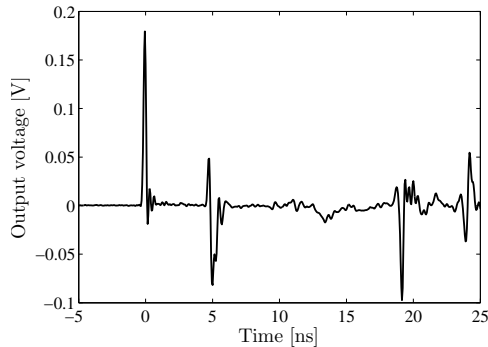
Figure 5.9: The raw D-dot sensor signal as captured by the oscilloscope. It is the raw waveform for the result of Fig. 5.7.

the attenuation. We implement this correction by transforming the measured signal to the frequency domain and dividing by the measured cable assembly S_{12} parameters.

5.2.4 Total experimental setup

The total experimental setup and the numerical process that is used in all the measurements with the D-dot sensor is shown in Fig. 5.8. This method was used for all the measurements with the first implementation of the nanosecond pulse source in Chapter 3.

The oscilloscope (LeCroy 3-GHz 20-GS·s^{-1} WavePro 7300A*) captures the waveform from the D-dot sensor via an attenuator. An example of a raw signal is shown in

---

*With the very short rise times of the nanosecond pulse source, we are operating the oscilloscope at the limit of its bandwidth, especially since we are measuring the differentiated pulses. However, tests with a borrowed 30-GHz LeCroy oscilloscope confirmed that we can accurately measure the signals

Fig. 5.9. It is the raw signal for the waveform shown in Fig. 5.7. This raw waveform is then processed in Matlab [116]. The first step is an offset correction and the correction for the attenuator. Then the signal is transformed to the frequency domain with the FFT (Fast Fourier Transform) where the cable correction with the inverse of the measured attenuation S_{12} is applied. Subsequently the inverse of the fitted transfer function of the D-dot sensor is applied before converting the signal back to the time domain with the inverse FFT (IFFT). The influence of the $\frac{1}{S_{12}(j\omega)}$-block was already shown in Fig. 5.7.

5.3 D-dot and B-dot sensors

The D-dot sensor of the previous section was found to be suitable to measure the high-voltage pulses from the pulse source and served mainly as a "proof of concept" for this measuring technique. However, we also need to be able to measure the current associated with the high-voltage pulses to be able to measure the power of the pulse and the energy of the pulse. Especially in the plasma experiments of Chapter 6 and 8 it will be crucial to know how much energy is dissipated by the plasma. A suitable sensor to measure the current is the B-dot sensor [110, 111].

5.3.1 Principle of operation

The B-dot sensor is an inductively coupled sensor. It is a small loop which picks up part of the magnetic field that is generated by the pulse as it passes the sensor position. To be able to measure voltage and current at the same position, we integrated two D-dot sensors into the same sensor body as two B-dot sensors. The reason we used two sensors of each type in the sensor body is to increase the signal-to-noise ratio of the measurements. Small amounts of oscilloscope noise will be integrated during the numerical processing of the data and will result in low-frequency oscillations and offsets which are difficult to remove. With two sensors capturing the same signal, we can average the results and the noise will be halved, resulting in a cleaner output signal.

Besides oscilloscope noise we also experience some small amount of interference from the experiment itself. This is present as a common-mode signal on the measuring cables which — despite numerous precautions — proves difficult to remove altogether. In the case of the D-dot sensors this problem is solved by increasing the sensor area and thus increasing the output voltage of the sensors (while retaining the same level of interference). The disadvantage of this method is that besides increasing C_{Ddot}, C_{par} will also increase. This results in a lower cut-off frequency above which the sensor will start to behave as a self-integrating sensor. Here the flexibility of our approach becomes apparent because we are able to measure the entire transfer function with the VNA and are able to correct for it in the frequency domain. Therefore, a sensor that works both in the differentiating and the self-integrating regime is not a problem for our method.

---

from the D-dot and B-dot sensors with the WavePro 7300A.
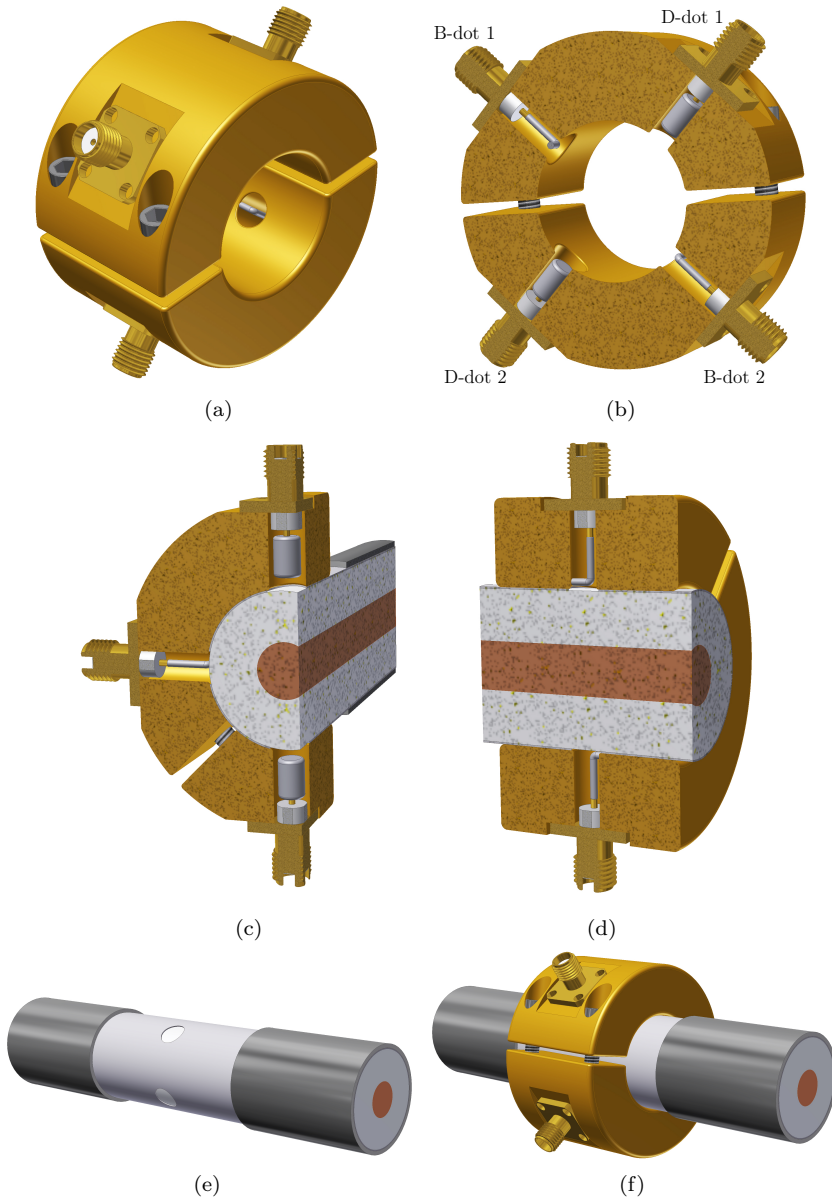
Figure 5.10: (a) The sensor body with two D-dot sensors and two B-dot sensors. (b) Cut-away drawing of the sensor body with the D-dot and B-dot sensors indicated. (c) A view of the D-dot sensor. The sensor electrode is significantly larger than in the previous D-dot sensor of Fig. 5.1. (d) A view of the B-dot sensor. It is a small loop that picks up part of the magnetic field generated by the nanosecond pulse. (e) The holes that we made in the outer conductor of the SA24272 cable to fit the sensors. (f) The sensor body can be mounted on the SA24272 cable via a clamp construction.
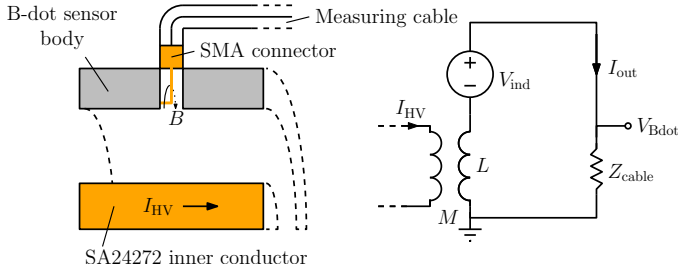
Figure 5.11: Schematic representation of the B-dot sensor circuit. The pulsed current I_{HV} generates a magnetic field which is partly picked up by the loop of the B-dot sensor. This induces a voltage in the sensor circuit.

In the case of the B-dot sensors the problem of interference is solved by an opposite orientation of the second B-dot sensor, which results in a positive output voltage on the first B-dot sensor and a negative output voltage on the second B-dot sensor in the case of a pulse passing in the positive direction. Now we can subtract the signals to obtain an output signal with half the oscilloscope noise and no interference (the interference from both sensors cancels).

Fig. 5.10 shows the new sensor body. It is a brass body and can be mounted onto the SA24272 cable in the same manner as the first implementation of the D-dot sensor. The two D-dot sensors are now bigger to achieve a higher output voltage. The principle of operation of the D-dot sensors is the same as described in Section 5.2.1, with the only difference that the sensors are now not operating purely in the differentiating regime anymore due to the higher capacitance values.

Fig. 5.11 shows the electrical equivalent circuit of the B-dot sensor system. Here V_{Bdot} is the voltage from the B-dot sensor, I_{HV} is the current through the inner conductor of the SA24272 cable, V_{ind} is the induced voltage along the B-dot electrode, I_{out} is the current in the B-dot sensor electrode, Z_{cable} is the impedance of the measuring cable, L is the inductance of the B-dot sensor electrode, and M is the mutual inductance of the B-dot sensor electrode and the conductors of the SA24272 cable. The induced voltage in the B-dot sensor is

$$V_{ind} = M\frac{dI_{HV}}{dt}. \tag{5.5}$$

Furthermore, we have

$$V_{Bdot} = I_{out}Z_{cable}. \tag{5.6}$$

The equation that describes the equivalent circuit of the B-dot sensor is found by applying the Kirchhoff voltage law:

$$M\frac{dI_{HV}}{dt} = L\frac{dI_{out}}{dt} + Z_{cable}I_{out}. \tag{5.7}$$
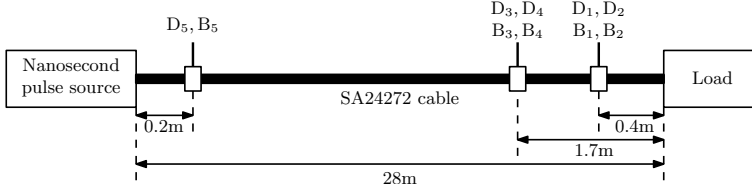
Figure 5.12: The final sensor configuration. The sensor body with only one D-dot and B-dot sensor is placed at the pulse source side. The two sensor bodies with two D-dot and two B-dot sensors is placed near the load.

From this equation the transfer function of the B-dot sensor is found as

$$H_{\text{Bdot}}(j\omega) = \frac{V_{\text{Bdot}}}{I_{\text{HV}}} = \frac{j\omega M}{j\omega \frac{L}{Z_{\text{cable}}} + 1}. \tag{5.8}$$

From this equation we see that the B-dot sensor is self-integrating when $j\omega \frac{L}{Z_{\text{cable}}} \gg 1$ and that it is working in the differentiating regime when $j\omega \frac{L}{Z_{\text{cable}}} \ll 1$. Just as with the D-dot sensor, it is not important in which regime our B-dot operates because we can measure the transfer function directly with the VNA.

The new B-dot and D-dot sensors are mounted on the long SA24272 cable that is connected to the final implementation of the nanosecond pulse source. The cable is around 28 m long and connects the pulse source to the corona-plasma reactor that is used in Chapter 6, 7 and 8. On this cable we mount three sensor bodies. Two bodies with two B-dot sensors and two D-dot sensors each and one body with just one B-dot sensor and one D-dot sensor. This last body is mounted at the output of the pulse source. It has only one sensor of each type because it will only be used to measure the voltage from the pulse source and not for energy measurements. The B-dot sensor in this body will be used to trigger the ICCD camera in Chapter 7. The other two bodies are mounted near the load and can be used for plasma energy measurements. The entire sensor configuration is shown in Fig. 5.12.

5.3.2 Calibration

The B-dot and D-dot sensors were again calibrated with the VNA using a similar setup as shown in Fig. 5.3. Figures 5.13a–c show the results. Besides the measured amplitude of the S_{12} parameters, the figures also show the fitted transfer functions. We used Eq. 5.3 and 5.8 for the fitting. Table 5.1 shows the accompanying sensor parameters.

The differences between D-dot sensors D_1–D_4 are caused by slight differences in the sizes of the sensor heads and the mounting positions. The sensors are very sensitive for these minute differences. The same is true for B-dot sensors B_1–B_4. The differences between D-dot sensor D_5 and the rest and B-dot sensor B_5 and the rest result from a slightly different design.

(a)

(b)

(c)
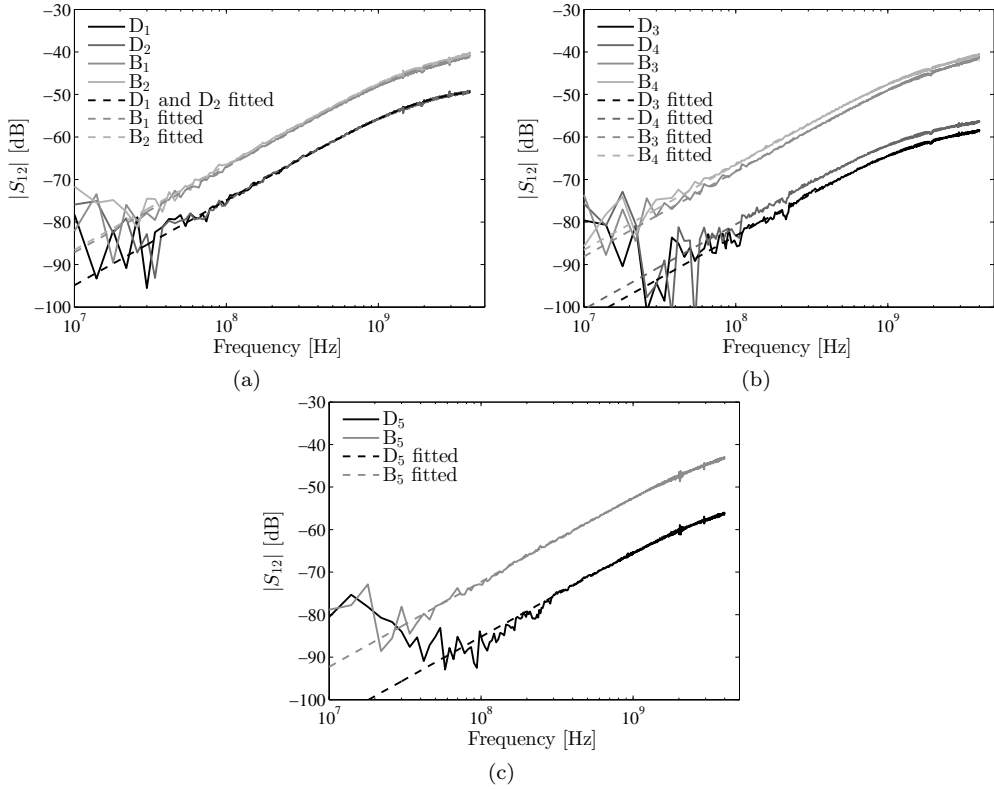
Figure 5.13: Magnitude of S_{12} of the D-dot and B-dot sensor measurements and the fitted values for (a) D_1, D_2, B_1 and B_2, (b) D_3, D_4, B_3 and B_4, and (c) D_5 and B_5

Table 5.1: Fitted sensor parameters

D-dot	C_{Ddot}	C_{par}	B-dot	M	L
D_1	5.75 fF	1.5 pF	B_1	0.70 pH	71 pH
D_2	5.75 fF	1.5 pF	B_2	0.75 pH	73 pH
D_3	2.2 fF	1.75 pF	B_3	0.63 pH	68 pH
D_4	3.0 fF	1.9 pF	B_4	0.75 pH	78 pH
D_5	1.75 fF	0.84 pF	B_5	0.39 pH	40 pH

The output voltage of the sensors will be much higher when compared with the first implementation of the D-dot sensor (compare Figs. 5.13a–c with Fig. 5.4). The output voltages of the B-dot sensors can be as high as several hundreds of volts when the nanosecond pulse source is operated at high voltages. The output voltages of the D-dot sensors are tens of volts and therefore significantly higher as compared with the first D-dot sensor. The penalty for this higher output voltage is that the frequency above which

the sensors enter the self-integrating regime is now within the bandwidth that we need for our measurements (this is evident in the transfer function as the bend in the straight line at around 2 GHz). However, because we carefully fitted the transfer function of the sensors, this is not be a problem. Another potential disadvantage of the bigger sensors is that all sensor parameters are higher (bigger capacitances and inductances), which lowers the point at which the sensors can start to oscillate. However, as we can see from the measurements in Figs. 5.13a–c there are no oscillations visible, so the upper frequency limit of our sensors is at least 4 GHz. When we measured the S_{12} parameters of the sensors up to a higher frequency it seemed that the sensors started to oscillate in the 6–8 GHz frequency range, which is much higher than frequency range we will operate the sensors in.

All sensors were also tested with the reed-relay pulse source and were found to be operating properly.

5.3.3 Total experimental setup

The total measuring setup with the D-dot and B-dot sensors that will be used in Chapters 6, 7 and 8 is the same as shown in Fig. 5.8. With the oscilloscope we are able to measure up to 4 channels at the same time. The only experimental difference between the B-dot sensors and the D-dot sensors is that the B-dot sensors will have a 40-dB attenuator instead of the 20-dB attenuator that the D-dot sensors use and that each oscilloscope channel has its own measuring cable assembly. These four cables were characterised separately with the VNA and will be accordingly corrected in Matlab. Likewise, each sensor has its own S_{12} parameters stored in Matlab that will be used in the numerical process. D-dot sensor D_5 was used for the measurements of the final implementation of the nanosecond pulse source in Section 3.3.

5.4 Summary and conclusions

In this chapter we presented high-frequency voltage and current sensors that we can use with our nanosecond pulse source. The type of sensors we used are D-dot and B-dot sensors that are able to measure the voltage and current through capacitive coupling and inductive coupling respectively. For implementing these sensors we can take advantage of the option to compactly mount them on the SA242727 cable that connects the nanosecond pulse source to its load. This enables us to measure the characteristics of each sensor very precisely with a vector network analyser. With these characteristics we can numerically reconstruct the voltage and current waveforms that passed the sensor positions. Our calibration approach, the mounting on the SA24272 cable and the post-processing of the results make these sensors very useful.

In a first implementation of the D-dot sensor we noted that its transfer characteristic must be corrected for. However, this could easily be integrated into the numerical method. Furthermore, this first implementation showed that a D-dot sensor of this type is very suitable to measure the output pulses of the nanosecond pulse source and that it provides accurate measurements of the very fast high voltage pulses.

For the very fast current measurements we employ B-dot sensors in the final implementation. It is implemented in the same body as the D-dot sensors, where we have three sensor bodies in total: two bodies with two D-dot sensors and two B-dot sensors each near the load and one sensor body with one of each type of sensor at the end of the nanosecond pulse source. The employ of two sensors of each type at the load side results in a lower influence of oscilloscope noise and interference. The interference was further reduced by using a differential B-dot system and by designing the sensors in such a way that their output voltage is high compared to the interference.

Calibration of the D-dot sensors and B-dot sensors showed that the sensors are not purely working in the differentiating regime anymore. However, because we were able to measure the transfer function of the sensors with the vector network analyser, this presented no issue. The D-dot and B-dot sensors will be used in the (energy) measurements of Chapters 6, 7 and 8.

Six

Matching a Nanosecond Pulse Source to a Corona-Plasma Reactor

---

Abstract

In this chapter we investigate the energy transfer from the nanosecond pulses to the plasma in the corona-plasma reactor. This energy transfer (or 'matching') should be as high as possible. We studied the effect of multiple parameters on matching, such as the reactor configuration, the pulse duration, the pulse rise time, and the energy density. The plasma is a highly dynamic load, which together with the pulse reflections on the cable coupler and in the corona-plasma reactor make matching our very short pulses to the plasma a challenge.

The pulse reflection on the reactor interface has a significant influence on matching, and should be as low as possible to transfer the most energy into the reactor. The reflection decreases as plasma develops. From this reflection we can calculate the reactor impedance as a function of time, and see that it decreases with time (due to the development of plasma) and applied voltage (due to a more intense plasma), and that it is slightly lower for negative pulses.

The matching results show that there is only a small effect on the matching between different wire diameters. Furthermore, a long reactor and a long pulse result in the best matching due to the more intense plasma that is able to develop in these conditions. Experiments show that the rise time has a significant effect on the matching: a short rise time results in better matching and for energy densities in the range 10–250 J·L^{-1} (the operating range in this thesis) the matching remains constant.

To decrease the pulse reflection in the reactor interface while maintaining a high electric field on the wire, we developed a multiple-wire inner conductor for the reactor which decreases the vacuum impedance of the reactor. The results were very encouraging and showed an energy transfer efficiency of over 90 percent. Finally, even without the multiple-wire reactor, we are able to achieve a very good matching (over 80 percent) between our pulse source and the reactor.

6.1 Introduction

Maximising the energy transfer of a pulse source to a plasma load is one of the main challenges to overcome in order to maximise the full potential of pulsed discharges for air-purification applications. This energy transfer efficiency is generally called the 'matching' of the pulse source to the corona-plasma reactor and a good matching is generally obtained when the impedance of the plasma load is similar to the output impedance of the pulse source.

In this thesis we are investigating the effect of very short pulses on plasma properties such as the propagation of the streamers in the plasma and the chemical efficiency. We know from literature that these very short pulses can be beneficial to plasma-processing applications [5–8, 11]. However, when the pulse duration of the applied pulses becomes short (nanoseconds with sub-nanosecond rise time), matching a pulse source to a corona-plasma reactor becomes a challenge. In this regime a corona-plasma reactor behaves as a transmission line and part of the applied high-voltage pulse will be reflected back to the pulse source. Therefore, this part of the pulse energy is lost and will not contribute to the initial plasma process. Since we will be working with sub-nanosecond rise time short pulses, it is especially useful to investigate matching of a pulse source to a corona-plasma reactor in detail. In particular we want to know: what is the reactor configuration that results in the best energy transfer efficiency?

6.1.1 Plasma load

An energy transfer efficiency of 100 percent from the pulse source to the plasma is only possible if the plasma is a perfectly matched load (if the output impedance of pulse source is equal to the impedance of plasma). However, the reality is much more complex. When a voltage pulse with a long rise time is first applied to a reactor, the reactor behaves as a capacitor. During the charging of this capacitor by the voltage pulse, streamers can initiate. Since the streamers have a resistive character the load of the high-voltage pulse now becomes part dissipative. However, the resistive part of the streamers is only between the high-voltage wire and the streamer head. Between the streamer head and the reactor wall only a displacement current can flow. The streamer can therefore be seen as a time-varying resistor with a time-varying capacitor in series. These first streamers are the primary streamers. When the streamers bridge the gap, they form a completely resistive load and reach the secondary streamer phase.

The result of this streamer development in time is that the plasma load undergoes three phases in which it is successively capacitive, part capacitive and part resistive and finally resistive. Therefore, the plasma load is a very dynamic and complex load. Achieving perfect matching in the primary streamer phase (part capacitive and part resistive) is nearly impossible. Unfortunately (from a matching point of view), with our very short pulses we expect that the streamers will mainly exist in the primary streamer phase. Furthermore, our voltage pulse has a short rise time, whereas in the analysis above we assumed a pulse with a long rise time. With a short-rise time pulse, reflections at the reactor interface and in the reactor become important and the voltage

in the reactor will change on short time-scales and might be very different at different positions in the reactor. Therefore, matching the pulses of our nanosecond pulse source to a corona-plasma reactor becomes very challenging.

6.1.2 Previous studies

At Eindhoven University of Technology, pulsed corona plasmas for air purification have already been studied for a long time [18, 23–26]. Naturally, matching the pulse source to the plasma was one of the topics that some of these studies treated. More specifically the conclusions of Yan [25] and Winands [18] on matching which are relevant for our work are listed below.

- Applied voltage: a higher voltage results in better matching. This effect was attributed to the generation of more parallel streamers a high voltages.
- Pulse duration: longer pulses match better than short pulses. For short pulses the streamers consist only of primary streamers, whereas for longer pulses secondary streamers can form as well. When a plasma consists of secondary streamers the corona-plasma reactor behaves as a resistive load and therefore the matching can become very high.
- A plasma with positive streamers can be matched better to the pulse source than a plasma with negative streamers.

These conclusions once more emphasise the challenge of matching a very short pulse to a corona-plasma reactor.

Previous studies into the energy transfer of a nanosecond pulse source to a corona-plasma reactor focused on changing a number of reactor and source parameters such as reactor length, reactor configuration, pulse amplitude, pulse polarity, pulse duration, pulse rise time, pulse source output impedance and DC bias voltage [29, 34, 117–125]. The results show a number of good matching methods. Naturally, changing the output impedance of the pulse source to the plasma load works well [122], but this is not always practical. Changing the plasma load itself would often be a more flexible solution. Changing the plasma load by changing reactor parameters such as length and electrode spacing works well in some instances [124, 125]. Another practical method of providing good matching is changing the plasma load by changing the parameters of the high-voltage pulse that generates the plasma, like we already showed in the conclusions of Yan and Winands. For instance, a short rise time and a high amplitude generate a low-impedance streamer plasma, which matches better to the source [34, 120, 125]. What all these results show above all is that matching is a complex process, which depends greatly on the used setups. Only some common conclusions can be found, like the increased matching with voltage.

One of the matching-tools that Yan en Winands used (as well as other researchers) is the use of a DC bias voltage [29, 117–119, 121, 125]. This DC voltage is superimposed on the pulsed voltage and has some significant advantages. First, a DC bias increases the electric field in the corona-plasma reactor and consequently results in a more intense

discharge and therefore increases the matching. Second, this DC bias can generally be added at a low cost and therefore offers a cheap method to vary the plasma behaviour and last, the DC bias offers a simple way to add energy to the plasma without the complexities of switching a high current and a high voltage. The downside to the DC-bias method is that the DC voltage has to be decoupled from the pulse voltage by a decoupling network, which can have an adverse effect on the properties of the pulse. In this chapter we introduce a method to add a DC bias voltage to the pulse voltage of a nanosecond pulse source without these adverse effects. These experiments were performed during a leave to Kumamoto University in Japan with the 5-ns triaxial Blumlein source developed by Wang *et al.* [6, 36]. The full report on this method is added in Appendix A of this thesis.

The parameter that commonly results in higher matching is a high E/n value (where E is the applied electric field and n is the gas density) in the plasma reactor. We already mentioned that increasing E (with the pulse voltage and a superimposed DC voltage) increases matching. The gas density can be varied by pressure and temperature. For instance, previous studies showed that a higher temperature (lower n) increases the dissipated plasma energy [66, 126, 127]. In a separate investigation from the main contents of this thesis we investigated the dependency of the matching and streamer propagation when the E/n value was changed by changing the pressure and the temperature. We showed that a higher E/n value (low pressure or high temperature) increases the energy consumption of the plasma and therefore leads to a better matching. The results of this study are presented in Appendix B.

Besides the experiments in Appendix B we always perform our experiments at room temperature and at atmospheric pressure in this thesis. Therefore the only puls parameter to vary E/n is the voltage in the reactor. Besides this matching parameter, the matching in our experiments will depend on the reactor configuration, as this configuration determines parameters like the initial transmission-line impedance and the electric field at the high-voltage wire. Due to the very short rise time of our pulses, we also have to consider pulse reflections on the reactor interface and in the reactor, because these reflections determine the voltage locally in the reactor and therefore influence the streamers.

6.1.3   Chapter organisation

In this chapter we investigate a number of corona-plasma reactor parameters to obtain a good transfer efficiency. We will use a coaxial corona-plasma reactor to obtain a large volume plasma required for efficient chemical processing of gasses. The parameters we vary to study the effects on matching are: pulse voltage amplitude, voltage polarity, pulse duration, pulse rise time, reactor inner-wire diameter, reactor inner-wire configuration, reactor length, and energy density.

With electrical measurements we are able to measure the pulse energy and the plasma energy and with ozone measurements we measure ozone concentrations. We measure these ozone concentrations to investigate whether changes in matching also reflect in the ozone yield of the plasma. This ozone yield indicates how efficiently
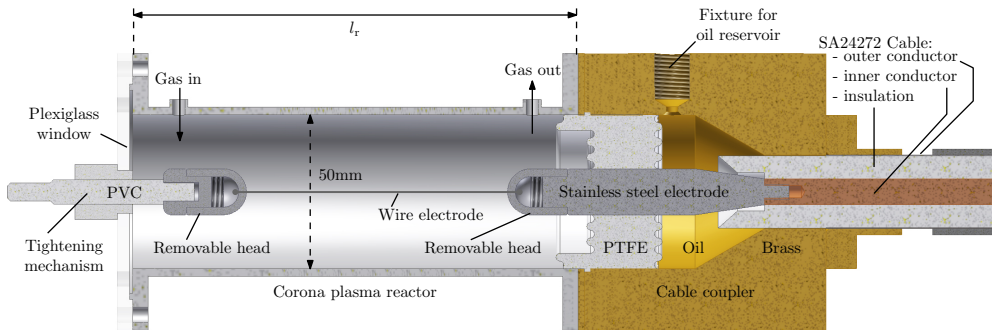
Figure 6.1: The corona-plasma reactor (the length of the reactor has been shortened for display purposes). On the right side of the sketch, the SA24272 cable is connected to the a cable coupler, much like the connection of the SA24272 cable to the nanosecond pulse source. The cable coupler is oil-filled for high voltage insulation. An oil reservoir (not shown) is connected on top of the coupler. The inner conductor of the cable is connected to a stainless-steel electrode with a removable head. Between the interface of the coupler and the reactor we placed a PTFE insulator and the reactor is connected to the cable coupler. The wire electrode is strung between the removable heads of the electrode and the tightening mechanism and is tightened by pulling the tightening mechanism outwards with a nut on a threaded body. Furthermore, the reactor has a gas inlet and a gas inlet for the process gas.

the plasma energy is utilised to generate ozone and is generally used as a monitor for plasma performance [5, 28, 36, 128–132].

In the next section we elaborate on the experimental setup and procedure to measure energies, ozone and how to determine the matching. The four subsequent sections present the matching and ozone yield results for when we vary the reactor wire diameter, the reactor length and pulse duration, the pulse rise time and the energy density respectively. These sections are followed by Section 6.7 which presents a multiple-wire reactor, Section 6.8 in which we discuss the observations on the difference between the matching between negative and positive pulses and Section 6.9 in which we shortly outline the new method we developed to add a DC bias voltage to a nanosecond pulse source. Finally, we present the summary and conclusions of this chapter.

6.2 Experimental setup and procedure

6.2.1 Corona-plasma reactor

In this chapter we use the final implementation of the nanosecond pulse source that was presented in Chapter 3. The nanosecond pulse source is connected to a SA24272 cable to transmit the output pulses to the load. Figure 6.1 shows the corona-plasma reactor we designed and connected at the other end of the SA24272 cable.

The corona-plasma reactor is a wire-cylinder reactor of length l_r. In our experiments we will use three different reactor lengths: 0.25 m, 0.50 m and 1.0 m. A thin wire of
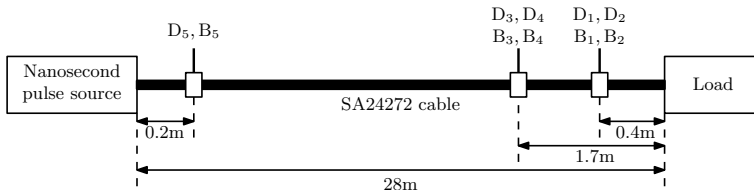
Figure 6.2: The sensor configuration. The sensor body at the pulse source side has only one D-dot and B-dot sensor. The two sensor bodies near the corona-plasma reactor have two D-dot and two B-dot sensors.

diameter d_i is strung between two removable heads as the high-voltage wire electrode of the reactor. The removable heads allow us to change the wire diameter by replacing the wire. We will use four different wire diameters: 0.3 mm, 0.5 mm, 0.7 mm and 1.0 mm. The Plexiglass window at the end of the reactor enables visual inspection of the plasma and a gas inlet and a gas outlet offers the possibility to flow a gas through the reactor.

The SA24272 cable is attached to the reactor via a custom-made cable coupler. It is oil-filled and internally supported by a PTFE part for high-voltage insulation and allows the cable to be connected to the reactor with a minimum of impedance mismatch. An oil reservoir (not shown) is mounted on top of the cable coupler to ensure that the cavity inside the coupler remains oil-filled.

6.2.2   Energy measurements

Energy measurements are crucial for our matching investigation, because to measure this matching we need to measure the energy that is consumed by the plasma, as well as the energy that was supplied by the nanosecond pulse source. For these energy measurements we developed the D-dot sensors and B-dot sensors of Chapter 5. Their positions are shown in Fig. 6.2.

With sensors D_5 and B_5 we could measure the energy from the pulse source, but then we would only have two channels of the 4-channel LeCroy WavePro 7300A oscilloscope left for the plasma energy measurements and we specifically integrated two sensors of each type in each of the load-side sensor bodies to decrease the influence of interference on our measurements. Likewise, with sensors D_1, D_2, B_1 and B_2 we could measure the energy that is dissipated by the plasma, but have no channels left to measure the supplied energy by the nanosecond pulse source. The solution to this problem is the use of sensors D_3, D_4, B_3 and B_4. We purposely situated these sensors at a distance from the reactor such that we can measure the incoming pulse as it arrives and then measure the reflected pulse from the reactor with enough time interval between these pulses (even at the 10-ns pulse duration setting of the pulse source). In this way we can calculate the plasma energy as the incoming energy minus the reflected energy.

Figure 6.3 shows an example of an energy measurement, starting with the measured voltage and current with sensors D_3–D_4 and B_3–B_4 respectively in Fig. 6.3a. By using

96
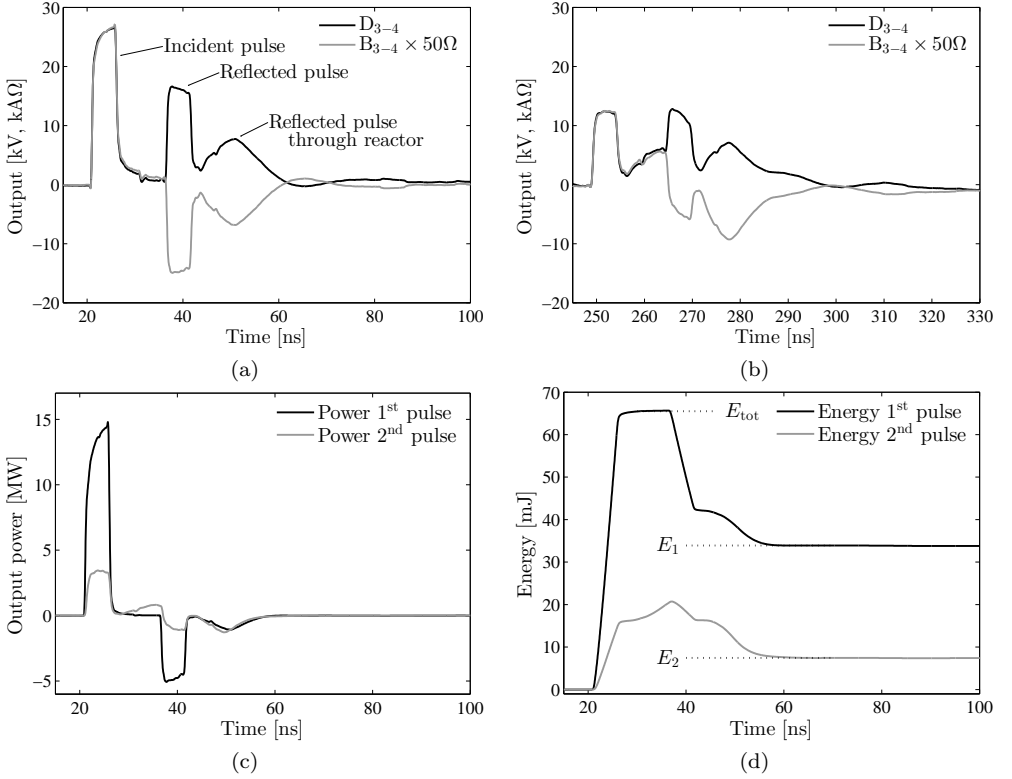
Figure 6.3: An example energy measurement. (a) The voltage and current measured by sensors D_3, D_4, B_3 and B_4. In this figure we can distinguish three pulses: the pulse that the nanosecond pulse generates and is transmitted over the SA24272 cable (incident pulse), the pulse that is reflected on the interface to the corona-plasma reactor (reflected pulse) and the pulse that is transmitted into the reactor, travels up and down the reactor and is then transmitted back into the cable (reflected pulse through reactor). (b) The waveforms that are measured after the pulse and its reflections have reflected back onto the pulse source and are reapplied to the reactor (2nd pulse). (c) The corresponding power of the waveforms of (a) and (b) (the waveforms are shifted about 230 ns for display purposes) and finally (d) shows the energies. The total applied energy to the reactor is indicated with E_{tot}, the energy that was consumed by the reactor as E_1 and the energy associated with the reapplied pulse as E_2.

this sensor position we can first see the complete 5-ns incident pulse from the pulse source passing (notice that this would still be the case for a 10-ns pulse). Figures 6.3c and 6.3d show the corresponding power and energy calculated from these waveforms.

The power and energy are calculated from the D-dot and B-dot sensors with:

$$\text{Power}(t) = I_{B_{3-4}}(t)V_{D_{3-4}}(t). \tag{6.1}$$

97

$$\text{Energy}(t) = \int_0^t \text{Power}(\tau)\, d\tau. \tag{6.2}$$

We see that we can measure the total applied energy to the reactor E_{tot} by taking only the contribution of the first incident pulse.

When the pulse passes the sensor position it encounters the reactor and will partly reflect back to the pulse source and partly transmit into the reactor. The amplitude of the reflected pulse is determined by the reflection coefficient R as

$$R = \frac{Z_{\text{r}} - Z_{\text{cable}}}{Z_{\text{r}} + Z_{\text{cable}}}, \tag{6.3}$$

where Z_{r} is the vacuum impedance of the reactor and Z_{cable} is the 50-Ω impedance of the SA24272 cable. The impedance of the gas-filled reactor is given by

$$Z_{\text{r}} = \frac{1}{2\pi} \sqrt{\frac{\mu_0}{\epsilon_0}} \ln \frac{d_{\text{o}}}{d_{\text{i}}}, \tag{6.4}$$

where μ_0 and ϵ_0 are the permeability and permittivity of vacuum respectively, d_{o} is the 50-mm inner diameter of the outer conductor of the reactor and d_{i} is the diameter of the wire electrode of the reactor. This reactor impedance will be higher than the cable impedance, so the reflected pulse will be positive. This is the reflected pulse as indicated in Fig. 6.3a.

The part of the pulse that is transmitted into the reactor propagates up and down the reactor, generating plasma, and transmits back into the SA24272 cable. This is the third, attenuated peak in Fig. 6.3a. It is severely attenuated and dispersed by the plasma. Part of the pulse inside the reactor will also reflect back into the reactor instead of transmitting into the SA24272 cable, but this part diminishes over time. A more detailed analysis of the reflected and transmitted waveforms inside the reactor and the cable will follow in Sections 6.2.4 and 7.2.

If we look at Fig. 6.3d then we see that the reflected pulse causes as a sharp decrease in energy of the first pulse because the energy of the reflected pulse moves in the opposite direction of the incident pulse. This opposite direction is also apparent from the current in Fig. 6.3a. The attenuated pulse from the reactor decreases the pulse energy even more. After this time the energy is stable. The energy that is measured at this point is the energy that is 'left' in the reactor and is therefore the energy that was dissipated by the plasma. This energy is indicated by E_1.

Figure 6.3b shows the reflected pulse after it has travelled down the SA24272 cable, reflected on the nanosecond pulse source and travelled back to the sensor position. This pulse is indicated in Fig. 6.3 as the second pulse. By this time it is severely attenuated and dispersed, but is still able to generate plasma if its amplitude is high enough. Figure. 6.3c shows that there is still significant power associated with this second pulse and Fig. 6.3d confirms that it still (re-)ignites the plasma. We already saw in [72] that the reapplication of the reflected pulses from our nanosecond pulse source can reignite a plasma up to as much as the tenth reflection. However, in that experiment we only dissipated a very small amount of energy in each reflection. Here,

with the larger reactor, the plasma dissipates a large amount of energy and therefore we only have to take the second pulse (the first reflection) into account. The third pulse will have a very low amplitude and dissipates a negligible amount of energy in the reactor.

The energy associated with the first reflection (the second pulse in Fig. 6.3b) is indicated in Fig. 6.3d as E_2. Both E_1 and E_2 will be used in all the matching calculations. Later they will also both be used for all the plasma-processing yield calculations of Chapter 8, but also for the ozone-yield calculations of the current chapter.

We can now perform all the energy measurements with just one sensor body. This allows for the use of two D-dot sensors and B-dot sensors for all measurements. This would not have been possible with sensors D_1, D_2, B_1 and B_2.

6.2.3 Matching definitions

To perform matching experiments we need to know how much energy was dissipated by the plasma with respect to the total applied energy. Therefore, we introduce two matching parameters: the initial matching η_i which only uses the energy of the first applied pulse and η_{tot} which also includes the energy of the first reflected pulse. They are calculated as

$$\eta_i = \frac{E_1}{E_{tot}}, \tag{6.5}$$

$$\eta_{tot} = \frac{E_1 + E_2}{E_{tot}}. \tag{6.6}$$

These matching definitions will be used in the sections on matching experiments.

6.2.4 Reactor impedance

In Fig. 6.3a we could clearly see that part of the incident pulse is reflected when it reaches the corona-plasma reactor. The amplitude of this reflected pulse was described by Eq. 6.3. However, the reflection coefficient is more complex than this equation shows. When plasma is generated in the reactor the impedance of the reactor Z_r changes. First, the plasma has the effect that the inner conductor diameter d_i in Eq. 6.4 increases artificially since a cloud of highly ionised plasma is generated around it. Second, the plasma consumes energy and will therefore get a more resistive character. Both of these effects result in a lower reactor impedance. Therefore, the reactor impedance (and by association the reflection coefficient) becomes time dependent. The reflection coefficient and transmission coefficient become

$$R(t) = \frac{Z_r(t) - Z_{cable}}{Z_r(t) + Z_{cable}}, \tag{6.7}$$

$$T(t) = \frac{2Z_r(t)}{Z_r(t) + Z_{cable}}. \tag{6.8}$$

We can calculate $R(t)$ from measured waveforms such as Fig. 6.3a by dividing the reflected pulse by the incident pulse as

$$R(t) = \frac{V_r(t)}{V_i(t)}, \tag{6.9}$$

where $V_i(t)$ and $V_r(t)$ are the incident and reflected pulse respectively (here we neglected the attenuation of the pulse over the 1.7 m of SA24272 cable that separates the D-dot and B-dot sensor body from the reactor). With $R(t)$ we can now calculate $Z_r(t)$ as

$$Z_r(t) = \frac{-[1 + R(t)]Z_c}{R(t) - 1}. \tag{6.10}$$

We can then calculate the transmitted pulse into the reactor $V_t(t)$ as

$$V_t(t) = V_i(t)T(t). \tag{6.11}$$

Figure 6.4 shows an example of a reactor impedance measurement. In Fig. 6.4a we see the measured incident and reflected pulse and the calculated transmitted pulse. The results show that when $T(t)$ is larger than 1 — which it will always be when the reactor impedance is higher than the cable impedance — the transmitted pulse amplitude is higher than the amplitude of the incident pulse. Therefore, when the matching is bad (large $R(t)$) the pulse amplitude at the beginning of the reactor is very high. However, this voltage will drop quickly when energy is dissipated in the reactor, because the associated impedance is large.

Figure 6.4b shows $R(t)$ and $T(t)$ for the example of Fig. 6.4a. Likewise, Fig. 6.4c shows the corresponding calculated impedance of the reactor. On the flanks of the applied pulse (before t_1 and after t_2) the coefficients are not valid. Therefore, in the remainder of this chapter the reactor impedance will only be shown for the time period t_1–t_2. The impedance in the example drops with time, which is expected due to the plasma.

With a wire diameter of 0.5 mm and a reactor inner diameter of 50 mm the vacuum impedance of the reactor, Eq. (6.4) gives an impedance of around 276 Ω for the reactor. Fig. 6.4c confirms this value as the initial impedance of the reactor.

6.2.5   Rise-time variation

One of the parameters of the high-voltage pulses which would be interesting to vary is the rise time. With our developed nanosecond pulse source we can change the pulse amplitude, polarity and duration, but varying the rise-time is difficult. One possibility would be to change the geometry of the spark gap in such a way that its parasitic inductance would be increased, thereby increasing the rise time of the pulses. However, this is not straightforward to accomplish and the pulse source was not designed for this eventuality.

A second method to change the rise time of the pulse would be to influence the propagation of the pulse over the SA24272 cable. This could be accomplished by

(a)

(b)

(c)
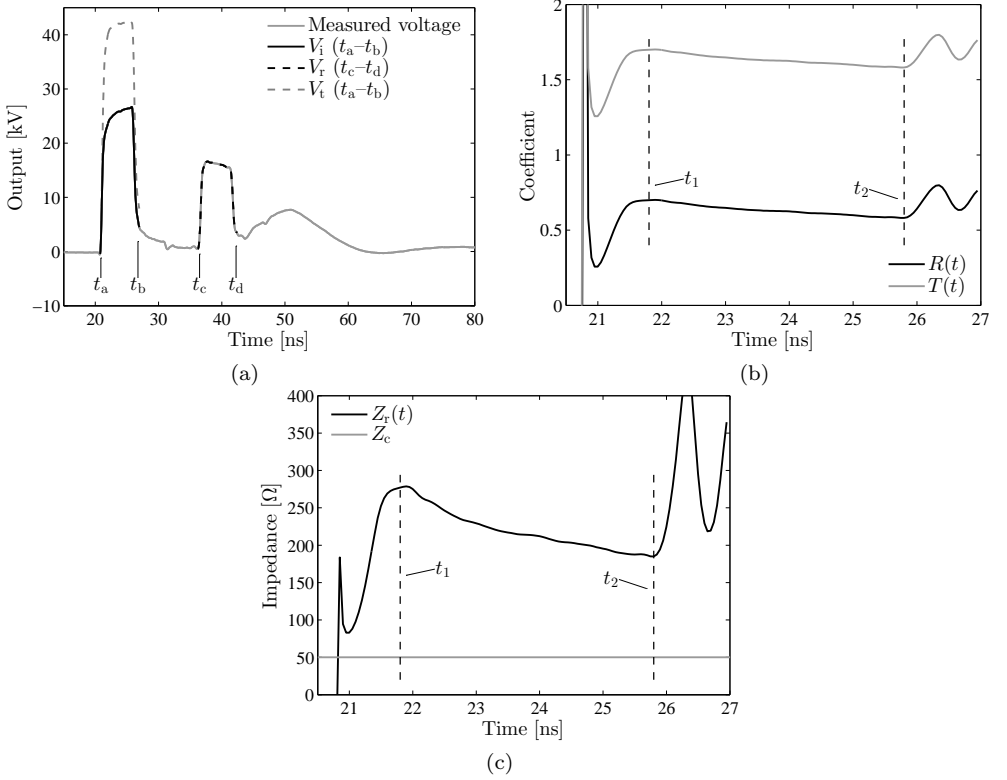
Figure 6.4: (a) The measured incident (V_i) and reflected pulse (V_r) from which the transmitted pulse (V_t) is calculated. (b) The calculated time-dependent reflection and transmission coefficients from the waveform of (a). (c) The calculated reactor impedance from the reflection coefficient of (b).

introducing an inductor in series with the cable, for instance by disconnecting the outer conductor of the cable and adding a loop of wire over the disconnected conductor. However, the outer conductor of the SA24272 cable is fragile and we are reluctant to interfere with it. Besides, a disconnected outer conductor also results in increased electric-field stresses in the cable insulation, which we want to avoid. Furthermore a high voltage drop would be present over the introduced inductance for a short time, which increases the complexity of the design.

A third option to vary the rise time of the pulse is to introduce an inductor into the corona-plasma reactor. Adding an inductor in series with the high-voltage wire of the reactor would require careful high-voltage engineering and varying the value of the inductor would be a complex task. It would be more straightforward to add the inductor in series with the outer conductor of the reactor, but then this outer conductor would not be grounded anymore for a short duration (when the pulse is

101
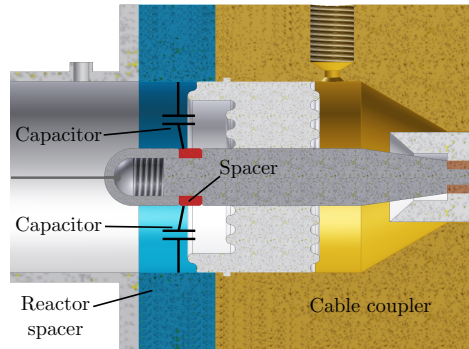
Figure 6.5: The cable coupler with added brass spacers (red-coloured and blue-coloured in the figure) to enable mounting of capacitors to increase the rise time of the applied pulses.

applied) and would be at a high-voltage potential, which is unwanted for safety reasons. Nevertheless, of all the solution consisting of introduction an inductor, it is the most straightforward.

A fourth option to change the rise time of the pulse is to introduce a capacitor in parallel with the reactor. This capacitor has to be connected at the beginning of the reactor, because of the short pulses and the associated transmission-line behaviour of the reactor. It is this solution that we used to change the rise time of the pulses.

To be able to connect the capacitor in the reactor we placed a brass spacer between the removable head of cable coupler of the reactor and the stainless-steel electrode. Figure 6.5 shows this method (refer to Fig. 6.1 for the complete reactor overview). The capacitor is mounted on this spacer. At the outer electrode we placed another brass spacer with mounting provisions. It is also shown in Fig. 6.5. The capacitor comprises in-series-connected 100-pF 10-kV capacitors. In the experiments we use three configurations: no capacitors, a string of three capacitors in series resulting in a total capacitance of 33 pF and two parallel strings of three capacitors in series resulting in a total capacitance of 67 pF.

In Section 7.2 we introduce a SPICE model of our corona-plasma reactor. Figure 6.6a shows the simulated transmitted waveforms when we add these capacitors to the SPICE model of our reactor. The results show that a successful change in the rise time can be realised. For more details on the SPICE model, refer to Section 7.2.

It is not possible to measure the waveforms in the real reactor directly, but the applied reactor waveform can be found indirectly through the method we described in Section 6.2.4. Waveform V_t is the transmitted waveform (the waveform applied to the reactor) that can be calculated from the incident waveform and the reflected waveform. If we apply this method to measurements on the reactor with the capacitors we find the waveforms of Fig. 6.6b. The waveforms after time t_r are not purely the applied waveforms anymore, because at this time the transmitted pulse has travelled up and
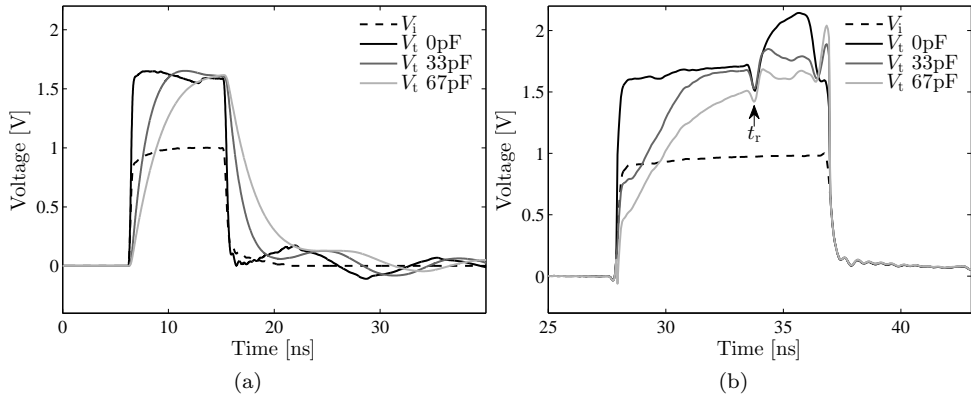
Figure 6.6: The rise-time variation of the 9-ns pulse. By adding capacitors in the corona-plasma reactor we can achieve a rise-time of 0.4 ns (no capacitor), 2.9 ns (33 pF) and 5.6 ns (67 pF). (a) SPICE simulations of the transmitted waveforms (normalised) in the reactor. (b) Transmitted waveforms (normalised) in the reactor calculated from measurements. In (b) the waveforms after time t_r should be ignored because the calculated waveforms are no longer the real transmitted waveforms.

down the reactor and adds to itself. However, if we consider the waveforms up to t_r we find (10–90 percent) rise times of 0.4 ns (no capacitor), 2.9 ns (33 pF) and 5.6 ns (67 pF) for the three reactor configurations. Deviations from the simulation mainly occur at the beginning of the pulse, where even with the capacitors in place, the pulse shows an initial sharp increase. This can be explained by the inductance that the real capacitors have and which will block the pulse from 'seeing' the capacitors for the first hundreds of picoseconds.

We will use the rise-time variation method described here for 9-ns pulses for the measurements on matching with different rise times and in Chapter 7 and Chapter 8 to change the rise time of the pulses and study the effect on streamer propagation and several plasma-processing applications respectively.

6.2.6 Ozone measurements

To verify whether the matching of the pulse source has an influence on the plasma chemistry we measured ozone concentrations in the exhaust of the reactor simultaneously with all energy measurements. This allows us to calculate an ozone yield. With the addition of the ozone measurements, Fig. 6.7 shows the total experimental setup for the measurements of this chapter.

We use synthetic air with less than 3 ppm H_2O content as the process gas in our reactor to obtain a controlled and reproducible environment in all our experiments. A mass flow meter (mfm) controls the gas flow into the reactor. In the exhaust of the reactor we placed a 30-mm optical path cell for UV absorption measurements. Optic
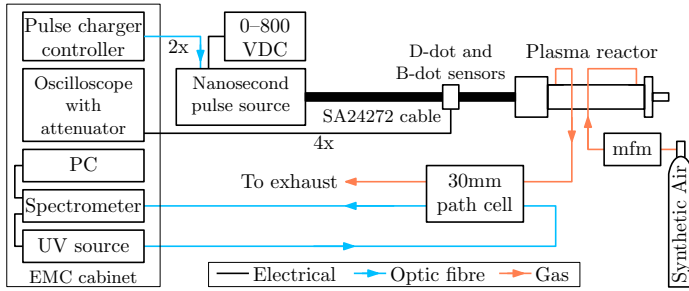
Figure 6.7: The total experimental setup. A 0–800-V DC power supply controls the charge voltage of the pulse forming line of the nanosecond pulse source and the pulse charger controller engages the driver circuits of the pulse chargers via optic fibres. The measurements with the D-dot and B-dot sensors were described in detail in the previous chapter. A bottle of synthetic air comprises the gas supply (through a mass flow meter) for the reactor. In the gas outlet of the reactor a 30-mm path cell is used for the UV-spectrometer measurements to measure ozone concentrations.

fibres connect the path cell to a UV source and an Ocean Optics HR2000 spectrometer. We measured the plasma-off and plasma-on spectra in the Hartley-band (230–290 nm) to obtain the ozone concentration. To minimise errors we used the absorption at 20 different wavelengths from 250-270 nm. The complete procedure is described in [18, p. 55–56].

With the measured ozone concentration C_{O_3} (in ppm) and the energies E_1 and E_2 we can define the ozone yield of the plasma G_{O_3} (in g·kWh^{-1}) as

$$G_{O_3} = \frac{\dfrac{C_{O_3}}{10^6} \times \dfrac{1}{V_\mathrm{m}} \times 48 \,[\mathrm{g} \cdot (\mathrm{mole}\,O_3)^{-1}]}{\dfrac{\dfrac{1}{F} \times 60 f_\mathrm{rr}(E_1 + E_2)}{3.6 \times 10^6 \,[\mathrm{J} \cdot \mathrm{kWh}^{-1}]}}$$
$$= \frac{C_{O_3} F \times 48 \times 3.6}{V_\mathrm{m} f_\mathrm{rr}(E_1 + E_2) \times 60}, \tag{6.12}$$

where V_m is the molar volume (24.5 L·mole^{-1} at room temperature), f_rr is the repetition rate of the pulse source and F is the gas flow (in L·min^{-1}). The expression can be further reduced if we introduce the energy density ε (in J·L^{-1}) as

$$\varepsilon = \frac{f_\mathrm{rr}(E_1 + E_2) \times 60}{F}. \tag{6.13}$$

The ozone yield then becomes

$$G_{O_3} = \frac{C_{O_3} \times 48 \times 3.6}{V_\mathrm{m} \varepsilon}. \tag{6.14}$$

6.2.7 Nanosecond pulse source

With the pulse-charger controller and the DC power supply we control the nanosecond pulse source. The pulse repetition rate and the charge time of the IGBTs of the pulse charger are controlled by the pulse charger controller in the EMC cabinet. The output voltage of the nanosecond pulse source is controlled by changing the DC charge voltages and the spark-gap distance. In general, for all measurements we set the DC charge voltage and adjust the spark gap accordingly. The DC charge voltages that we used in the experiments of this chapter were 200 V, 300 V, 400 V, 500 V and 600 V. Furthermore, we always perform experiments with both positive and negative pulse polarities.

6.3 Matching results and discussion: wire diameter

In this section and Section 6.4, 6.6, 6.5 and 6.7 we experimentally investigate the matching of the pulses from the nanosecond pulse source to the corona-plasma reactor for different reactor parameters and experimental settings.

The first reactor parameter we investigate is the diameter of the wire electrode d_i in the reactor. If we look at Eq. 6.4 we see that if we want to get the impedance of the reactor as close as possible to the impedance of the SA24272 cable, d_i should be as large as possible. For a perfect 50-Ω impedance d_i should be 21.7 mm. However, if we look at the electric field at the wire electrode it follows that d_i should be as small as possible to obtain the highest electric field:

$$E_{\max} = \frac{2V_0}{d_i \ln \frac{d_o}{d_i}}, \tag{6.15}$$

which is Eq. 2.6 restated, where V_0 is the amplitude of the applied voltage pulse. If the electric field at the wire is high, E/n is higher and the plasma will consequently dissipate more energy, which increases the matching.

Therefore a contradiction exists. To get the pulse from the nanosecond pulse source to propagate into the reactor d_i has to be large to lower Z_r, but then almost no plasma will develop because $E_{\max}$ is too low. Likewise, if we have a small d_i, $E_{\max}$ can be high, but the incoming pulse is transmitted poorly into the reactor because of the high Z_r that a small d_i ensures. Both a low Z_r (large d_i) and a high $E_{\max}$ (small d_i) will increase matching, so d_i has to be chosen such that the matching has an optimum.

6.3.1 Energy measurements

Experimental setup and method

In our experiments we use four values of d_i to investigate which results in the best matching: 0.3 mm, 0.5 mm, 0.7 mm and 1.0 mm. For these experiments we use a reactor length l_r of 1 m, a flow of synthetic air through the reactor F of 5.0 L·min^{-1}, a pulse duration Δt of 5 ns and a pulse repetition rate f_{rr} of 100 Hz. When we then
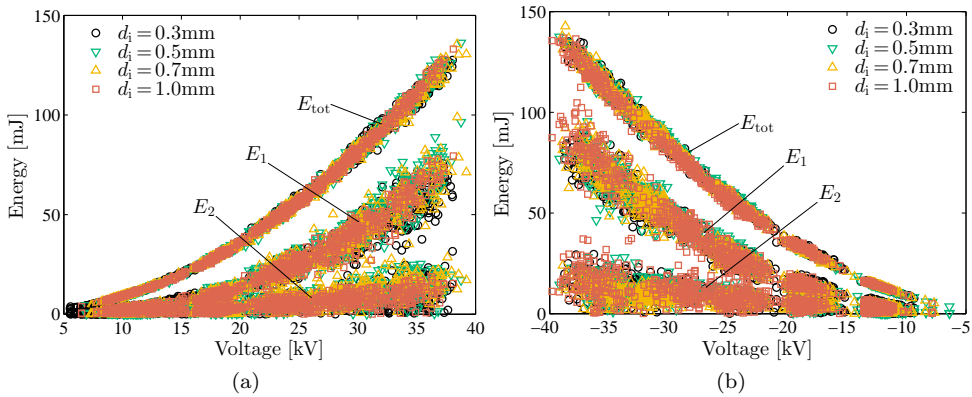
Figure 6.8: Raw data for the total pulse energy (E_{tot}), the energy dissipated in first pulse (E_1) and the energy dissipated in the first pulse reflection 230 ns later (E_2) for (a) positive voltages and (b) negative voltages. Experimental settings: $f_{rr} = 100$ Hz, $\Delta t = 5$ ns, $l_r = 1.0$ m and $F = 5.0$ L·min^{-1}.

measure the energies E_{tot}, E_1 and E_2 the results look like the results of Fig. 6.8. Now the disadvantage of the oil spark gap (large standard deviation on the output voltage amplitude) becomes an advantage; for just five spark-gap settings we are able to measure energies in the range of 5–40 kV.

The results of Fig. 6.8 are very scattered because of the standard deviation on the energy measurements (and on the pulse voltage due to the spark gap). This standard deviation is the result of the noise on the individual D-dot and B-dot measurements and translate into an error on the energy measurements. Furthermore, a streamer plasma is a stochastic process, which results in a natural standard deviation on plasma energy measurements. This explains why the standard deviation on the plasma energies E_1 and E_2 are larger than the standard deviation on the applied energy E_{tot}. By taking hundreds of measurements for each pulse source setting we are able to make use of voltage binning: we divide the voltage range in steps of several kV and for each of these bins we display the mean value of the measurements (voltage and energy) in this bin. The resulting cleaned results are shown in Fig. 6.9.

Error bars

For display purposes, we omit error bars in the figures of this chapter (and the remaining chapters of this thesis).

Figure. 6.8 gives an impression of the standard deviation on the energy measurements. When we calculate the matching with (6.5) and (6.6) we divide two energies with this standard deviation. As a result, the error on the matching results for low voltages is higher than for high voltages. Likewise, the error on the ozone yield results (and in Chapter 8 on the NO-removal yield results and the CO-production yield results)
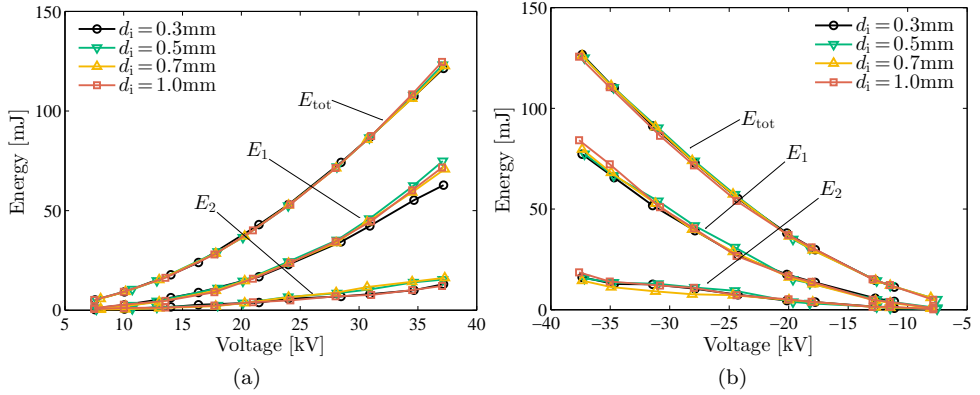
Figure 6.9: The cleaned result from the raw energy data (Fig. 6.8) for (a) positive voltages and (b) negative voltages.
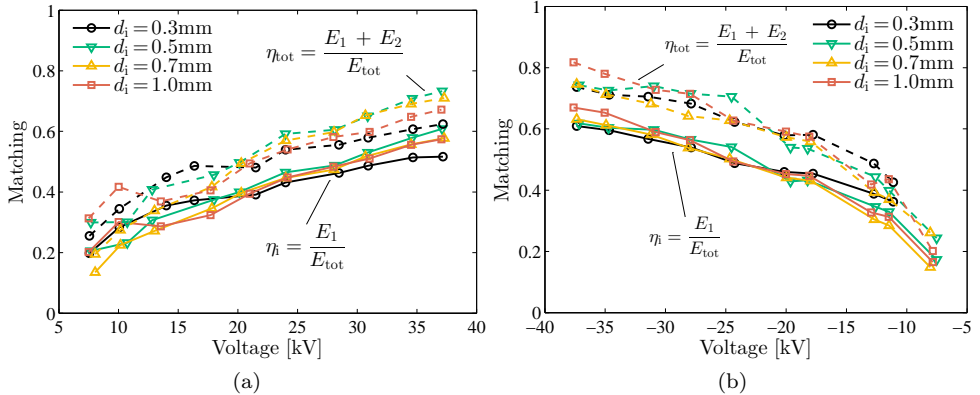
Figure 6.10: The matching of the pulses to the corona-plasma reactor calculated with the data from Fig. 6.9 for (a) positive voltages and (b) negative voltages. The matching is calculated with E_1 (solid line) and with $E_1 + E_2$ (dashed line) respectively.

is highest for the situation where only little ozone/NO/CO is produced/removed and the dissipated plasma energy is low. This is the case for low voltages and in Section 6.4 for short reactor lengths.

Results

The results of Fig. 6.9 show that there is no big difference in plasma dissipation between the different wire diameters. To clarify this we have to look at the matching parameters.

With the matching definitions of Eq. 6.5 and 6.6 we can generate Fig. 6.10. Obviously, η_{tot} is higher than η_i, but what is also interesting is that the matching increases
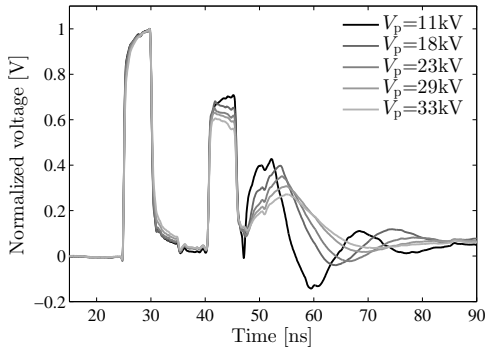
Figure 6.11: Normalised output voltage as a function of the pulse voltage. Experimental settings: $f_{rr} = 100\,\text{Hz}$, $\Delta t = 5\,\text{ns}$, $d_i = 0.5\,\text{mm}$, $l_r = 1.0\,\text{m}$ and $F = 5.0\,\text{L}\cdot\text{min}^{-1}$.
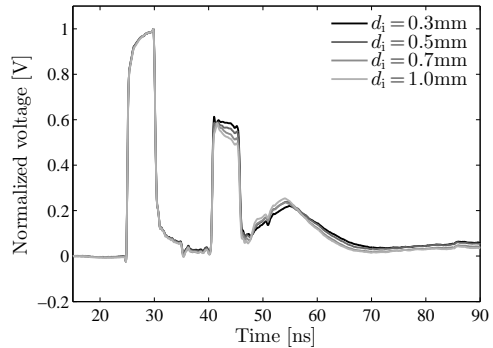
Figure 6.12: Normalised output voltage as a function of wire diameter. Experimental settings: $f_{rr} = 100\,\text{Hz}$, $\Delta t = 5\,\text{ns}$, $V_{pulse} = 33\,\text{kV}$, $l_r = 1.0\,\text{m}$ and $F = 5.0\,\text{L}\cdot\text{min}^{-1}$.

with the applied voltage. This is in accordance with for instance [123–125, 133, 134] and can be explained by the fact that at higher voltages a more intense plasma is generated, which increases the energy consumption of the plasma, but also decreases the impedance of the reactor. Both these phenomena result in a better matching. Therefore, the conclusion of Yan [25] and Winands [18] that a higher voltage results in better matching also applies to our reactor and furthermore confirm that a high E/n value increases matching.

When we compare the different wire diameters the result is that there is no significant difference in matching between the different diameters. Only $d_i = 0.3\,\text{mm}$ seems to underperform for both polarities. A striking difference between the matching results of both pulse polarities is that negative pulses match better on average than positive pulses. This is the opposite of what most researchers find and also runs contrary to the conclusion of Winands, who found that positive pulses match better. We explain this result in more detail in Section 6.8.

The wire resulting in good overall similar matching for both polarities is the 0.5-mm wire. It will be this wire that we will use in the remainder of the experiments.

Figures 6.11 and 6.12 show an additional display of the measurements. First, Fig. 6.11 shows the normalised voltage for five different voltage amplitudes V_p when the 0.5-mm wire was used. It shows that the amplitude of the reflected pulse (refer to Fig. 6.3a for the terminology) decreases in time when a higher voltage is applied. The reason for this effect is that during the application of the incident pulse on the reactor, plasma is generated. This decreases the reactor impedance while the pulse is being applied. This results in a lower value of the reflection coefficient and therefore in a larger part of the pulse being transmitted into the reactor and a lower part of the pulse being reflected back towards the pulse source. Figure 6.13 confirms that the reactor impedance indeed decreases when the applied voltage increases and when time passes.
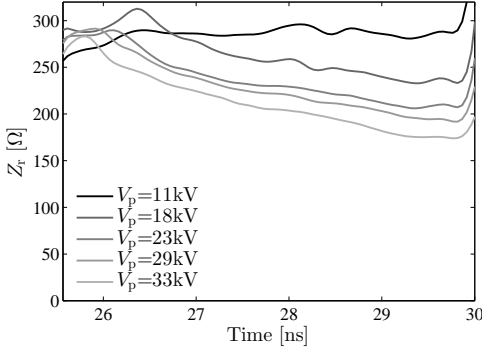
Figure 6.13: Reactor impedance as a function of the pulse voltage calculated with the waveforms of Fig. 6.11.
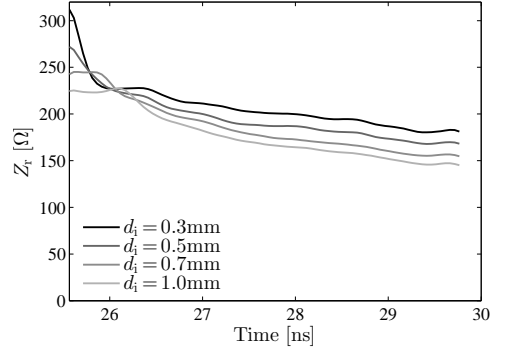
Figure 6.14: Reactor impedance as a function of wire diameter calculated with the waveforms of Fig. 6.12.

We already mentioned earlier that this is one of the reasons a higher applied voltage increases matching (besides the higher E/n in the reactor). Another observation from Fig. 6.11 is that the reflected pulse through the reactor has a lower amplitude and that it is longer for a higher applied voltage. The reason for this effect is that more energy is consumed by the plasma at higher voltages, which increases the attenuation and dispersion of the pulse in the reactor.

Second, Fig. 6.12 shows the normalised voltage for the 33-kV measurements of the different wire diameters. Earlier we stated that a larger d_i would result in a lower reflection coefficient and this is demonstrated in Fig. 6.12 by the slightly lower amplitude of the reflected pulse for $d_i = 1.0$ mm. This amplitude increases as d_i decreases. On the other hand, the 0.3-mm wire was able to consume more energy in the plasma, which results in a slightly lower and longer reflected pulse trough the reactor. The amplitude of the reflected pulse through the reactor increases with d_i, indicating that a plasma with larger wire diameter is unable to consume as much of the energy that is transmitted into the reactor.

Figure 6.14 confirms the lower reactor impedance for thicker wires. The initial values of the reactor impedances correspond well with the theoretical values calculated with Eq. 6.4; for $d_i = 0.3$ mm, 0.5 mm, 0.7 mm and 1.0 mm the calculated impedances are $307\,\Omega$, $276\,\Omega$, $256\,\Omega$ and $235\,\Omega$ respectively.

Figures 6.12 and 6.14 confirm all the assumptions we made about the effect of d_i. However, in practice, the difference in matching between the different wires is very small.

6.3.2 Ozone measurements

We measured ozone concentrations generated by the plasma simultaneously with the energy measurements. Figure 6.15 shows the results for each setting. Aside from the lower ozone concentrations for the 0.3-mm wire, all results are very similar.
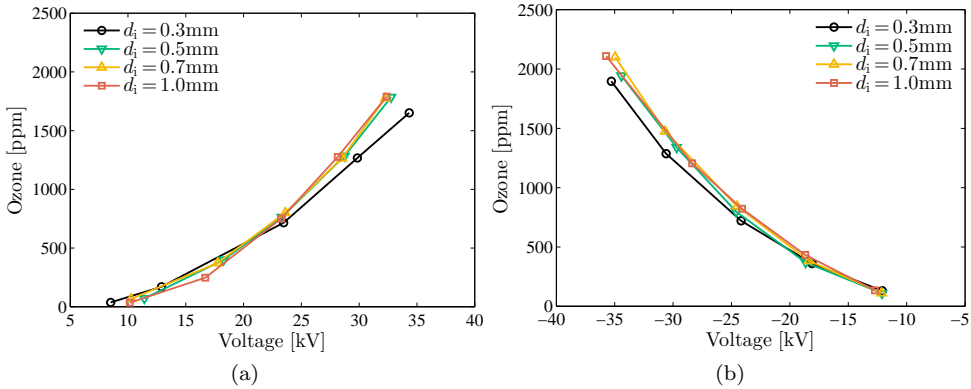
Figure 6.15: Ozone concentrations which were measured simultaneously with the energy measurements of Fig. 6.8 for (a) positive voltages and (b) negative voltages.

Figure 6.16: The ozone yield calculated from the results of the energy measurements of Fig. 6.8 and the ozone measurements of Fig. 6.15 for (a) positive voltages and (b) negative voltages.

The ozone measurements have a very low time resolution (several spectra per second) as compared to the energy measurements. Therefore we can only show average values of the ozone yield. Figure 6.16 shows the ozone yields. The yields were calculated with Eq. 6.12. The results show that the ozone yields when different wire diameters were used vary very little and that the only conclusion that can be drawn is that the plasma generated with positive pulses perform slightly better than the plasmas generated with negative pulses. This last observation is not consistent with the results of Winands who found that a negative pulse results in a higher ozone production [18]. Another inconsistency with other studies is that the ozone yield appears to increase slightly with the applied voltage in our measurements.

A final observation from the ozone yield results is that the yields are high for

a corona plasma. This shows that very short pulses are efficient for ozone production. Other studies with corona plasma reactors report efficiencies in the range of 15–100 g·kWh^{-1} [28, 128, 129, 132], with the exception of Wang *et al.* who report a very high yield of over 200 g·kWh^{-1} [36]. We will discuss ozone generation in more detail in Chapter 8 and only use the ozone-yield results in the remainder of this chapter as a comparison between different reactor configurations.

6.4 Matching results and discussion: reactor length

With the inner-wire diameter of the reactor chosen as 0.5 mm, we now turn our attention to the length of the reactor. It was already shown in by Namihira *et al.* and Matsumoto *et al.* in [135] and [124] that the matching of a nanosecond pulse source to a reactor improves as the reactor becomes longer. However, in that study, a 7-ns FWHM (Full Width Half Max) pulse with a rise- and fall time of around 3 ns was used. In our experiments we can use pulses of 0.5 ns to 10 ns duration and therefore a longer reactor might not always result in the best matching. Also, our pulses have a rise- and fall time that are an order of magnitude shorter than the pulses from the triaxial Blumlein line pulse source used in [135] and [124].

The length l_p over which a pulse with duration Δt is present in the reactor (in air) is given by

$$l_p = c\Delta t, \tag{6.16}$$

where c is the speed of light in vacuum. Therefore, a 1-ns pulse is only 0.3 m 'long' in air, which is shorter than our longest reactor. The propagation of such a pulse through a long reactor is a complex phenomenon and will be studied in Chapter 7.

For the experiments in this section we used all combinations of three different pulse durations (1, 5 and 9* ns) and three different reactor lengths (0.25, 0.50 and 1.0 m). Furthermore, each experiment was again performed at five different DC charge voltages and for both positive and negative pulse polarities at a repetition rate of 100 Hz and with a gas flow rate of 5 L·min^{-1}.

6.4.1 Energy measurements

Figure 6.17 shows the results of the energy measurements. An overall observation is that the matching significantly decreases when the reactor length decreases. The reason for this decrease is that the pulse is present in the reactor for a shorter time in a short reactor and consequently is unable to dissipate the same amount of energy as in longer reactor. This effect is observed for all three pulse durations. This indicates that there is no optimal reactor length for each pulse duration in the range of reactor lengths we investigated. Moreover, it means that our results are in agreement with the results with the lower-rise-rate pulse that were achieved in [135] and [124].

---

*The maximum pulse duration of the nanosecond pulse source is 10 ns, but due to the inductor we added to the end of the PFL it is very difficult to change the gap distance of the spark gap at 10 ns, which results in a practical maximum pulse duration of 9 ns.
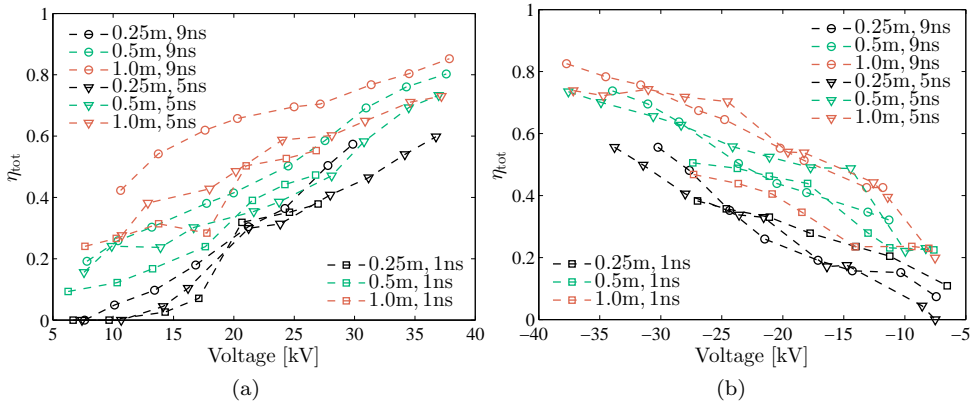
Figure 6.17: The matching of the pulses to the corona-plasma reactor (using E_1 and E_2) for different reactor lengths and pulse durations for (a) positive voltages and (b) negative voltages. Experimental settings: $f_{rr} = 100\,\text{Hz}$, $d_i = 0.5\,\text{mm}$ and $F = 5.0\,\text{L}\cdot\text{min}^{-1}$.

A second observation is that longer pulses appear to match better to the reactor. This effect is independent of the reactor length. However, the effect is stronger for longer reactor lengths and also appears to be somewhat stronger for positive pulse voltages. This is an indication that very short pulses are unable to generate plasma effectively; they are too short at these voltages. If we would be able to go to much higher voltages shorter pulses might also be able to match well, but we are limited by arc discharges that occur at the end of the reactor at high voltages. The arc discharges occur at the end of the reactor because at this position the pulse reflects and because the pulses have such a short rise time the voltage at the end of the reactor will almost double in amplitude. Chapter 7 will discuss the propagation and optical plasma observations of the plasma in much more detail.

The effect that longer pulses match better to the reactor was already observed by Winands [18]. He attributed this effect to the very resistive nature of secondary streamers, which are present for a longer time for longer pulses. In Chapter 7 we will see that we mainly have primary streamers in our reactor for most conditions. Therefore, there is no significant contribution of secondary streamers in our matching results. In our case, the streamers dissipate the energy while propagating through the reactor. For longer pulses, the streamers propagate for a longer time and reach further into the reactor, thereby dissipating more energy than when short pulses are used.

If we look at the 5-ns matching results, we see that negative pulses again match slightly better than positive pulses. However, for the 9-ns pulses the positive pulses appear to match better. The length of the reactor has no great effect on the difference between negative and positive pulses. We address this observation in more detail in Section 6.8.
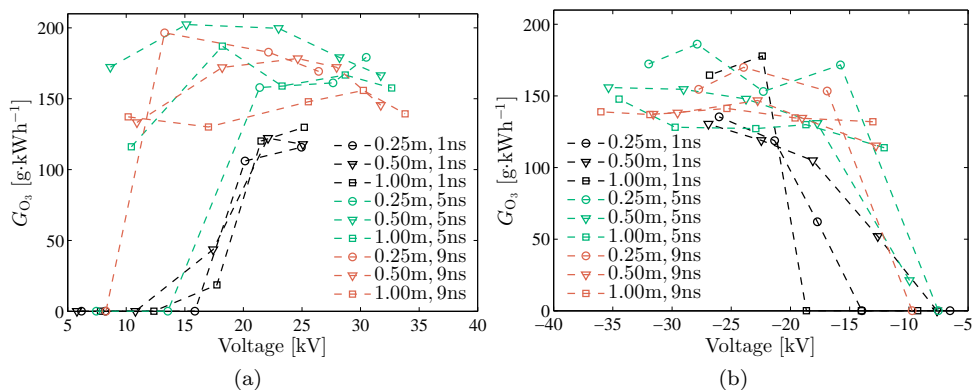
Figure 6.18: The ozone yield calculated from ozone measurements which were performed simultaneously with the energy measurements for Fig. 6.17 for (a) positive voltages and (b) negative voltages.
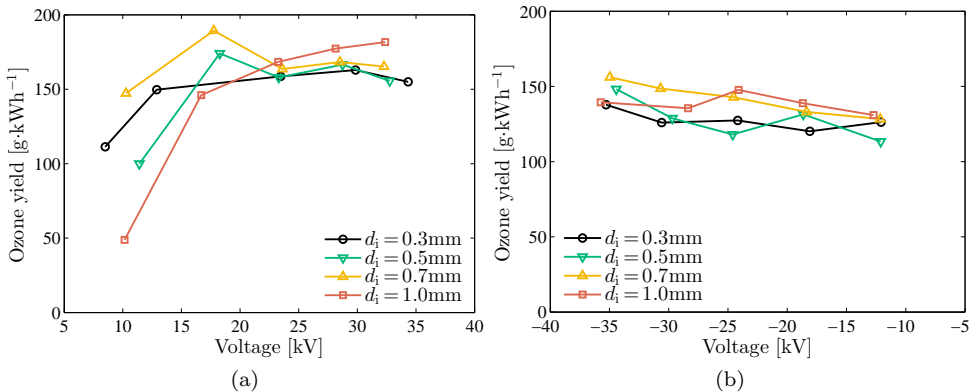
6.4.2 Ozone measurements

If we look at the results of the ozone measurements in Fig. 6.18 we see no significant difference in ozone yield between different reactor lengths. Now the differences in the results, if any, seem to be more the result of pulse duration. For positive pulse voltages the 1-ns pulses perform less well than the longer 5-ns and 9-ns pulses. This difference is less pronounced at negative pulse voltages.

The ozone-yield results of the last measurements are a first indication that the pulse duration in itself is not the determining factor in the efficiency of a plasma, because the shortest pulse duration performed less well than longer pulse durations. The result might be different at higher voltages, but we are unable to perform those measurements due to arc discharges. In Chapter 8 we will investigate the effect of pulse duration and rise time on ozone yield (and other applications) in more detail.

In the experiments with a variable plasma-reactor length we obtained the best matching in the longest reactor and there was no significant difference in ozone yield between the different reactor lengths. Therefore, we will use the 1-m reactor in all future plasma experiments.

6.5 Matching results and discussion: rise time

Up to this point, we have investigated matching only for the unaltered pulses from the nanosecond pulse source. In this section we will briefly discuss matching for pulses with different rise times. We use the method described in Section 6.2.5 to change the rise time of a 9-ns positive pulse from $0.4\,\mathrm{ns}$ to $2.9\,\mathrm{ns}$ and $5.6\,\mathrm{ns}$. Furthermore, we used a repetition rate of $20\,\mathrm{Hz}$ and a gas flow rate $2\,\mathrm{L}\cdot\mathrm{min}^{-1}$. Figures 6.19 and 6.20 show the matching results and ozone-yield results respectively.
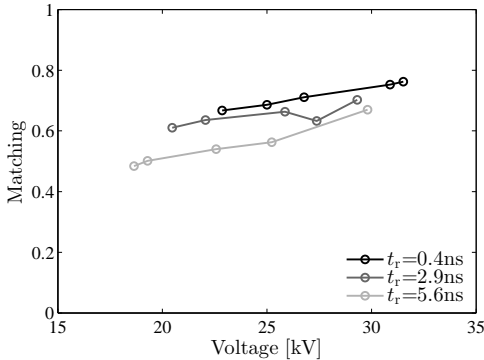
Figure 6.19:   Matching as a function of the rise time for a 9-ns positive pulse. Experimental settings: $f_{rr} = 20$ Hz and $F = 2.0$ L·min^{-1}.
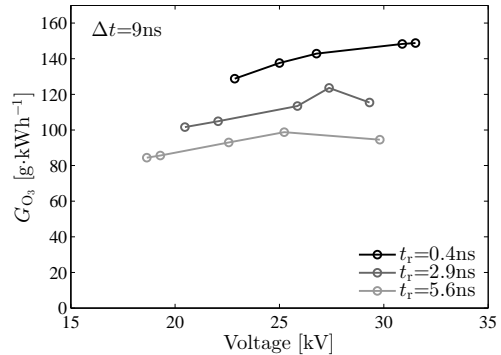
Figure 6.20: The ozone yield calculated from ozone measurements which were performed simultaneously with the measurements of Fig. 6.19.

The matching results indicate that a longer rise time results in lower matching. The ozone yields are lower for the pulses with the longer rise time are lower as well. The reasons for these effects will be further investigated and discussed in Chapters 7 and Chapter 8.

6.6   Matching results and discussion: energy density

In a practical implementation of a transient plasma application there are two important application aspects: yield and throughput. So far we have only focussed on yield and this will remain the primary investigation target in this thesis. However, gas throughput is also an important issue because it determines how much gas flow can be treated by the plasma in a given amount of time. Therefore, in this section we look at the energy density ε (in J·L^{-1}) of the plasma, which is given by Eq. 6.13.

From this equation we see that there are two parameters to change the energy density independently (while keeping the output voltage of the pulse source constant):

- change the repetition rate while keeping the gas flow rate constant;
- change the gas flow rate while keeping the repetition rate constant;

We changed the repetition rate in the range 10–100 Hz while keeping the flow constant at 1 L·min^{-1} and in a second experiment we changed the flow in the range 0.5–6 L·min^{-1} at a repetition rate of 50 Hz. The pulse voltage was 30 kV (both polarities) and had a pulse duration of 5 ns. The measurements resulted in an energy density from 10 to 250 J·L^{-1}, which is in the range that is often used in plasma-processing applications [1,19,21,27,28,66,118,131,136]. Figures 6.21 and 6.22 show the matching results and ozone-yield results of these experiments respectively.
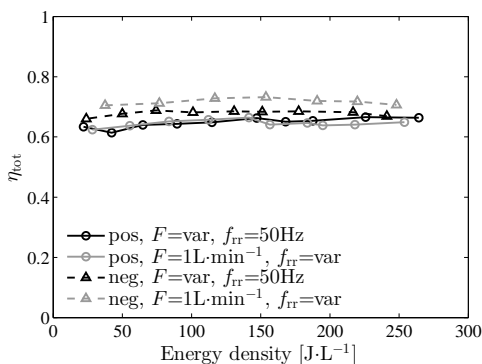
Figure 6.21: Matching as a function of the energy density. The energy density was varied by varying the repetition rate of the pulse source and the gas flow rate through the reactor for both positive and negative 30-kV 5-ns pulse voltages.

Figure 6.22: The ozone yield calculated from ozone measurements which were performed simultaneously with the measurements of Fig. 6.21.

The results show that matching is independent of the energy density up to $250 \, \text{J} \cdot \text{L}^{-1}$. Moreover, the method by which we change the energy density results in around the same matching. The other observation is that the negative pulses again match slightly better and that the positive pulses again obtain a slightly higher ozone yield. A general observation is that the ozone yield decreases with the energy density. We will give more detail on this process in Chapter 8.

The results of this section indicate that increasing the energy density comes at a cost in the ozone yield, but that even at high energy densities the performance of the plasma is still quite good. Another important result is that the matching is constant for the range of energy densities that we will use in the plasma-processing experiments of Chapter 8.

6.7 Multiple-wire inner conductor

In the first part of Section 6.3 we explained that using a small wire diameter in the reactor would increase matching because a plasma ignites sooner on the wire because of the higher electric field — calculated with Eq. 6.15 — that is associated with a small wire diameter (as opposed to a large wire diameter). However, a smaller wire diameter would also increase the reflection coefficient — calculated with Eq. 6.3 — and therefore more energy is reflected at the reactor interface, which decreases matching. This analysis was confirmed by the experiments of that section.

The best way to transmit the largest part of the incoming pulse into the reactor is by increasing the wire diameter substantially. However, to still be able to ignite a plasma, the electric field at the wire has to be high enough, which is a condition that
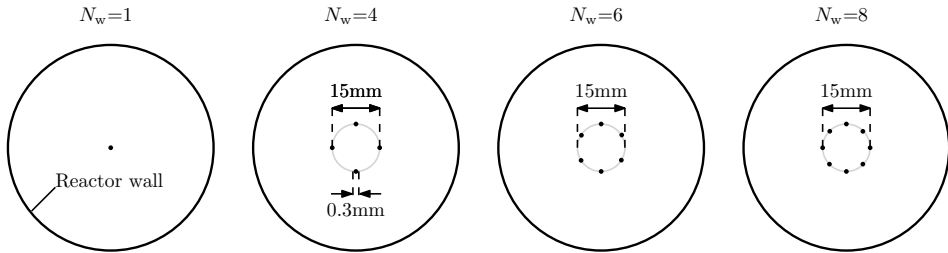
Figure 6.23: The four configurations used in the multiple-wire experiments. From the left to the right the inner conductor is made up of 1, 4, 6 and 8 wires respectively. For the multiple-wire configurations, the 0.3-mm thick wires are placed in a circle with a 15-mm diameter.

is not satisfied with a solid conductor. Therefore, we propose a multiple-wire inner conductor of the reactor.

We mount these wires on the circumference of the removable heads of the reactor (refer to Fig. 6.1). Therefore, the radial spacing between the wires is 15 mm. To investigate the effect of such an inner conductor we tested four configurations with a different number of wires N_w. We used $N_w = 1$, 4, 6 and 8. The diameter of the wires is 0.3 mm. Figure 6.23 shows the four configurations.

With the multiple-wire conductor the electric field close to the wires will be high, but not as high as with a single-wire conductor. However, the electric field is high enough for plasma to be able to ignite on the wires. Further removed from the wire the electric field will drop off quickly, but because the inner conductor is closer to the grounded electrode in the multiple-wire configuration, the average electric field in the gap is higher for this configuration as compared to the single-wire setup. This might significantly affect the propagation of the streamers and therefore the matching. A downside of the multiple-wire configuration is that the plasma volume might be smaller because there is no plasma inside the 15-mm diameter circle of the multiple-wire electrode.

Figure 6.24 shows the plasma that is generated by the different wire configurations. Note that the first image was not taken with the lens axis parallel to the reactor axis, but slightly askew to be able to see the plasma. The other images were taken with the lens axis parallel to the reactor axis to visualise the pattern of the plasma.

It is clear that the plasma with the multiple-wire configurations is not as homogeneous as with the single-wire conductor. This is expected because the plasma will ignite only on the wire-positions and therefore not the entire volume is filled with plasma.

It is very difficult to tighten each wire to the same extent in the multiple-wire configuration. Inevitably, the wire tension will not be identical for each wire, causing some wires to be slightly closer to the reactor wall. This is especially true for the 6-wire and 8-wire configurations. This is evident in the pictures as the uneven intensity of the plasma for different wires; for the 4-wire configuration the plasma is even in

$N_w=1$ $N_w=4$ $N_w=6$ $N_w=8$
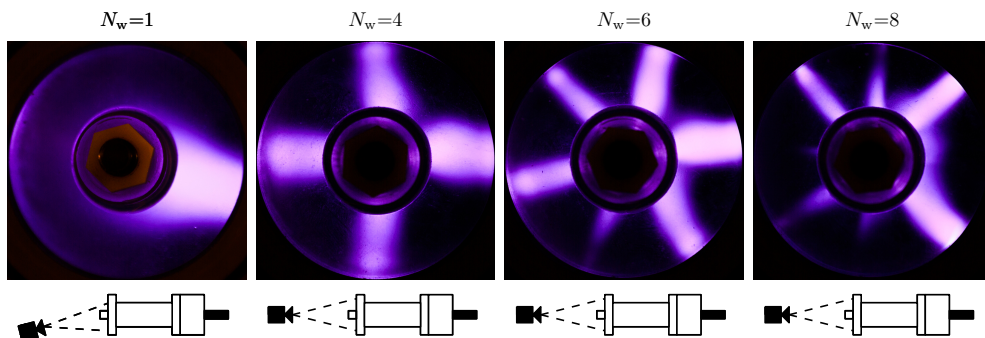
Figure 6.24: The plasma generated by the different multiple-wire inner conductors. The photographs were taken with a Canon 7D with a 300-mm lens at f/9 and with an exposure time of 10 s. Note that the left-most photo was taken off-axis to visualise the plasma of the 1-wire configuration (the symbols beneath the photos depict the camera position with respect to the reactor).

intensity, but with the 6-wire inner conductor some of the wires generate less plasma. For the 8-wire configuration it is even worse. The explanation for the increase in plasma unevenness when the amount of wires increases is likely that the wire-tension differences in the wires increases because more wires are used and the process to tighten them becomes more difficult.

Figure 6.25 shows the matching results of the experiments with the multiple-wire inner conductors for a 5-ns pulse. The results show that matching of over 90 percent is possible for the 4-wire configuration and that all multiple-wire configurations outperform the 1-wire conductor. One of the reasons the 4-wire configuration works better than the 6-wire and 8-wire configurations is likely the same reason the plasma is uneven in Fig. 6.24: the effect of uneven tension in all the wires. The second possible reason is that as N increases, the resemblance of the inner conductor to a solid conductor increases. There will likely be a value for N where the matching is optimal.

We added the results of the multiple-wire experiments to the waveforms in Fig. 6.12 to see the effect on the reflection coefficient when a multiple-wire conductor is used. Figure 6.26 shows the results. It is obvious from the reflected pulse that the multiple-wire configurations result in a much lower reactor impedance. This is the primary reason for the better matching results. Figure 6.27 shows the reactor impedances corresponding to the waveforms of Fig. 6.26. Here it is again obvious that using a multiple-wire reactor results in a much lower reactor impedance.

Figure 6.28 shows the ozone yields for the multiple-wire experiments. These results indicate that the ozone yield is very similar for all configurations. Therefore, the better matching of the multiple-wire configuration, combined with the similar ozone yields, suggests that the total yield of a reactor with a multiple-wire inner conductor is higher than with the conventional 1-wire solution that is generally employed in coaxial plasma reactors. Furthermore, the non-homogeneous plasma that we observed in Fig. 6.24
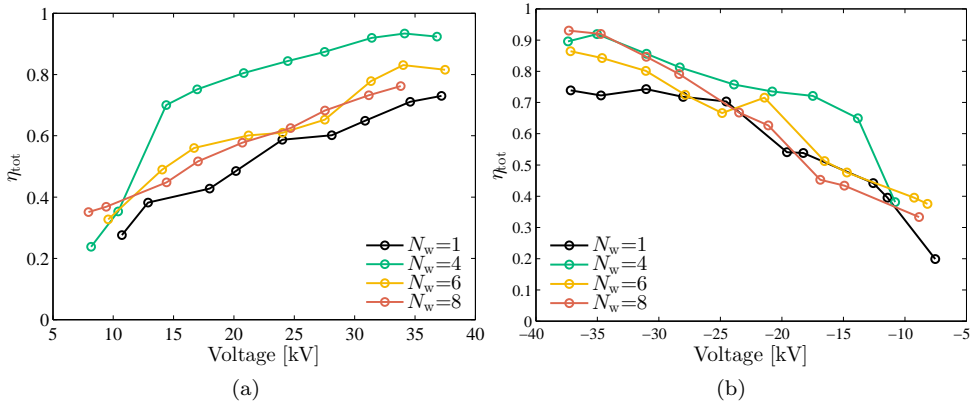
Figure 6.25: The matching of the pulses to the corona-plasma reactor for different numbers of wires comprising the inner conductor for (a) positive voltages and (b) negative voltages. Experimental settings: $\Delta t = 5\,\text{ns}$, $f_{\text{rr}} = 100\,\text{Hz}$, $l_{\text{r}} = 1.0\,\text{m}$ and $F = 5.0\,\text{L·min}^{-1}$.
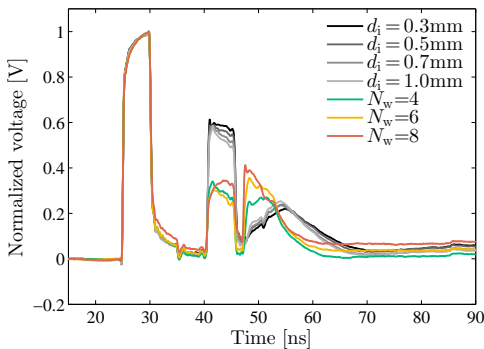
Figure 6.26: The same figure as Fig. 6.12, but now with the multiple-wire results added. The reflected pulses are now much lower in amplitude, indicating better matching.
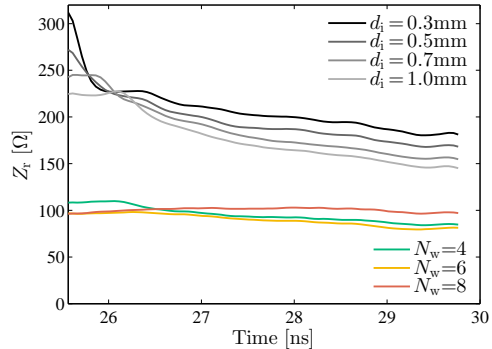
Figure 6.27: The calculated reactor impedances for the waveforms of Fig. 6.26. Again we see the better matching of the multiple-wire configurations.

apparently has no detrimental effect on the ozone generation.

In conclusion, the multiple-wire reactor that we developed in this section shows improved matching over the generally used 1-wire reactor. However, we will not employ this reactor in this thesis for the streamer development and plasma-processing experiments of Chapters 7 and 8. This is in part because we developed the multiple-wire reactor only after a large portion of the results of Chapters 7 and 8 were already obtained and in part because using a multiple-wire reactor greatly increases the complexity of the streamer-propagation measurements of Chapter 7. It will be left for future work to perform several interesting experiments with the multiple-wire reactor:
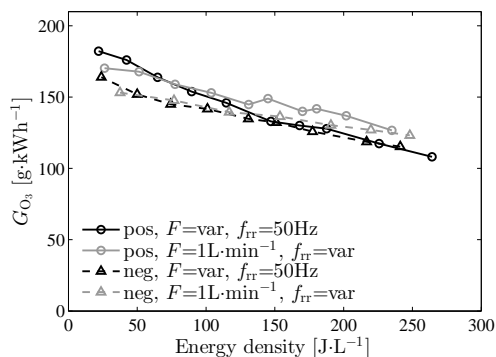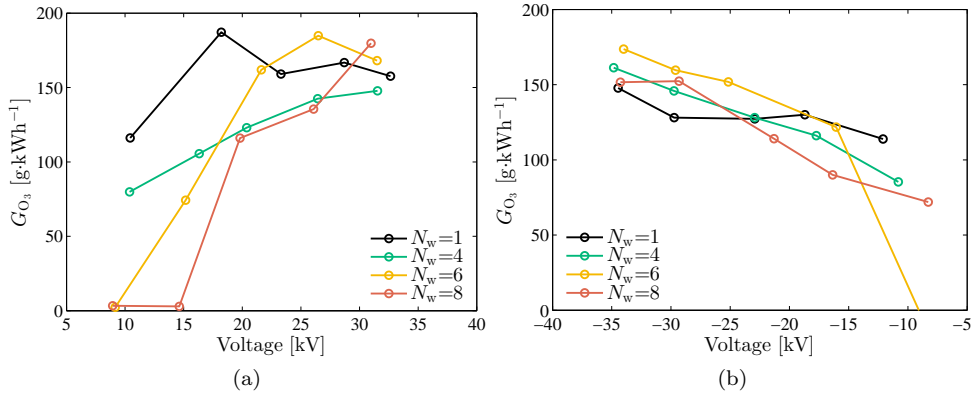
Figure 6.28: The ozone yield calculated from ozone measurements which were performed simultaneously with the energy measurements for Fig. 6.25 for (a) positive voltages and (b) negative voltages.

- optimise the number of wires in the reactor (with equally tight wires);
- optimise the diameter of the circle in which the wires are placed;
- perform streamer-propagation measurements with the setup of Chapter 7 (it will be specifically interesting to investigate whether a secondary streamer phase exists when multiple wires are used);
- perform plasma-processing experiments such as we perform in Chapter 8.

6.8 Positive vs. negative streamers

In the previous sections we found that negative pulses sometimes resulted in a better matching than positive pulses. This is surprising because other studies show that positive pulses match significantly better to a plasma reactor [125, 134]. Furthermore, negative streamers generally initiate at a higher voltage than positive streamers, making our observations even more peculiar [125, 134, 137]. The reason that positive voltages result in more streamer activity and consequently in a better energy utilisation by the plasma is one of the reasons that most studies only focus on positive streamer discharges.

If we want to discover what the mechanism is for the improved matching for negative pulses with our system as compared to other studies we have to focus on the very significant difference between our high-voltage pulses and the pulses others used: our pulses have a very short rise time and are applied after transmission over a long cable. Therefore pulse reflections on the cable coupler and the associated reactor impedance become a significant aspect of the matching process.

In Figs. 6.29 and 6.30 we compare the 0.5-mm wire positive and negative results of Fig. 6.10 at different voltage amplitudes. The impedance of the reactor energised with negative pulses is lower than when we used positive pulses. Since this lower impedance
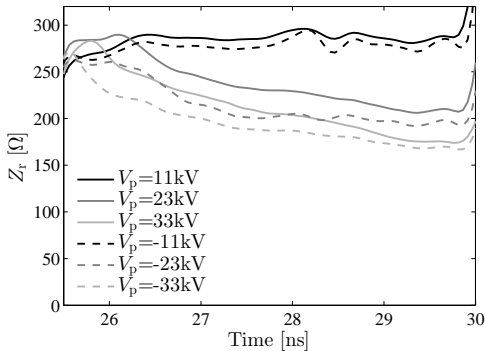
Figure 6.29: The difference in reactor impedance for the negative and positive results of the 0.5-mm wire plasma experiments of Section 6.3. The reactor impedance for the negative pulses is slightly lower.
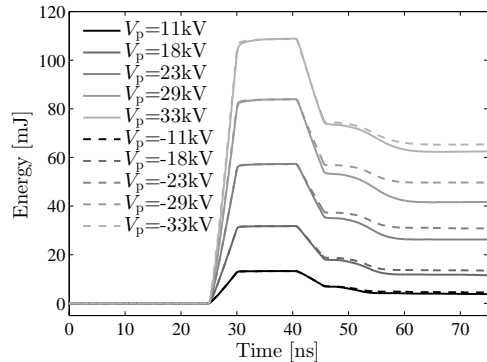
Figure 6.30: The energy measurements for negative and positive pulses for the 0.5-mm wire plasma experiments of Section 6.3. The consumed plasma energy for the negative pulses is slightly higher.

is closer to the 50-Ω output impedance of the SA24272 cable, negative pulses have better matching, which can also be seen in the energy measurements of 6.30. This indicates that the pulse reflection is less for negative pulses, which is an effect that can only occur when a more dissipative plasma is generated or when the wire diameter increases (see the results of Section 6.3).

To explain the negative vs. positive matching results we assume that there has to be a time-dependent effect that originates from the difference between the inception of positive and negative streamer inception.

6.8.1 Inception cloud

There are two (not mutually exclusive) possible phenomena that would explain the matching results from the streamer inception mechanisms. The first is the inception cloud.

Lately it has been observed, in air and in nitrogen, that when a fast voltage pulse is applied to a sharp electrode, a fast ionisation front is generated around this electrode. This ionisation front propagates towards the counter electrode and is called the inception cloud [17,138–141]. The inception cloud forms a highly ionised region around the high-voltage electrode. The associated high conductivity virtually increases the electrode size and therefore the applied potential on the electrode is transported to the edge of the inception cloud. When the electric field on the edge of this virtual electrode becomes equal to the critical field strength E_{crit} the ionisation cloud destabilises and breaks up into streamers.

If we apply the concept of the inception cloud to our wire-cylinder reactor then we

120

find the radial electric field $E(r)$ at the edge of the inception cloud as

$$E(r) = \frac{V_{\mathrm{p}}}{r\ln\frac{d_{\mathrm{o}}}{2r}}, \tag{6.17}$$

where V_{p} is the applied voltage pulse amplitude, d_{o} is the outer diameter of the corona-plasma reactor and we assume that the complete voltage potential is transported to the edge of the inception cloud. If we then set the electric field to E_{crit} we find

$$d_{\mathrm{max}} \ln \frac{d_{\mathrm{o}}}{d_{\mathrm{max}}} = \frac{2V_{\mathrm{p}}}{E_{\mathrm{crit}}}, \tag{6.18}$$

where d_{max} is the maximum inception cloud diameter.

Therefore, the maximum diameter of the inception cloud is dependent on the voltage and the pressure (through E_{crit}), which was also found in [138, 139, 141]. Other observations were that the inception cloud in air is larger than in nitrogen [16, 141], that even in large gaps in air at atmospheric pressure inception clouds are present [142, 143], that a high rise-rate results in a more stable inception cloud and that a high repetition rate results in a smaller inception cloud [144]. However, the most important property of the inception cloud for our investigation is that a negative inception cloud can achieve a diameter that is very close to d_{max}, whereas a positive inception cloud breaks up sooner than that and therefore achieves a smaller diameter [140, 145]. This effect was attributed to the stabilising effect of electron drift on the propagation of negative ionisation fronts.

We have no reason to expect that the results in literature on the inception cloud that were all found for point-plate geometries will not apply for our wire-cylinder geometry. The other difference between our investigation and the other studies is our very high rise-rate of around 50–$100\,\mathrm{kV}{\cdot}\mathrm{ns}^{-1}$, which is at least an order of magnitude higher than in the other studies. However, if we can apply the previous findings on the inception cloud to our investigation then we can assume than the inception cloud around the wire is larger when we use negative pulses to energise our reactor. This virtually increases the diameter of the wire as compared to when we use positive pulses and therefore the impedance of the reactor will decrease. Consequently, the matching increases.

If we use Eq. 6.18 for a 20-kV pulse and E_{crit} as $30\,\mathrm{kV}{\cdot}\mathrm{cm}^{-1}$ then we find a maximum inception cloud diameter of $6.6\,\mathrm{mm}$, which is large enough to significantly decrease the impedance of the reactor. However, if we use the same equation for a 30-kV pulse, we find that there is no solution for $E_{\mathrm{crit}} = 30\,\mathrm{kV}{\cdot}\mathrm{cm}^{-1}$. In reality, the inception cloud will have a final conductivity and therefore not the entire voltage potential is transported to the edge of the inception cloud and we estimate that d_{max} will be in the range of 3–$7\,\mathrm{mm}$ for an applied voltage of 20–$35\,\mathrm{kV}$. Optical measurements are necessary to show whether we have such an inception cloud around our electrode.

In Chapter 7 we will show results of ICCD imaging of the plasma, where we will revisit this discussion in Section 7.7.

6.8.2   Initial streamer velocity

The second reason for the improved matching of the negative pulses could originate from the initial streamer propagation velocity. Almost all studies on positive and negative streamer propagation show that streamers generated by positive pulses propagate faster than those generated by negative pulses [38, 134, 146–151]. However, due to the support of electron drift, negative streamers should propagate faster for a similar electron distribution and field enhancement at the tip of the streamer [152]. That this is not the case in experiments and simulations is because the positive streamers have a more concentrated and smaller head and therefore have a higher field enhancement [145]. Most interestingly however, is that the simulations of Luque *et al.* show that it takes some time for the negative streamer head to become diluted by electron drift, and for the positive streamer head to become concentrated [145]. Therefore, after the inception of the streamers, negative streamers will propagate faster. Since the tails of the streamers are highly ionised and therefore highly conductive, this phenomenon can also virtually increase the wire diameter in the reactor, again leading to increased matching. Therefore, if negative streamers propagate faster than positive streamers in the initial stages of the plasma development, the matching for negative streamers will be better. We will revisit this discussion in Section 7.7 as well.

6.8.3   Total matching effects

The difference in matching between negative and positive polarity was significant for 5-ns pulses, but for 9-ns pulses the difference was very small and in favour of the positive pulses. In this case, it seems likely that for longer pulses the more traditional matching effects become important. For a longer pulse the streamers can propagate further, even reaching the grounded electrode. Therefore, more energy can be consumed by the plasma. This effect can become more important than the initial streamer phases, such as the inception cloud and the initial streamer velocity. In Chapter 7 we will see that there is another effect that can effect matching: thick streamers at the end of the reactor due to the wire-tightening mechanism of the reactor. This has no effect on the initial matching such as we see in Figs. 6.29 and 6.30, but might affect the matching for longer pulses. We will revisit this discussion in Section 7.7 as well.

6.9   Matching with a DC bias voltage

We mentioned in the introduction that one of the methods to improve matching is the use of a DC bias voltage [29, 117–119, 121, 125]. This DC voltage is superimposed on the pulsed voltage and has some significant advantages. The downside to the DC-bias method is that the DC voltage has to be decoupled from the pulse voltage by a decoupling network, which can have an adverse effect on the properties of the pulse. In this section we briefly show a method we developed to add a DC bias voltage to the pulse voltage of a nanosecond pulse source without these adverse effects. These experiments were performed during a visit to Kumamoto University in Japan with the
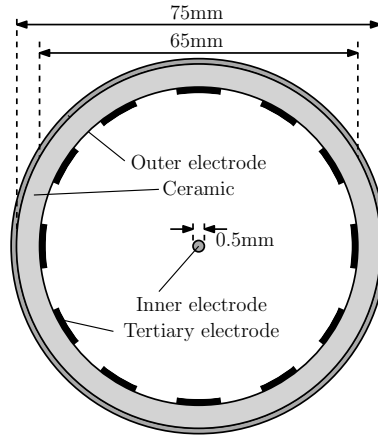
Figure 6.31: Cross-section of the coaxial corona-plasma reactor (not to scale). Tertiary electrodes are placed over a ceramic layer on the outer electrode. A DC bias voltage is applied to these tertiary electrodes.
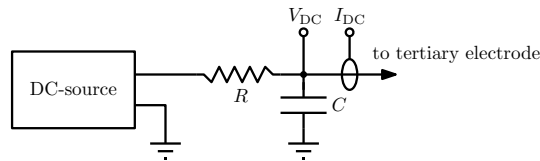
Figure 6.32: The DC circuit. The output of this circuit is connected to the tertiary electrodes of the corona-plasma reactor. Resistor R limits the charging current of buffer capacitor C and also prevents any transients from the nanosecond pulse to damage the DC source.

5-ns triaxial Blumlein source developed by Wang *et al.* [6,36]. The full report on this method is added in Appendix A of this thesis.

The advantage of our DC-bias method is the way we add the DC voltage to the pulse source. A conventional method to superimpose the pulse voltage onto the DC voltage is by using a coupling capacitor to decouple the pulses from the DC voltage [18,25]. This is done by connecting a capacitor between the pulse source and the high-voltage wire of the reactor. With the very short rise time of our pulses, this coupling capacitor has to be mounted very locally to avoid a deterioration of the pulse shape. Achieving the incorporation of a compactly connected capacitor is difficult. We avoid this difficulty by applying the DC bias voltage to extra electrodes in the reactor. Figure 6.31 shows this method. It shows a coaxial corona-plasma reactor, just like we use in this chapter, but with a dielectric layer added on the outer electrode of the reactor. On top of this layer we add the extra electrodes (tertiary electrodes) for the DC bias.

Normally, to increase the voltage (and thus E/n) in the reactor with a DC bias, the

(a)

(b)
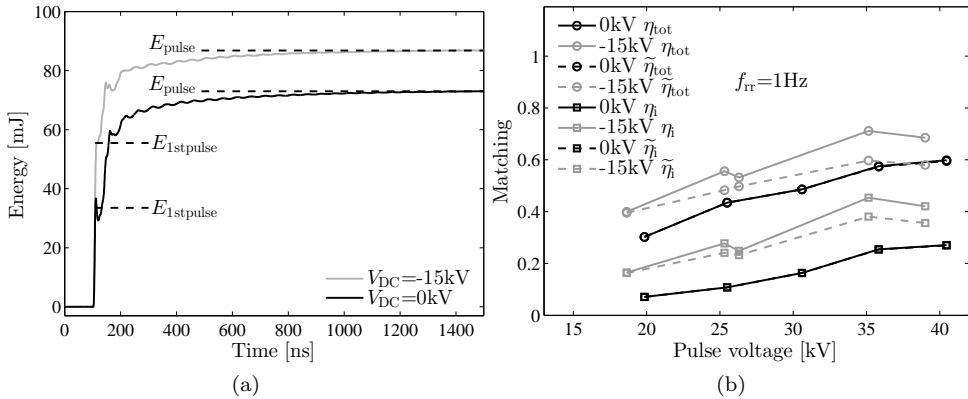
Figure 6.33: (a) Improved matching with a DC bias: by adding -15 kV on the tertiary electrode, the matching of the main pulse to the corona-plasma reactor is increased. (b) Matching as a function of the applied voltage with (grey lines) and without a DC bias (black lines). The matching is improved significantly, even when we correct for the energy from the DC power supply (grey dashed line).

DC voltage is added to the pulses with the same polarity. However, our DC electrodes are situated on side of the grounded electrode. Therefore, to increase the electric field in the reactor, we use negative pulses with a positive DC bias and vice versa. Figure 6.32 shows how we add the DC bias to the electrodes via a decoupling network that can be placed entirely outside of the reactor and does not have to be compactly incorporated in the nanosecond pulse source system.

Figure 6.33 shows some examples of the results and shows that the matching can be increased significantly with the reactor with the DC bias. With this reactor we showed an initial matching that improved by a factor of 1.2–2. The full report on this method and all the results is added in Appendix A of this thesis.

6.10 Summary and conclusions

In this chapter we investigated the energy transfer of the pulses from the nanosecond pulses to the plasma in the reactor. This energy transfer, or 'matching', should be as high as possible, because the rest of the energy is lost in the system and does not contribute to the plasma-processing application. We studied the effect of multiple parameters on matching, such as the reactor configuration, the pulse duration, the pulse rise time and the energy density. The plasma is a highly dynamic load which together with the pulse reflections on the cable coupler and in the reactor make matching our very short pulses to the plasma a challenge. Furthermore, previous studies into matching showed that a plasma with only primary streamers shows very poor matching; the secondary streamer phase (the resistive streamer phase) was required to obtain

good matching. Since our plasma mainly has a primary streamer phase, the challenge of matching is complicated even further.

The main conclusions of this chapter are listed below.

- The first conclusion in this chapter was that the reflection of the pulse on the cable coupler significantly influences matching. This reflected pulse travels back to the pulse source, while the transmitted pulse into the reactor generates plasma. The reflected pulse arrives back at the reactor after it has travelled up and down the SA24272 cable. This second pulse still generates a significant amount of plasma. For the matching calculations we used the total dissipated plasma energy. Furthermore, from the first reflection on the cable coupler we could determine the reactor impedance as a function of time for the first few nanoseconds.

- To minimise the reflection at the cable coupler (thereby increasing the energy transfer to the reactor) the inner-wire diameter of the reactor should be as large as possible. However, for a large-diameter wire, the electric field in the reactor will be lower and less plasma will develop, which decreases the energy dissipation. From experiments with wire diameters of 0.3 mm, 0.5 mm, 0.7 mm and 1.0 mm we found an optimum in these two contradicting effects at the 0.5-mm wire diameter, even though the differences in matching between the wire diameters were very small. A surprising effect was that the negative pulses matched better than the positive pulses. A possible origin of this effect is the size of the inception cloud (which can become larger for negative polarities) and the initial streamer velocity (which can become higher for negative streamers).

- Matching experiments with different reactor lengths (0.25 m, 0.5 m and 1 m) and different pulse durations (1 ns, 5 ns and 9 ns) showed that the longest reactor and the longest pulses result in the best matching. The explanation for this effect was that for a longer reactor and a longer pulse, the streamer plasma has more time to develop and to dissipate the energy from the applied pulses. Therefore, we chose the 1-m reactor as the reactor for the remaining experiments in this thesis.

- For all experiments, higher applied voltages resulted in better matching. This was also observed by other researchers. However, where their plasma had a secondary streamer phase, we have only primary streamers. Nevertheless, the result that a higher voltage results in a more intense plasma is the same and our pulses are so short that a significant current can flow even in the primary streamer phase.

- Experiments with pulses with different rise times showed that a short rise time results in better matching.

- For energy densities in the range 10–250 J·L^{-1} (the operating range in this thesis) the matching remains constant.

- To decrease the pulse reflection in the reactor interface while maintaining a high electric field on the wire we developed a multiple-wire inner conductor for the reactor which decreases the vacuum impedance of the reactor. The results were very encouraging and showed matching of over 90 percent.

- With a new method to add a DC bias voltage to the reactor, we can avoid

the difficulties of the conventional DC-bias method and still obtain a significant increase in matching between a nanosecond pulse source and a reactor. We used this reactor on a nanosecond pulse source and showed an initial matching that improved by a factor of 1.2–2. The full report on this method and all the results is added in Appendix A of this thesis.

A final conclusion of this chapter is that even without the multiple-wire reactor, we are able to achieve a very good matching (over 80 percent) between our pulse source and the reactor, which shows that even a plasma with just a primary streamer phase can be matched to a pulse source if certain conditions are met (short rise time, high voltage, optimal reactor configuration, etc.). In the next chapters we will explain and use some of the results of the matching experiments.

Seven

Streamer Development and Propagation

Abstract

In this chapter we investigate the development and propagation of streamers in a wire-cylinder reactor to study the effect of reactor length, pulse duration, pulse amplitude, pulse polarity, and pulse rise time on the generated streamers. More specifically, we are interested in the coverage of the streamers in the reactor to relate this to the plasma-processing results of the next chapter. We study the streamers by ICCD imaging with a fully automated setup with which we are able to image the streamers in the entire corona-plasma reactor as a function of time and position in the reactor. From the images, we calculate streamer lengths, streamer propagation velocities and streamer widths. We also develop a SPICE model of the reactor to support the analysis of the streamer propagation results.

The results show that the propagation of the high-voltage pulse determines the streamer propagation. As the pulse travels through the reactor, it generates plasma and attenuates and disperses. At the end of the reactor, it reflects and adds to itself. These propagation effects on the local voltage at different positions in the reactor increase for a longer reactor or a shorter pulse. This local voltage determines the streamer properties at that position. The streamer velocities are higher for a higher voltage, which results in longer streamers. Furthermore, the streamer widths are slightly larger for a higher voltage. Additionally, the rise time of the applied pulse has a significant effect on the streamer development and propagation. For a lower rise rate, the streamers initiate at a later time, have a lower propagation velocity (and therefore a shorter length), and have a lower width.

7.1   Introduction

In this chapter we investigate the development and propagation of streamers in a wire-cylinder reactor as a function of time and position in the reactor. These streamers will be generated by the high-voltage pulses from the nanosecond pulse source that we presented in Chapters 2 and 3.

The main motivation to study the development and propagation of streamers in our corona-plasma reactor is that we have to visualise the streamer plasma to understand and explain the experimental results that we obtained in the previous chapter on matching and the results of our plasma-processing measurements on ozone generation, NO removal and CO_2 conversion that we will present in the next chapter. Specifically we are interested in the total coverage of the streamers in the reactor, because the high-energy electrons and therefore the radicals needed for air-purification processes are generated in the streamer head and the path of the streamer [153–159]. Therefore, the coverage of the streamers in the reactor directly influences the chemical activity in the reactor. However, when the streamers cross the gap between the electrodes, secondary streamers can form [151, 155, 160, 161]. The electrons in the secondary streamers are less energetic — typically only 1–2 eV as compared to 5–10 eV for primary streamers — and consequently the radical generation in these streamers is different than in primary streamers [151, 160]. Some studies show that the energy yield of oxygen radicals are highest in the primary streamer phase [5, 154], whereas others claim a higher oxygen-radical energy yield in the secondary streamer phase [162, 163]. Therefore, to investigate this further, we want to optimise the streamer coverage such that it should be as large as possible without generating secondary streamers.

Because the pulses are short in comparison with the length of the reactor, the development and propagation of the streamers will be dictated by the pulse propagation and reflections in the reactor. Consequently, the streamer development changes on very short time scales and will be dependent on the position in the reactor. For example, a 1-ns pulse is only 30 cm 'long' in air if we assume that the pulse propagates with the speed of light in the reactor. Therefore, the total coverage of the streamers in the reactor will be different at different positions along the reactor.

7.1.1 Streamer propagation

Streamer propagation velocity

There are many studies on streamer development and propagation under pulsed voltage conditions [11, 16, 24, 123, 134, 138, 139, 141, 144–151, 160, 164–172]. For instance, several researchers have reported on streamer propagation velocities for a range of voltages and rise times. This streamer propagation velocity is an important parameter for the streamer discharge in our coaxial reactor because it determines how far a streamer can propagate and therefore influences the total coverage of the streamers in the plasma reactor. It is generally found and understood that a higher applied electric field increases the streamer propagation velocity and that the velocities are in the range of 10^5–10^7 m·s^{-1} [16, 24, 138, 146, 148, 151, 160, 168, 172]. Furthermore, various experiments show that negative streamers generally have a lower propagation velocity than positive streamers [134, 146–151], which is surprising because negative streamers propagate through electron drift and positive streamers propagate against the electron drift through photoionisation (and to a lesser extent background ionisation) [15, 16, 167]. Therefore, for identical field enhancement at the streamer head, and a

similar electron distribution, a negative streamer is expected to propagate faster [152]. Luque *et al.* showed that negative streamers indeed travel faster initially, but that due to broadening of the streamer head, the field enhancement at the streamer head decreases, which decreases its velocity [145]. At the same time, the positive streamer head remains smaller during propagation and therefore the field enhancement remains higher, leading to a faster velocity of the positive streamer. The initial higher velocity of negative streamers is a phenomenon which we already mentioned in Chapter 6 as one of the possible explanations for the better initial matching of negative pulses to our corona-plasma reactor as compared to positive pulses.

Besides the applied voltage amplitude, the rise rate of the applied voltage also influences the streamer propagation velocity. Most studies found that the velocity increases when the rise rate increases [147, 149, 151, 169, 170]. This effect was explained by the fact that streamers initiate while the high-voltage pulse still rises and therefore initiate at a lower voltage when the rise rate is low. Furthermore, when the rise rate is high, the complete voltage is applied to the reactor in a shorter time, which enhances the streamer velocity. However, recently the homogeneous discharge regime preceding the streamer discharge — called the inception cloud (on which we already commented in Section 6.8) — has attracted the attention of researchers [17, 138–141, 144]. It was found that when the rise rate of the voltage is high, this inception cloud can become larger, taking more time to break up into streamers [144]. Since the formation of this inception cloud is a slow process compared to the streamer propagation, the net result is that it takes longer for streamers to start propagating at high rise rates and therefore the total travel time is longer. However, at atmospheric pressure the inception cloud is much smaller than at the low pressures these experiments were performed at [138, 139, 141]. It is therefore expected that the inception cloud will not play a significant role in our experiments in this chapter (in Section 6.8 we already estimated that the inception cloud will have a diameter of around 3–7 mm at most and might have an effect on matching) and that a high rise rate will result in a higher streamer velocity in our experiments.

Streamer diameter

A second streamer parameter which is often investigated is the streamer diameter (or streamer width) [16, 134, 151, 160, 164, 165, 168]. It is generally found that, just as the streamer propagation velocity, the diameter of the streamer head increases with the applied voltage [134, 151, 160, 165]. The relevance of the streamer diameter to our investigation is that we are interested in the plasma volume and besides how far a streamer propagates (determined by the propagation velocity) the streamer diameter also increases the plasma volume.

Electrode geometry

The electrode geometries of the experimental setups in which researchers have studied streamer propagation vary. The majority have used point-plate geometries which are

very useful for fundamental streamer research because of optical accessibility and reproducibility [11, 16, 123, 134, 138, 139, 141, 144, 148, 150, 160, 165–167, 171, 172]. Some used wire-plate geometries [151, 164] and only a few have looked at coaxial geometries [20, 24, 146, 168]. Especially the coaxial geometries are interesting because it is the electrode configuration that we use and that is often employed in air-purification research (e.g. [3, 19, 21, 27, 117, 119, 135, 173]). Unfortunately, most observations of the plasma in a coaxial geometry have only been done at one position in the plasma reactor and the effects of pulse propagation in the reactor have not been considered so far.

A study that includes the effects of pulse propagation on streamer development over a longer length of transmission line is the study by Pokryvailo *et al.*, who used a 6-m long two-wire transmission line and generated a corona plasma with a 5-ns 100-kV pulse [174]. They found that the plasma light intensity decayed along the line and that this effect was more or less independent on the applied voltage. However, no information was given on any plasma parameters.

Another study that considers the propagation of a high-voltage pulse when plasma is generated was performed by Van Heesch *et al.* [175]. They used a coaxial reactor for pulsed corona experiments and monitored the pulse with electrical measurements (no imaging measurements) for a pulse with a 5-ns rise time and found that the pulse attenuated severely over 4 m due to the corona plasma.

In this chapter we will also study the effect of the pulse propagation through a transmission-line system with very short pulses, but we will show streamer parameters such as the streamer distance travelled, the streamer velocity and the streamer diameter as a function of time and position in the coaxial reactor. In this way we get a unique and very insightful view on nanosecond transient plasma generation in a coaxial corona-plasma reactor.

7.1.2 Chapter organisation

After this introduction, we show a SPICE (Simulation Program with Integrated Circuit Emphasis) model of the corona-plasma reactor to model the voltage waveforms in the reactor as a function of time and position in the reactor. Then, Section 7.3 presents the experimental setup we used in this chapter, followed by the first two results sections in which we show results of ICCD-imaging experiments for different pulse-source parameters in a 2-m reactor and a 1-m reactor respectively. Subsequently, Section 7.6 shows results of similar experiments, but then with the rise time of the applied pulses as the main variable.

We conclude this chapter with two short sections, the first considering the matching of the pulse source to the reactor and the second discussing the differences between the reactor we used in this chapter and the reactor we used in Chapter 6 and will use in Chapter 8. Finally, Section 7.9 presents the conclusions.
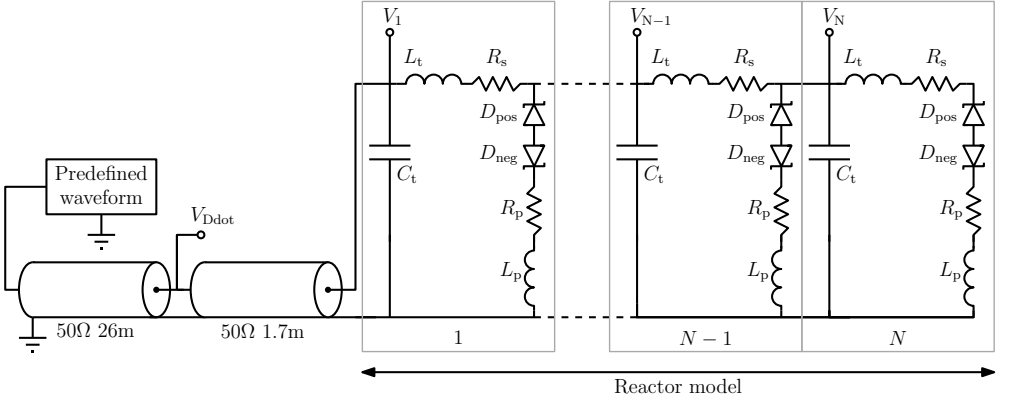
Figure 7.1: The SPICE model of the corona-plasma reactor. It consists of N sections of distributed transmission lines with a dissipative branch in addition to the standard transmission-line components. The dissipative branch models the dissipation by the plasma and consists of a resistor switched by Zener diodes. Two ideal transmission lines (left side) model the SA24272 cable that connects the pulse source to the reactor. The pulse source is modelled with a pre-defined waveform.

7.2 Reactor SPICE model

To better understand the propagation and development of the streamers in the corona-plasma reactor, we developed a SPICE model of the reactor. This model is not meant as an exhaustive plasma model, but rather as a simple electrical equivalent model of the reactor. It will allow us to derive an approximation of the voltage waveforms in the reactor to understand what transmission-line effects will be relevant for the streamer propagation and development.

7.2.1 SPICE model

The SPICE model of the coaxial (wire-cylinder) corona-plasma reactor is shown in Fig. 7.1. It consists of N identical sections. Each section contains a distributed capacitance C_t and a distributed inductance L_t. The distributed capacitance is calculated with

$$C_\text{t} = \frac{2\pi\epsilon_0 l_\text{r}}{N \ln \frac{d_\text{o}}{d_\text{i}}}, \tag{7.1}$$

where l_r is the length of the reactor, d_o and d_i are the outer and inner conductor diameters of the reactor respectively and N is the number of sections in the model. Similarly we can define the distributed inductance as

$$L_\text{t} = \frac{\mu_0 l_\text{r}}{2\pi N} \ln \frac{d_\text{o}}{d_\text{i}}. \tag{7.2}$$

131

The distributed resistance of the wire in the reactor is represented by R_s in the SPICE model. It is calculated as the resistance of the outer shell of the wire that is bounded by the skin depth δ and is calculated with

$$R_s = \frac{l_r}{\sigma_{ss}[d_i^2 - (d_i - \delta)^2]\pi N},$$ (7.3)

where σ_{ss} is the conductivity of the stainless-steel wire and δ is calculated as

$$\delta = \sqrt{\frac{1}{\pi f \mu_0 \sigma_{ss}}},$$ (7.4)

where f is the frequency at which the skin depth is considered.

The distributed components C_t, L_t and R_s are the classical parameters of a transmission line (with losses in the dielectric neglected) [62].

We added a resistive load R_p to model the plasma in the reactor. We can verify the validity of the use of a resistor as a simple model for a plasma by looking at the results of Fig. 6.9, which shows that the dissipated plasma energy increases with the square of the applied voltage. This is similar to the energy dissipation of a resistor.

In the real reactor, the plasma develops only after a certain voltage threshold has been crossed: the inception voltage [176]. We model this behaviour with a Zener diode, because a Zener diode starts conducting above a certain voltage V_{br}. When the Zener is conducting, a current will flow through the resistive load R_p, which results in energy dissipation in this resistor (and the Zener diode). Therefore, the combination of the Zener diode in series with a resistor models the plasma: above an inception voltage the plasma will dissipate energy proportional to the square of the voltage. Furthermore, we used two Zener diodes in each branch to differentiate between the positive and negative inception voltage of the plasma. We used the same method successfully in a DBD model in [177].

The last component in the SPICE model of the reactor is the inductor L_p in series with R_p. We placed this inductor in series with R_p because in the real plasma, a streamer needs time to develop. The longer a high-voltage pulse is applied, the further the streamer propagates and the more energy it dissipates. Inductor L_p ensures that more energy can be dissipated in R_p when a longer pulse is applied, because the rate with which the current through the resistor can increase is now determined by the inductor. Therefore, a higher current can be achieved for longer pulses.

Of course, our simulation method is just an approximation of the real plasma behaviour. A better, but more complex method to model one of the streamers in SPICE would be to replace R_p in the model with a time- and applied-voltage dependent resistor in series with a time- and applied-voltage dependent capacitor, because a streamer has a certain capacitance from its head to the cylinder wall and a certain resistivity in its tail, which both depend on the time and the applied voltage. However, to model this dependency would be complex and would require extensive fitting of the SPICE modelling results to the measured waveforms. At present, we did not undertake this higher level of modelling, but it might be worthwhile to investigate this in a future

Table 7.1: SPICE model parameters for a 1-m reactor.

Parameter	Value
N	128
l_r	$1\,\mathrm{m}$
d_o	$50\,\mathrm{mm}$
d_i	$0.5\,\mathrm{mm}$
C_t	$93.8\,\mathrm{fF}$
L_t	$7.2\,\mathrm{nH}$
L_p	$1.5\,\mathrm{nH}$
R_s	$0.1\,\Omega$
R_p	$22.5\,\mathrm{k\Omega}$
$V_\mathrm{br,pos}$	$4\,\mathrm{kV}$
$V_\mathrm{br,neg}$	$5\,\mathrm{kV}$

study, as it will give a better approximation of the waveforms in the reactor. For instance, the high amount of dispersion that the pulse experiences in the reactor due to the plasma is not correctly predicted in the current model and would require the higher level of modelling.

Table 7.1 gives all the relevant parameters of the SPICE model for a 1-m reactor. We used a model with 128 sections. If we consider that the pulse travels with the speed of light, then one section represents $1/128 \times 1/3 \cdot 10^8 = 26\,\mathrm{ps}$ of pulse propagation, which is around one order of magnitude shorter than the rise time of the pulses. Therefore, using $N = 128$ is allowed. Furthermore, experimentation revealed that using more sections is unnecessary.

The physical parameters of the reactor (l_r, d_i and d_o) give the transmission-line parameters C_t and L_t. With a frequency of around $100\,\mathrm{MHz}$ (the main average frequency component of the 5–9-ns pulses) we then find a value of around $0.1\,\Omega$ for R_s. Subsequently, we varied values for L_p, R_p and the breakdown voltages of the Zener diodes ($V_\mathrm{br,pos}$ for D_pos and $V_\mathrm{br,neg}$ for D_neg) to fit the experimentally measured energy dissipation by the plasma. We chose $V_\mathrm{br,neg}$ higher than $V_\mathrm{br,pos}$ because the inception voltage of negative streamers is generally higher than the inception voltage for positive streamers [125, 134, 137].

The total SPICE model of Fig. 7.1 consists of the 1-m reactor model and two transmission lines that represent the SA24272 cable. These transmission lines are ideal and have the same time delay as the real cables. At the position of the D-dot and B-dot sensors we measure the output voltage V_Ddot. Additionally we measure the current at the same point to calculate the energy that is dissipated by the reactor model. The two transmission lines are excited with a predefined waveform. This waveform is the actual pulse that was measured in experiments with D-dot sensors D_3 and D_4. Figure 7.2 shows the predefined waveforms for a 5-ns and 9-ns pulse. To change the amplitude of the predefined waveform we scale the waveform. This means that voltage-dependent spark-gap effects such as those that were shown in Fig. 3.24 are not accounted for in
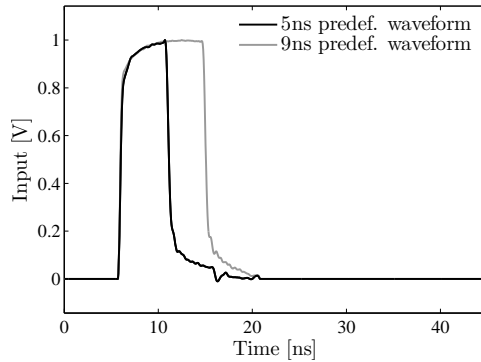
Figure 7.2: The predefined waveforms (normalised) that we used in the model of Fig. 7.1. These waveforms were taken from the experiments of Chapter 6.
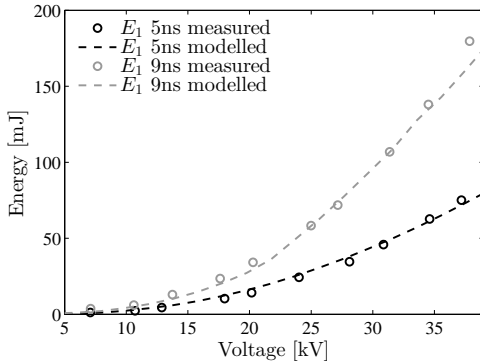
Figure 7.3: A comparison between the modelled plasma energy dissipation (dotted lines) and the measured plasma energy dissipation (circles). There is a good agreement between the model and the experiments.
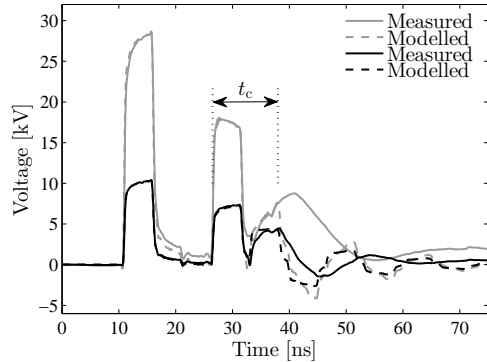
Figure 7.4: A comparison between the modelled waveforms and the experimental waveforms for a 5-ns pulse at two different output voltages. The results agree well until around 38 ns.

the SPICE model.

7.2.2   Results

Figures 7.3 and 7.4 present some comparisons between the experimental results and the modelled results. A very good agreement is found between the dissipated plasma energy for 5-ns and 9-ns pulses that we used in this example. Furthermore, as Fig. 7.4 shows, the reflected pulse and therefore the impedance of the reactor is also faithfully modelled (for at least the duration of the pulse). After the reflected pulse, the model still shows good agreement for 6.5 ns longer. Consequently, the modelled and measured results
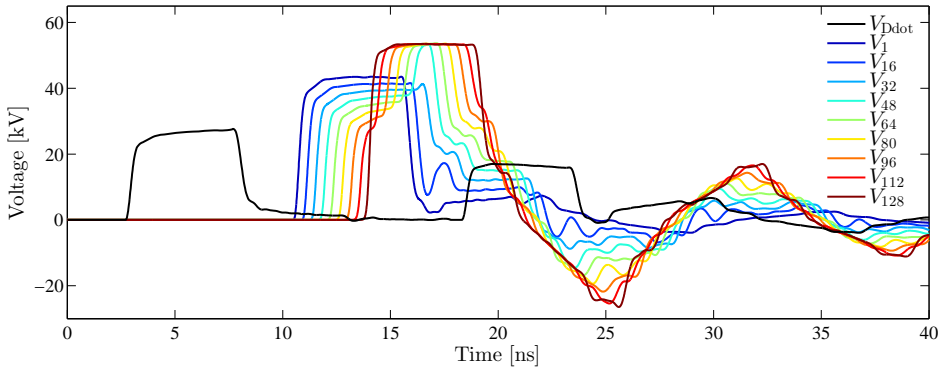
Figure 7.5: SPICE simulation results of the 1-m reactor. The waveforms are the voltages at various positions in the reactor (from V_1 at the pulse-source side of the reactor, to V_{128} at the end of the reactor). Noteworthy are the increased pulse amplitude due to mismatch when the incoming pulse (V_{Ddot}) enters the reactor and the voltage doubling at the end of the reactor.

show a good agreement for a total time of t_c (indicated in Fig. 7.4). After that time, the modelled results and the measured results start to deviate. This is the result of the complexity of the plasma behaviour. When streamers are generated, they have to be modelled as a voltage- and time-dependent resistor with a voltage- and time-dependent capacitor in series, as we already mentioned. Furthermore, the electrical pulse has to propagate through the body of growing streamers, which also has significant effects on the pulse propagation and consequently changes the inductance of the system locally. After $t = 38$ ns the measured result shows a severely dispersed pulse. This dispersion is not correctly predicted by the SPICE model.

Figure 7.5 shows an example of the simulated voltage profiles in the reactor as a function of time and position. When the pulse enters the reactor it increases in voltage due to mismatch (V_1). It attenuates as it propagates through the reactor and finally reflects off the end of the reactor (V_{128}). Here it adds to the incoming pulse, causing a doubling of the voltage. As the pulse propagates back towards the boundary of the transmission line and the reactor, it continues to add to the incoming wave until it reaches the boundary. Now it encounters the lower impedance of the cable. Therefore, it reflects back into the reactor once more. In the real reactor, the pulse will already be very dispersed at this point and therefore these later stages of pulse reflections in the SPICE results will not be so significant. However, the first stages of the pulse reflection are modelled quite well as we will see later.

The streamer development will depend on the time- and position-dependent voltage in the reactor. Therefore we will use the voltage profiles of the SPICE simulations in the discussion of the results of this chapter.

7.3 Experimental setup and procedure

The streamer development in our corona-plasma reactor depends on the propagation of the very short pulses through the reactor. Therefore, we need to be able to visualise the streamers both as a function of time as well as a function of position in the reactor. This results in a significant amount of experiments and data, which is why the experiments will be automated. We use ICCD photography to capture individual images (of streamers generated with individual pulses) and later stitch them together to generate an overview of the entire reactor. With these images we study the streamer propagation as a function of the pulse duration, pulse voltage, pulse polarity and pulse rise time.

This section presents the experimental setup we used for the experiments in this chapter, which includes the camera system, the reactor, the pulse source, the automation system, and the data processing of the results.

7.3.1 Nanosecond pulse source

We use the nanosecond pulse source that we presented in Chapters 2 and 3 to generate the streamer plasma under investigation in the current chapter. We use it at high voltages ($> 20\,$kV) to observe the plasma (at low voltages there is hardly any plasma to observe) and at pulse durations Δt of 1, 5 and 9 ns. We use both positive and negative polarity pulses. Ideally, we would use a large number of pulse source settings, but even with the limited amount of settings we selected, the number of experiments is substantial.

The output voltage of the nanosecond pulse source is not constant due to the oil spark gap (see Section 3.4). Therefore, whenever we state a voltage that we used for an experiment, this voltage is the mean amplitude of the pulse source at a certain setting. Furthermore, the repetition rate for all the experiments in this chapter was 3 Hz, the gas in the reactor was synthetic air, and the pressure was atmospheric.

The nanosecond pulse source is controlled by the charge voltage on its pulse forming line. This charge voltage is generated by the pulse charger modules we presented in Chapter 4. These pulse charger modules are controlled via optic fibre by a pulse charger controller. This controller can be controlled by a computer over a RS232 connection. We will give more information on the entire control structure of the experimental setup of this chapter in Section 7.3.3.

7.3.2 Camera system and the corona-plasma reactor

The ICCD-camera system and the corona-plasma reactor are an important part of the experimental setup and will be described here.

ICCD camera

To image the plasma we used a 4 Picos-DIG ICCD camera from Stanford Computer Optics. It has a minimum exposure time of 200 ps and its CCD has a resolution of
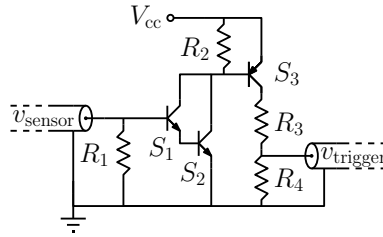
Figure 7.6: The schematic of the camera trigger circuit. It transforms the very short D-dot- or B-dot-sensor signal to a longer pulse on which the ICCD camera can trigger reliably.

Table 7.2: Trigger circuit components

Component	Value
R_1	$15\,\mathrm{k\Omega}$
R_2, R_4	$100\,\Omega$
R_3	$33\,\Omega$
S_1, S_2	NPN BF240
S_3	PNP F324
V_{cc}	$10\,\mathrm{V}$

780×580 pixels. We attached a Sigma 70–300 F4–5.6 DG MACRO lens to the camera and enclosed it in an EMC cabinet.

Trigger circuit

An important part of the camera system is the camera triggering. The internal delay of the camera is around 65 ns, but not known exactly. Therefore, to keep the SA24272 cable as short as possible, the camera should be triggered as quickly as possible after the spark gap of the pulse source switches. If we are to achieve a 1-ns time resolution in our measurements, the jitter on the camera trigger should not exceed several hundreds of picoseconds. A suitable trigger signal can be taken from the D-dot or B-dot sensor on the pulse source side of the SA24272 cable (D_5 or B_5). However, the pulses from the D-dot and B-dot sensors are too short for the camera to trigger on. Therefore we developed a fast trigger circuit for the camera.

The trigger circuit is shown in Fig. 7.6. The circuit uses high-frequency transistors and ensures that the sensor signal initiates a longer pulse at the output of the circuit. Table 7.2 lists the circuit components.

Figure 7.7 shows the input and output of the trigger circuit. It shows that the trigger circuit successfully transforms the short input pulse into a longer pulse for the camera. The circuit only triggers on the positive pulses from the sensor signal, which means that an additional delay of the duration of the pulse from the pulse source is
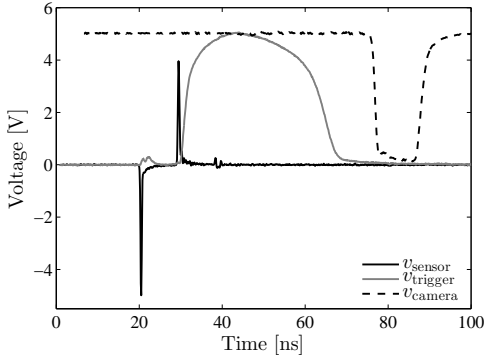
Figure 7.7: The waveforms in the trigger circuit. The circuit transforms the positive peak from the sensor into a longer pulse for the ICCD camera trigger. The camera signal confirms that the camera has triggered.
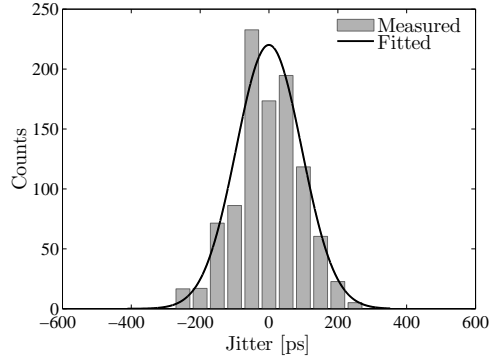
Figure 7.8: A histogram of the time jitter between the sensor signal and the trigger-confirmation signal of the camera. The jitter is within an acceptable range of several hundreds of picoseconds.

generated in the circuit in the case of a negative output pulse (as is the case for the signal in Fig. 7.7). An output on the camera shows that it has indeed triggered on the pulse from the trigger circuit. The jitter between this camera output and the sensor signal is shown in Fig. 7.8 for 1000 shots. The figure shows that the jitter is within the acceptable range of several hundreds of picosecond and has a standard deviation of 95 ps.

Camera frame and reactor

The corona-plasma reactor and the camera system that we used in this chapter are described in [178] and were developed to investigate the propagation of the streamers in a 2-m long reactor. We will describe these components here briefly for clarity, but the details can be found in [178].

We used a reactor that has a window along its length to be able to look into the reactor. Figure 7.9 shows this reactor. It is 1 m long and two of these reactors can be connected in series to create a 2-m long reactor. The reactor has a gas-tight polycarbonate (PC) window to allow imaging of the plasma. The U-shaped reactor can be connected to the cable coupler on the SA24272 cable in the same way as our normal coaxial reactor. Apart from the cable coupler, we also re-used the wire-tightening mechanism from Chapter 6 (Fig. 6.1) with the U-shaped reactor.

Figure 7.10 shows the entire camera setup. It is a 3-m long aluminium frame which holds all the components. Two of the U-shaped plasma reactors connected in series can hang from the frame, where one of the reactors can be connected to the cable coupler on the SA24272 cable. From beneath, the camera can look into the reactor through a mirror. The resulting image area of the photos is $53 \times 71 \, mm^2$ A stepper motor can then move the camera over the rails on which the camera is mounted. In this way

Overview
Cross section

50mm

PC window
Wire electrode
Reactor wall

1m
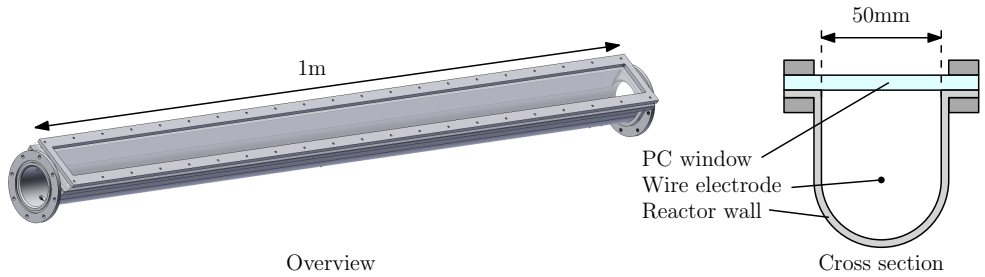
Figure 7.9: An overview drawing of the 1-m corona-plasma reactor with a polycarbonate window (left) and a cross section of this reactor (right). The reactor has a U-shaped cross section that allows the ICCD camera to image the inside of the reactor. Two of these 1-m reactors can be connected in series to obtain a 2-m long reactor.

3m

SA24272 cable

Cable coupler

Plasma reactor

Aluminium frame

1.5m

Mirror
Camera EMC cabinet

Stepper motor

Rails

0.56m

Figure 7.10: A drawing of the 3-m long aluminium frame that houses the reactor and the ICCD camera. The ICCD camera is mounted in an EMC cabinet and can look at the U-shaped reactor via a mirror. The entire EMC cabinet can be moved over the length of the aluminium frame on rails. It is moved by a stepper motor that can be controlled by a computer.

Figure 7.11: A schematic of the automated experimental setup. A computer controls the camera and the camera position via optic fibre. For each photo the computer generates a pulse with the pulse source and records the waveforms from D-dot sensors D_3 and D_4 and B-dot sensors B_3 and B_4 from the oscilloscope.

nearly the entire length of the reactor can be imaged[*]. Both the stepper motor and the camera can be fully controlled by a computer.

7.3.3 Automation

Figure 7.11 shows the total experimental setup. The entire setup is fully automated and can be controlled by software on a computer. For each measurement we can set the number of x-positions the camera takes photos at (in steps of 5 cm), the exposure time of the camera t_e, the delay of the camera t_d, the gain of the camera U_g and the amount of photos the camera takes at each setting. We have to adjust the nanosecond pulse source manually (spark-gap distance, PFL length and DC-charge voltage for the pulse charger), but once it is set, the computer controls the pulse generation with the pulse charger controller. With all the parameters set, the computer sends the camera to the first x-position and starts taking photos at all the user-specified t_e-, t_d- and U_g-settings before moving the camera to the next x-position. For each photo the computer generates a pulse with the pulse source and records the waveforms from D-dot sensors D_3 and D_4 and B-dot sensors B_3 and B_4 from the oscilloscope. More details can be found in [178].

7.3.4 Data processing

The result of the automation of the entire setup is that we can perform a significant amount of experiments automatically. However, this also results in a significant amount of data from the oscilloscope and the camera, which has to be stored and sorted. This is the first of two steps of the data-processing process that we apply to the raw data

---

[*]Unfortunately, it turned out that the very beginning of the reactor (at the side of the cable coupler) is not reached by the camera. Therefore, we are unable to image the first 12.5 cm of the reactor.

and consists of sorting the data by its camera settings and storing the data in an SQL database.

The second step in the data processing is the calculation of the plasma parameters. These are parameters which are automatically calculated by software from the ICCD images from the SQL database. Figure 7.12 shows an example of this procedure. Figure 7.12a gives a raw image with lines added to indicate the reactor wall and the HV wire of the reactor. The bright dots are the streamers. From the raw image, the software script determines with a brightness-threshold value in which areas the streamers are active in the top half of the image. The envelope of this active streamer area is then calculated and filtered with a moving average filter, which results in a filtered streamer profile. Figure 7.12c shows this filtered streamer profile. From the profile, the streamer lengths[†] are calculated as the local maxima from the streamer profile. Subsequently, the streamer widths are calculated as the FWHM from the individual peaks (representing separate streamers) of the streamer profile. Figure 7.12d shows these streamer widths.

In Fig. 7.12b we added the relevant information to the raw image (with a colour map applied) to show how the calculated parameters relate to the raw data. The complete procedure can be found in [178].

To ensure that we always use the streamer-length data from streamers that propagate in the plane of focus, we only take the maximum streamer length of each image to calculate the streamer lengths for a certain experimental setting. Furthermore, we use the same procedure that was used in Figure 7.12 for the top half of the image to calculate the plasma parameters for the bottom half of the image.

We should mention that the method with which we calculate the streamer widths (from the streamer profiles) is not the method that should ideally be used. A more generally used method would be the one used in [16,134,138]. First, we need to isolate the head of each streamer and then calculate an intensity profile averaged along the propagation direction. From this intensity profile, the full width at half maximum (FWHM) is then the streamer diameter. Because the method that we used in this chapter is different from the FWHM-method, the absolute value of the streamer diameters that we report may not be directly compared with other diameters reported in literature, because they might be slightly different. However, the relative differences in streamer diameter that we find in this chapter are still relevant. It will be left for a future update of the data processing to implement the FWHM-method for streamer-diameter determination.

7.3.5   Short-exposure and long-exposure experiments

We can differentiate between two types of experiments in this chapter: short-exposure experiments and long-exposure experiments.

[†]Whenever we mention the *streamer length* we mean the distance normal to the wire electrode that the streamer head has travelled from the high-voltage wire electrode towards the wall of the reactor.

(a)

(b)

(c)

(d)
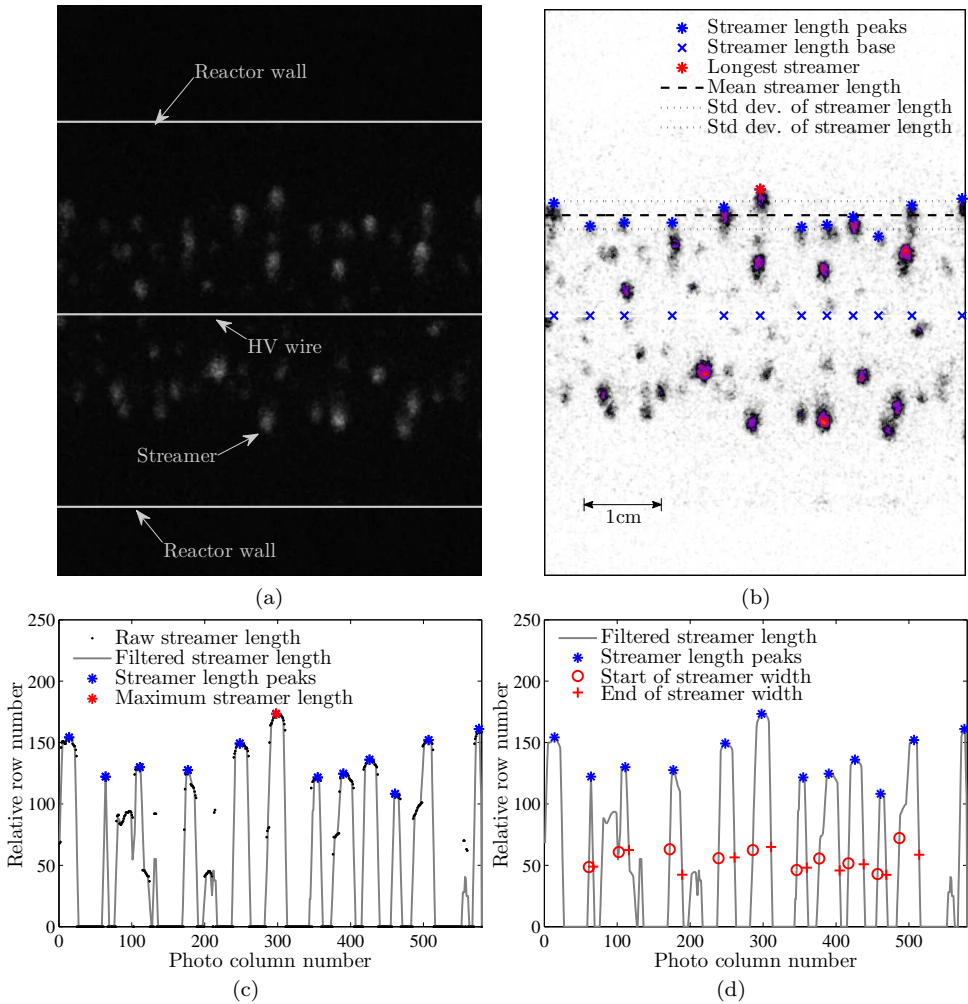
Figure 7.12: An example of how the streamer length and the streamer widths are calculated from the raw images. The raw image in (a) is taken near the end of the reactor for a 9-ns pulse, a camera delay of 9 ns and a voltage of 36 kV. In (a) we added lines for the reactor wall and the high-voltage wire. The bright dots are the streamers. (b) The automated script detects the position of the streamers from a filtered streamer profile. This streamer profile is generated from the image by applying a brightness-threshold value above which the brightness is deemed to come from light emission from the streamers. We applied a colour map to the raw image for clarity. The streamer lengths are calculated from the filtered profile in (c) as the local maxima. The same profile is then used to calculate the streamer widths in (d) as the FWHM value of the peaks in the profile. Detailed information can be found in [178].

In the short-exposure experiments we fix the output voltage and pulse duration of the pulse source and let the camera run through all the x-positions (in steps of 5 cm) at 1-ns exposure times with steps in the camera delay of 1 or 2 ns. In this way we get a complete time-resolved and space-resolved picture of the streamer development and propagation. In these experiments, we always set the pulse source to a high output voltage (usually above 30 kV) to get the most information out of the images (if we lower the output voltage too much, there is very little to see in the images). For each camera-setting the camera takes 20 photos so that we can average the calculated plasma parameters at each setting. This averaging is required because of the standard deviation on the output voltage of the nanosecond pulse source (see Fig. 3.25). Ideally, we would take even more photos at each setting, but this would be extremely time consuming. Each of the automated short-exposure time experiments can take up to 3 hours to finish when 20 photos are taken at each setting, after which it takes another hour to process all the data into the SQL database and calculate all the plasma parameters. Therefore, the amount of these experiments we can perform is limited by time. The majority of the experiments in this chapter are short-exposure experiments.

The second type of experiments are long-exposure experiments. We set the camera exposure time to 100 ns and the camera delay to 0 ns so that we capture the entire discharge with each photo. The camera then runs through all the x-positions. Here, we let the camera take 100 photos at each position. The gain of the camera for all the long-exposure experiments was 760 V. These experiments take a considerably shorter time to complete (because the camera delay is fixed) and give information about the volume of the reactor that the streamers occupy: the plasma volume. Because these experiments take a shorter time, we can perform more experiments in the same time it would take to perform a short-exposure experiment. Consequently, we can analyse the plasma volume for different voltage amplitudes and pulse durations.

7.3.6 Second pulse

When a pulse is applied to the reactor, part of the pulse is reflected on the cable coupler and propagates back towards the pulse source and part of the pulse propagates through the reactor and what is left of it then also propagates towards the pulse source. Together, they form a total reflected waveform, which reflects on the pulse source and is consequently re-applied to the reactor around 230 ns later than its first arrival at the reactor. As a result, new plasma can develop. In the previous chapter we showed in Fig. 6.3 that this new plasma can still dissipate some energy. While we recognise that it would be interesting to investigate this effect with the ICCD-imaging setup of the current chapter, we did not perform such experiments in detail. A preliminary investigation did not show interesting features such as were observed by Nijdam *et al.* in [179].

7.4 Results: pulse duration variation in a 2-m reactor

This section is the first of three results sections. Here we present the results on the streamer development and propagation in a 2-m reactor with the pulse duration of the pulse source as the main parameter under investigation.

We first performed short-exposure experiments for a 2-m reactor because a long reactor gives more insight in the propagation of the streamers with respect to the propagation of the pulse in the reactor. We used positive and negative 1-ns, 5-ns and 9-ns pulses in the reactor at a fixed output voltage. The camera delay t_d for these experiments was increased in steps of 2 ns and the exposure time t_e of the camera was 1 ns for the 1-ns and 9-ns experiments and 2 ns for the 5-ns experiments (due to time limitations we were unable to perform the 5-ns experiments again for 1-ns exposure times). The gain U_g of the camera was fixed for all experiments in this section (980 V).

It will take some time for the first plasma to develop (the first light we capture with the camera) after the pulse enters the reactor. However, with the short rise time of the pulses we use, it is reasonable to assume that this time delay is very short and that the time of first light in the reactor corresponds to the time at which the pulse is applied to the reactor with a delay of a few nanoseconds at most. However, we never verified this delay experimentally because we have no information on the exact time elapsed in the ICCD camera between the trigger moment and the moment of image capture. The time line that we use for all the images in this chapter have $t = 0$ as the time at which we observe the first light in the reactor.

7.4.1 ICCD images

We present the results of each of the 5-ns and 9-ns experiments as a series of images, each representing a moment in time and showing the entire reactor. We generated it by stitching together all the individual ICCD images taken with a common camera delay at different x-positions. Furthermore at each x-position and for each camera delay we averaged over the 20 photos that were taken. Figure 7.13 shows the end result. In all the images, the bottom is the beginning of the reactor (the side of the SA24272 cable) and the top is the end of the reactor. The correspondence of the images with the reactor geometry is indicated at $t = 15$ ns in the negative 5-ns results. The total length of the reactor that we can observe ($x = 1.87$ m) is also indicated in Fig. 7.13a, as well as the colour map that we used for all the images in this chapter.

The first observation from Fig. 7.13 is that the 5-ns streamers seem brighter than the 9-ns streamers during the first few nanoseconds. This is due to the differences in camera exposure time and therefore we can draw no conclusions from the relative intensity between the pulse durations. However, when we look at either the 5-ns or the 9-ns images we can compare the brightness for negative and positive pulses and see that the negative streamers are slightly less bright than the positive streamers, indicating a slightly lower field enhancement at the tip of for the negative streamers.

The second observation is that the propagation of the voltage pulse through the reactor determines the development of the streamers. As the pulse moves through the
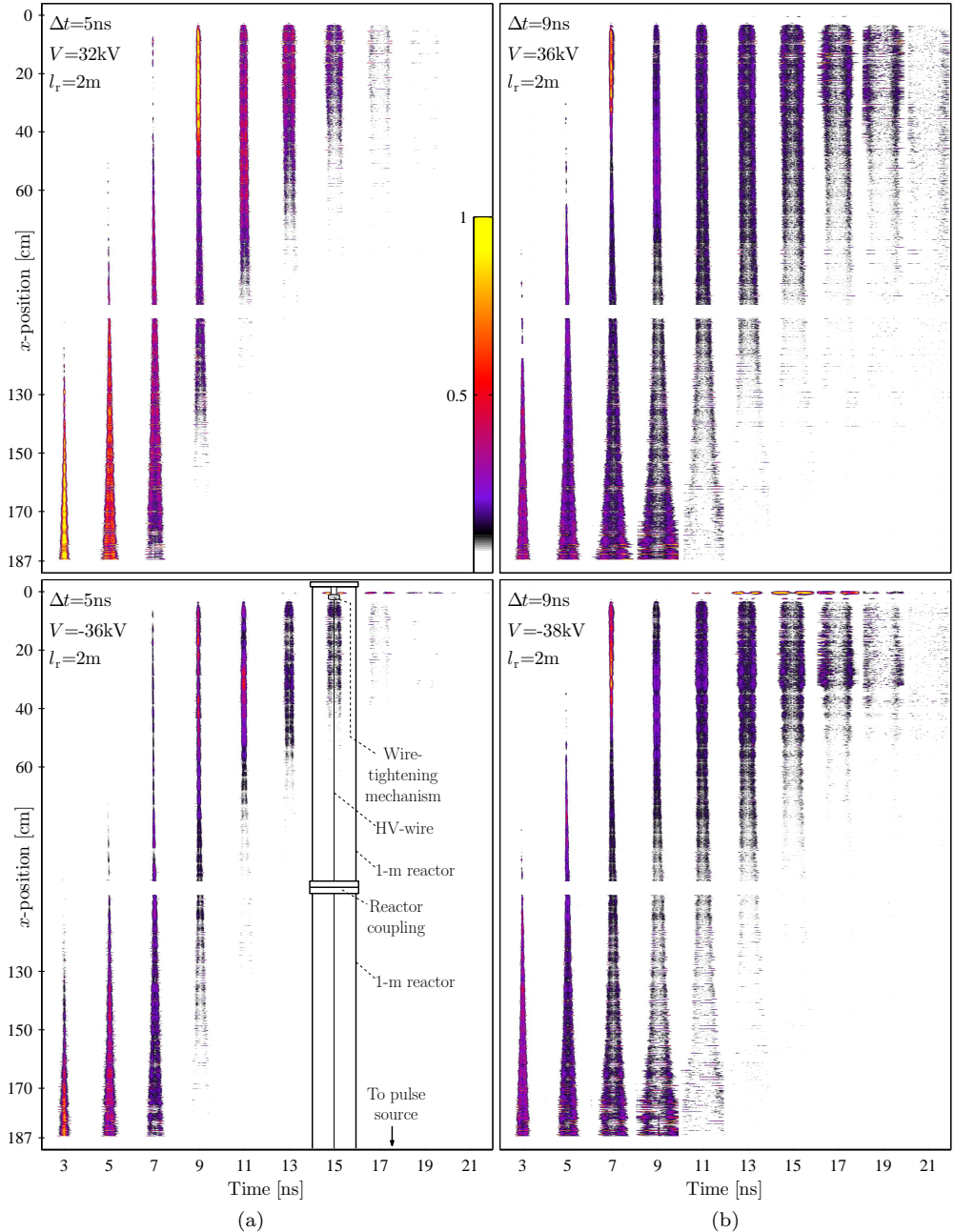
Figure 7.13: Streamer development and propagation in time for (a) a 5-ns positive (top) and negative (bottom) pulse and (b) a 9-ns positive (top) and negative (bottom) pulse in a 2-m reactor. The exposure time of the 5-ns images and 9-ns images is 2 ns and 1 ns respectively. The colour bar in (a) will be used in all the ICCD images of this chapter.
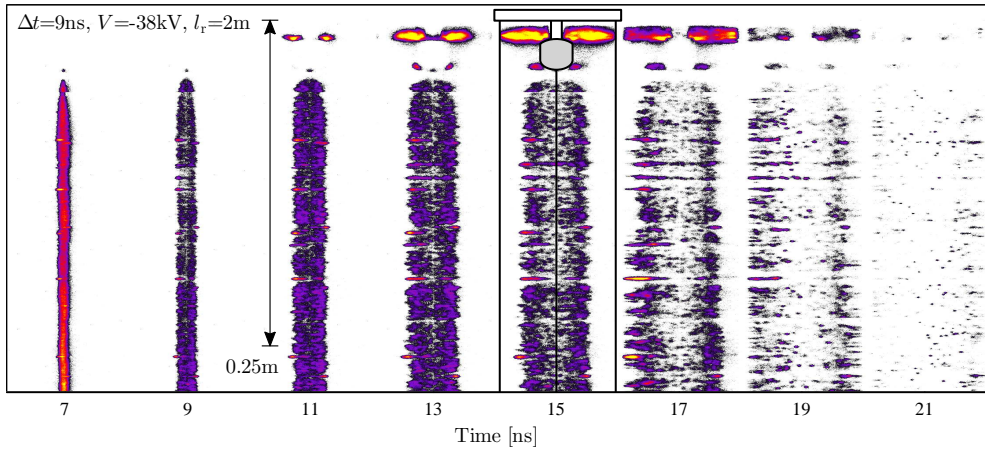
Figure 7.14: A close-up of the negative 9-ns results of Fig. 7.13. Thick streamers develop from the triple point caused by the metal-air-PVC interface of the wire-tightening mechanism behind the stainless-steel removable head. The image at $t = 15$ ns shows a sketch of this removable head and the reactor.

reactor, so does the initiation of the streamers.

When we look at the bottom of each image (beginning of the reactor) it appears that after streamer initiation, the streamers propagate towards the wall of the reactor for a duration of about $\Delta t + 1$ ns before they extinguish. In other words: once the external electric field disappears, the streamers only propagate 1 ns longer before extinguishing. At the end of the reactor (top of the image) the streamers propagate further after this additional 1 ns because here an external field is present for a longer time. This extended time the field is present is caused by the incoming pulse that reflects at the end of the reactor and adds to the incoming pulse. Therefore, the field is present for a longer time (depending on the x-position), as well as it increases the total electric field when the incoming pulse and the reflected pulse overlap. This causes the increase in streamer length near the end of the reactor. We will look into this effect in more detail in the section on the SPICE simulations and streamer length.

If we compare our results with the results of Pokryvailo *et al.* [30] we note that the plasma-size decay that they observed for an increasing position along the wire is also present in our results. They attributed this decay to a decrease in the voltage amplitude along the wire, which is also the reason we observe the decay here. This decay in voltage along the transmission line when a plasma is present was also shown by Van Heesch *et al.* [175].

Thick streamers

An interesting feature presents itself in Fig. 7.13 when we compare the results of the negative pulses with the results of the positive pulses: the thick streamers at the

end of the reactor (top of the images).   It is only vaguely present in the positive discharges, but very significant in the negative discharges. Figure 7.14 shows a closer look at the negative 9-ns results. To understand the origin if the thick streamers, we must re-examine Fig. 6.1 and the stainless-steel removable head of the wire-tightening mechanism of the reactor. The body of this mechanism is made out of PVC (polyvinyl chloride) and has a dielectric constant of around 3.   At the back of the stainless-steel head, the metal meets the PVC and creates a triple point (metal - air - PVC) and causes local electric field enhancement [52]. This triple point is where the thick streamers at the end of the reactor originate. This is especially apparent when looking at Fig. 7.14 at $t = 15\,\text{ns}$ where we added the geometry of the reactor and the wire-tightening mechanism (there also appear some smaller streamers on the rounded edge of this head).

The electric field due to the triple point is very high [52]. When electrons appear in this region (either by field emission from the electrode when the applied voltage is negative, or due to ionisation processes) they recombine at the electrode when the applied voltage is positive. If the electrons came from ionisation, then positive ions will remain behind and screen the triple point. However, when the applied voltage is negative, the electrons are accelerated away from the triple point and can form streamers, which might explain why the thick streamers are more pronounced for negative pulses.

Obviously, the thick streamers at the end of the tightening mechanism are unwanted and are an unexpected artifact of the reactor, because they will consume a significant amount of energy from the nanosecond pulse and only produce a small-volume plasma. Furthermore, the thick streamers are different (including a secondary-streamer phase) from the main streamers under investigation and form a highly-ionised channel that will heat up and eventually lead to a spark breakdown. We observe this spark breakdown if we increase the voltage too much (above 40–50 kV, depending on the pulse duration and the reactor length).   Besides the spark breakdown, the ionised channel that is generated by the thick streamers will also have an electron distribution with more low-energy electrons and will have different radical-generation properties than the primary streamers in the main plasma [5, 162].

In a future implementation of the tightening mechanism we will address the triple point to prevent the generation of thick streamers. However, the experiments of this chapter ran parallel with (and partly succeeded) the plasma-processing experiments of Chapter 8 and time did not allow us to redo all these experiments. Therefore, in this thesis all results were obtained with the tightening mechanism in the reactor that can lead to these thick streamers in some cases.

A second observation from Fig. 7.14 is that there are several preferred places on the high-voltage wire on which streamers originate. This is likely due to small surface irregularities on the wire that cause electric-field enhancement.

Primary and secondary streamers

If we examine the images carefully (also the single images that are not shown here) we find no evidence of secondary streamers; all the streamers we observe appear to be
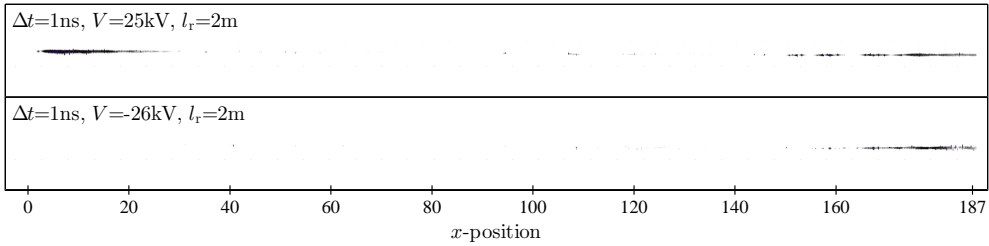
Figure 7.15: The streamer plasma generated by (a) a 1-ns positive pulse and (b) a 1-ns negative pulse. The right side of each image is the start of the reactor (high x-position). The images are averages of all ICCD images taken at each position (so they are averaged over time) to show that at 1-ns pulse duration, very little plasma develops.

primary streamers. Secondary streamers often appear as a glow on the wire electrode after the primary streamer crossed the gap [11, 38, 151]. This glow eventually spreads into the gap when the voltage is applied for a longer time. That we do not see these effects (except in the thick streamers at the wire-tightening mechanism) indicates that we have no pronounced secondary streamer phase or that it is too weak to appear in the images.

Branching

In a point-plate electrode geometry, streamers often branch at high pressures (such as atmospheric pressure with which we work) [144, 166, 167, 180, 181]. In our images, we see almost no evidence of streamers branching or merging which might be due to the much more directed electric field in our reactor as compared to point-plate electrodes. Also, the interaction between parallel-propagating streamers will have an effect [182, 183]. In our study we will not investigate branching any further.

1-ns experiments

Besides 5-ns and 9-ns experiments, we also performed experiments with a 1-ns pulse. However, these results were not very useful as is demonstrated by Fig. 7.15. This figure shows the images of the 1-ns experiments, where we averaged the images over time and over the x-position and illustrates that a pulse duration of 1 ns hardly produces any plasma. The voltage amplitude will have to be increased significantly before anything useful might be seen. Therefore, we leave the 1-ns experiments out of our study in this chapter.

Inception cloud

A final observation from the ICCD images is that there is no significant-sized inception cloud visible (even when zoomed in). We will comment more on the inception cloud in Section 7.7.
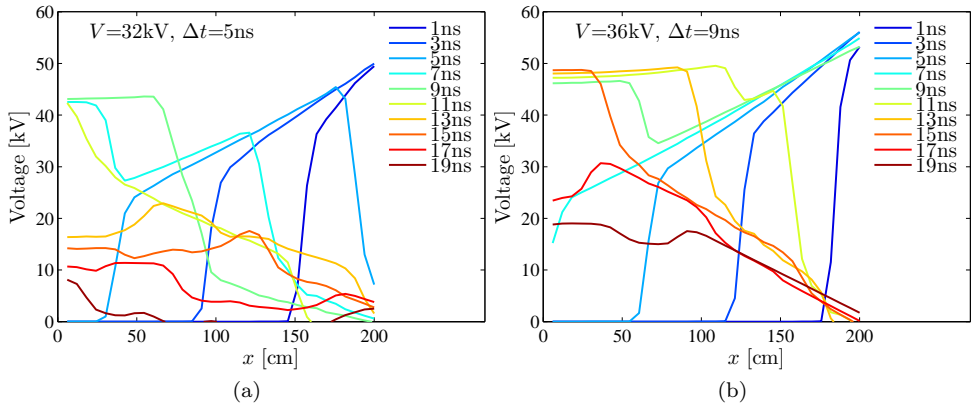
Figure 7.16: SPICE simulation results for (a) a 5-ns positive pulse and (b) a 9-ns positive pulse at the same applied pulse amplitude as in the 2-m reactor experiments. The figures show the voltage amplitude in the reactor at each position and as a function of time (presented similarly as the streamer lengths in Fig. 7.17).

7.4.2 SPICE simulation

Before we discuss the streamer length, we show SPICE-simulation results of the voltage profiles in the reactor.

To get a better insight into the voltage in the reactor, we introduced a SPICE model of the reactor in Section 7.2. We can use it now to simulate the voltage at each position in the reactor. These simulations will be useful in the next section on streamer length.

We connected two of the reactor models in series to obtain a 2-m reactor model and adjusted the amplitude of the predefined waveform to the amplitude of the voltages that we used in the real experiments. We only model the positive results, because the SPICE model lacks the incorporation of the thick streamers at the end of the reactor. Figure 7.16 shows the results of the simulations and presents the voltage in the reactor at each position for different times, which is similar to Fig. 7.17 in which we will show the streamer length, but now we show the voltage instead of the streamer length.

The simulation results show that when the pulse enters the reactor it travels through the reactor and attenuates in time, until it reflects on the open end of the reactor, reverses direction and adds to the incoming pulse. When the reflected pulse encounters the cable coupler it will reflect again. This second reflection adds to the voltage in the reactor and has the net result that it keeps the voltage higher at the end of the reactor. In the real reactor the pulse dispersion will be a cause for the voltage to be present longer at the end of the reactor and this second reflection will be less pronounced. It is this second reflection in the simulations and the absence of sufficient dispersion that causes the difference between the model and the measurements after the duration of 11.5 ns that we commented on earlier in Section 7.2. However, these two effects

149

both result in a longer time the voltage is present at the end of the reactor, so for the discussion in the next part, the simulated voltages after 11 ns are still valid.

7.4.3 Streamer length

One of the main motivations for the experiments of this chapter is to study the effect of very short pulses on the distribution of the plasma in the reactor. From the results so far we could see that this streamer coverage is not homogeneous. To get a more quantitative evaluation of this coverage we look at the streamer length as a function of x-position and time. This streamer length is one of the plasma parameters that is automatically calculated by the software. Figure 7.17 shows the streamer lengths for the 5-ns and 9-ns experiments in the 2-m reactor.

The results give us a very unique insight into a streamer plasma generated with very short pulses in a coaxial reactor. Even more than Fig. 7.13 we can see from just one figure the entire development and propagation of the streamer discharge as a function of position in the reactor and as a function of time.

If we first look at just Fig. 7.17a we see that the streamer length at each x-position becomes on average about 10–15 mm, but that this length is reached at very different times of the discharge. At the beginning of the reactor (high x-position) the streamers start propagating as the pulse arrives and stop at around $\Delta t + 1$ ns, which can now be more clearly seen. A little further into the reactor the streamers propagate slightly less far, because the pulse has lost some of its energy and consequently the voltage (and thus the electric field) will be lower at that position (also shown in Fig. 7.16a). This behaviour dominates the first 1 m of the reactor. However for $x = 0$–100 cm the behaviour is different, because the pulse reflects on the open end of the reactor (also shown in Fig. 7.16a). The effect that the voltage is now present for a longer time and that the voltage is higher can clearly be seen in the length of the streamers. Even though the pulse has already dissipated part of its energy in propagating along the reactor, the voltage-doubling at the end of the reactor causes the streamers to propagate further than the streamers in the beginning of the reactor. However, this is not the only reason for the longer streamers at the end of the reactor.

In Section 7.2 we noted that the pulse severely disperses in the reactor (as compared to our simulations). This causes the electric field to be present even longer in parts of the reactor as time passes and this can be seen by the propagation of the streamers near the end of the reactor, because they propagate for a longer time than expected. For instance, at $x = 20$ cm, the plasma front arrives at $t = 6$ ns. If this would coincide with the arrival of the 5-ns pulse (which will most likely not be the case, as the pulse will precede the plasma front by some unknown delay t_{du}) and we assume that the pulse travels with the speed of light then the electric field would be present at this position for $\Delta t + 2 \times 0.2/3 \cdot 10^8$ (the time needed to travel the remaining distance to the end of the reactor and back)-$t_{du} = 6.3$ ns-t_{du}. If we add the self-propagating time of the streamers of 1 ns, then the streamers should stop propagating at around $t = 13$–14 ns-t_{du}, but Fig. 7.17 shows that the streamers stop propagating at around 19 ns. This can only happen if the external electric field is present for a longer time than we
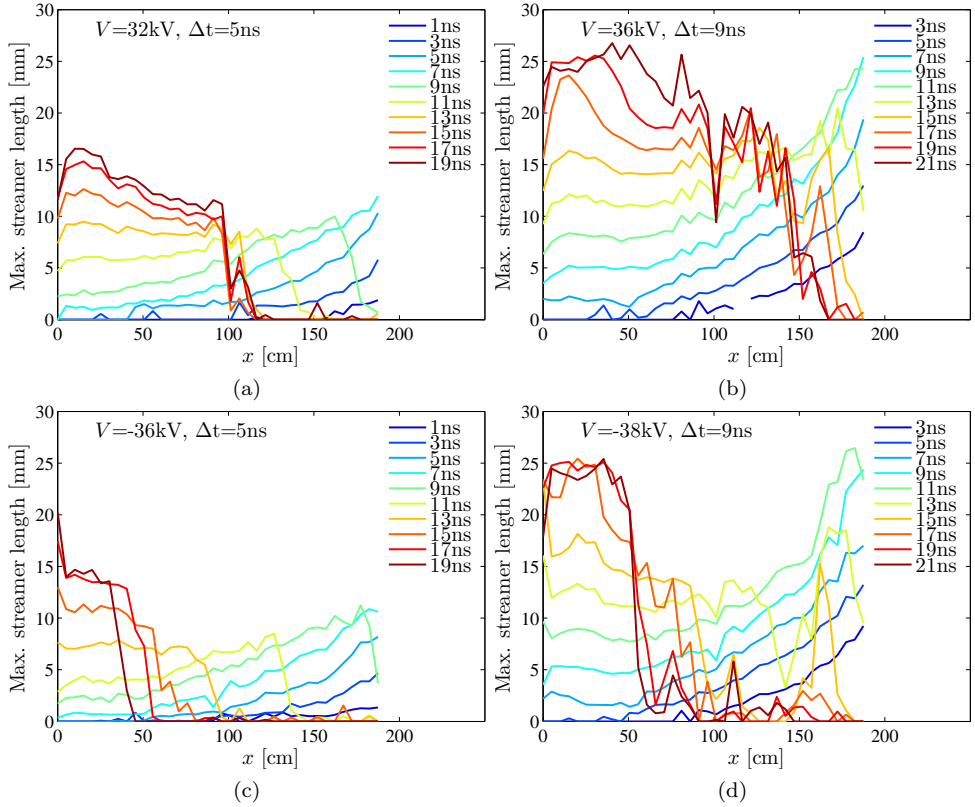
Figure 7.17: A quantitative representation of the maximum streamer lengths (averaged over the results from 20 photos at each position and each time) calculated from the results of Fig. 7.13 for (a) the positive 5-ns experiments, (b) the positive 9-ns results, (c) the negative 5-ns results and (d) the negative 9-ns results. The left side of each figure corresponds to the end of the reactor (low x-position). Comparing the results in (a) and (b) to the results of Fig. 7.16a and b there is a good agreement between the simulated voltages in the reactor and the measured streamer lengths if we consider that a streamer can propagate as long as an external electric field is applied.

expected. This is plausible if we consider dispersion of the pulse by the plasma. The validity of this claim can be tested by repeating the experiments on a 1-m reactor, because at the end of this reactor the pulse will be less dispersed because it has only travelled half the length of the reactor as compared to the 2-m reactor experiments. Therefore the additional propagation time of the streamers will be lower. We will revisit this discussion in Section 7.5 where we present results on experiments with the 1-m reactor.

The propagation of the 9-ns positive pulse in Fig. 7.17b is very similar to that

of the 5-ns pulse, only now the electric field is present for a longer time due to the longer pulse, which we showed in Fig. 7.16b. This increases the streamer length at all positions, but the analysis that we applied to the 5-ns results applies as well for the 9-ns results. One significant difference is that at the end of measurement (at around 19–21 ns) the streamers are still present over a longer length in the reactor. This is also caused by the longer pulse length and consequently the plasma coverage in the 2-m reactor is larger for when we use the 9-ns pulses as compared to the 5-ns pulses.

If we now compare the positive-pulse results in Figs. 7.17a and b with the negative-pulse results in Figs. 7.17c and d then we see that the general development of the streamers is very similar. However, one significant difference is the streamer propagation at the end of the reactor (low x-position). In the positive results we saw that the streamers propagate quite far in the second half of the reactor and attributed this to the pulse reflection at the end of the reactor and the dispersion of the pulse due to the plasma. This effect is also present in the negative results, but now over a much shorter length of the reactor. The reason for this difference are likely the thick streamers at the end of the reactor that we discussed previously. These thick streamers dissipate a significant amount of energy, which decreases the pulse voltage and therefore the applied electric field. Consequently, the streamers can propagate less far. Therefore, the plasma coverage is larger and more homogeneous when we use the positive pulses as compared to the negative pulses.

A second effect of the thick streamers is that they can drastically decrease the reactor impedance at the end of the reactor due to their high conductivity, in the worst-case approaching a short circuit. In the event of a short circuit, the voltage reflection at the end of the reactor will not add to the incoming pulse, but will subtract from the incoming pulse. In reality the thick streamers will not cause a complete short circuit, but their low impedance makes the reflection at the end of the reactor less ideal and more complex and will lower the voltage amplitude.

7.4.4 Streamer propagation velocity

In the introduction we already mentioned that a higher applied voltage results in a higher streamer propagation velocity [16, 24, 138, 146, 148, 151, 160, 168, 172]. In the streamer-length discussion we showed that for the 2-m reactor the voltage is highest at the beginning and at the end of the reactor, so we would expect the highest streamer propagation velocities there. Besides the voltage amplitude, the time the voltage is applied is also important to sustain the streamer propagation. Therefore, we should also see higher streamer velocities for the 9-ns experiments.

We calculate the streamer propagation velocity v as a function of time delay t_d and x-position directly from the streamer-length results as

$$v(x, t_\mathrm{d}) = \frac{s_{\mathrm{x}, t_\mathrm{d}} - s_{\mathrm{x}, t_{\mathrm{d}-1}}}{t_\mathrm{d} - t_{\mathrm{d}-1}}, \tag{7.5}$$

where $s_{\mathrm{x}, t_\mathrm{d}}$ is the streamer length at time t_d and $s_{\mathrm{x}, t_{\mathrm{d}-1}}$ is the streamer length at time $t_{\mathrm{d}-1}$ (one delay time previously).
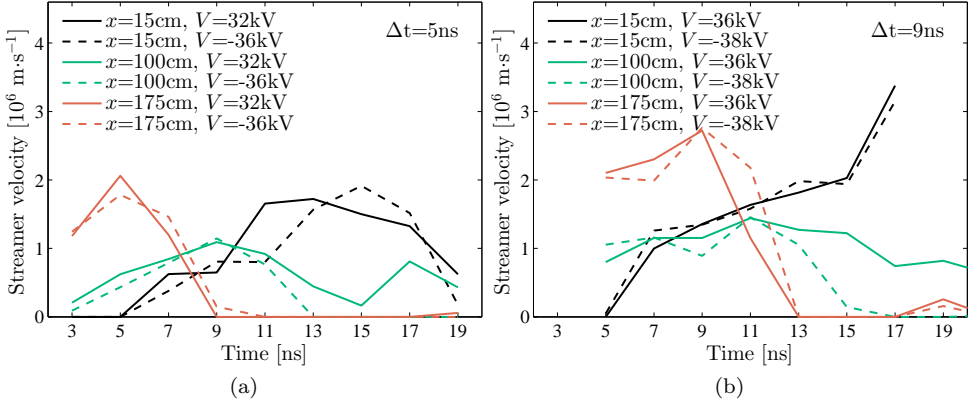
Figure 7.18: Streamer propagation velocities as a function of time at three different positions in the 2-m reactor for (a) the 5-ns experiments and (b) the 9-ns experiments. The velocities were calculated from the streamer length results of Fig. 7.17. For averaging purposes the results for $x = 15\,\text{cm}$ and $x = 175\,\text{cm}$ also include the results of 5 cm on either side of these x-positions. The $x = 100\,\text{cm}$ includes the results of 10 cm on either side ($x = 100\,\text{cm}$ itself is not included because of the reactor coupling).

Figure 7.18 shows the streamer velocity at different positions and pulse polarities in the reactor for the 5-ns measurements (Fig. 7.18a) and the 9-ns measurements (Fig. 7.18b). For averaging purposes the results for $x = 15\,\text{cm}$ and $x = 175\,\text{cm}$ also include the results of 5 cm on either side of these x-positions. The $x = 100\,\text{cm}$ includes the results of 10 cm on either side ($x = 100\,\text{cm}$ itself is not included because of the reactor coupling). The figures show that our assumptions about the streamer velocities are correct: the velocities are highest at the beginning and at the end of the reactor and are also (slightly) higher for the 9-ns pulses. In general, the streamer velocities are in the same range of 10^5–10^7 m·s^{-1} as other studies.

In the 5-ns results on streamer propagation, there was no streamer crossing observed in the reactor. Therefore, the streamer velocities show an increase when the streamers initiate, followed by a relatively flat section until the streamers quench. Only at $x = 175\,\text{cm}$ does the velocity start at a high value before dropping. This is because the streamers are already propagating at that position at $t = 3\,\text{ns}$. As expected, the velocity in the middle of the reactor is lower due to the lower voltage at that position.

There is very little difference between the positive and the negative streamer velocities. The only difference is the velocity at $x = 100\,\text{cm}$ after $t = 9\,\text{ns}$, but this is due to the difference in streamer length at that point because of the thick streamers at the end of the reactor for negative pulses.

The 9-ns results are similar to the 5-ns results, except now the streamers reach the outer electrode for $x = 15\,\text{cm}$. This is evident from the sharp increase in velocity at $t = 15\,\text{ns}$. Also, the velocities are slightly higher for the 9-ns pulse as compared to the 5-ns pulse. This can be explained by the increased time for which the voltage is present

for 9-ns pulses; for the 5-ns pulses the voltage drops again when the pulses are not very far across the distance between the electrodes. The difference between positive and negative pulses is again negligible apart from the effects of the thick streamers in the case of negative pulses.

The result that there is no significant difference between the velocities of negative and positive streamers is remarkable, considering that most studies show that negative streamers are slower [38, 134, 145–151]. However, some show that the differences between positive and negative streamers become smaller for high applied electric fields and higher rise rates. For instance, Briels *et al.* showed in a point-plate geometry that at high pulsed voltages (above $50 \, \mathrm{kV}$ with a rise time of $15 \, \mathrm{ns}$), the velocities of negative streamers were only slightly lower than for positive streamers. Furthermore, Winands *et al.* showed that in their wire-plate reactor the velocities of positive and negative streamers were around $1.2 \times 10^6 \, \mathrm{m \cdot s^{-1}}$ and $0.4 \times 10^6 \, \mathrm{m \cdot s^{-1}}$ respectively for pulses with a rise rate of $1.5 \, \mathrm{kV \cdot ns^{-1}}$, but appeared to become $2 \times 10^6 \, \mathrm{m \cdot s^{-1}}$ for both polarities when the rise rate increases to $2 \, \mathrm{kV \cdot ns^{-1}}$ [151]. Additionally, Wang *et al.* showed a similar effect in a corona-plasma reactor when they compared results from two studies [38,146]. For a pulse with tens of nanosecond rise time they showed that negative streamers (-93 kV applied voltage) propagated twice as slow as positive streamers (60 kV applied voltage): $0.6 \times 10^6 \, \mathrm{m \cdot s^{-1}}$ as compared to $1.2 \times 10^6 \, \mathrm{m \cdot s^{-1}}$ for positive streamers [146]. When they used a much faster pulse, with a rise rate of around $40 \, \mathrm{kV \cdot ns^{-1}}$ at a peak voltage of around $100 \, \mathrm{kV}$ (both negative and positive) they showed that the velocity of the streamers become similar: $6.7 \times 10^6 \, \mathrm{m \cdot s^{-1}}$ for negative streamers as compared to $8.0 \times 10^6 \, \mathrm{m \cdot s^{-1}}$ for positive streamers [38]. It is at the moment unclear if the electric fields in our reactor are high enough (and have a high enough rise rate) to cause the streamers to have a similar propagation velocity and what the underlying mechanisms are. We are not aware of any other studies comparing streamer propagation for negative and positive pulses with the subnanosecond rise time of our pulses, so we are unable to compare our results with others. However, it seems that for the rise time of the pulses we used and the voltage amplitudes we used, the streamer velocities of positive and negative pulses are nearly identical. One comment we should make is that the voltage amplitude in the experiments with the negative pulses is $2 \, \mathrm{kV}$ higher, which might (partly) account for the similar streamer velocities.

7.4.5 Streamer width

The width of the streamers, or streamer diameter, is not a parameter that we have investigated and analysed extensively. This is mainly because we focused more on the propagation of the streamers, but partly because the streamer widths varied very little and therefore have no significant effect on the plasma volume. It is a parameter that we intend to investigate further in future work. Here we just show the general results.

Figure 7.19 shows the streamer-width results for the streamers generated with the 9-ns pulse in the 2-m reactor. It shows that once the streamers are generated, their width remains quite constant at 1.5–$2 \, \mathrm{mm}$. Only after the streamers quench does the streamer width drop quickly. The streamer width is rather constant along the
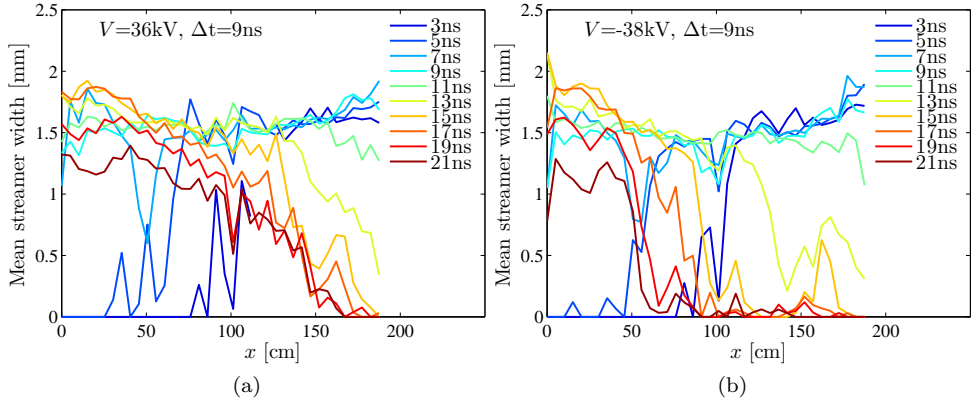
Figure 7.19: Streamer width as a function of time and position for the 9-ns (a) positive and (b) negative pulses in the 2-m reactor. Unlike the streamer propagation velocity, the streamer width appears to be only slightly dependent on the external electric field.

reactor, which indicates that, unlike the streamer velocity, the voltage has only a small effect on the streamer width in our experiments. In other studies, the voltage had a much greater effect on the diameter: the diameter increased with the applied voltage [134,151,160,165]. However, in these other studies, often a point-plate geometry was used, where we use a wire-cylinder reactor where neighbouring streamers will have an effect on a propagating streamer [182, 183]. Furthermore, we are working with such a short rise time that comparable studies are difficult to find. However, in our experiments the streamer width is slightly dependent on the voltage as well: for lower voltages the width is smaller. This can be seen by the dip in the streamer widths in the middle of the reactor. This effect is slightly more pronounced for the negative streamers, which is the same effect we saw in the streamer lengths and can be attributed to the lower voltage in the middle of the reactor as compared to the positive streamers.

Another observation is that, just as with the streamer velocities, there is no significant difference between the negative and positive streamers. This is again contrary to some other studies [151], but consistent with others [134].

We have not shown the results for the streamer width of the streamers generated with the 5-ns pulses because these results are similar to the 9-ns results and add no new information.

7.4.6 Conclusions 2-m reactor

From all the results in this section we can conclude that the voltage in the reactor at each position and at each time is the result of a complex interaction with the plasma and the reactor and that the streamer length seems proportionally related to it. Therefore, to obtain the most homogeneous plasma, the voltage in the reactor should be as constant as possible, which is not the case in the 2-m reactor and will likely only

be worse for even longer reactors (due to the increased effect of pulse propagation). Furthermore, there is very little difference between the negative and positive pulse experiments, besides the formation of unwanted thick streamers at the end of the wire-tightening mechanism of the streamers. If the thick streamers would not exist, the results would most likely be very similar. As a result, the streamer propagation velocities of the negative and positive streamers are near identical. Likewise, the streamer widths show no significant difference and are only slightly dependent on the voltage (a higher voltage results in a larger streamer width). The streamer width is a parameter that, together with the streamer length, determines the volume in the reactor that the streamers propagate through and produce radicals in. Therefore, the streamer-length and streamer-width results indicate that there is no significant difference in streamer coverage (apart from the effects of the thick streamers) between positive and negative streamers in the 2-m reactor. Furthermore, due to the long length of the reactor and the effect of pulse propagation through the reactor, it seems unlikely that a complete coverage of the reactor without generating secondary streamers is possible in the 2-m reactor for the pulse durations we use in this thesis.

7.5 Results: pulse duration variation in a 1-m reactor

In this chapter we first performed short-exposure experiments for a 2-m reactor because a long reactor gives more insight in the propagation of the streamers with respect to the propagation of the pulse in the reactor. However, in our plasma-processing experiments of Chapter 8 we will use a 1-m reactor. Therefore, in this section we will first discuss the results of short-exposure experiments on a 1-m reactor, followed by results of long-exposure experiments. For these short-exposure experiments we used 5-ns and 9-ns duration voltage pulses of both polarities. We used a 1-ns exposure time for all images, steps of 1 ns in the delay time and a camera gain of 980 V.

7.5.1 ICCD images

Figure 7.20 shows the ICCD results of the short-exposure experiments for the 1-m reactor for the 9-ns pulse (positive and negative) and the 5-ns pulse.

If we compare the 9-ns positive and negative images, we see again that the negative streamers are slightly less bright. More noticeable is that this time there are also thick streamers for the positive pulses, which were absent in the 2-m positive results. They are also present in the negative results and are larger and brighter there. That indicates that the biggest problem with the triple point is still with the negative polarity pulse, but that now the pulse has still a high enough amplitude after 1 m that it is able to ignite the thick streamers for the positive pulses as well. Furthermore, we observe from the images that the plasma-volume coverage is much more homogeneous as compared with the 2-m results, which indicates that for a shorter reactor the pulse reflections become less of a defining factor for the 9-ns pulse. However, if we look at the results of the positive 5-ns pulse we see that here the plasma coverage is still far
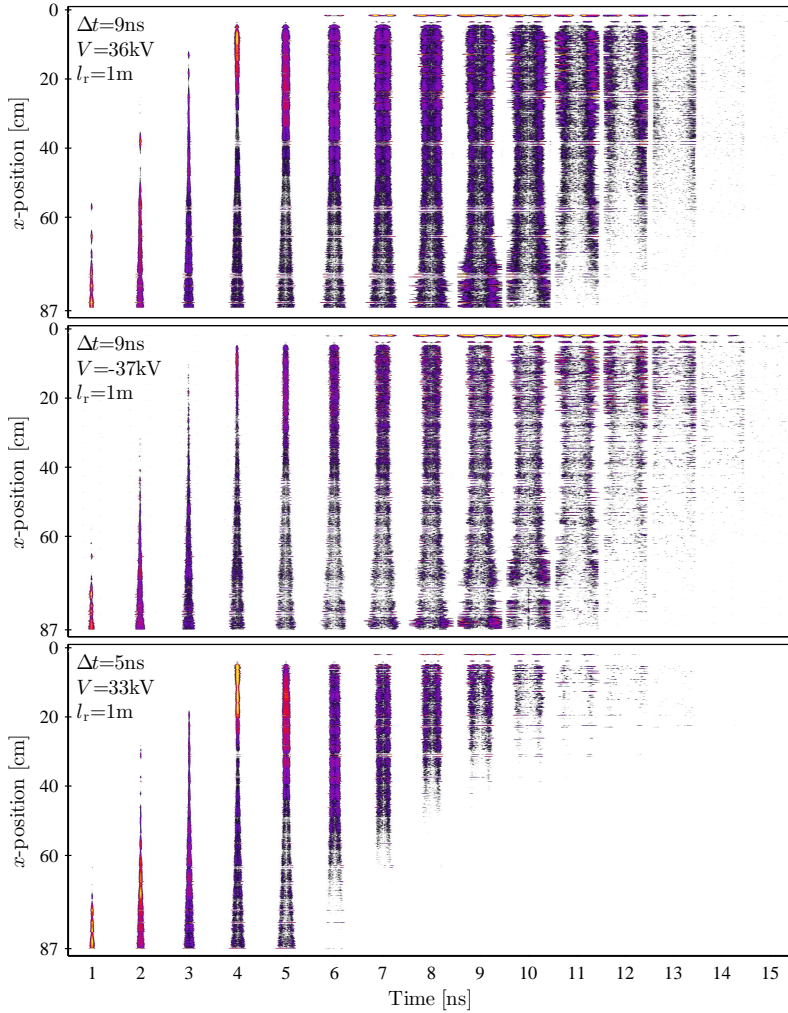
Figure 7.20: Streamer development and propagation in time for a 9-ns positive pulse (top), a 9-ns negative pulse (middle) and a 5-ns positive pulse (bottom) in a 1-m reactor. The exposure time is 1 ns for all images and each image is the stitched average of 20 photos at each position.

from homogeneous. In other words: the longer the reactor is, the longer the pulses have to be to achieve a homogeneous plasma coverage. This seems obvious, but it is a good point to make from the results of our experiments.
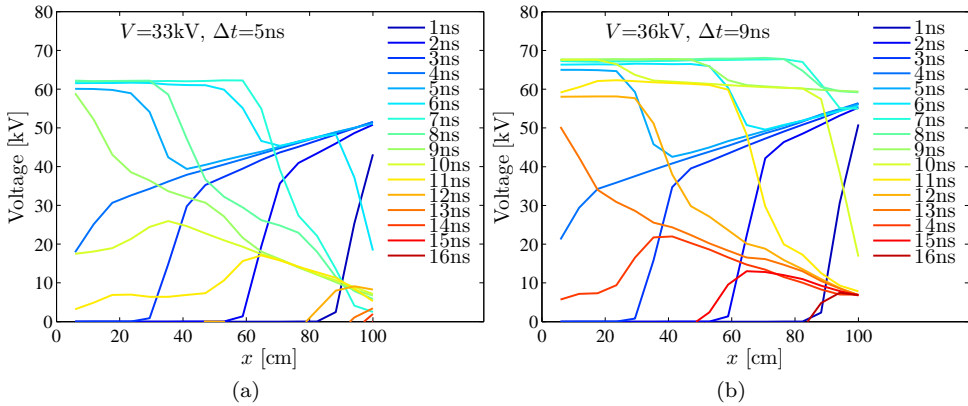
Figure 7.21: SPICE simulation results for (a) a 5-ns positive pulse and (b) a 9-ns positive pulse at the same applied pulse amplitude as in the 1-m reactor experiments. The figures show the voltage amplitude in the reactor at each position and as a function of time.

7.5.2 SPICE simulations

Figure 7.21 shows SPICE simulation results of the voltage in the 1-m reactor as a function of position and time. Just like the streamer lengths, the maximum voltage in the 1-m reactor for the 9-ns pulse is much more homogeneous than in the 2-m reactor. The voltage in the 1-m reactor for the 5-ns pulse still shows higher values at the end of the reactor. Due to a shorter length over which the pulse can attenuate, the voltage at the end of the reactor is higher for the 1-m results as compared to the 2-m reactor.

7.5.3 Streamer length and propagation velocity

Just as with the 2-m reactor experiments, we can present the results of the ICCD images of the 1-m reactor experiments in a quantitative way by plotting the calculated streamer lengths as a function of time and position. Figures 7.22a–c show these results.

We can immediately see that now the streamer coverage in the reactor is quite homogeneous for the streamers generated with the 9-ns pulses (both polarities). The results show a slight dip in the middle of the reactor, but this dip is not nearly as significant as with the 2-m reactor. The dip in the middle is again slightly larger for the negative results, which could be the result of the more intense thick streamers at the end of the wire-tightening mechanism. These results agree well with the SPICE simulations in Fig. 7.21b, which show a more homogenous voltage along the reactor as compared to the 2-m results.

Figure 7.22c now clearly shows that a 5-ns pulse is not long enough to achieve a homogeneous plasma coverage, which was also reflected in the simulated voltages in Fig. 7.21a. However, the streamers in the 5-ns experiments propagate further towards the reactor wall at the end of the 1-m reactor as compared to the 2-m reactor. This is
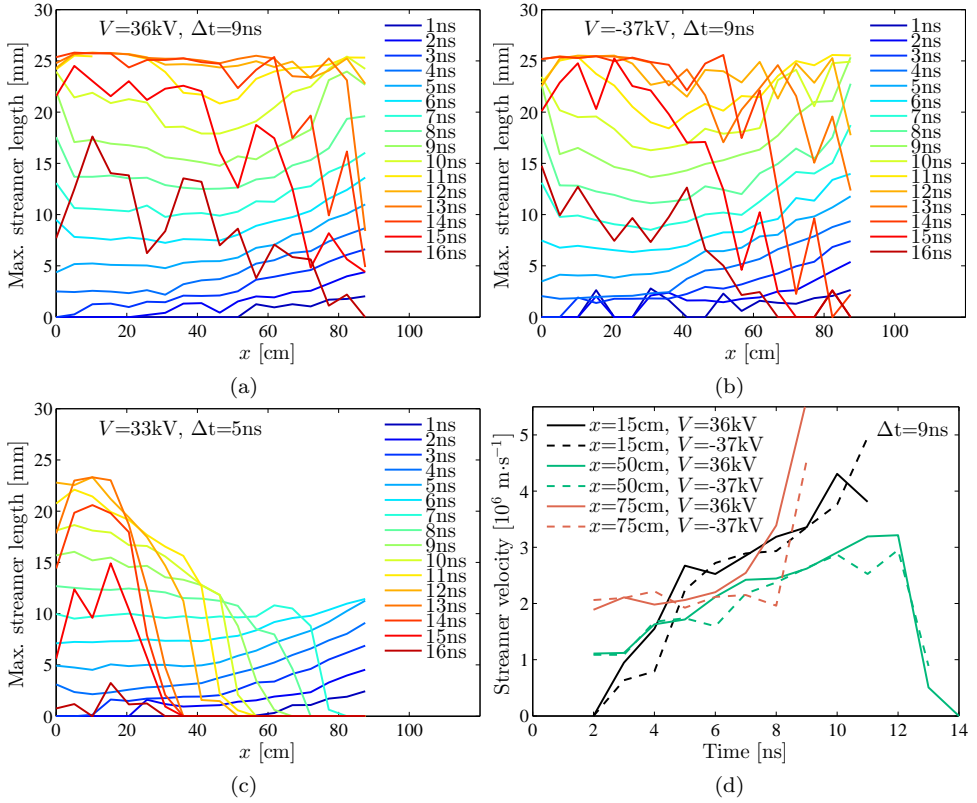
Figure 7.22: A quantitative representation of the maximum streamer lengths (averaged over the results of 20 photos at each position and each time) calculated from the results of Fig. 7.20 for (a) the positive 9-ns experiments, (b) the negative 9-ns experiments and (c) the positive 5-ns experiments. Comparing the results in (a) and (c) to the results of Fig. 7.21 there is a good agreement between the simulated voltages in the reactor and the measured streamer lengths. (d) shows the streamer propagation velocities at different positions in the reactor for the positive 9-ns results.

due to the increased voltage at the end of the reactor because now the pulse attenuation is less at the end of the reactor (because it is shorter). Also the 9-ns results show longer streamers on average due to higher voltages as compared to the 9-ns results in the 2-m reactor.

In the section on streamer length of the 2-m reactor we noticed that the streamers at the end of the reactor (low x-position) propagated for a longer time than we expected the external electric field to be present and attributed this effect to the dispersion of the pulse in the reactor due to the propagation through the plasma. This dispersion causes the voltage to be present for a longer time. We then argued that the dispersion increases

when the pulse travels longer through the reactor and therefore the dispersion should be less pronounced when the pulse reaches the end of the 1-m reactor as compared to the end of the 2-m reactor. In the 2-m reactor, the streamers propagated for an additional $5\,\text{ns}+t_{\text{du}}$ (where t_{du} is the unknown delay between the arrival of the pulse and the streamer initiation) for the 5-ns positive pulse after the pulse should have passed if we assume a non-dispersed pulse and include the 1-ns self-propagating time of the streamers. If we look at the 1-m results at $x = 20\,\text{cm}$ in Fig. 7.22c then the streamers start propagating at $t = 2\text{--}3\,\text{ns}$ and propagate until around $t = 12\text{--}13\,\text{ns}$. At $x = 20\,\text{cm}$ the electric field would be present for $\Delta t + 2{\times}0.2/3{\cdot}10^8$ (the time needed to travel the remaining distance to the end of the reactor and back)-$t_{\text{du}} = 6.3\,\text{ns-}t_{\text{du}}$ if the pulse would not be dispersed. If we add the self-propagating time of the streamers of $1\,\text{ns}$, then the streamers should stop propagating at around $t = 9.3\text{--}10.3\,\text{ns-}t_{\text{du}}$, while in the experiments they stop at around $t = 12\text{--}13\,\text{ns}$. So now the streamers propagate for around $3\,\text{ns}+t_{\text{du}}$ longer than if the pulse was not dispersed. This is about half as long as in the case of the 2-m reactor, which gives a good indication that the dispersion increases as the pulse travels along the reactor and that this is indeed the reason for the longer-than-expected streamer propagation times. One might even argue that what we call the 1-ns self-propagation time of the streamer is already due to pulse dispersion at the very beginning of the reactor.

In Fig. 7.22d we show the streamer propagation velocity of the streamers in the 9-ns experiments (both polarities). In general, the results are very similar as those of the 2-m reactor, only now the streamers also reach the outer cylinder of the reactor at the beginning of the reactor (high x-position). Because the thick streamers were now present at both polarities, the streamer velocity results are even more identical than for the 2-m reactor. If we consider that the amplitude of the negative pulses was $1\,\text{kV}$ higher than that of the positive pulses the negative streamer velocities might be slightly lower than the positive streamer velocities if identical voltage amplitudes were used, but even then the negative and positive results would be very similar. One significant difference between the 1-m and 2-m results is that the streamer velocity at the end of the reactor is higher in the 1-m reactor. This is the result of the higher voltage at the end of the reactor as compared to the 2-m reactor. In comparison, the streamer velocity at the beginning of the 1-m reactor is comparable to the streamer velocity at the end of the reactor.

7.5.4   Streamer width

The widths of the streamers in the 2-m reactor varied very little with the position in the reactor (and thus the applied voltage). However, in the middle of the reactor the streamer widths were slightly lower; an effect which was worse for the negative polarities (just as the streamer lengths showed a greater dip in the middle for the negative results). This indicated that the streamer width depends on the voltage in the reactor. However, the dependency is weak.

Figure 7.23 shows the streamer widths for the 1-m reactor experiments with the 9-ns pulse (both polarities). Just as with the streamer lengths in the 1-m reactor,
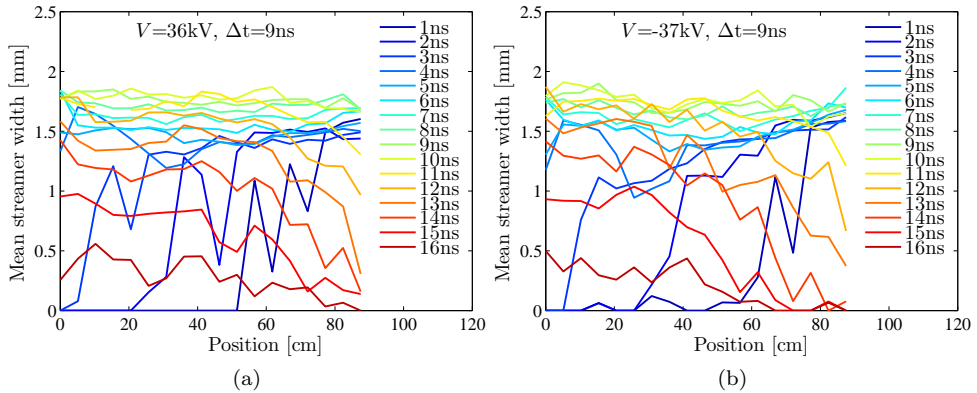
Figure 7.23: Streamer width as a function of time and position for the 9-ns (a) positive and (b) negative pulses in the 1-m reactor. Where the streamer width showed a slight dip in the middle of the reactor for the 2-m experiments, the streamer width is now more constant along the reactor length.

the streamer widths are much more constant along the length of the reactor when we compare the results with the 2-m experiments. This was to be expected, because we already argued and simulated that for the 9-ns pulse the maximum voltage along the reactor is more constant. This results in the more constant streamer width.

The streamer lengths showed a slightly larger dip in the middle for the negative streamers in the 1-m reactor. If we look at Fig. 7.23b we also see that the streamer width exhibits a slight dip as compared to the positive streamers, which again confirms that even though the effect is small, the pulse-propagation effects also affect the streamer width.

7.5.5 Streamer profiles

A disadvantage of the short-exposure experiments is the large amount of time the experiments cost and therefore we only performed these for a limited range of pulse parameters. However, it would be very insightful if we could obtain the plasma coverage for different voltage amplitudes. Therefore, we performed long-exposure experiments. In these experiments we trade time information for voltage flexibility. We took images at an exposure time of 100 ns and a camera gain of 760 V and consequently captured the whole discharge in each image. At each position we captured 100 images for averaging purposes. From these images we calculated the maximum streamer lengths, just as with the short-exposure experiments. Figure 7.24 shows the resulting profiles that indicate what distance the streamers travelled.

We already knew from Fig. 7.15 that a pulse duration of 1 ns results in very little plasma activity. Therefore we used a pulse duration of 2 ns for the long-exposure images as the shortest pulse duration. However, as Fig. 7.24 shows, at this pulse

161

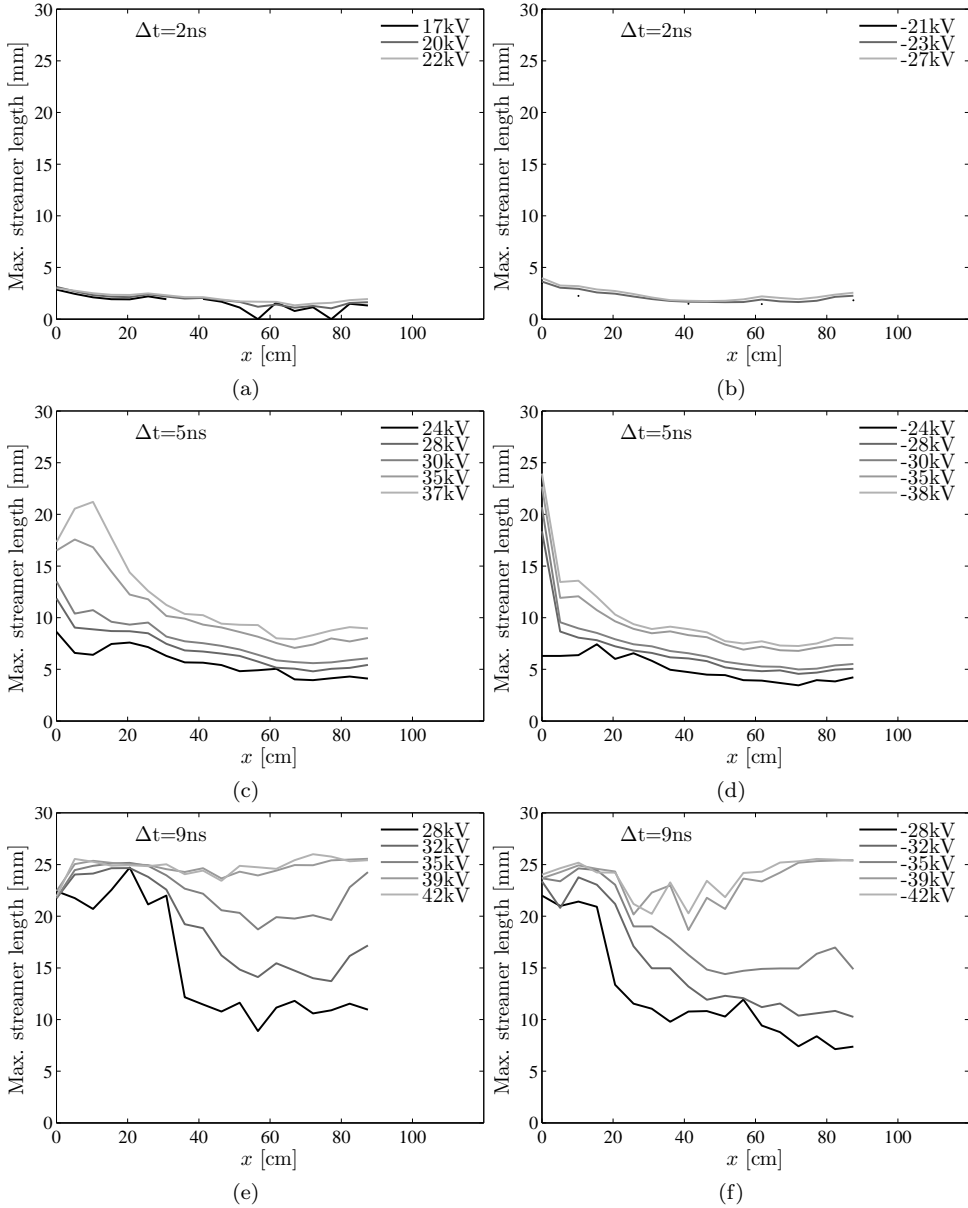Figure 7.24: The results of the long-exposure experiments for (a) a positive 2-ns pulse, (b) a negative 2-ns pulse, (c) a positive 5-ns pulse, (d) a negative 5-ns pulse, (e) a positive 9-ns pulse and (f) a negative 9-ns pulse. The results show the streamer length as a function of voltage and position in the reactor. Time dependency is exchanged for voltage dependency in these experiments.

duration there is still little plasma activity. The 5-ns and 9-ns pulse duration results give more information.

The 5-ns results show that the profile shapes scale with the voltage and that the streamer lengths for the positive voltages are slightly larger as compared to the negative voltages, even showing streamer crossing at the end of the reactor (low x-position). The streamer crossing at $x = 0$ for the negative voltages indicate that there is a thick streamer present at the end of the reactor. Therefore, the result that the streamer lengths are smaller for negative voltages are once more likely the result of these thick streamers. Another explanation could be that for lower applied voltages the differences in propagation velocity between positive and negative streamers become visible, but without the time information we are unable to comment on this with the results of our long-exposure measurements.

The results for the 9-ns pulse duration at the highest voltages are comparable with what we already saw in the results of the short-exposure experiments. However, for lower voltages the homogeneity of the streamer coverage becomes worse for the negative voltages (when compared with the positive voltages). At these lower voltages the pulse propagation through the reactor becomes an important factor again (for the streamer coverage) and the results become similar to what we saw in the 2-m reactor for higher voltages.

In Chapter 8 we will relate the streamer profiles to the results of the plasma-processing experiments.

7.5.6 Conclusions 1-m reactor

In the short-exposure experiments on the 1-m reactor we saw in this section that the streamer coverage is more homogeneous than in the 2-m reactor, which indicates that for a shorter reactor the pulse propagation effects become less significant when similar pulses are used. However, the pulse propagation effects still dominate the streamer development and propagation, especially for the shorter 5-ns pulses. Due to the shorter reactor, the voltage at different positions in the reactor remains higher and more constant than in the 2-m reactor and consequently, on average, the streamer lengths and velocities are higher. As a result of the more constant voltage, the streamer width is also more constant. Therefore, from the short-exposure images we can conclude that the reactor volume the streamers propagate through is more homogenous along the reactor (and larger) as compared to the 2-m reactor. However, from the long-exposure experiments we see that for lower applied voltages the streamer coverage is still not homogeneous for a 1-m reactor.

The main conclusion for the pulse-duration experiments is then: a high voltage, a short reactor and a long pulse result in the most homogeneous streamer coverage. We mentioned in the introduction that we want to optimise the streamer coverage such that it is as homogenous as possible without generating secondary streamers. From the results in this section and the preceding section, we can conclude that the closest we can come to this optimal coverage are the 9-ns results in a 1-m reactor. However, even in that situation secondary-streamer effects might occur and this optimal plasma

coverage might not be achievable with these short pulses in a 1-m reactor. A study with (significantly) longer pulses than 9-ns pulses (but with the same rise time) would be needed to study this effect any further.

7.6 Results: rise-time variation

In the previous section, pulse duration, pulse voltage (amplitude and polarity) and reactor length were the main parameters whose effect was studied with the ICCD experiments. In this section we investigate the rise time of the pulses as a parameter.

In the introduction we already mentioned the previous work that was performed on streamer investigation with the rise rate as a parameter. The main conclusion appeared that the streamer propagation velocity is higher when a high rise-rate pulse is applied. An exception occurs when the ionisation cloud becomes large (then the total travel time of the discharge increases), but we showed in the previous sections that no significant-sized inception cloud can be observed in our experiments.

We varied the rise time of the pulses with the method that we described in 6.2.5. We use three different rise times of the 9-ns pulse in this section: 0.4 ns, 2.9 ns and 5.6 ns. Combined with the used (positive) voltages this results in rise rates of around $75 \, \mathrm{kV \cdot ns^{-1}}$, $9 \, \mathrm{kV \cdot ns^{-1}}$ and $5 \, \mathrm{kV \cdot ns^{-1}}$ respectively. For each of these settings we performed short-exposure experiments where we took 20 images at each position and for each camera-delay setting. The exposure times of the images is 1 ns, the camera delay was incremented with steps of 1 ns and the gain of the camera was again 980 V.

7.6.1 ICCD images

Figure 7.25 shows the ICCD images for the three different rise-time experiments, presented in the same way as in the previous section. The results show that there is less plasma when the rise rate decreases. Furthermore, where the streamers initiate immediately for the 0.4-ns rise-time pulse, it takes at least 3 ns longer for the streamers to show for the 5.6-ns rise-time pulse. This delay is due to the longer time it takes for the electric field to increase in the reactor as compared to the shorter rise-time pulses. Therefore it takes longer for the streamers to initiate at a low rise rate and when they do, they initiate at a lower voltage as compared to the streamers generated with higher rise-rate pulses. Furthermore, the gain-setting of the camera was again identical for all the measurements and consequently some early streamer-development effects might not be observed in the images.

Another observation from the ICCD images is that the thick streamers at the end of the reactor only appear for the 0.4-ns rise-time results. This indicates that the voltage at the end of the reactor is higher at that setting as compared to the longer rise-time pulses.
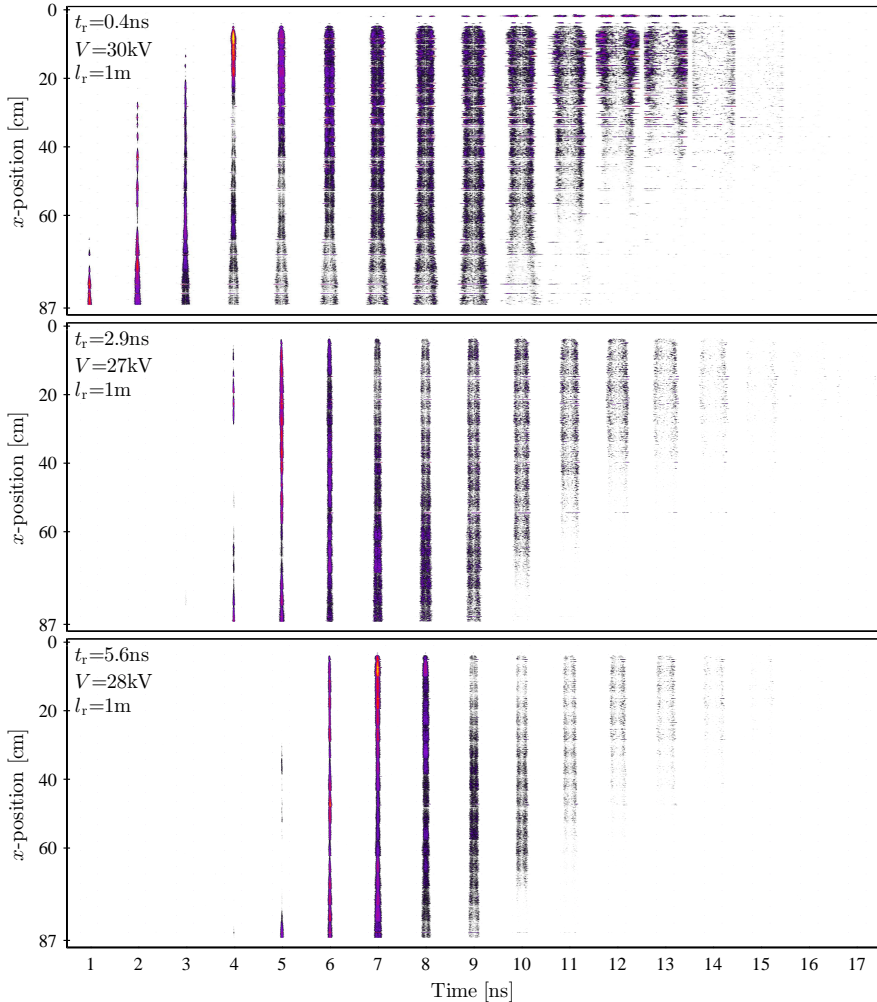
Figure 7.25: Streamer development and propagation in time in the 1-m reactor for a 9-ns positive pulse with three different rise times: 0.4 ns (top), 2.9 ns (middle) and 5.6 ns (bottom). The exposure time is 1 ns for all images and each image is the stitched average of 20 photos at each position.

7.6.2   Streamer length and propagation velocity

Figures 7.26a–c show the streamer-length results of the ICCD images for the three different rise-time pulses. The difference in streamer length is now immediately obvious. The results show significantly shorter streamers when the rise rate decreases, but also that the streamers are longest at the end of the reactor (low x-position) regardless of
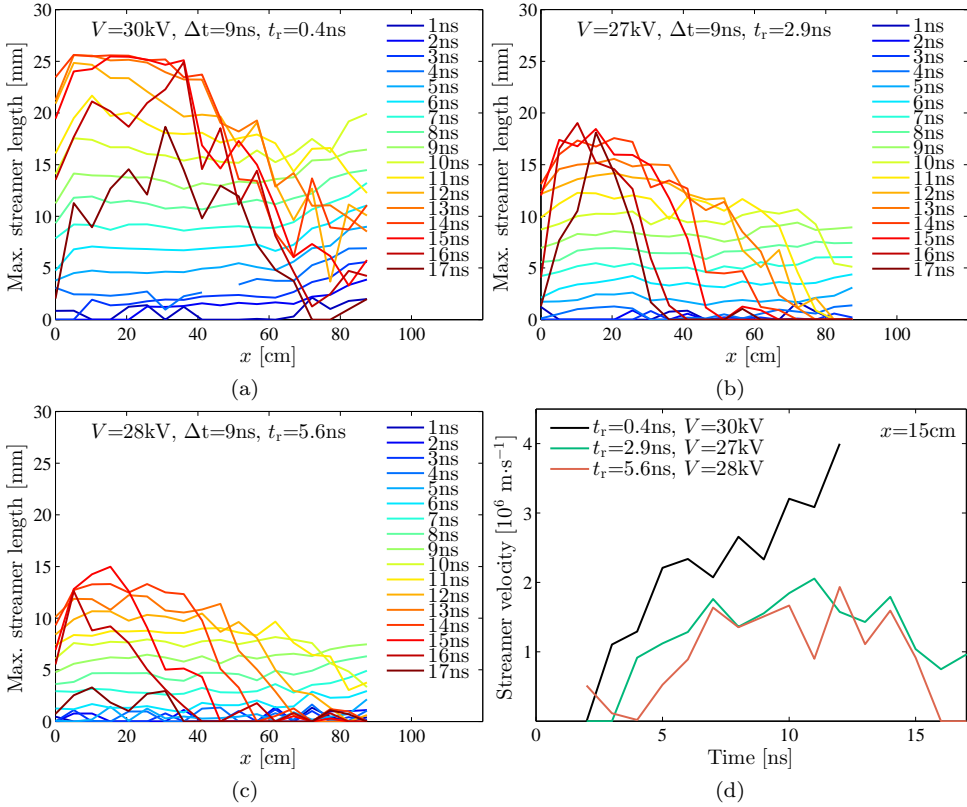
Figure 7.26: A quantitative representation of the maximum streamer lengths (averaged over the results of 20 photos at each position and each time) calculated from the results of Fig. 7.25 for (a) the 0.4-ns rise-time experiments, (b) the 2.9-ns rise-time experiments and (c) the 5.6-ns rise-time experiments. (d) shows the streamer propagation velocities at $x = 15\,\mathrm{cm}$ for the three different rise times.

the rise rate. This indicates that even for the longer rise times the pulse propagation effects through the reactor remain important.

Figure 7.26d shows the velocity at $x = 15\,\mathrm{cm}$ for the three different rise-time pulses. The 0.4-ns rise-time result is much like in the previous section, but the results for the longer rise times are significantly lower because the corresponding streamer lengths were shorter.

Four possible reasons why the velocities are higher for the higher rise-rate pulses are listed below .

- The first reason is that the average applied voltage was slightly lower for the 2.9-ns rise-time (27 kV) and 5.6-ns rise-time (28 kV) pulses as compared to the 0.4-ns rise-time pulses (30 kV) and we (as well as others in literature) already showed

that the streamer propagation velocity is higher for a higher applied voltage. At equal applied voltages the differences between the streamer velocities for the two slowest rise-time settings in Fig. 7.26 would likely be slightly more pronounced.

- The second reason is that the inception voltage for a pulsed corona discharge is higher for a higher rise rate [3]. It takes some time for a discharge to initiate, and therefore when the voltage rises over a long time, the streamers initiate before the complete voltage is applied across the gap [123,151]. For the short rise-time pulses it takes some time for a streamer to initiate as well, but when they do, it will be at a higher voltage as compared to the long rise times. When streamers initiate at a higher voltage, the electric-field enhancement at the streamer head is greater and therefore they propagate faster. Furthermore, it takes much longer for the entire voltage to be across a certain part of the reactor for the 5.6-ns rise-time pulse as compared to the 0.4-ns rise-time pulse. Therefore, it takes much longer before the streamer experiences the full electric field for the longer rise-time pulses.

- A third reason originates from the pulse reflection in the reactor. When the 0.4-ns rise-time pulse reflects at the end of the reactor, it adds to itself and almost doubles in voltage. When the 5.6-ns rise-time pulse reflects at this position, it also adds to itself, but due to the relatively long rise-time the voltage will not double, but will be significantly lower. This can be seen from the SPICE simulation results of Fig. 7.27. From these simulations we can also see that it takes much longer for the complete voltage to be applied to the reactor for the longer rise-time pulses, which we mentioned in the previous point.

- A last possible reason for the higher streamer propagation velocity is that the electron density in the streamers can become higher for the shorter rise-time pulses. The discharge will be homogeneous in its very first stages after applying the electric field. An ionisation cloud can form, but we already showed in the ICCD results that there is no significant-sized cloud visible in our experiments. Therefore this homogeneous first stage of the discharge will be extremely short before it destabilises into streamers. However, in this first stage the electron density can grow to a higher value when the external electric field is applied in a shorter time (as compared to a slower rise-time pulse) [184]. The electron density in the generated streamers will consequently also be higher which means that the conductivity of the streamer is higher. A higher-conductivity channel will then result in a higher field enhancement at the streamer head because the voltage drop across the streamer will be lower.

7.6.3 Streamer width

In the sections on the effects of pulse duration on the streamer development and propagation we saw that the streamer width at a position in the reactor depended on the

Figure 7.27: SPICE simulation results for (a) the 0.4-ns rise-time experiments, (b) the 2.9-ns rise-time experiments and (c) the 5.6-ns rise-time experiments in the 1-m reactor. The figures show the voltage amplitude in the reactor at each position and as a function of time. The results show that the maximum voltage in the reactor for a long rise time is lower and that it is reached after a longer time as compared to a shorter rise time.

applied voltage at that position; when the voltage increased, the streamer width increased. With the streamer-length results and the SPICE simulations we showed three properties of the voltage in the reactor for different rise times:

- the voltage at the end of the reactor is higher than at the beginning of the reactor;
- the overall voltage is higher when the rise rate of the applied pulse is higher;
- for a low rise rate it takes longer for the complete voltage to be applied to a certain point in the reactor.

These properties should be reflected in the calculated streamer widths. Figure 7.28 shows these streamer widths for the three different rise times.

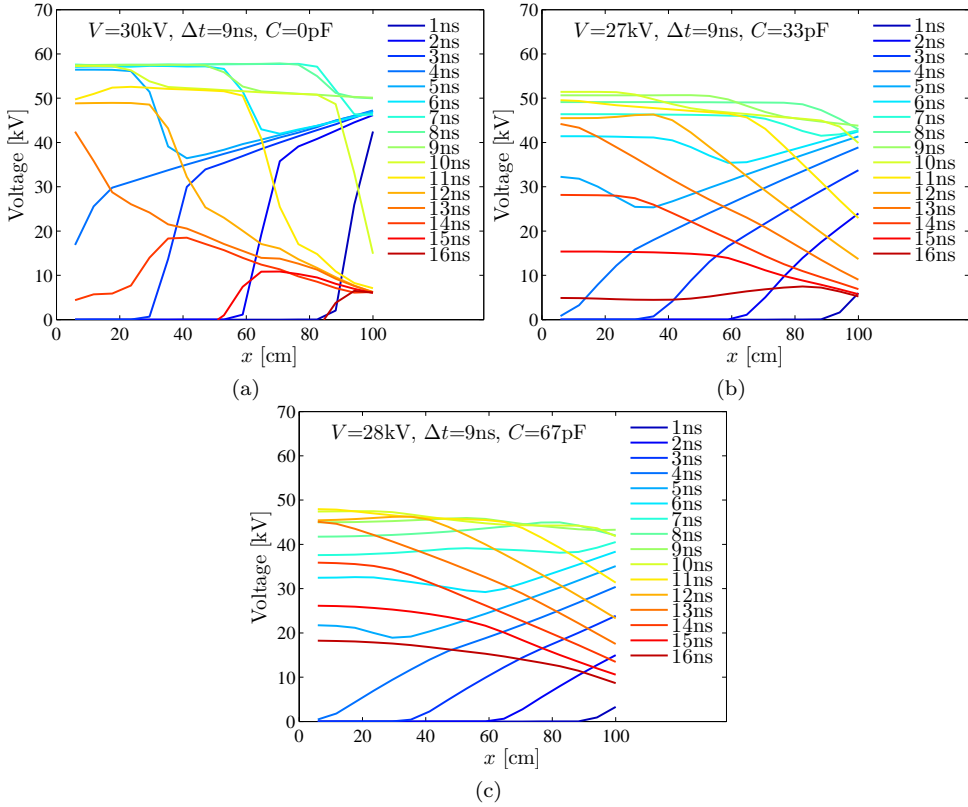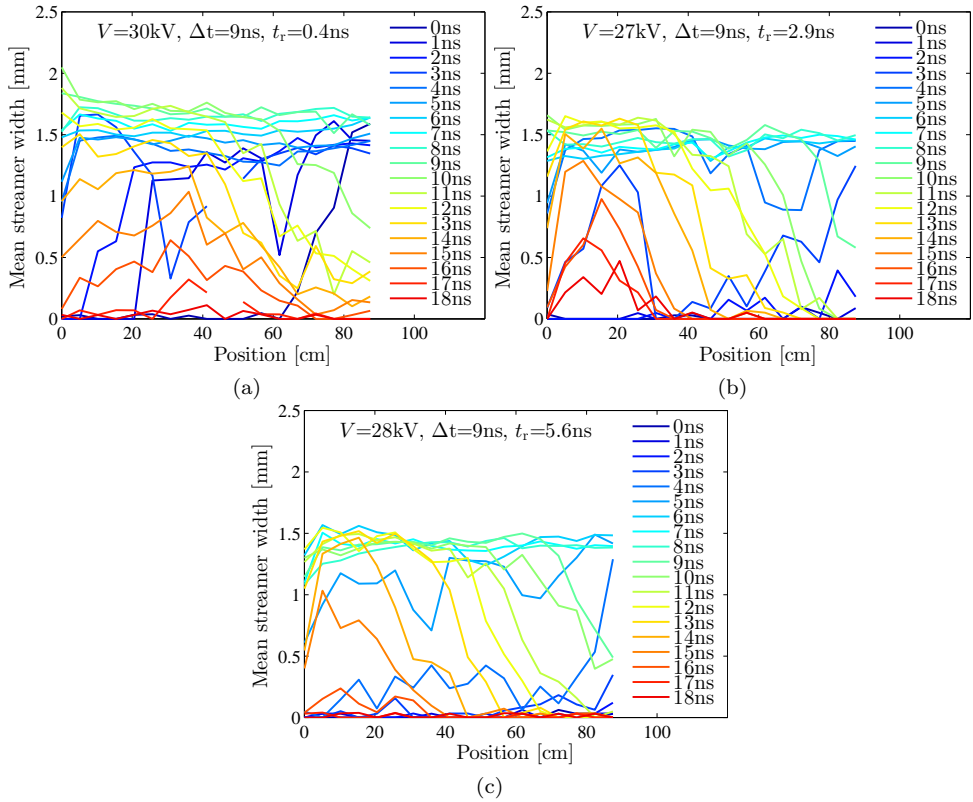Figure 7.28: The streamer width as a function of position and time for (a) the 0.4-ns rise-time experiments, (b) the 2.9-ns rise-time experiments and (c) the 5.6-ns rise-time experiments in the 1-m reactor.

The results agree well with the three stated voltage properties: the streamer width is slightly higher at the end of the reactor (low x-position), is higher for a short rise-time pulse and achieves its maximum at a later time for a longer rise-time pulse. Because the streamers are wider for a longer time when a short-rise-time pulse is used, the volume the streamers propagate through in the reactor is largest for streamers generated with short-rise-time pulses.

7.6.4   Plasma energy

A final parameter that is worthwhile mentioning is the plasma energy. We saw in this section that the streamer lengths are significantly shorter when a long rise-time pulse is used. Consequently the streamer coverage is poor. We measure the plasma energy for different voltages for the three different rise times to investigate whether a lower
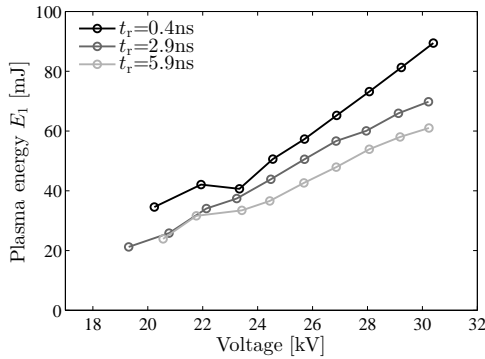
Figure 7.29: The dissipated plasma energy for the three different rise-time pulses as a function of voltage. The results show that a short rise-time results in a higher plasma energy.

streamer coverage also results in a lower plasma energy dissipation. Figure 7.29 shows the results.

The figure shows the dissipated plasma energy in the first pulse (so only E_1 and not $E_1 + E_2$ when we refer to Fig. 6.3) at different voltages. These results were obtained for one voltage setting of the pulse source, but due to the standard deviation on the voltage, we could bin the results to obtain the results in the figure (just as we showed in Fig. 6.8). The results indicate that a shorter rise time also results in a higher energy dissipation of the plasma. However, where the plasma coverage of the 5.6-ns rise-time pulse was around 2 times lower than that of the 0.4-ns rise-time pulse, the respective plasma energy is only between 1.2–1.5 times lower.

In the next chapter we will show what the effects of the variation in rise rate are on various plasma-processing applications and compare them with the results from this chapter.

7.6.5   Conclusions rise time

The results of this section show that streamers generated with a high rise rate are longer than streamers generated with a lower rise rate due to a higher streamer velocity. This higher streamer velocity is the result of a higher voltage at which the streamers initiate at higher rise rates and the overall higher voltage in the reactor due to a larger effect of pulse reflections. Due to the higher voltage the streamers are also slightly wider at high rise rates. At a lower rise rate the streamers reach their maximum width at a later time and remain at this size for a shorter time. All these effects together result in a larger volume the streamers propagate through for short-rise-time pulses as compared to a long-rise-time pulse. It is therefore expected that more radicals are produced at high rise rates. This is an effect which we will investigate in Chapter 8.

7.7   Matching: positive vs. negative streamers revisited

In the chapter on matching our nanosecond pulse source to a coaxial corona-plasma reactor we discovered that, for some experiments, negative pulses match better to the reactor. More specifically, the application of negative pulses results in a lower reactor impedance for the first few nanoseconds. Therefore the initial matching of the negative pulses to the reactor is better than that for positive pulses. We then argued in Section 6.8 that the inception cloud and/or the initial velocity of the streamers might play a role in the initial matching, because other researchers showed that the size of a negative inception cloud can become larger than a positive inception cloud and that the initial velocity of negative streamers is higher than for positive streamers. Both a large inception cloud, as well as a high initial streamer velocity result in a virtually increased inner-conductor diameter and therefore a decreased corona-plasma reactor impedance (thereby improving the matching). We subsequently stated that the ICCD images might confirm or refute our arguments. We estimated a maximum diameter of the inception cloud of 3–7 mm. Unfortunately, the resolution of our images is too low to state with certainty whether there is an inception cloud. We can confirm that if there is an inception cloud, it is smaller than 3–7 mm, because a cloud larger than 2–3 mm should be visible in our images. Furthermore, we have too little detail in the streamer-velocity measurements to confirm or refute that negative streamers have a faster initial velocity.

The calibration of the automated ICCD-camera setup, which correlates the photos to the exact positions on the wire electrode, is such that once the focal distance of the lens is changed to zoom in on the wire electrode, the calibration information is lost. The calibration is a complicated procedure and takes a considerable amount of time [178]. Therefore, it will be left as future work to get a closer look at the wire electrode and confirm or refute the inception-cloud argument and the initial-streamer-velocity argument.

We also saw in Chapter 6 that the total-matching differences between negative and positive pulses was more pronounced for 5-ns pulses (as compared to 9-ns pulses). In addition we showed that negative pulses have a lower ozone yield than positive pulses. With the results of the ICCD images we believe that these effects are caused by the thick streamers at the end of the reactor. They have to consume a significant amount of energy to be able to decrease the voltage at the end of the reactor to explain the streamer-length results for the negative streamers. The thick streamers become significant for 9-ns pulses and therefore the energy consumption of these streamers might decrease the difference in total matching that is caused by initial streamer development effects (of which we still have no confirmed information) on the initial matching: the energy that is consumed by the thick streamers for the negative pulses can be consumed by the main plasma for the positive pulses, since the thick streamers are less pronounced for positive pulses.
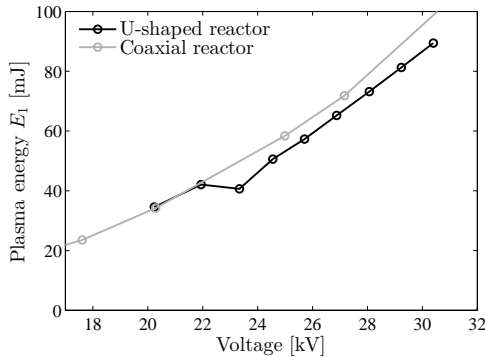
Figure 7.30: The difference in dissipated plasma energy as a function of voltage for the U-shaped reactor that we used in this chapter and the coaxial reactor we used in Chapter 6 and will use in Chapter 8. The results are very similar with a slightly lower plasma energy for the U-shaped reactor.

7.8 Application to the coaxial reactor

Before we present the conclusions of this chapter, we should make an important note on the results of this chapter. All results were obtained in the U-shaped reactor, whereas we used a coaxial reactor for all the matching experiments. Furthermore, in the next chapter we will use the coaxial reactor for all the plasma-processing experiments. It is therefore important to note the differences and similarities between these two reactors.

We already mentioned in the section on the experimental setup that the U-shaped reactor was designed to be as similar as possible as the coaxial reactor. They have the same diameter, the same length and use the same cable coupler and wire-tightening mechanism. This means that the effects of the thick streamers that we observed at the end of the reactor will also be present in the coaxial reactor. Furthermore, an electric-field calculation showed that the electric field inside the U-shaped reactor will be very similar to the electric field in the coaxial reactor [178].

Despite the similarities between the reactors, the streamers will not propagate directly towards the ICCD camera, because there is no counter electrode in that direction. Therefore, it is likely that (slightly) less streamers are generated in the U-shaped reactor and therefore that the dissipated plasma energy is lower. Figure 7.30 shows this dissipated plasma energy for both reactors. The results show that the dissipated plasma energies are very similar for both reactors, with slightly less dissipation for the U-shaped reactor, as we expected.

Because there are so many similarities between the two reactor designs and because the dissipated plasma energies are very similar, we are confident that most of the phenomena observed in this chapter will be similar in the coaxial reactor and that we can therefore reasonably apply the general observations in this chapter to the results we find in Chapter 8.

7.9 Summary and conclusions

In this chapter we investigated the development and propagation of streamers in a wire-cylinder reactor to study the effect of reactor length, pulse duration, pulse amplitude, pulse polarity and pulse rise time on the generated streamers. More specifically we were interested in the coverage of the streamers in the reactor to relate this to the plasma-processing results of the next chapter. We studied the streamers by ICCD imaging with a fully-automated setup with which we were able to image the streamers in the entire reactor as a function of time and position in the reactor. From the images we calculated streamer lengths, streamer propagation velocities and streamer widths. We also developed a SPICE model of the reactor to support the analysis of the streamer propagation results.

The main results of this chapter are listed below.

- The developed SPICE model of the corona-plasma reactor gives insight in the pulse propagation in the reactor and the simulated voltage profiles agree well with the observed streamer lengths.
- The propagation of the high-voltage pulse determines the streamer propagation. As the pulse travels through the reactor, it generates plasma and attenuates and disperses. At the end of the reactor it reflects and adds to itself. Due to this reflection, the voltage at the end of the reactor is higher than in the middle of the reactor. These propagation effects on the local voltage at different positions in the reactor increase for a longer reactor or a shorter pulse.
- Thick streamers are generated at the wire-tightening mechanism of the reactor due to a field-enhancing triple point. These streamers are most intense for a negative polarity pulse and likely consume a significant amount of energy. This results in a lower streamer coverage when we use negative pulses as compared to positive pulses.
- The voltage at a certain position in the reactor determines the streamer properties at that position. The velocities are in the range of 1–4×10^6 m·s^{-1} and are higher for a higher voltage, which results in longer streamers at higher voltages. Furthermore, the streamer widths are in the range 1–2 mm and are larger for a higher voltage. However, the dependency is weak.
- The rise time of the applied pulse has a significant effect on the streamer development and propagation. For a lower rise rate the streamers initiate at a later time, have a lower propagation velocity (and therefore a lower length) and have a lower width. We attributed these effects to several possible reasons, such as the lower voltage in the reactor due to the decreased influence of the pulse reflection, the lower voltage at which the streamers initiate and a lower streamer conductivity.
- The two possible mechanisms that might explain the better initial matching of the negative pulses that we saw in Chapter 6 — the inception cloud size and the initial streamer velocity — could not be observed from the results of this chapter because the resolution of the images was too low. However, the thick

streamers that originate at the end of the reactor might explain why the difference in matching between positive and negative pulses decreases for longer pulses.

- Even though the reactor we used in this chapter is U-shaped (for imaging purposes), the dimensions are the same as the coaxial reactor we used in Chapter 6 and will use in Chapter8. Therefore, the electric field in a large part of the reactor will be similar for both reactors and we showed that the dissipated plasma energy is only slightly lower in the U-shaped reactor. Therefore, we believe we can reasonably apply the observations of this chapter to the results we find in Chapter 8.

Eight

Plasma Processing

Abstract

In this chapter we applied our nanosecond pulse technology to three plasma processes: ozone generation, NO removal, and CO_2 conversion.

For ozone generation, secondary-streamer effects appear to have a slight influence on the ozone yield: if the pulse duration increases and/or the voltage increases in such a way that streamers can start to cross the gap in the reactor (and therefore the plasma-volume expansion decreases and secondary-streamer effects can appear), the ozone yields decrease. Furthermore, negative pulses result in a lower ozone yield, which could be explained by the effect of the thick streamers at the end of the reactor.

For NO removal, we see a similar effect of pulse duration and applied voltage as for the ozone generation, but the effect of the pulse duration is slightly different: long pulses result in the highest NO-removal yield. However, the NO-removal process is fundamentally different: besides removing NO, the plasma also produces NO and this production is more pronounced in the primary-streamer phase, which is why the pulse polarity has almost no influence on the NO-removal yield (only on the by-product formation).

The rise time of the pulses has a much more significant effect on ozone generation and NO removal than the pulse duration: a long rise time results in a lower enhanced electric field at the streamer heads, which consequently reduces the production of radicals required for ozone generation and NO removal, and decreases the plasma volume. Consequently, the resulting ozone yields and NO-removal yields are lower.

Finally, we show results of experiments in a CO_2 plasma, which is significantly different from the plasma in synthetic air with respect to matching and yields; the results show that we can obtain energy efficiencies of CO_2 conversion which are low and comparable with other techniques.

The main conclusions are that the plasma generated with our nanosecond pulses is very efficient for ozone generation and NO removal, but that other technologies might be more suitable for CO_2 conversion.

8.1   Introduction

The main part of this thesis describes the nanosecond pulse technology and how it interacts with the plasma (matching and streamer propagation). In this chapter we apply the nanosecond pulse technology to air purification.

Air purification is a technology that has been extensively studied for many kinds of non-thermal plasma — such as dielectric barrier discharges (DBDs), corona streamer plasmas, gliding arc discharges, etc. — and many kinds of air-purification applications [1]. In fact, the studies would be much to numerous to list them all in this introduction. What this shows is that the topic is actively researched, but also that no final solution or an optimal technology has been found for all applications. One of the main underlying reasons is that not each air-purification application benefits from the same type of plasma conditions. For example, naphthalene removal (a fuel-gas tar) benefits from a high process temperature [26], whereas ozone production decreases at high temperatures [129, 131].

An obvious choice to make for us in this thesis is: to which application do we apply our nanosecond pulse technology? Some of the classical air-purification processes are the production of ozone [28, 119, 131, 132, 185] and the removal/conversion of nitrogen oxides (NO_x) [12, 27, 29, 31, 117, 185–187], sulfur oxides (SO_x) [29, 34, 188, 189], volatile organic compounds (VOCs) [21, 190–192], tar [26, 193], odour [194–196], particulate matter (PM) [29, 196] and biological particles [196–200]. Recently, CO_2 conversion has become a hot topic as well due to the implications of CO_2 as a greenhouse gas and the possibility to convert CO_2 to CO as an ingredient to produce synthesis gas [201, 202]. With our nanosecond pulse technology we will investigate some of the mentioned air-purification processes to verify the performance of the technology and to better understand the involved mechanisms.

Of all the plasma processes, ozone generation and NO_x removal/conversion are most often used by researchers as a monitor for their plasma performance. For this reason we chose ozone production and NO removal as the main plasma processes to apply our nanosecond pulse technology to. As a third process, we measure CO production from CO_2.

8.1.1   Chapter organisation

After this introduction, we will describe the three plasma processes in the next section, explaining the relevance of the plasma processes and some of the important reaction pathways that are involved in each process. Then, Section 8.3 describes the experimental setup that we used in this chapter, where the most important new additions to the setup are a conventional pulse source with a longer pulse duration and new gas diagnostics. In the subsequent three sections we then show the results and the discussion of these results for each of the three plasma processes that we chose. Finally, we present the conclusions.

8.2 Plasma processes

8.2.1 Ozone generation

Strictly speaking, ozone generation is not purely an air-purification process, as its main use is cleaning polluted water [203]. However, the ozone in this cleaning process is mainly produced with non-thermal plasma. Especially DBD-plasmas are often used because of their ease of construction and design [2]. Nonetheless, ozone production remains one of the favourite processes to measure the performance of a plasma, because it is an indirect measure for oxygen radical production [5]. It is for this reason that we chose ozone production as the first plasma process.

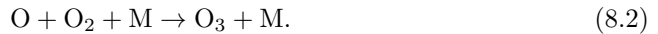To generate ozone with a plasma in pure oxygen, an oxygen molecule first has to be dissociated by electron impact (at an energy cost ΔW).

$$O_2 + e \rightarrow O + O + e \qquad \Delta W = 6.0\,eV \tag{8.1}$$
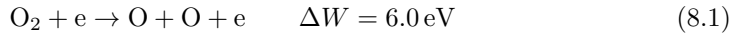
The oxygen radicals then react with oxygen and a third collision partner (M) to form ozone:

$$O + O_2 + M \rightarrow O_3 + M. \tag{8.2}$$

When the feeding gas is not pure oxygen, but synthetic air, part of the available energetic electrons that are generated by the plasma will be used for excitation and dissociation of nitrogen.

$$N_2 + e \rightarrow N_2^* + e \qquad \Delta W = 6.2\,eV \tag{8.3}$$

$$N_2 + e \rightarrow N + N + e \qquad \Delta W = \sim 9\,eV \tag{8.4}$$
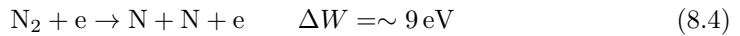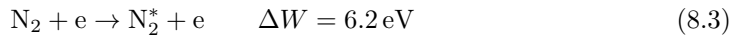
Some of the excited nitrogen species can again form oxygen radicals, but (part of) the nitrogen radicals will result in the formation of by-products that do not contribute to ozone formation or even lead to the destruction of ozone. A very extensive overview of ozone generation is given in [18, Section 2.5].

The yields of ozone generation in air that researchers report are generally in the range of 15–150 g·kWh^{-1} [28,128,129,132,185] for different types of plasmas and reactor configurations. Wang *et al.* report yields as high as 239 g·kWh^{-1*} with their nanosecond pulse source and show in an extensive map (which we showed in Fig. 1.4d) the comparisons between different discharge methods and the very good results of nanosecond pulsed discharges [36]. In Chapter 6 we showed that the ozone yield with our nanosecond pulse source and our corona-plasma reactor can reach 170–190 g·kWh^{-1}, indicating that we obtain very high ozone yields as well.

8.2.2 NO removal

The release of NO$_x$ into the environment due to the combustion of fossil fuels is still a major environmental problem and is strictly controlled by rules and regulations.
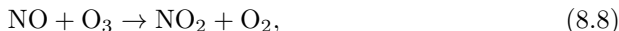
---

*They calculate their ozone yields (and NO removal yields) at a temperature of 0° C and therefore overestimate the yields by almost 10 percent. However, the results are still excellent.

Consequently, the possibility of non-thermal plasmas to reduce the amount of NO_x makes it one of the most studied air-purification applications in the field of plasma processing. It is therefore an important application to apply our nanosecond pulse technology to and to compare our results with that of other researchers.

Just as with ozone production, the first step in the NO-removal process is the generation of radicals by the plasma. The experiments are all performed in synthetic air, so the plasma generates oxygen radicals and excited nitrogen species and radicals. The interaction of these species with NO and the associated by-products are complex and we only mention some of the important reaction pathways here [129, 204, 205].

When NO is present in the gas, the reactions that convert NO to other species in the presence of the plasma are:

$$NO + O + M \rightarrow NO_2 + M, \tag{8.5}$$

$$NO + N \rightarrow N_2 + O, \tag{8.6}$$

$$2NO + O_2 \rightarrow 2NO_2, \tag{8.7}$$

$$NO + O_3 \rightarrow NO_2 + O_2, \tag{8.8}$$

where the ozone in (8.8) is formed through (8.2). During this period the concentration of NO_2 increases as the concentration of NO decreases. At the same time, by-products N_2O and N_2O_5 are formed from NO_2 through

$$NO_2 + N \rightarrow N_2O, \tag{8.9}$$

$$NO_2 + O_3 \rightarrow NO_3 + O_2, \tag{8.10}$$

$$NO_2 + NO_3 + M \rightarrow N_2O_5 + M. \tag{8.11}$$

Consequently, once NO is removed, O_3, NO_2, N_2O and N_2O_5 will be the main by-products. The by-product NO_2 can be further removed from the gas by increasing the energy density of the plasma considerably. However, this increases the formation of the other by-products. Therefore, a corona plasma alone is not enough to remove all pollutants from an air stream.

In a real NO-removal application the air will not be dry synthetic air (as we use), but will contain significant amounts of H_2O. In the presence of H_2O, the N_2O_5 and NO_2 will be converted to HNO_3 through

$$H_2O + N_2O_5 \rightarrow 2HNO_3, \tag{8.12}$$

$$NO_2 + OH + M \rightarrow HNO_3 + M. \tag{8.13}$$

The formed HNO_3 can then be removed by subsequent water-scrubbing technology or by an additional chemical reactor [205]. Further reduction of the by-products could be realised by in-plasma or post-plasma catalysis [206–208]. In this chapter we will show NO concentrations, as well as concentrations of the by-products, but mainly focus on the NO-removal efficiency.

Unfortunately, besides converting NO to other compounds, the plasma also generates NO. Two important reactions that produce new NO with oxygen and nitrogen

radicals are

$$N + O \rightarrow NO, \tag{8.14}$$
$$NO_2 + O \rightarrow NO + O_2. \tag{8.15}$$

As we mentioned earlier, NO_x reduction is perhaps one of the most studied air-purification applications. Consequently, the reported removal efficiencies are very diverse. Some examples that are worth mentioning are that of Matsumoto *et al.* [8] and Van Veldhuizen *et al.* [117]. Matsumoto *et al.* use the same type of 2-ns and 5-ns triaxial Blumlein source as used by Wang *et al.* (who reported the very high ozone yields) and reported NO-removal efficiencies of up to $1.2 \, \text{mol·kWh}^{-1}$ (equal to a cost of 31 eV per NO molecule) at 50 percent NO removal with an initial NO concentration of 200 ppm (again overestimating the yield). Van Veldhuizen *et al.* performed NO-removal experiments (300 ppm initial NO concentration) at elevated gas temperatures and achieved 50 percent NO removal at a cost of 20 eV per NO molecule (equal to $1.8 \, \text{mol·kWh}^{-1}$). While these results are very good, most studies report much lower NO-removal efficiencies.

8.2.3 CO_2 conversion

With the depletion of the world's fossil fuel reserves, alternative energy resources are in full development. Renewable energy sources such as solar power and wind power are likely candidates for future energy generation, but are intermittent. Therefore, an energy storage method is needed to make these renewable energy sources more useful. One of the proposed storage methods is the conversion of CO_2 into CO for the production of synthesis gas during periods of energy surplus from the renewable energy sources [201, 202]. This synthesis gas can then be used for energy generation when renewable energy sources are not producing energy. Consequently, by converting CO_2 to CO, renewable energy sources become more viable and emissions of the greenhouse gas CO_2 are reduced.

One of the attractive methods of converting CO_2 into CO is by using a non-thermal plasma, because a plasma can be switched on and off quickly and can therefore react fast to fluctuations in the energy output of renewable energy sources [202]. At low pressures, microwave plasmas have shown very good energy efficiencies for CO_2 dissociation [209, 210]. The reason this method works so well is that the most energy efficient way to dissociate CO_2 is through vibrational excitation, for which only very low electron energies (1–2 eV) are required [202, 210]. However, in a more practical approach the plasma would have to be operated at atmospheric pressure, which motivates studies on CO_2 dissociation with atmospheric DBD plasmas [211–216]. The use of a DBD plasma offers an economic method to generate a non-thermal plasma, but energy efficiencies are often below 10 percent and not all the mechanisms of CO_2 dissociation in DBDs are fully understood [211].
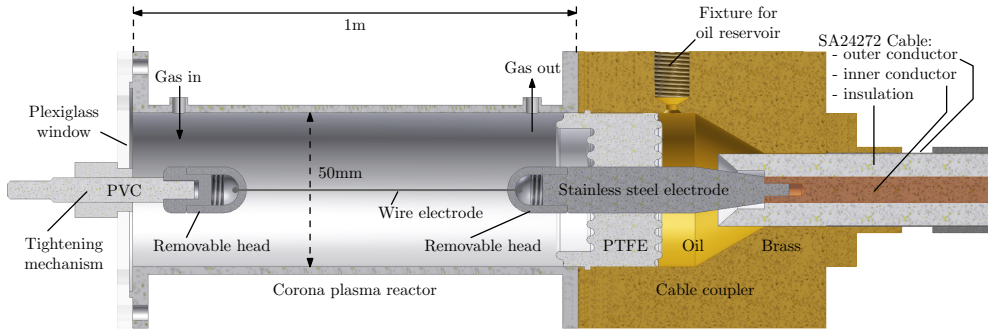
Figure 8.1: The corona-plasma reactor (the length of the reactor has been shortened for display purposes). For the plasma-processing experiments we use the gas ports on the reactor indicated as 'Gas in' and 'Gas out'.

The CO_2 dissociation reactions requiring the lowest amount of energy are

$$CO_2 \rightarrow CO + O, \tag{8.16}$$

$$CO_2 + O \rightarrow CO + O_2, \tag{8.17}$$

where in both reactions CO_2 is thermally dissociated. The net result of these reactions is two CO molecules that cost $2.9\,\mathrm{eV}$ (on average) each to produce. However, these reactions require very high temperatures [202]. In a DBD plasma and a pulsed corona plasma CO_2 will be mainly excited through electron-impact collisions, upon which the excited CO_2 will dissociate. This reaction to CO costs considerably more energy [211, 217]. Therefore, we suspect that the plasma generated with our nanosecond pulses will not be very energy efficient. Nevertheless, it is worthwhile to verify this experimentally.

8.3   Experimental setup

In this section we describe the experimental setup that we used for the plasma-processing experiments. We used two different pulse sources: the nanosecond pulse source developed in this thesis and a more conventional (nanosecond) pulse source. Furthermore we used two types of quantitative gas diagnostics: UV-absorption spectrometry for ozone measurements and FT-IR (Fourier Transform Infrared) absorption spectrometry for the NO_x experiments and the CO_2 experiments.

8.3.1   Corona-plasma reactor

The corona-plasma reactor that we used in all the experiments of this chapter is the 1-m reactor (with the 0.5-mm wire electrode) that we introduced in Chapter 6. We show it here again in Fig. 8.1.
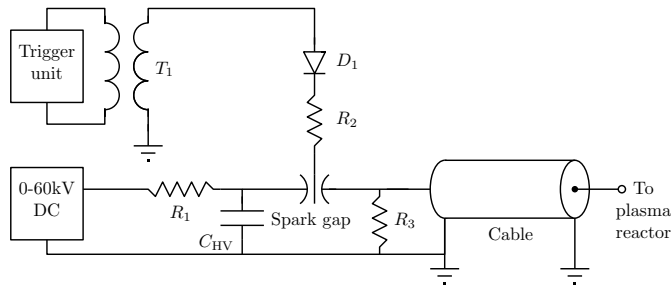
Figure 8.2: The schematic representation of the conventional nanosecond pulse source. It is a pulse source in which a charged capacitor is discharged into a cable by a (triggered) spark gap.

8.3.2 Nanosecond pulse source

For the majority of the experiments in this chapter we used the nanosecond pulse source that we developed in Chapter 2 and Chapter 3. The SA24272 cable connecting the pulse source to the reactor is the same 28-m cable that we used in Chapter 6 and 7. The long cable attenuates and disperses the pulse slightly and thereby increases the rise time from around 200 ps to 400 ps. However, to be able to compare the results of Chapter 6 and Chapter 7 with the results of the current chapter, we kept the cable length the same.

8.3.3 Conventional pulse source

Figure 8.2 shows a more conventional pulse source. We used it for some of the experiments in this chapter to be able to compare the plasma-processing results obtained with our the nanosecond pulse source with results of a slower pulse source.

The principle of operation of the conventional nanosecond pulse source is relatively straightforward. A high-voltage DC source charges capacitor C_{HV} (600 pF) via current-limiting resistor R_1 (6 MΩ) in less than 10 ms. The spark gap (a multiple-gap spark gap [218]) is triggered by a 30-kV trigger pulse from a separate circuit. The trigger pulse has a rise time of several microseconds and is applied to an electrode in one of the gaps of the multiple-gap spark gap. Resistor R_2 protects the trigger circuit from transient voltages. When the spark gap switches, C_{HV} is discharged into the 50-Ω cable and the resulting pulse is applied to the reactor. Resistor R_3 (250 Ω) consumes a small amount of energy during this phase. The main purposes of R_3 is to dissipate the remaining energy in the circuit once the plasma quenches. The output polarity of the pulses is determined by the DC source and is always positive for our experiments.

The cable at the output of the conventional nanosecond pulse source is a 50-Ω RG218 cable of 3 m which has a different diameter than the SA24272 cable. Furthermore, a coupler is connected at the end of the cable to connect the pulse source to a high-temperature setup that we will not discuss in this thesis. Integrated in this
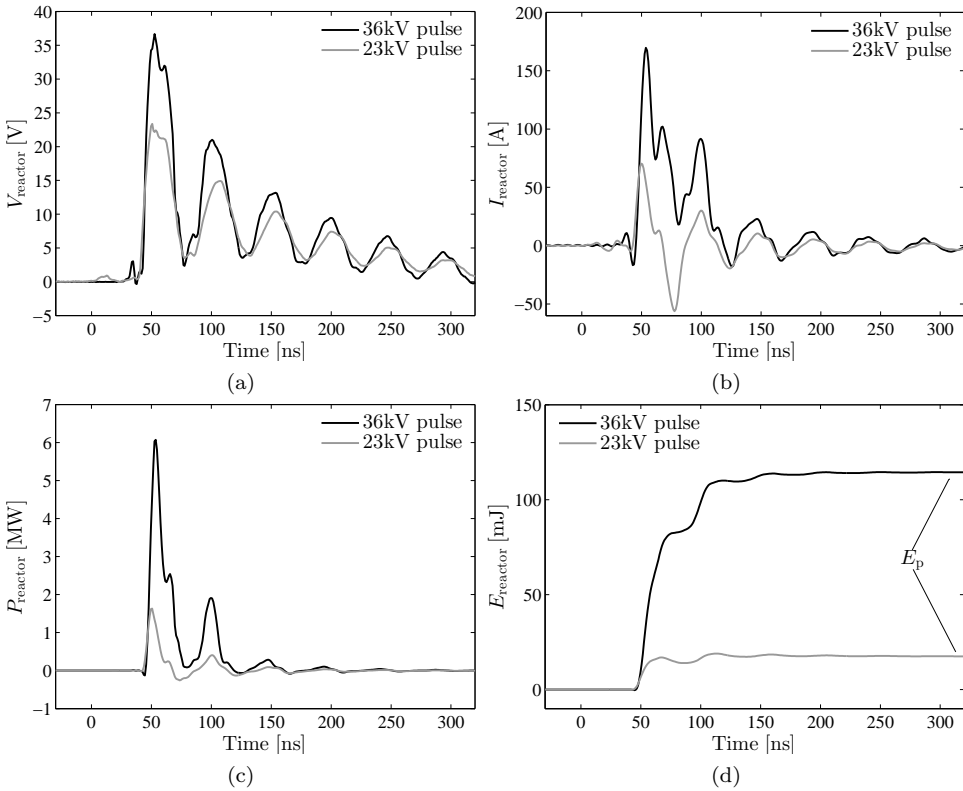
Figure 8.3: Example waveforms measured at the beginning of the corona-plasma reactor for two different output voltages of the conventional nanosecond pulse source. The figure shows (a) the reactor voltage, (b) the reactor current, (c) the reactor power (calculated from the voltage and current) and (d) the reactor energy (calculated from the power).

coupler are a capacitive voltage sensor and a Rogowski current sensor. Together with passive integrators connected at the wall of the EMC cabinet these sensors form a D-I (Differentiating-Integrating) system [32]. To conveniently make use of these sensors we designed an extension for this coupler to connect our reactor to the conventional nanosecond pulse source with a minimum of impedance mismatch. We then measured the voltage and current for all the experiments with this pulse source with the existing D-I system.

Figure 8.3 shows examples of the voltage, current, power and energy measured with these sensors (V_{reactor}, I_{reactor}, P_{reactor} and E_{reactor} respectively) for two different voltage amplitudes. The small signal in front of the main pulse (at 10 ns for the 23-kV pulse and at 35 ns for the 36-kV pulse) is due to the trigger signal of the spark gap. The rise time of the pulses is 5.7 ns, which is very close to the rise time of 5.6 ns that the pulses from our nanosecond pulse source have when we use a 67-pF capacitor in the

reactor. However, the pulse duration of the pulses from the conventional pulse source is 22 ns. Furthermore, the reflections from the reactor are reapplied to the reactor much faster than in our nanosecond pulse source due to the short length of the RG218 cable.

The power that is transferred to the corona reactor P_{reactor} is calculated from the measured reactor current and reactor voltage according to

$$P_{\text{reactor}}(t) = I_{\text{reactor}}(t) V_{\text{reactor}}(t). \tag{8.18}$$

The energy that is transferred into the corona reactor E_{r} is then calculated as

$$E_{\text{reactor}}(t) = \int_0^t P_{\text{reactor}}(\tau) \, d\tau. \tag{8.19}$$

From the energy and power measurement we see that most energy is dissipated by the plasma during the first pulse. During the first reflection (at around 80 ns) another significant amount of energy is dissipated by the plasma. However, from the second reflection onward the energy dissipated by the plasma becomes almost zero. This development of energy dissipation during the applied pulses (first pulse and reflections) is very similar to when we use the nanosecond pulse source (see Chapter 6). The energy that we use for the calculations of yields in this chapter for the conventional nanosecond pulse source is the end value of the energy E_{p} (indicated in Fig. 8.3d).

8.3.4 UV-absorption spectrometry

In this chapter we investigate three plasma processes: ozone generation, NO removal and CO_2 conversion. In all of these processes, ozone is formed. In the last two processes we measure the ozone with the FT-IR-method described in the next section. However, when we generate ozone in synthetic air (the first plasma process) we measure ozone with the UV-absorption-spectrometry method that we used in Chapter 6 and described in Section 6.2.6. Figure 8.4 shows the experimental setup for this process when we use the nanosecond pulse source. It is the same as Fig. 6.7.

8.3.5 FT-IR absorption spectrometry

In our experiments on NO removal and CO_2 conversion we use FT-IR (Fourier Transform Infrared) absorption spectrometry to measure the significant compounds in these processes [219]. Figure 8.5 shows the total experimental setup for these measurements. The nanosecond pulse source setup is the same as for the ozone measurements, but we exchanged the UV-spectrometer setup for the FT-IR spectrometer setup. This setup consists of a Bruker Tensor 27 FT-IR Spectrometer (with a MCT 318/Z detector) in its own EMC cabinet. It measures the FT-IR spectra in the exhaust of the reactor in a 20-cm path cell.

Another addition to the setup is a Testo 350 XL flue-gas analyser. This system samples the gas at the inlet of the reactor to determine input NO and NO_2 concentrations. It is only used for calibration and to determine the initial concentration of NO in the gas supply and is turned off during plasma operation.
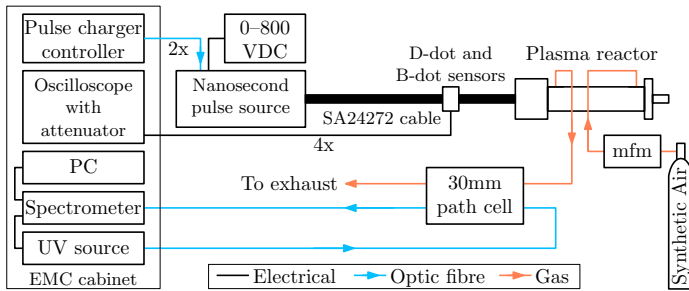
Figure 8.4: The total experimental setup for the ozone measurements. In the gas outlet of the reactor a 30-mm path cell is used for the UV spectrometer measurements to measure ozone concentrations. It is the same setup that was used in Chapter 6.
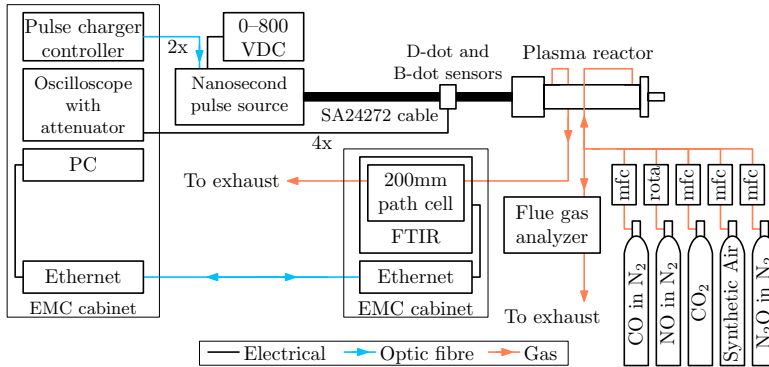
Figure 8.5: The total experimental setup for the NO-removal experiments and the CO_2-conversion experiments. The nanosecond pulse source setup, the electrical diagnostics and the reactor are the same as in the ozone measurements. The UV-spectrometer is replaced by a FT-IR system which consists of a FT-IR spectrometer with a 200-mm long gas cell which is optically connected to a PC. The FT-IR setup is placed in its own EMC cabinet. Additionally, a flue gas analyser is added for NO-calibration and NO_2-calibration measurements.

The gas supply has been expanded substantially compared to the ozone setup. The gas cylinders with CO (10000 ppm) in N_2 and N_2O (10000 ppm) in N_2 are only used for calibration and can be added to the gas supply with mass-flow controllers ('mfc' in the figure). The gas cylinder with NO (10000 ppm) in N_2 is used to supply the initial concentration of NO to synthetic air in all the NO-removal experiments and is added with a rotameter ('rota'). Furthermore, synthetic air and CO_2 are the bulk gasses during the NO-removal experiments and the CO_2-conversion experiments respectively.

FT-IR spectra

The relevant compounds we measure for the NO-removal experiments are: NO, NO_2, N_2O, O_3, N_2O_5 and HNO_3. Figure 8.6 shows these compounds for a plasma-off experiment (Fig. 8.6a) and a plasma-on measurement (Fig. 8.6b). The relevant compound we measure for the CO_2-conversion experiments are: CO and O_3. Figure 8.6c shows these compounds for a plasma-on measurement.

The list below gives the spectral ranges we used to determine the concentrations of the different compounds.

- **NO** This is the most important compound for the NO-removal experiments. It has a strong absorbance in the range 1790–1960 cm^{-1} [220]. However, due to a strong presence of N_2O_5 in plasma-on conditions (compare Fig. 8.6a with Fig. 8.6b) we only use the range 1880–1960 cm^{-1} for the NO measurements.
- **NO_2** This compound has a strong absorbance in the range 1560–1655 cm^{-1}, which we will use for the NO_2 measurements.
- **N_2O** This compound has a strong absorbance in the range 2170–2270 cm^{-1} [220], which we will use for the NO_2 measurements.
- **O_3** Ozone is formed in both the NO-removal experiments and the CO_2-conversion experiments. It has the strongest absorbance in the range 970–1080 cm^{-1} [220], which we will use for the O_3 measurements.
- **N_2O_5** The spectra for N_2O_5 were taken from the data of Hisatsune *et al.* who first extensively measured these spectra [221]. Later, it was discovered by Lovejoy *et al.* and Cantrell *et al.* that part of the spectra attributed to N_2O_5 had overlap with HNO_3 [222, 223]. These areas are coloured light gray in Fig. 8.6b. Calibration of N_2O_5 is very difficult and we did not attempt it. Therefore we only present qualitative data on N_2O_5 in this chapter. We use the peak at 750 cm^{-1} to obtain the N_2O_5 data, because it has the highest absorbance.
- **HNO_3** HNO_3 absorbance is highest at the peak at 1325 cm^{-1}, however we first need to subtract the N_2O_5 peak from the HNO_3 peak [223]. Just as with N_2O_5, we did not attempt a calibration of HNO_3 and only present qualitative data in this chapter.
- **CO** This is the most important compound for the CO_2-conversion experiments. We will use the absorbance in the range 2050–2240 cm^{-1} [220].
- **CO_2** This compound has an extremely high absorbance and is always saturated for the CO_2-conversion measurements. We compensate for CO_2 in the software.
- **H_2O** Water has (among others) a very strong absorbance in the range 1250–2175 cm^{-1} [220] and will always be present. We compensate for it in the software to be able to measure NO and NO_2.

Calibration

We used three types of calibration to determine the linearity and the calibration factors for the relevant compounds of this chapter.
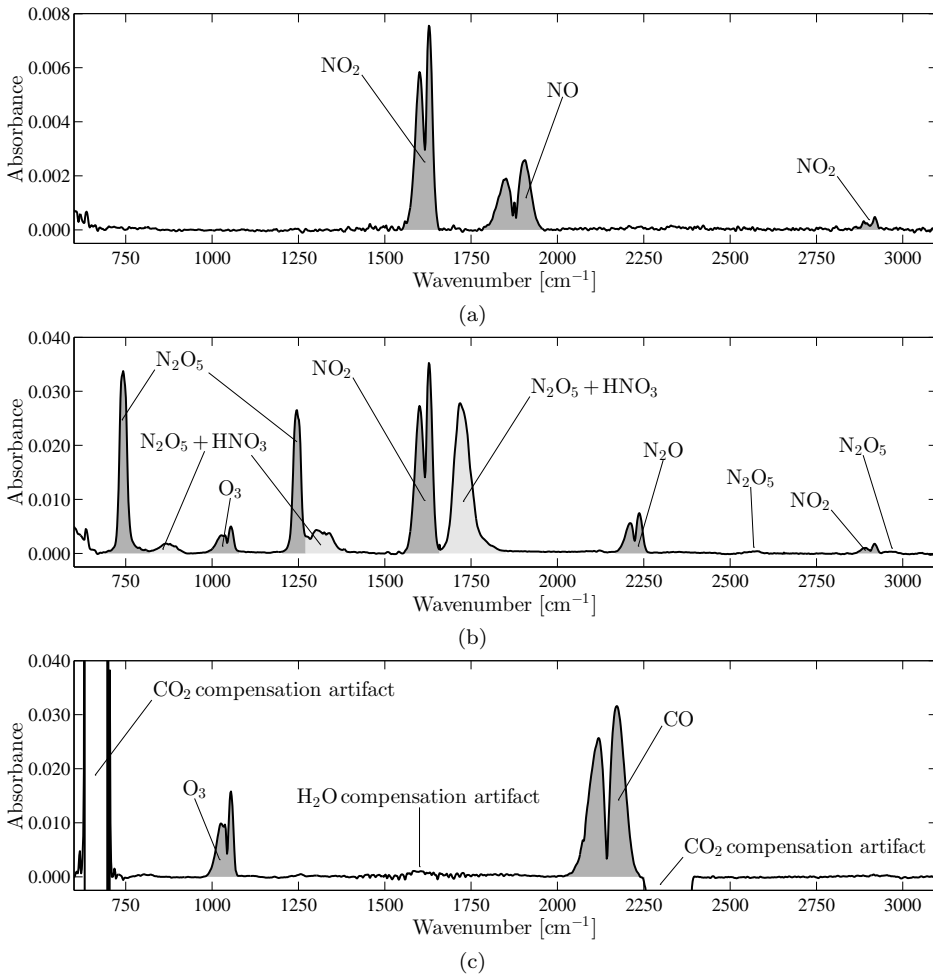
Figure 8.6: Examples of FT-IR spectra measured with the FT-IR spectrometer for (a) NO and NO_2 for plasma-off measurements during the NO-removal experiments, (b) NO, NO_2, N_2O_5, N_2O, HNO_3 and O_3 for plasma-on measurements at a high energy density (all NO is converted) during the NO-removal experiments and (c) CO and O_3 for plasma-on measurements during the CO_2-conversion experiments. Note that the Absorbance-axis has a different scale for (a).

The first calibration method is to dilute a gas with known gas composition to different concentrations of a compound. By plotting the absorbance area of the FT-IR measurements versus the different concentrations, a calibration curve can be plotted from which the calibration factor can be obtained. Also, when the concentration of the compound increases too much, the curve will not be linear anymore. From this point we can obtain the linear range of the measurement. We used this calibration method

for CO (by using a gas cylinder with $10000\,\mathrm{ppm}$ of CO in nitrogen) and N_2O (by using a gas cylinder with $10000\,\mathrm{ppm}$ of N_2O in nitrogen).

The second calibration method is similar to the first method and was used for NO and NO_2. However, no mass-flow controller was available for corrosive gasses. Therefore we diluted the flow of a 1 percent-NO gas cylinder ($10000\,\mathrm{ppm}$ NO in nitrogen) with synthetic air and measured the NO and NO_2 concentrations with the calibrated Testo gas analyser. By changing the concentration of NO and NO_2 we were again able to plot a calibration curve.

The last calibration method is used for O_3 and uses the UV-absorption measurements to calibrate the FT-IR spectrometer.

8.3.6 Yields

Here we give the definitions that we use for the yields of the different plasma processes of this chapter.

Ozone production

The ozone-yield calculation we use for the experiments with the nanosecond pulse source was already presented in Chapter 6. We restate it here:

$$G_{O_3} = \frac{C_{O_3} \times 48 \times 3.6}{V_m \varepsilon}, \tag{8.20}$$

where G_{O_3} is the ozone yield (in $g\cdot kWh^{-1}$), C_{O_3} is the ozone production (in ppm), V_m is the molar volume ($24.5\,\mathrm{L\cdot mole^{-1}}$ at room temperature and atmospheric pressure) and ε is the energy density which is defined as

$$\varepsilon = \frac{f_{rr}(E_1 + E_2) \times 60}{F}, \tag{8.21}$$

where $E_1 + E_2$ is the total dissipated energy by the plasma (in J), F is the gas flow (in $L\cdot min^{-1}$) and f_{rr} is the repetition rate of the pulse source (in Hz).

For the conventional pulse source we use the same calculation, but replace $E_1 + E_2$ with E_p (see Fig. 8.3d).

NO removal

We calculate the yield of the NO removal in the same way as the ozone-production yield, but without converting the amount of mole to grams. Therefore we obtain the NO-removal yield G_{NO} (in $mol\cdot kWh^{-1}$) with

$$G_{NO} = \frac{C_{\Delta NO} \times 3.6}{V_m \varepsilon}, \tag{8.22}$$

where $C_{\Delta NO}$ is the amount of removed NO (in ppm). For the conventional pulse source we replace $E_1 + E_2$ with E_p in the calculation of the energy density.

Alternatively, we can define the energy cost W_{NO} (in eV per NO molecule removed) that is often used in literature as

$$W_{NO} = \frac{V_m \varepsilon \times 37.3}{C_{\Delta NO} \times 3.6} = \frac{37.3}{G_{NO}}. \tag{8.23}$$

CO_2 conversion

The main result of the CO_2-conversion experiments is the production of CO. Therefore, the yield discussed in those experiments will be the CO-production yield, or CO yield. We define this CO yield G_{CO} (in mol·kWh^{-1}) in the same way as the NO-removal yield as

$$G_{CO} = \frac{C_{CO} \times 3.6}{V_m \varepsilon}, \tag{8.24}$$

where C_{CO} is the amount of produced CO (in ppm). For the conventional pulse source we replace $E_1 + E_2$ with E_p in the calculation of the energy density.

In the same way we define the energy cost W_{CO} (in eV per CO molecule produced) as

$$W_{CO} = \frac{V_m \varepsilon \times 37.3}{C_{CO} \times 3.6} = \frac{37.3}{G_{CO}}. \tag{8.25}$$

8.4   Ozone production

In this section we describe the experiments of the first plasma-processing application: ozone processing.

8.4.1   Results from Chapter 6

The results of Chapter 6 showed that

- the ozone yield decreases with the energy density;
- the ozone yield slightly increases with the applied voltage at some settings;
- the ozone yield is higher for positive applied voltages;
- the pulse duration has no significant effect on the ozone yield;
- the ozone yield decreases when the rise time of the applied pulses increases.

The effect that a higher energy density decreases the ozone yield was also reported in [8, 28, 36, 129, 131, 136]. This effect is called *discharge poisoning* and happens when ozone is generated in air. This process is the result of an increase in the concentration of NO_x and an increase in the gas temperature with energy density. Both of these effects promote the reaction of ozone with NO_x and consequently reduce the ozone concentration [129–131].

At first glance, the second observation is in contradiction with the first observation because a higher applied voltage increases the energy density, which according to the
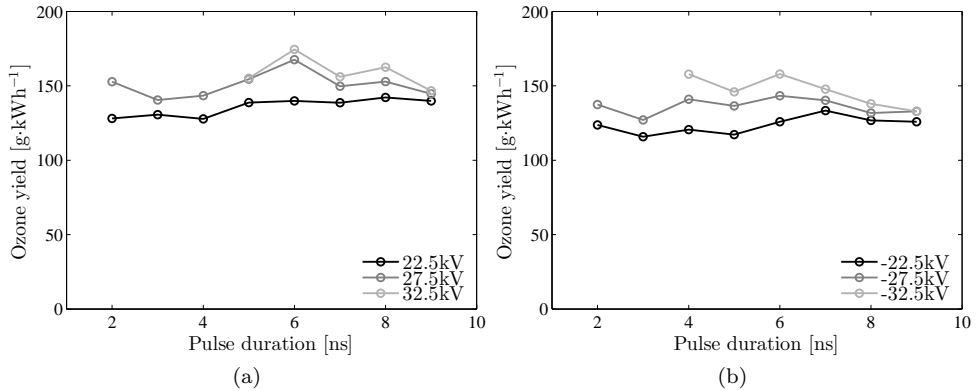
Figure 8.7: Ozone yields for different pulse source settings for (a) positive voltages and (b) negative voltages for $f_{rr} = 100\,\mathrm{Hz}$ and $F = 5\,\mathrm{L{\cdot}min^{-1}}$.

first observation should decrease the ozone yield. In some of the studies that we cited the ozone yield indeed decreased with the applied voltage [8, 36, 136], but in other studies the yields increased with the applied voltage [119, 132], just as in some of our experiments. Therefore, the effect that the voltage amplitude has on the ozone yield appears a specific effect for each reactor configuration and the consequent streamer phases (primary, or primary+secondary) at each applied voltage.

We know from Chapter 7 that the streamer velocity is higher for a higher applied voltage due to an increased enhanced electric field at the streamer head. This streamer head generates radicals needed for the ozone production as long as it propagates through the reactor. Because of the increased enhanced electric field at the streamer head due to a higher applied voltage, the radical production will be higher as well. So as long as the streamer propagates, a higher voltage can increase the radical production. However, we saw in Chapter 6 that the dissipated plasma energy also increases significantly with the voltage, so both the radical production and the plasma energy are higher at higher voltages. It then depends on how much both these parameters increase whether the resulting ozone yield will be higher at higher voltages. In our case, this appears to be the situation at most pulse source settings.

We discuss the last three observation from Chapter 6 in the next parts.

8.4.2 Pulse duration

We saw in Chapter 6 that there was no significant effect of pulse duration on the ozone yield. Here we verify this observation by performing ozone yield measurements for eight different pulse durations (2–9 ns) at three different voltages for both polarities. Figure 8.7 shows the results of this measurement.

The results show some variation with pulse duration, but only very slightly. The ozone yields are slightly higher in the middle of the range of pulse durations and

decrease when the pulse duration is increased further.

We know from the previous chapter that the streamers in our corona-plasma reactor are mainly primary streamers. Especially from Fig. 7.24 it is clear that only somewhere in the range $\Delta t = 6\text{–}9$ ns streamers start to cross the reactor at some points in the reactor at applied voltages of 25 kV and higher. Therefore, in general it holds for pulse durations up to 6 ns that an increase in pulse duration increases the plasma volume. Only when the voltage becomes higher, or the pulse duration longer, will the plasma volume stop increasing due to crossing streamers. For these pulse-source settings where the plasma volume stops increasing, the ozone yield appears to decrease. When the pulse duration increases even more at high voltages, the yield decreases further. Therefore, as long as the plasma volume can expand (by increasing the voltage or the pulse duration) the ozone yield is constant or even increases slightly, but when the plasma-volume expansion decreases, the ozone yield also decreases. However, we should note that all these changes in the ozone yield are very slight.

From Chapter 7 we know that we have no visible secondary-streamer phase when the streamers have crossed the gap, but there have to be some secondary effects such as the onset of secondary streamers that are not visible with the ICCD-imaging method of Chapter 7 or the heating of the streamer channel. Therefore, when the plasma volume stops increasing, secondary-streamer effects will increase.

Van Heesch et al. [5] and Eichwald et al. [154] show that the oxygen-radical energy yield is lower in the secondary-streamer phase as compared to the primary-streamer phase. If the streamers in our plasma cross the gap, secondary-streamer effects might start to occur and according to Van Heesch et al. and Eichwald et al. the oxygen-radical energy yield would consequently decrease. This would explain why the ozone yields decrease in our plasma when the plasma volume is unable to expand any further. However, Ono et al. [162] and Komuro et al. [163] show that oxygen radicals are mainly (energy efficiently) produced in the secondary-streamer phase, which is in contradiction with the findings of Van Heesch et al.. Komuro et al. claim that the fact that Van Heesch et al. used moist air instead of dry air (as Komuro et al. and Ono et al. use) might be a possible reason for this contradiction. Furthermore, they note that in the discharge of Eichwald et al. the secondary streamer is short compared to the primary streamer (where their own streamers are more than half of the length of the primary streamer) and that therefore the oxygen radical yield of the primary and secondary streamer are much closer. In our plasma the secondary streamers will be very short, and therefore the findings of Eichwald et al. are more applicable to our plasma. The pulses used by Van Heesch et al. are also significantly shorter than used by Komuro et al., Ono et al. and Eichwald et al.. We used even shorter pulses with a much shorter rise time. Without using significantly longer pulses (with the same short rise time as the pulses from our nanosecond pulse source) it is not possible to draw concrete conclusions from our results with respect to radical generation in the primary and secondary-streamer phase, but our results might be explained from a higher oxygen-radical formation energy efficiency in primary streamers, which would be in agreement with Van Heesch et al. and Eichwald et al..

A second effect that would explain the lower ozone yield when the plasma volume

stops increasing and when secondary-streamer effects occur is the heating of the channels of the streamers that crossed the gap in the reactor. At higher temperatures, the ozone production decreases [129, 131]. Therefore, the oxygen-radical energy yield might be higher in the secondary-streamer phase, as Komuro *et al.* and Ono *et al.* argue, but due to the increased temperature the ozone production remains lower.

A third effect that we have to consider is that as the streamer approaches the grounded electrode, the electric field at the streamer head increases significantly due to the close proximity of the ground electrode. Therefore, just before the streamers cross the gap in the electrode, the radical formation will be enhanced. Consequently, just before the plasma volume stops decreasing, there is a phase in which radical production is enhanced.

A final effect, which we did not take into account, is the effect of the reflected pulse that is reapplied 230 ns later (after it has reflected on the nanosecond pulse source). We see no significant plasma development (with the ICCD camera) during the time period in which this reflected pulse is applied to the reactor, but we know from the matching measurements that there is still some energy dissipation during this time period.

All these effects contribute to the total ozone production and for our experiments result in a slightly lower ozone yield when the plasma volume stops increasing and secondary-streamer effects start to occur. What the precise cause is of this decrease will be a combination of the four effects and will have to be determined either experimentally or with numerical modelling in future work.

8.4.3 Pulse polarity

In Chapter 6 we first noticed that applying negative pulses resulted in a better matching of the pulse source to the reactor (in several experimental conditions) than when we use positive pulses, but that the associated ozone yield was lower. In Chapter 7 we then discovered the presence of thick streamers on the tightening mechanism of the reactor that likely dissipate a significant amount of energy. Due to this loss in energy, the streamer development in the reactor was affected in such a way that the total streamer volume was smaller than when positive pulses were used. Since the thick streamers at the end of the reactor will exist for a large part in the secondary-streamer phase, consume a significant amount of energy and result in a smaller plasma volume, the ozone yield for the negative pulses will be lower. This is in contradiction with some other studies, which found higher ozone yields for negative pulses (e.g. [5, 185]). Here we will analyse the results with a different method to try to understand this discrepancy.

With the ICCD setup of the previous chapter it is possible to follow the streamer development in the reactor on a very short time scale. It is therefore possible to calculate the total plasma volume for each time step from the streamer width, the streamer length and the number of streamers[†]. If we would then calculate the total

---

[†]We have not commented on this parameter before, but in principle we could calculate the number
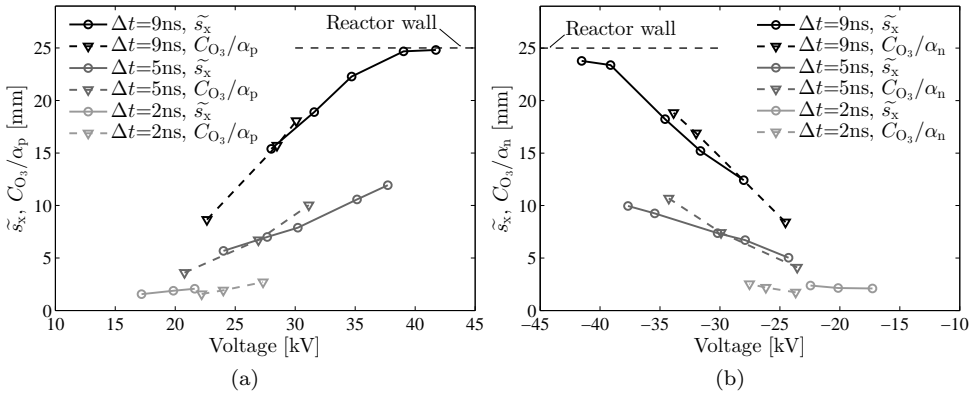
Figure 8.8: A comparison between scaled ozone concentrations (C_{O_3}/α) and the average streamer length ($\widetilde{s_x}$) in the reactor for (a) positive and (b) negative polarities. The α-parameter is the scaling parameter for the ozone concentrations and is chosen such that the results show a good fit. The α-parameter is different for both polarities and is higher for the negative pulses.

plasma volume for a number of applied voltages and pulse durations at both polarities, we could relate the measured ozone concentrations to the calculated plasma volume and might arrive at an ozone yield per plasma volume unit. Unfortunately, this requires the data from a large amount of experiments, which we do not have at this moment. However, with the data we have from Chapter 7 we can relate the ozone concentrations to the average streamer lengths at different applied voltages and pulse durations for both polarities.

In Fig. 7.24 we showed the average maximum streamer lengths as a function of the position in the reactor for different applied voltages and pulse durations for both polarities. If we take the average of these streamer lengths $\widetilde{s_x}$ (in mm) for each experimental setting, we can compare these average streamer lengths to the ozone production at the same settings in the current chapter by dividing the ozone production with a constant α. Here, α has the unit ppm·mm^{-1} and is selected in such a way that the results have a good fit. Figure 8.8 shows the results if we perform this fitting for both polarities.

The available data is not extensive, but the results show a reasonable fit between the scaled ozone production and the average streamer length in the reactor. This indicates that the plasma generated with the short-rise time pulses might have an inherent parameter that relates the amount of ozone it produces to the dimensions of the plasma in the primary-streamer phase. This result could be made stronger if we could apply the aforementioned technique of calculating the exact plasma volume (using the streamer length, streamer width and the number of streamers) to a more extensive set of data. These experiments will be left for a future study. However, here we already have an indication that such a parameter might be found.

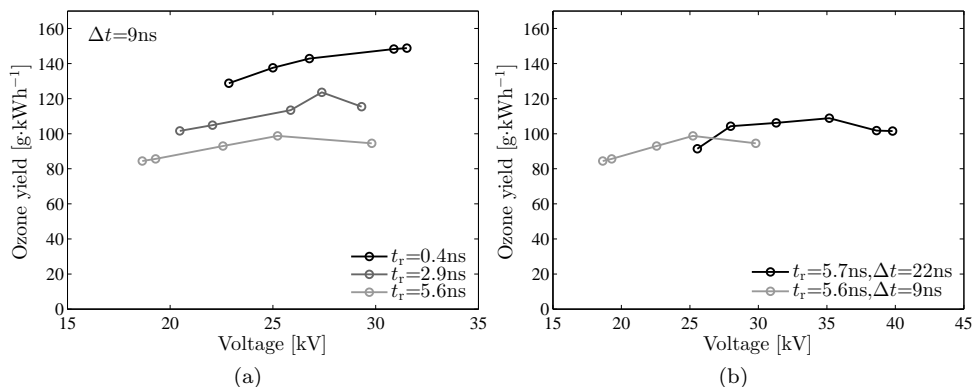of streamers as well from the ICCD data.

Figure 8.9: Ozone yields for pulses with different rise times. In (a) we used the pulses from the nanosecond pulse source with 9-ns pulse duration with three different rise times for $f_{rr} = 20\,\mathrm{Hz}$ and $F = 2\,\mathrm{L\cdot min^{-1}}$. In (b) we compared the ozone yield of the 5.6-ns rise time pulse of the nanosecond pulse source of (a) with the yield of the conventional pulse source. The experimental settings for the measurements with the conventional pulse source were the same as for (a).

For the results of Fig. 8.8 the parameters α_p and α_n are the α-values for the positive and negative results respectively and are $155\,\mathrm{ppm\cdot mm^{-1}}$ and $170\,\mathrm{ppm\cdot mm^{-1}}$ respectively. These values indicate that the negative plasma is more effective per mm of average streamer length in generating ozone. We have no way of relating this to the dissipated plasma energy because we have no information on the energy dissipated by the thick streamers, but it is a strong indication that the negative streamers in the main plasma are actually more effective at generating ozone when compared to positive streamers. Consequently, this result is in agreement with what other researchers found.

8.4.4 Rise time

In Section 6.2.5 we showed how we can change the rise time of our nanosecond pulses. In that chapter we also showed that the matching and ozone yield decrease when the rise time increases (we show the yield results here again in Fig. 8.9a). Then, in Chapter 7 we showed that the rise time has a significant effect on the streamer propagation: when the rise time increases, the streamers propagate less far, have a (slightly) smaller diameter and propagate slower. Consequently, the streamer volume in the reactor is significantly lower. At the same time, the dissipated energy is also lower, but not significantly lower. If we then consider that the main source of radicals required for ozone production is the enhanced electric field at the streamer head, then the result that a longer rise time results in a lower ozone yield in our reactor is not surprising.

In addition to our nanosecond pulse source we used the conventional pulse source that we introduced in Section 8.3.3 to perform ozone production experiments. The

pulses from this pulse source have a similar rise time as the longest rise time from our nanosecond pulse source, but with a longer pulse duration of 22 ns. Figure 8.9b shows the comparison between the results of the two different pulse sources. We see that the ozone yields are very similar, which is further proof that the rise time is a very important parameter for the ozone yield for these short pulses. We could argue that at a pulse duration of 22 ns the streamers could enter the secondary-streamer phase, but we have no ICCD-imaging results with the conventional pulse source. If the 22-ns pulse would have the same 0.4-ns rise time as the unaltered pulses from our nanosecond pulse source we could reasonably assume that the streamers would enter the secondary-streamer phase. However, when we look at Fig. 7.26 we see that for the 5.6-ns rise time of the nanosecond pulse source, the streamers are much slower. Therefore at 22 ns the streamers might just cross the gap and will likely be primary streamers still. Consequently, their behaviour should be similar to the streamers generated with the 5.6-ns rise time pulse from the nanosecond pulse source and Fig. 8.9b confirms this. It even shows the slight trend that the ozone yield increases with the applied voltage.

In conclusion, the rise time of the applied pulses has a very significant effect on the streamer propagation (as we saw in Chapter 7) and therefore on the ozone yield as well. In future experiments, the use of longer pulses with the same short rise time as the fastest pulse from our nanosecond pulse source would be very useful to determine what the most important parameter for ozone production is — rise time or pulse duration — when the streamers also exist for a significant time in the secondary-streamer phase.

8.4.5 Optimal parameters for ozone production

After all the experiments on ozone production in this thesis, the obvious question is: what is the optimal pulse source setting to produce ozone (and therefore oxygen radicals)?

The parameter α, indicating the amount of ozone produced per unit of average streamer length in the reactor that we introduced in Section 8.4.3, indicated that a negative streamer might have a higher effectiveness in generating ozone. Unfortunately, due to the thick streamers at the end of the reactor this was not reflected in the ozone yield measurements of negative pulses. However, when the triple-point issue causing these thick streamers is resolved, negative pulses might result in a higher ozone yield than when positive pulses are used. On the other hand, the (slightly) better matching for negative pulses might also decrease in the absence of the thick streamers, which brings us to the most critical point: the system yield.

Obviously, it is beneficial to have a high ozone yield, but if the energy transfer of the pulse source to the reactor at that particular setting is low, the total yield of the reactor as an entire system can still be low. Therefore we require good matching and a high ozone yield simultaneously. We calculate the system yield with

$$\text{System yield} = G_{O_3} \times \eta_{\text{tot}}, \tag{8.26}$$

where η_{tot} is the total matching of the pulse source to the reactor.
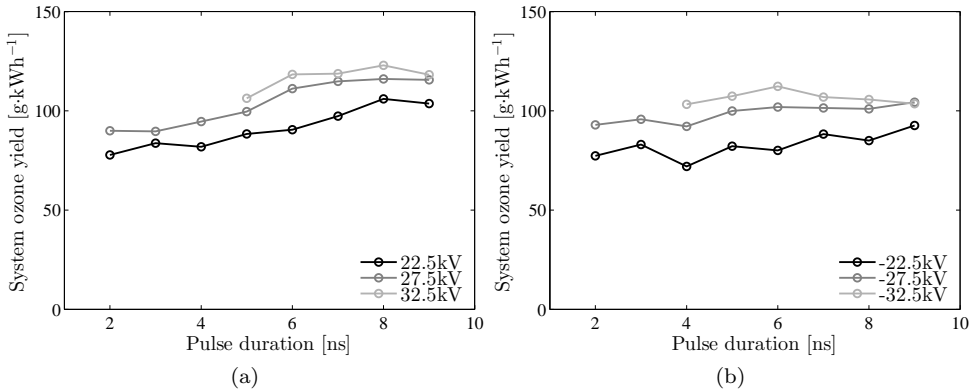
Figure 8.10: The total system yield for ozone production for (a) positive voltages and (b) negative voltages. The ozone yield results of Fig. 8.7 were multiplied by the matching of the pulse source to the reactor at those settings to obtain the system yield. The results show that using positive, long pulses at a high voltage results in the highest system yield.

The results of this section showed that the rise time has to be as short as possible for the highest yield. Furthermore, we showed in Chapter 6 that the matching of the long-rise time pulses is lower, so we only calculate the system yield for the shortest rise time pulses. Figure 8.10 shows the system yield as a function of the pulse duration and voltage amplitude for the short-rise time pulses.

The nearly constant ozone yield, coupled with the increased matching for longer pulses, results in a system yield that increases with the pulse duration. Furthermore, due to better matching and a high ozone yield at higher applied voltages, the system yield increases with the voltage as well. If we then consider that the longest pulses and the highest voltages generate the highest ozone concentration, the optimal pulse source parameters for ozone generation in dry synthetic air are 8–9-ns positive pulses at the highest voltage we used.

On a final note it would be very beneficial in future experiments to have the use of even longer pulses (with the same short rise time) than we put forth in this thesis. For instance, if we could perform further experiments (ICCD-imaging and plasma processing) with pulses of 10–30 ns, the differences in ozone yields — and possibly even the differences in matching — would likely increase. Then, there would be a clear secondary-streamer phase and the argumentation of this section could be made stronger. The same effect might be achieved with a higher applied voltage. For this to work, we have to resolve the issue of the thick streamers by improving the design of the wire-tightening mechanism.

With the current design of the nanosecond pulse source we could easily increase the pulses by increasing the length of the pulse forming line. This would require a much longer pulse source housing (up to 3.5 m for a 30-ns pulse) and the pulse chargers would have to be adapted to charge the larger load of a longer pulse forming line.

8.5   NO removal

In this section we present the results of the NO-removal experiments.

8.5.1   Pulse polarity and initial concentration

Just as with the ozone-production experiments, we start by varying the pulse duration, pulse amplitude and pulse polarity of the applied pulses and study the effect on the plasma process. In this first part we begin with the effect of the pulse polarity. We used three different pulse durations (2 ns, 5 ns and 9 ns) at three different voltages for both amplitudes. We used an initial concentration of 220 ppm NO in synthetic air for these measurements. This value is in the range of 200-300 ppm that is often used by other researchers and gives a good approximation of a typical flue-gas composition. Figure 8.11a and Fig. 8.11b show the results of the FT-IR measurements as a function of the energy density. Later we will show the corresponding NO-removal yields, but here we first focus on the formed compounds.

The results of the experiment show that the concentration of the various compounds is mainly the result of the energy density and not so much the result of different pulse durations and voltages.

When the energy density increases, the concentration of NO decreases and the concentration of NO_2 increases through reactions (8.5)–(8.8). Meanwhile NO_2 can be converted to by-products N_2O and N_2O_5[‡] through reactions (8.9)–(8.11), but as long as NO is present in the reactor the contribution of these reactions is minor. Once the NO concentration becomes low (at around 40–50 $J \cdot L^{-1}$) the production of NO_2 from NO decreases and reactions (8.9)–(8.11) become dominant in the formation of by-products. Furthermore, once all NO is removed from the gas and the NO_2 concentration becomes low, O_3 is not lost anymore to reaction (8.8) and its concentration can increase significantly (as we see for the negative-polarity results).

Initial NO concentration

Before we compare the results of both polarities, we first show results of an experiment in which we varied the initial concentration of NO (135 ppm, 225 ppm and 420 ppm) to see the effect this has on the formed compounds. We used 9-ns, 31-kV, positive pulses for these experiments and varied the pulse repetition rate to increase the energy density. Figure 8.11c shows the results.

The first observation from the results is that for the lowest two concentrations, all NO is converted, but that for an initial concentration of 420 ppm the NO concentration stabilises at a non-zero concentration. Mizuno *et al.* encountered a similar effect for high initial NO concentrations and attributed the effect to the destruction of ozone at

---

[‡]In this discussion, keep in mind that the N_2O_5 results are not calibrated. To obtain the concentrations in the figures, we multiplied the absorbance in the N_2O_5 range with an arbitrary constant number. Therefore, the N_2O_5 concentrations in the figures could be much lower than they are represented.
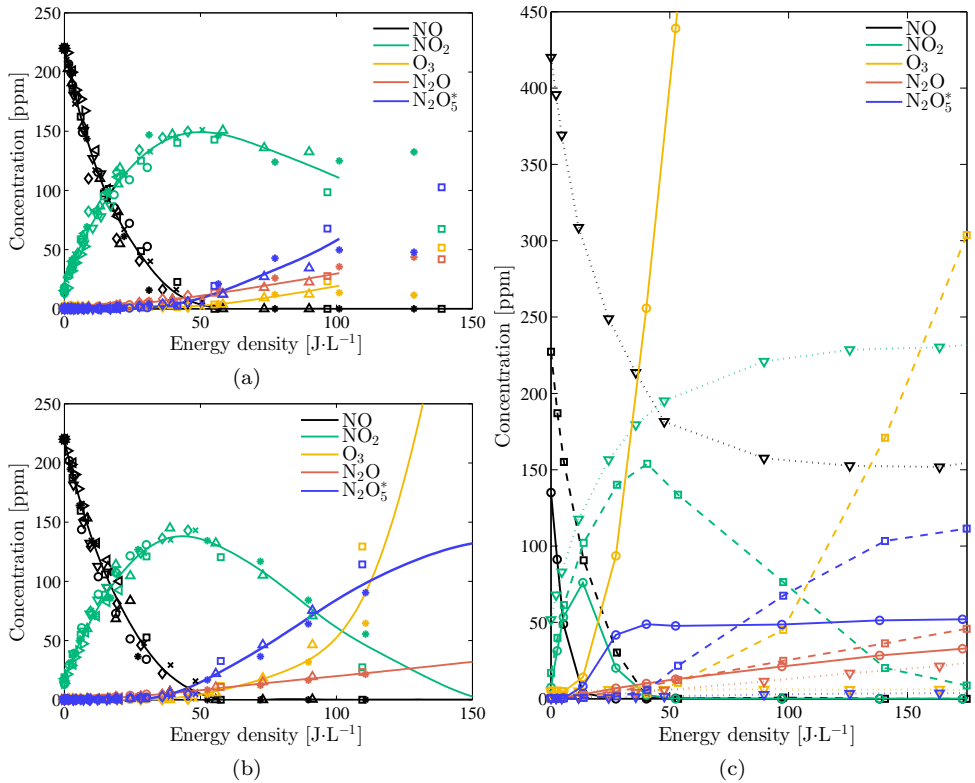
Figure 8.11: The results of the FT-IR measurements for (a) positive pulses and (b) negative pulses for the NO-removal experiments at different applied voltages and pulse durations at a flow of $4\,L \cdot min^{-1}$. The energy density is changed with the pulse repetition rate. The initial concentration of 220 ppm of NO is converted to NO_2, N_2O, O_3 and N_2O_5 by the plasma. The figure shows the raw values (the markers) and the fitted values. The fitted lines were fitted with the inclusion of raw results up to $250\,J \cdot L^{-1}$ for the negative pulses and up to $100\,J \cdot L^{-1}$ for the positive pulses (at higher energy densities some experiments showed unexpected results). The markers represent measurements with a pulse duration and applied voltage (positive and negative amplitude respectively) of: (○) 2 ns (29 kV and -31 kV), (▽) 2 ns (23 kV and -24 kV), (▷) 2 ns (17 kV and -15 kV), (△) 5 ns (32 kV and -33 kV), (×) 5 ns (24 kV and -25 kV), (◁) 5 ns (16 kV and -17 kV), (□) 9 ns (37 kV and -38 kV), (∗) 9 ns (30 kV and -29 kV) and (◇) 9 ns (19 kV and -20 kV). (c) The results of FT-IR measurements for 9-ns 31-kV positive pulses for three different initial concentrations of NO: 135 ppm (solid line), 225 ppm (dashed line) and 420 ppm (dotted line) at a flow of $4\,L \cdot min^{-1}$. *Note that the N_2O_5 concentration is not calibrated.

high energy densities [187]. A lower ozone concentration would consequently reduce the conversion of NO to NO_2 and of NO_2 to NO_3 (and consequently to N_2O_5) through reactions (8.8) and (8.10)–(8.11) respectively. However, we can see from the ozone

concentrations of the 135-ppm and 225-ppm results that the ozone concentration still increases at high energy densities, so the energy density is not yet high enough to decrease the ozone concentrations significantly. Furthermore, the N_2O_5 concentration also still increases, indicating that in our process ozone is still important through reactions (8.10)–(8.11).

An important clue to explain our results is the concentration of N_2O. For N_2O to form, NO_2 and nitrogen radicals have to be available for reaction (8.9). According to the results, the concentrations of NO and NO_2 are zero for the 135-ppm results at high energy densities, yet the N_2O concentrations steadily increases with the energy density, indicating the presence of NO_2. Therefore, the NO production reaction (8.14) has to play an important role. The constant production of new NO will result in new NO_2, which will consequently be converted to N_2O. (This also shows that for these experiments, reaction (8.9) is preferred over (8.10) because the N_2O_5 concentration does not increase significantly at higher energy densities and only increases when the NO_2 concentrations are high.) Therefore, from the 135-ppm results we can conclude that besides NO removal, the plasma also constantly produces new NO and the subsequent by-products. This was also observed by Beckers *et al.* for low-level NO_x removal [27].

At an initial NO concentration of 225 pm all NO can be removed, but it already takes a considerably higher energy density to remove all NO_2 (as compared to the 135-ppm results), indicating that the production of NO by the plasma, and back reactions from NO_2 to NO, such as (8.15), start to dominate. At an initial NO concentration of 420 ppm the NO can not be completely removed anymore and appears to converge to an end value. The same is true for NO_2 and it therefore appears that the production of NO from NO_2 through (8.15) and vice versa through (8.5), (8.7) and/or (8.8) dominates the process at high energy densities. Consequently, the production of the other by-products is almost completely suppressed. The production of some N_2O indicates that some nitrogen radicals are used to convert NO_2 into N_2O, but that most NO_2 and nitrogen radicals are involved in other reactions.

From the results it appears that the nanosecond pulsed plasma is unable to remove high NO concentrations. Fortunately, there are methods available to overcome this issue. For instance, the addition of C_2H_4 to the plasma greatly enhances the NO removal due to the formation of other types of radicals in the plasma [187]. We did not perform experiments with additives, so results of these type of experiments will be left for future work. Also the addition of H_2O will reduce the NO_2 concentrations and will consequently result in more NO removal at higher initial concentrations as we will see later and was also mentioned in [187].

Finally, we look at the NO-removal yield for the experiments with different initial NO concentrations. Figure 8.12 shows these results. If we consider that at higher initial concentrations the production of NO and the interaction with NO_2 increases, it is not surprising to see the highest NO-removal yield for the lowest initial concentration. Furthermore, the results show very high yields at 50 percent removal for the 135-ppm concentration of $2.5\ \text{mol}\cdot\text{kWh}^{-1}$ (or 14.9 eV per NO molecule) and even for the 225-ppm results the yields are very high at around $1.75\ \text{mol}\cdot\text{kWh}^{-1}$ (or 21.3 eV per NO molecule) and are therefore amongst the highest reported values in literature.
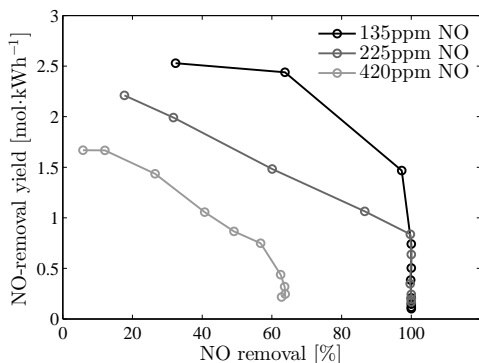
Figure 8.12: The NO-removal yields as a function of the amount of removed NO for the results of Fig. 8.11c. The results show that the yield decreases when the initial NO concentration increases.
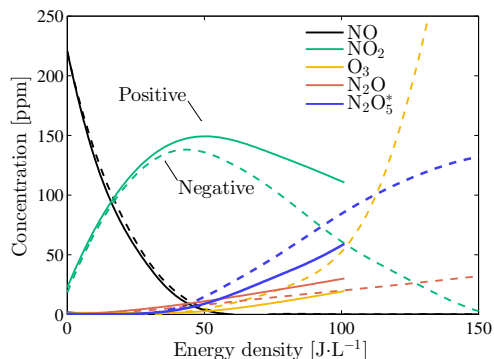

Figure 8.13: The fitted results of Fig. 8.11 for the positive pulses (solid line) and the negative pulses (dashed line). The NO removal is very similar for both polarities, but the by-product concentrations differ slightly.

Polarity

In Fig. 8.13 we compare the fitted concentrations of the compounds in Fig. 8.11a and Fig. 8.11b of the positive and negative polarity pulses. The differences in NO removal are not significant and indicate a slightly better result for positive pulses. If we consider that the results of the first plasma process in this chapter, ozone generation, showed that the ozone yields were higher for positive pulses, the NO-removal results are surprising. For ozone generation a higher number of oxygen radicals produces more ozone. Furthermore, excited nitrogen species produced in the primary-streamer phase (which is more pronounced for the positive pulses) result in a further increase in oxygen radicals [18, Section 2.5]. Therefore, we expected the NO-removal to be more efficient for positive pulses, because one of the important NO-removal reactions is the oxidation of NO through (8.5), which requires oxygen radicals. It therefore appears that for positive pulses the production of NO through (8.14) (and the back conversion of NO_2 to NO) is more pronounced than for negative pulses, which consequently keeps the NO concentrations higher than expected. Likewise, the NO_2 concentrations are higher. In fact, if we compare the positive results with the negative results, the results are very similar to when we compare the 225-ppm results with the 135-ppm results in Fig. 8.11c (only less pronounced).

For the production of NO through reaction (8.14), nitrogen radicals are required. Therefore, if the production of NO by the plasma is more pronounced for positive pulses, it is likely that more nitrogen radicals are produced for the positive pulses. Furthermore, the production of N_2O through (8.9) also requires nitrogen radicals and is also higher for positive pulses. The generation of nitrogen radicals requires higher energies than oxygen radicals as we see from reactions (8.1) and (8.4) and because primary streamers produce electrons with a higher energy than secondary streamers,

more nitrogen radicals will be produced in the primary streamers. With our previous conclusion that the primary-streamer phase is slightly more pronounced for positive pulses, this could explain the small differences in polarities: for positive pulses we have more nitrogen radicals and therefore a higher production of NO and N_2O. That we did not see these effects with the ozone-generation process is that according to Fig. 8.11c ozone production is not influenced much if the initial concentration of NO and NO_2 are low (for instance above $50 \, J \cdot L^{-1}$ for the 135-ppm results). Only at very high energy densities will the effects of NO and NO_2 become significant [129–131]. We see this effect in Fig. 6.22, where we now also see that the positive ozone yields decrease more significantly with the energy density than the negative yields, which can again be explained with the results from the current section.

8.5.2 Pulse duration and voltage amplitude

In the ozone-generation measurements of Section 8.4 we showed that the ozone yield increased slightly with the pulse duration, increased more significantly with the voltage and that these effects diminish at the longest pulse durations (6–9 ns). Furthermore, the ozone yields were lower for negative pulses. Figure 8.14 shows the NO-removal yields as a function of the amount of NO removed for different voltages and pulse durations. The results are listed below and are very similar to the observations on ozone yields of the ozone-generation experiments of Section 8.4.

- On average the NO-removal yields are slightly lower for negative pulses, but the difference is not as pronounced as with the ozone-generation experiments.
- The NO-removal yield increases with the applied voltage. This effect seems larger than with the ozone-generation experiments, but we have to keep in mind that the differences between the lowest and highest applied voltages are larger for the NO-removal experiments.
- At longer pulse durations the differences in NO-removal yields are smaller between the different applied voltages at that pulse duration.
- The NO-removal yield increases slightly with the pulse duration, but are very similar when the same voltage amplitudes are used.

These general observations show that there are slight differences in the yields between the ozone-generation experiments and the NO-removal experiments. However, while the governing reactions are very similar, one process is a generation process and the other a removal process. In the latter, the amount of remaining pollution significantly influences the plasma process (as we saw in the previous part) and therefore the yields. A direct comparison between the two processes can therefore not be made.

Some of the observations on the NO-removal yields can again be explained from the imaging results. A lower voltage reduces the field enhancement at the tip of the streamer and therefore the radical generation and the streamer velocity (and consequently the plasma volume). The energy the streamers dissipate will consequently also be lower, but that the net result is a lower radical-generation yield seems likely. For
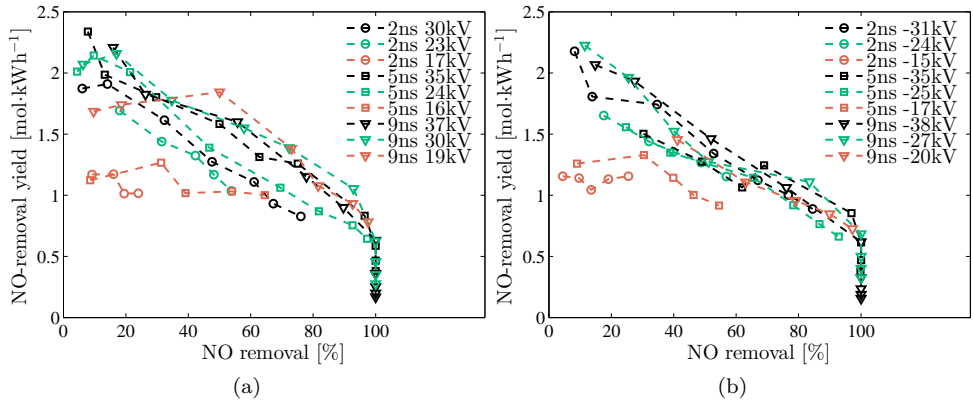
Figure 8.14: The NO-removal yields for different pulse durations and applied voltages for (a) positive pulses and (b) negative pulses for the results of Fig. 8.11 as a function of the percentage of the removed NO.

short pulse durations, the applied voltage can increase significantly before the streamers can cross the gap at these short durations. Only the ratio of radical formation in the primary streamer to the dissipated energy by the streamers then influences the NO-removal yield. From the results we see for the 2-ns results that an increased voltage increases the NO-removal yield. To a lesser extent, this is also true for the 5-ns measurements, but for the 9-ns measurements this is not true anymore. Here the yields are not very dependent on the applied voltage. If we again consider that for the 5-ns and 9-ns pulses the streamers can cross the gap in the reactor at some positions, and that this number of positions increases with the applied voltage, then radicals are formed partly after the primary-streamer phase. Furthermore, the energy dissipation by the plasma still increases with the pulse duration and applied voltage, so the NO-removal yield will consequently not increase anymore.

The argumentation put forth in the previous paragraph is the same as for the ozone-generation experiments and explains many of the observations on the NO-removal experiments, but there are still some small deviations. For instance, from the argumentation we would expect that the NO-removal yields would be (slightly) lower for the 9-ns pulses than for the 5-ns pulses and also that there would be a larger difference between the pulse polarities due to the thick streamers, but this is not the case. However, as mentioned, in the NO-removal process the production of NO is also a very important parameter and with an initial concentration of 220 ppm of NO that we used in these experiments, these effects can become significant as we showed in Fig. 8.11c.

The analysis of the results is further complicated because the differences in NO-removal yields between various settings is small. Just like we concluded at the end of the ozone-generation section, it would be beneficial to have the use of longer pulses (or a higher voltage) with the same short rise time to be able to comment further on the effect of the secondary-streamer phase and to see if the similarities between
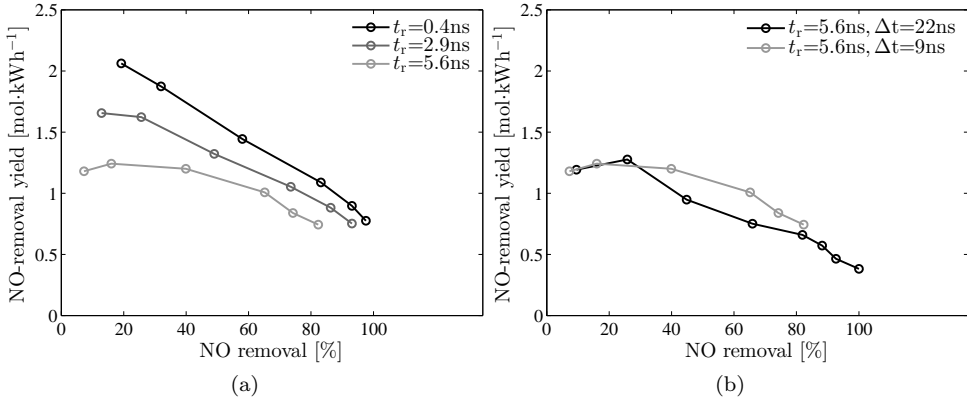
Figure 8.15: NO-removal yields for different rise-time pulses. In (a) all pulses were the 9-ns pulses from the nanosecond pulse source with a 30-kV amplitude and different rise times. The gas flow was $2\,\mathrm{L\cdot min^{-1}}$ of synthetic air with $220\,\mathrm{ppm}$ NO. In (b) the NO-removal yields for the 5.6-ns rise time pulses from the nanosecond pulse source (same experimental conditions as (a)) are compared with NO-removal yields for the 5.7-ns rise time pulse from the conventional pulse source (38-kV pulses at $F = 2\,\mathrm{L\cdot min^{-1}}$).

the ozone-generation experiments and the NO-removal experiments still hold, or that they start to deviate. For instance, for longer pulses Fujiwara *et al.* and Kakuta *et al.* already showed that a long pulse duration decreases the NO-removal yield as compared to shorter pulses with the same rise time [9,10].

Finally, we observe that at 50 percent NO removal we obtained a NO-removal yield of around $1.75\,\mathrm{mol\cdot kWh^{-1}}$ (which corresponds to a cost of $21\,\mathrm{eV}$ per NO molecule). This yield is very high compared to other studies and might even be increased further by finding an optimum process temperature [117], by adding hydrocarbons into the gas stream [187] or by an indirect method where ozone is generated with the plasma and is then added to a gas stream containing NO [185].

8.5.3   Rise time

In the ozone-generation measurements of Section 8.4 we showed that the ozone yield decreased significantly when we used pulses with a longer rise time. From the matching results of Chapter 6 and the ICCD-experiments of Chapter 7 these results could be readily explained: the energy dissipation by the plasma decreases with an increased rise time, but the plasma volume decreases much more significantly. In addition, the electron density in the streamers is lower and the enhanced electric field at the streamer tip is lower. The result that a longer rise time decreases the ozone-generation yield then comes as no surprise and we expect the same result for the NO-removal experiments. Figure 8.15a confirms this expectation.

In Fig. 8.15b we compare the results of the 5.6-ns rise time pulse from the nanosec-
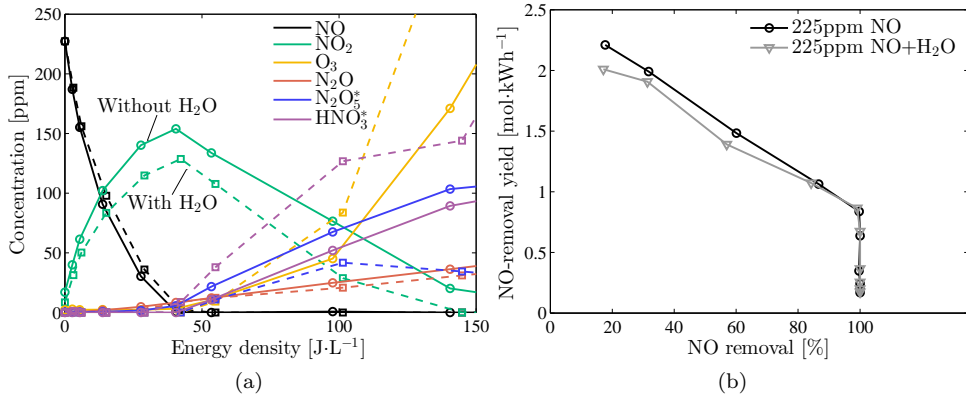
Figure 8.16: NO-removal experiments with and without added H_2O. In (a) the various compounds are shown for a gas stream with water vapour (dashed line) and without water vapour (solid line) for an initial concentration of 225 ppm of NO for $F = 4\,L\cdot min^{-1}$). The pulses were 9-ns 35-kV positive pulses. In (b) we compare the NO-removal yields for both experiments. *Note that the N_2O_5 and HNO_3 concentrations are not calibrated.

ond pulse source with the results of the 5.7-ns rise time pulse of the conventional pulse source. Just as with the ozone-generation experiments, the results are very similar, again indicating that the rise time is a very important parameter for the plasma-processing yields.

8.5.4 H_2O addition

As a last experiment we used compressed ambient air with $4500\,(\pm 1500)$ ppm of H_2O and performed NO-removal measurements . Figure 8.16a compares the results of these measurements to NO-removal measurements with dry synthetic air. The effect of the H_2O is that reaction (8.13) becomes important. As a result, NO_2 is used that would be used for the generation of N_2O and N_2O_5 (through NO_3) if no H_2O was present. Therefore, the concentrations of NO_2, N_2O and N_2O_5 are lower when H_2O is added. Likewise, the concentration of HNO_3 is higher until all NO_2 is used.

If we look at the NO-removal yields in Fig. 8.16b we see that the addition of H_2O slightly lowers the NO-removal yield. This is because of the energy that is used for OH-radical generation and would otherwise have been used to generate oxygen radicals that could be used for the oxidation of NO through (8.5). Likewise, less energy is available for the generation of nitrogen radicals that could reduce NO through (8.6).

This experiment shows that by using moist air, less by-products are formed at the cost of an increased HNO_3 concentration. However, HNO_3 can be removed from the gas stream by conventional means.
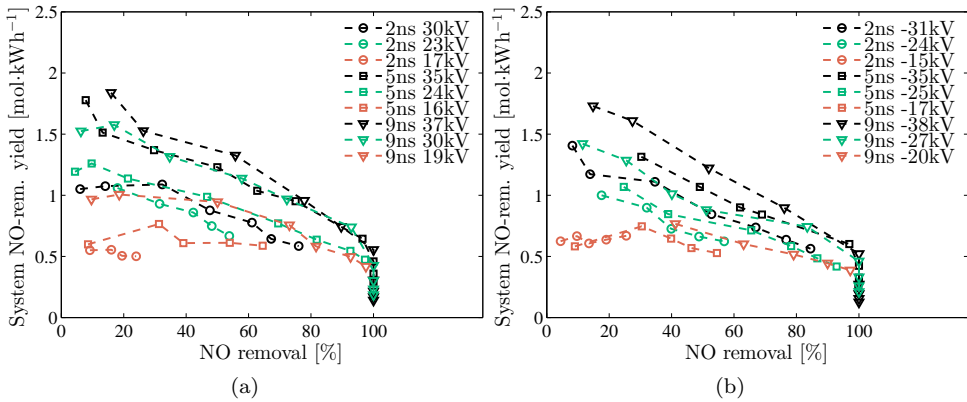
203

Figure 8.17: The total system yield for NO-removal for (a) positive voltages and (b) negative voltages. The NO-removal yield results of Fig. 8.14 were multiplied by the matching of the pulse source to the reactor at those settings to obtain the system yield. The results show that using long pulses at a high voltage results in the highest system yield.

8.5.5 Optimal parameters for NO removal

Just as with the ozone-generation experiments we can calculate the total system yield with

$$\text{System yield} = G_{NO} \times \eta_{\text{tot}}. \tag{8.27}$$

Figure 8.17 shows the system yield for the NO-removal experiments. Due to the better matching at longer pulse durations and higher voltages, as well as the higher NO-removal yields at longer pulse durations and higher voltages, the system yields are consequently highest for the longest pulses and the highest voltages. Therefore, the optimal pulse source parameters for NO-removal are the longest available pulses of our nanosecond pulse source at the highest voltage. Furthermore, for a lower by-product formation of NO_2 and N_2O, a negative polarity is preferred. However, if a lower ozone concentration and a lower N_2O_5 concentration is required, positive pulses are preferred. These results might be different at different initial NO concentrations.

8.6 CO_2 conversion

In this section we present the results of the CO_2-conversion experiments.

8.6.1 Pulse duration and voltage amplitude

The first remark we have to make is that a plasma generated in pure CO_2 is different from a plasma generated in synthetic air (as we used for the previous two plasma processes). For instance, we observed spark breakdowns at much lower voltages at the

end of the reactor when we used CO$_2$ as compared to when we used synthetic air. Therefore, we first consider the matching.

Matching

We performed CO$_2$-conversion experiments for different applied voltages for three different pulse durations (2 ns, 5 ns and 9 ns) at both polarities. Figure 8.18a shows the matching results for these experiments. If we compare these results with matching results in synthetic air (Fig. 6.17) we see a completely different result: the matching in the case of CO$_2$ is not very dependent on pulse duration and even appears to be higher for the shortest pulse duration for positive pulses. For a plasma in synthetic air the matching was better for the longest pulses. Also, the applied voltage has a less pronounced influence on matching for the CO$_2$ plasma; where the matching increased significantly with the applied voltage for synthetic air, the matching is much more constant for CO$_2$. Furthermore, the difference in matching between the different voltage polarities is also larger; the negative pulses result in significantly better matching.

The matching results indicate that the CO$_2$ plasma exhibits different behaviour than the plasma in synthetic air, which also results in some practical limitations. The lower matching for positive pulses means that the transmitted pulse into the reactor is higher as compared to negative voltages due to a higher reflection coefficient (and therefore a higher transmission coefficient). It also means that less energy is dissipated by the plasma. Consequently, the pulse voltage amplitude in the reactor remains very high and when the pulse reflects at the end of the reactor, the voltage at this position becomes so high due to the voltage doubling that spark discharges appear at applied voltages as low as 30 kV for a 9-ns pulse. To fully understand this effect we would have to perform experiments with the ICCD-imaging setup of the previous chapter. We did not perform these experiments at present and therefore we can unfortunately not comment on the behaviour of the CO$_2$ plasma in great detail.

CO yield

Figure 8.18b shows the CO yield for the same experimental settings as the matching results of Fig. 8.18a. Here we see the opposite of the matching results: positive pulses result in a more efficient plasma, even though the results are quite mixed. Bak *et al.* observed a similar effect when they increased the pressure of their nanosecond pulsed CO$_2$ plasma (10-ns pulses): an increased pressure increased the matching (which is the opposite of a plasma in synthetic air; see Appendix B), but lowered the CO yield [217]. They also showed that at higher reduced electric fields (E/n) the fraction of energy used in electron-impact collisions with CO$_2$ favours reactions with high electron energies. Therefore, if E/n is high, CO$_2$ is dissociated less energy efficiently. Therefore, our results could indicate that for negative pulses E/n is higher in the reactor and consequently the CO yield is lower. Generally, a higher E/n value also results in better matching (for oxygen/nitrogen plasmas), which might explain the matching results, but this would have to be investigated further.
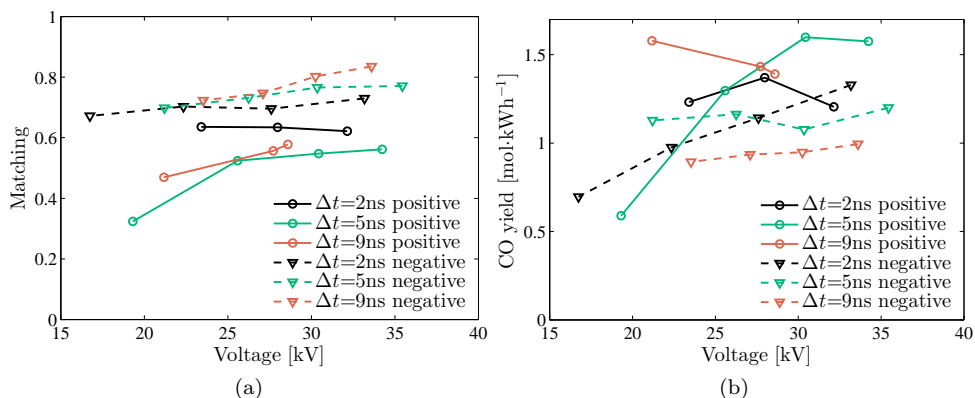
Figure 8.18: (a) Matching results for positive (solid line) and negative (dashed line) pulses for different pulse durations for the CO_2 plasma (f_{rr} =20 Hz and $F = 2\,L \cdot min^{-1}$). The matching results in CO_2 are significantly different than in the plasma in synthetic air (compare with Fig. 6.17). (b) The CO yield results for the experiments in (a). The yields show that negative pulses result in a lower CO yield.

That a positive corona results in a higher CO yield than a negative corona was also seen for a DC corona by Horvath *et al.* [224].

We also measured ozone concentrations for the CO_2 experiments, but the concentrations were too low to make any statements about ozone production.

8.6.2   Rise time

Just as with the ozone-generation and NO-removal experiments, we vary the rise time of the nanosecond pulse source and compare the CO yields. Likewise, we compare the results of the 5.6-ns rise time of the nanosecond pulses with the results of the conventional pulse source. Figure 8.19 presents the results. The yields still depend on the rise time of the applied pulses of the nanosecond pulse source, just as for the ozone yields and NO-removal yields, but the effect is less pronounced. Also, the results of the conventional pulse source are very similar to the (negative) results of the nanosecond pulse source. Unfortunately, without ICCD-imaging results and a deeper investigation into CO_2 plasmas, we are unable to comment on the results any further.

8.6.3   Comparison with a DBD plasma

The CO-yield results with the nanosecond pulse source show maximum values of up to around $1.5\,mol \cdot kWh^{-1}$. This is equal to around 25 eV per CO molecule, or an energy efficiency of around 11–12 percent if we consider that the lowest amount of energy it would cost to dissociate a CO_2 molecule is 2.9 eV. These results are similar to those found by Bak *et al.* who also used short pulses (10-ns pulse duration, 4-
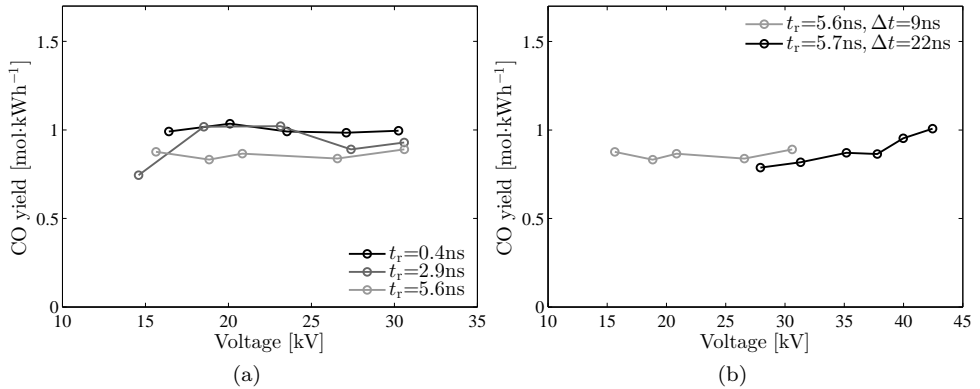
Figure 8.19: CO yields for different rise-time pulses. In (a) all pulses were the negative 9-ns pulses from the nanosecond pulse source with different rise times at a repetition rate of 20 Hz. The gas flow was $2\,\mathrm{L{\cdot}min^{-1}}$ of CO$_2$. In (b) the CO yields for the 5.6-ns rise time pulses from the nanosecond pulse source (same experimental conditions as (a)) are compared with NO-removal yields for the 5.7-ns rise time pulse from the conventional pulse source ($f_{\mathrm{rr}} = 20\,\mathrm{Hz}$ and $F = 2\,\mathrm{L{\cdot}min^{-1}}$).

ns rise time) [217], and to the results of the DBD plasma of Brehmer [211]. These energy efficiencies are low compared to other discharge types, like a gliding arc plasma (43 percent) [225] or a DC-corona plasma (56 percent) [224]. However, in the latter experiment these energy yields where obtained in a static gas environment; the yields decreased significantly when the gas was flowing.

Recently, Ponduri *et al.* [215] and Douat *et al.* [216] obtained CO$_2$-conversion results in a DBD plasma which they shared with us. The results were obtained in a similar setup as Brehmer *et al.* used, but at a different geometry to generate only a few microdischarges. Consequently, they operated their DBD in a similar energy-density range as we operate in with our nanosecond pulsed plasma. Figure 8.20 shows the comparison of their results with our results of the nanosecond pulse source and the results of the conventional pulse source. Here the ratio k_{CO} is the fraction of CO in CO$_2$ calculated with

$$k_{\mathrm{CO}} = \frac{C_{\mathrm{CO}}}{C_{\mathrm{CO}_2}}, \tag{8.28}$$

where C_{CO} and C_{CO_2} are the concentrations of CO and CO$_2$ respectively.

Unlike ozone production, the CO concentration increases proportionally with the energy density. In fact, Bremer *et al.* and Ponduri showed over a wide energy-density range that the CO concentration is mainly determined by the energy density and the fraction of remaining CO$_2$ [211, 226]. If we compare the results in Fig. 8.20 with the high-energy-density results of Brehmer [227, Figure 4.3] then all the results lie on one straight line (on a logarithmic scale).

Of course, there are some differences in the results presented in Fig. 8.20. Especially
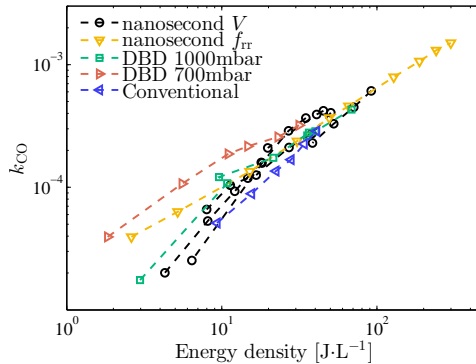
Figure 8.20: The fraction of CO that is produced in CO_2 as a function of the energy density. The results show that the amount of CO increases with the energy density, irrespective of what type of plasma is used. We varied the energy density of the nanosecond pulse source in two ways: by varying the voltage (nanosecond V) and by varying the repetition rate (nanosecond f_{rr}). Furthermore, we added the results of the conventional pulse source and the results of a DBD plasma. These DBD results were taken with permission from [215] and [216].

for low energy densities the results diverge. This is as much from errors on the measurements as from the different types of plasma. However, the results show that DBD plasmas perform equally well or better than our nanosecond pulses. The conventional pulse source performs slightly less well. Again, without ICCD imaging results and a deeper investigation into CO_2 plasmas, we are unable to comment on the results any further.

8.6.4 Optimal parameters for CO production

We again define the system yield as

$$\text{System yield} = G_{CO} \times \eta_{\text{tot}}. \tag{8.29}$$

Figure 8.21 shows this system yield for the results of Fig. 8.18. The results show very little difference in system yield for the different pulse durations and pulse polarities. The only parameter that changes the system yield is the applied voltage. Therefore, there is not one optimal setting for the pulse source for CO_2 conversion with the nanosecond pulse source. Only a higher voltage increases the system yield.

8.7 Summary and conclusions

In this chapter we applied our nanosecond pulse technology to three plasma processes: ozone generation, NO removal and CO_2 conversion. The yields of these processes are summed up in Table 8.1 and 8.2, which show the plasma yields and the system
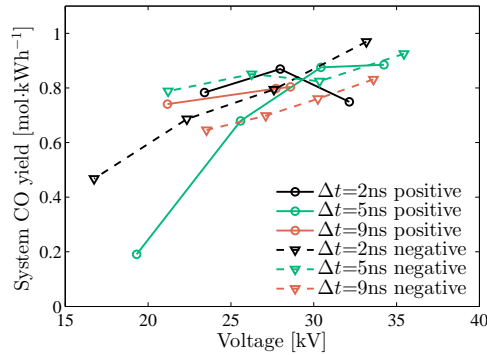
Figure 8.21: The system CO yield for the results of Fig. 8.18. Note that the scale of the yield is different than that of Fig. 8.18b. The results show that the system yield is relatively independent on pulse duration and pulse polarity. Only a higher applied voltage increases the yield.

Table 8.1: Influence of pulse parameters on plasma yields.

	Ozone generation	NO removal	CO_2 conversion
Amplitude ↑	+	+	+
Rise time ↓	++	++	+
Pulse duration ↑	+/-	+	+/-
Positive polarity	+	0	+

Table 8.2: Influence of pulse parameters on system yields.

	Ozone generation	NO removal	CO_2 conversion
Amplitude ↑	+	++	++
Rise time ↓	+++	+++	+
Pulse duration ↑	+	++	+/-
Positive polarity	+	0	+/-

yields of the three processes respectively. The '+'-symbols indicate how strong the yields increase with the stated parameter, the '+/-'-symbol indicates that the yield can either decrease or increase, depending on other settings and a '0' indicates that the yields do not significantly depend on that parameter.

A more extensive summary of the results and the main conclusions are listed below.

Ozone generation

- The plasma volume and the consequent streamer phase (primary/secondary) appear to influence the ozone yield slightly. When the pulse duration and/or the applied voltage increases, the plasma volume increases until streamers start to

cross the gap in the reactor (Chapter 7). As long as the plasma volume can increase, the ozone yield increases slightly with the pulse duration and more significantly with the applied voltage. Due to higher electric fields in the reactor for these settings (which also cause the increase in plasma volume) the enhanced electric field at the streamer head is higher and therefore the generation of radicals required for ozone production is higher, increasing the ozone production. The ozone production increases more significantly than the dissipated energy by the streamers, thereby increasing the ozone yield. When the pulse duration and/or the applied voltage is increased further, streamers start to cross the gap in the reactor and the increase in plasma volume slows and finally stops (Chapter 7). At this point secondary-streamer effects can become important and the ozone yields start to decrease.

- Secondary streamer effects appear to be important in the nanosecond pulsed plasma for ozone production, decreasing the ozone yield. However, longer pulses would be required to investigate this effect further. Alternatively, a higher applied voltage will also increase secondary-streamer effects, but for that to work the triple point on the wire-tightening mechanism has to be fixed to prevent spark breakdown at the end of the reactor.

- Negative pulses result in a plasma with a lower ozone yield due to the effect the thick streamers have on the plasma volume (a strong secondary-streamer phase in the thick streamers and a lower volume of primary streamers).

- Increasing the rise time of the applied pulses decreases the ozone yield due to a much smaller plasma volume (Chapter 7) that is generated with only slightly less energy. A longer pulse from a conventional pulses source, with a similar rise time as a short pulse from the nanosecond pulse source, results in a similar ozone yield, indicating that as long as there are no secondary-streamer effects, the ozone yield appears to be determined by the rise time rather than the pulse duration.

- The maximum obtained ozone yields (including the results of Chapter 6) were around $170–190 \, \text{g·kWh}^{-1}$ in synthetic air which is high compared to other pulsed corona plasmas.

- The optimal parameters for ozone production are a long pulse duration at the highest, positive voltage if we include the energy transfer of the pulse source to the plasma (which is highest for a high voltage and a long pulse duration).

NO removal

- NO can be removed very efficiently from synthetic air with yields as high as $2.5 \, \text{mol·kWh}^{-1}$ (or $14.9 \, \text{eV}$ per NO molecule) for a 135-ppm initial NO concentration at 50 percent removal and even for the 225-ppm results the yields are very high at around $1.75 \, \text{mol·kWh}^{-1}$ (or $21.3 \, \text{eV}$ per NO molecule) at 50 percent removal. These yields are among the highest reported in literature. However, for higher concentrations the yields decrease significantly. From an analysis of all the by-products formed in the plasma with NO, we could conclude that due to the

production of NO by the plasma, at high NO concentrations the NO concentration will be in equilibrium with the NO_2 concentration at high energy densities, inhibiting further removal of NO. Solutions to this problem were suggested.

- Positive and negative plasmas remove NO with almost the same yield. This is surprising, since we expected positive pulses to outperform negative pulses, just as with ozone production. However, due to the more pronounced primary-streamer phase of the positive plasma, more nitrogen radicals are generated, which promotes the formation of new NO.

- Longer pulse durations and higher applied voltages increase the NO yield, just as with ozone generation. However, the pulse-duration effect is more pronounced, even though the differences in yield between the various settings are small. Longer pulses (or higher voltages) are required to analyse the effect of pulse duration and the consequent secondary-streamer effects on the NO-removal process in more depth.

- Just as with ozone production (and for the same reason), the NO yields decrease with an increase in rise time. In addition, the use of longer pulses with a similar rise time as short pulses result in a similar NO-removal yield.

- The optimal parameters for NO removal are again a long pulse duration at the highest voltage due to the high NO yields and good matching of the pulse source to the plasma at these settings. Depending on which by-product is preferred, negative pulses (more ozone and N_2O_5) or positive pulses (more N_2O and NO_2) can be used and result in roughly the same NO-removal yield. We also showed that with addition of H_2O, by-product formation can be decreased (at the cost of an increased HNO_3 concentration, which can be removed with conventional techniques).

CO_2 conversion

- The main conclusion from the CO_2-conversion experiments is that the CO_2 plasma behaves differently than the plasma in synthetic air. Therefore, the imaging results of Chapter 7 are not valid to explain the observed phenomena.

- Matching of the pulse source to the plasma indicates that a negative pulse matches better, but the CO yields were higher for positive pulses. The yield results might indicate that the reduced electric field for negative streamers is higher than for positive streamers in CO_2.

- A longer rise time still influences the yield (just as with the ozone-generation process and the NO-removal process), but the effect is much less pronounced.

- A comparison between CO-production results for different plasmas (including DBD plasmas) showed that the CO production mainly increases with the energy density.

- Due to the lower CO yield at settings that show poor matching and vice versa, there is no optimal pulse duration for CO production. Only the applied voltage increases the total yield.

- The maximum energy efficiency of the CO_2 conversion with our plasma was around 11–12 percent.
- Based on the results we argue that our nanosecond pulse technology should not be used to generate CO_2 plasmas with the aim of energy-efficient CO generation. We showed results of DBD plasmas that were just as good, or better than our results, while DBD plasmas can generally be generated with much less effort and cost than our nanosecond pulse technology.

Nine

Conclusions, Recommendations, and Outlook

We started this thesis by explaining that non-thermal plasmas offer a possibility to replace conventional air-purification technology because these plasmas have very important advantages over conventional techniques. However, the efficiency of the plasma technology has to be increased, and a nanosecond pulsed corona plasma could be a solution.

In this thesis we showed that we can indeed significantly increase the yields of a number of processes (ozone generation and NO removal), but at the same time we showed that the penalty for these high efficiencies for NO removal can be an increased by-product formation and that it is not necessarily a good technique for CO_2 conversion. However, we can conclude that using very fast-rising, short high-voltage pulses is a good way to improve the efficiency of plasma-based air purification, and that the main parameter that brings about this increased efficiency is the rise time of the short pulses.

Using extremely short pulses for air purification comes with new challenges, such as the development of the pulse source, the measurement of the very fast high-voltage pulses, the energy transfer on such short time scales towards the plasma, the strong dependence of the plasma development on the complicated high-voltage pulse propagation in the system and how to optically observe the corona plasma. By careful design and thorough analysis we were able to face these challenges, and as a result provided new insights and knowledge for the research area of plasma processing with nanosecond high-voltage pulses.

In this conclusion we provide a summary of all the conclusions and achievements of the project. We start by briefly summarising the project goals. Then, in the subsequent three sections we evaluate these goals separately. We summarise the achievements and conclusions and provide recommendations for each goal. Finally, we present an outlook for the future.

9.1 Project goals

In this thesis we investigated the effect of very fast nanosecond pulses on transient-plasma generation with the purpose of air purification. The goals of this work could be divided into three categories:

- development of repetitive, adjustable-parameter, nanosecond pulse technology;
- study of the interaction between the nanosecond pulse technology and the plasma;
- application of the nanosecond pulse technology to air-purification applications to study the effect of the high-voltage pulse parameters on the process yield.

9.2 Nanosecond pulse technology

Nanosecond pulses have been used for around two decades to generate non-thermal plasmas for air-purification applications; however, recent studies show that even shorter pulses ($<$10 ns, which is about one order shorter than commonly used) can be very beneficial for these applications. Currently, researchers have achieved the generation of pulses that are still relatively long ($>$10 ns), have a long rise time (several nanoseconds), and/or are not square-shaped. Furthermore, a parametric study to investigate the effect of the pulse duration, rise time, and voltage (amplitude and polarity) is lacking (but strongly needed) for these short pulses. Our aim was to develop nanosecond pulse technology that can deliver this wide variety of pulses.

9.2.1 Nanosecond pulse source

We designed and built a repetitive (up to several kHz), flexible, single-line nanosecond pulse source with a rise time of several hundreds of picoseconds, with variable pulse duration from 0.5 ns to 10 ns and an adjustable amplitude of $\pm$0–50 kV. The main achievements and conclusions from this part are listed below.

- For the very short pulses we required, the frequencies involved are so high that the geometry of the pulse source dominates the pulse formation and therefore, 3D time-domain EM simulations were successfully used to design and model the nanosecond pulse source. Starting from basic theory and implementing this in the 3D time-domain EM solver of CST Microwave Studio we showed that we could obtain a very precise prediction of the pulse waveform. Thus, we were able to perform experiments on variable pulse duration ideas purely in simulations to verify the feasibility of these ideas.
- With the results of the theory and simulations we built a pulse source that generates 0.5–10-ns, 0–50-kV, sub-nanosecond rise-time, positive and negative pulses and verified its operation experimentally. The topology used is a single-line pulse source in which a pulse forming line (PFL) is charged in microseconds and is then discharged in nanoseconds into a matched coaxial cable that connects to the load. By varying the charge voltage and the length of the PFL, the pulse voltage (amplitude and polarity) and the pulse duration can be changed flexibly.

- For the first time at Eindhoven University of Technology we implemented an oil spark gap switch in a pulse source and showed that we could obtain extremely fast switching (up to 120 kV in several hundreds of picoseconds) at high repetition rates (up to several kHz) with this switch. Furthermore, an erosion study showed that we can operate the switch for a long time before electrodes have to be changed.

- We were able to identify and solve design issues with simulations (SPICE and 3D EM) and therefore were very flexible in our design. For example, we showed with simulations and in experiments that the connection of the pulse charger to the PFL of the nanosecond pulse source has to be sufficiently decoupled to obtain square-shaped output pulses without a plateau behind the pulse.

9.2.2 Microsecond pulse charger

The PFL of the nanosecond pulse source is charged with a microsecond pulse charger that we developed. We used microsecond pulses because shorter pulses would be able to cross the oil spark gap through capacitive coupling, and longer pulses would result in a lower hold-off voltage of the oil spark gap. The main achievements and conclusions from this part are listed below.

- We designed a compact ± 0–60-kV, 2–4-µs solid-state pulse-charger module, again starting from theory. We then used SPICE simulations to verify the design; finally, we built two pulse-charger modules in an IGBT implementation and connected them in series to obtain a maximum output voltage of 120 kV (positive and negative polarity). The maximum repetition rate of the pulse-charger modules is well over several kHz and can be used on a maximum load of 100 pF when connected in series, or 200 pF when used as stand-alone modules. Furthermore, optical triggering of the gates of the IGBTs and a compact build ensure reliable operation.

- The pulse-charger modules are short-circuit proof, and were designed so that they can also be used as stand-alone microsecond pulse sources for different applications, such as DBD plasmas for which we will use such a module in future work.

9.2.3 D-dot and B-dot sensors

Solutions to measure the very fast high-voltage and high-current pulses from our nanosecond pulse source are not readily available. Therefore, we took the challenge and developed our own very high-frequency sensors to measure these pulses. The main achievements and conclusions from this part are listed below.

- We developed D-dot and B-dot sensors with a bandwidth of over 4 GHz and integrated them on the coaxial cable connecting the pulse source to the load. The advantage of this method is that the sensors can be calibrated using both a time-domain method and a frequency-domain method before the cable is installed

in the nanosecond pulse source setup. A further advantage of this calibration method is that the sensors are not limited to working only in the differentiating regime or only in the self-integrating regime, because we can calibrate both regimes. We corrected the measured signals for the transfer function of the measuring cables and the sensors utilising software.

- By placing the sensors close to the corona-plasma reactor (but not directly near it), we are able to measure the incoming pulse energy and the energy dissipated by the plasma at just one sensor position. This saves oscilloscope channels and allows the use of two sensors of each type at this position for averaging purposes.
- Due to the installation of the sensors on a coaxial cable, our developed sensors are very versatile and could be used in any pulsed-power system where a coaxial cable connects a pulse source to its load.

9.2.4 Recommendations

We are very satisfied with the nanosecond pulse technology we developed and expect many more years of research to follow with it at Eindhoven University of Technology, transient-plasma related or otherwise (such as in the field of bioelectrics [39, 40]). However, we will end this section with some recommendations that would make the technology even better suited for future research.

- In its current implementation, it is difficult to adjust the rise time of the pulses. A network could be designed and integrated in the pulse source between the spark gap and the cable with which the rise time could be adjusted. This is not a trivial task and would require extensive 3D-EM simulation. However, we are confident that such a network can be designed and implemented.

- The SA24272 coaxial cable connecting the pulse source with the corona-plasma reactor can not be easily removed from the pulse source. We suggest that the coupling to the pulse source and the reactor be made easy to disconnect so that multiple cables can be used (with different lengths, for instance). In this way, several experiments can be run in parallel where the pulse source is time-shared between the experiments.

- We showed in Chapter 3 that the standard deviation on the amplitude of the output voltage of the pulse source is significant due to the oil spark-gap switching. It would be useful to decrease this standard deviation by implementing a triggered spark gap or by using flow-control techniques in the oil spark gap, which is an option indicated by other researchers.

- A final recommendation regards the sensors. At the moment we have sensors to measure the voltage and current waveform from the pulse source and the plasma energies, but we have no detailed information on the plasma current inside the reactor. It would be useful to have a new set of sensors at multiple positions in

the reactor, measuring electric fields and magnetic fields, to measure and calculate plasma/streamer currents and possibly even electric fields of streamers. An ultimate goal would be to obtain the position-dependent energy density of the plasma to relate to the ICCD-imaging results. However, to extract useful information from the data of such sensors would require an extensive investigation.

9.3 Transient plasma interaction

The second project goal in this thesis was to investigate the interaction of the very short high-voltage pulses generated by the pulse source with the transient plasma generated in a coaxial corona-plasma reactor. We did this by studying the electrical energy transfer efficiency of the pulse source to the plasma ('matching') and by optically observing the generated streamer plasma with time-resolved and space-resolved ICCD imaging.

9.3.1 Matching

A transient plasma is a highly dynamic load, which makes matching the pulse source with a fixed 50-Ω output impedance to the reactor and the plasma a challenge. Moreover, due to the high-frequency nature of the pulses, pulse reflections at the plasma-reactor interface and at the end of the reactor complicate the matching even further. We have investigated the matching with an extensive study for various pulse-source parameters and reactor geometries. The main achievements and conclusions from this part are listed below.

- Pulse reflections on the cable coupler significantly influence the matching, showing that the impedance of the reactor should be as close as possible to 50 Ω. We made use of these reflections by calculating time-dependent reflection coefficients and transmission coefficients to determine the time-dependent reactor impedance. This reactor impedance shows good agreement with calculated values and decreases in time and with an increased applied voltage due to the plasma development. Therefore, good matching is achieved for the longer pulses with a high voltage amplitude, since for these parameters the plasma develops most rapidly and extensively in the reactor. For the same reason, a short rise time increases the matching. By systematically varying parameters of the reactor, we obtained a wire-cylinder reactor with which matching of over 80 percent is possible. This shows that even with the short pulses with which we work, we are able to realise a good energy transfer to the plasma.
- When negative pulses are used, the matching is generally (slightly) better than when positive pulses are used. As a possible explanation, we proposed a larger inception cloud and the higher initial streamer velocity for negative streamers. A larger inception cloud and/or a higher initial streamer velocity result in an artificially increased inner-wire diameter and consequently a lower reactor impedance. Unfortunately, we could not verify these possibilities experimentally.

- The matching improves significantly if the vacuum impedance of the reactor is closer to the 50-Ω output impedance of the pulse source. For this reason, we implemented the new idea of using a multiple-wire reactor, which significantly decreases the vacuum impedance of the reactor, while maintaining a high electric field on the high-voltage electrode for streamer generation by using multiple thin wires as the high-voltage electrode. We applied the multiple-wire reactor to our nanosecond pulse source and showed that we could achieve matching of over 90 percent.
- As a last method, we were able to significantly improve the matching by applying a DC-bias voltage to the corona reactor. During a research visit to Kumamoto University in Japan, we introduced a novel way to apply a DC bias electric field to a corona reactor by means of integrated bias electrodes. A dielectric layer is installed on the cylinder wall of a wire-cylinder corona-plasma reactor. On top of this layer we apply tertiary electrodes, to which we apply the DC bias voltage. With this method we eliminate the issue of pulse deterioration by the coupling network for the DC voltage that a traditional implementation has. We used this reactor on a nanosecond pulse source and showed an improved initial matching by a factor of 1.2–2, depending on the pulse parameters.

9.3.2 Streamer development and propagation

To investigate the streamer development in the corona-plasma reactor, we developed a fully automated ICCD-imaging setup to take time-resolved and space-resolved images of the plasma for various pulse source settings. The main achievements and conclusions from this part are listed below.

- The development and propagation of the streamers in the reactor depend on the voltage profiles in the reactor. Due to a complex interaction of the pulse propagation, the pulse reflection at the end of the reactor, and the energy the streamers dissipate as a result, these voltages vary in time and position. Consequently, when the pulse is short with respect to the reactor length, the voltage profiles in the reactor are far from homogenous, and as a result the coverage of the streamers in the reactor is not homogenous because a higher voltage at a position in the reactor results in a higher streamer velocity (and consequently a longer streamer). Furthermore, the streamer width slightly increases with the voltage.
- We developed a SPICE model of the reactor to simulate the voltage inside the reactor as a function of time and position. Comparison with experimental results shows good agreement, but also shows that a more extensive model would be required to correctly model the pulse dispersion due to the plasma. Nevertheless, the model is a useful tool to predict the voltage profiles in the reactor and to explain obtained ICCD-imaging results.
- The rise time of the pulses has a significant influence on the streamer properties: the streamers propagate faster, have longer length, and are wider for shorter rise

times. With the simulated voltage profiles we showed that at least part of this observation can be explained by the higher voltage levels in the reactor for faster rise-time pulses. However, other effects such a higher inception voltage for fast rise-time pulses likely also play an important role.

- Positive and negative pulses result in similar streamer properties, such as the streamer width, streamer length, and streamer velocity. Only the streamer coverage was less homogeneous for negative pulses due to unexpected thick streamers originating from a triple point on a reactor feature.

9.3.3 Recommendations

In this thesis we have unravelled, in detail, the complex interaction of nanosecond high-voltage pulses with the transient plasma in the corona-plasma reactor, and have obtained a significant amount of important results on the various processes that play an important role during these short timescales. However, with an investigation of this nature, especially with the new setups we developed, there remain unanswered questions and new questions appear. We list some of the most relevant recommendations below (and some will be included in the recommendations of the last project goal).

- Even though we already achieved good matching of over 80 percent, we showed that with two new types of reactor, we could improve the matching (to over 90 percent with the multiple-wire reactor). Both of these reactors will have to be investigated further. For instance, the multiple-wire reactor can be endlessly varied in its geometry (number of wires, wire radii, etc.). Simulations and experiments will have to show what the optimal geometry is. Furthermore, the reactor with a DC bias was developed as a versatile bias reactor: on the tertiary electrodes we can also apply (microsecond) pulsed voltages or RF-voltages to improve the matching of the nanosecond pulse. These options have to be explored. As an ultimate matching reactor, the multiple-wire reactor can be combined with the DC-bias reactor.
- The possibility of using a cable with a higher impedance than 50 Ω can be investigated with the purpose of increasing the matching. The nanosecond pulse source will have to be adapted accordingly, but since the plasma is (initially) a high-impedance load, it is a worthwhile option to explore.
- With the ICCD-imaging setup we have a unique tool to couple the matching observations with the imaging results. In this thesis we have shown some interesting results, but there is still much to be explored. For instance, we need to take a much closer look at the high-voltage wire with an ICCD camera during the inception of the streamer plasma to investigate whether the higher initial matching for negative pulses is indeed caused by a larger inception cloud or faster initial streamers.
- An interesting question that arose was: why are the streamer parameters for positive and negative pulses so similar in our experiments (while for longer, slower rising pulses there is a distinct difference)? Together with the influence of the rise

219

time of the pulses on the streamer properties, this will be an interesting topic for a more extensive experimental investigation combined with theoretical streamer modelling.

9.4   Air purification processes

The final goal of the project was to investigate the effect of the short pulses on plasma-processing applications. We chose three applications: ozone generation, NO removal, and CO_2 conversion. The main achievements and conclusions from this part are listed below.

- The maximum ozone plasma yields for our nanosecond pulsed transient plasma are around 170–190 g·kWh^{-1}, which is very high compared to other studies. The yields only slightly depend on different pulse parameters. The plasma volume and the consequent streamer phase (primary/secondary) slightly influence the ozone yield. When the pulse duration and/or the applied voltage increase, the plasma volume increases until streamers start to cross the gap in the reactor. As long as the plasma volume can increase, the ozone yield increases. However, when streamers start to cross the gap, secondary streamer effects can become important, and the ozone yields start to decrease. Furthermore, the ozone yield is lower for negative pulses. The effects of the thick streamers for negative pulses decrease the plasma volume and are a likely cause of the lower ozone yield.
- The optimal settings for ozone generation (high system yield and high throughput) are the longest pulses we used at the highest positive voltages we used due to the very high matching at these settings, combined with the higher ozone plasma yields for positive pulses.
- NO can be removed very efficiently from synthetic air with our nanosecond transient plasma, with yields as high as 2.5 mol·kWh^{-1} (or 14.9 eV per NO molecule), which are among the highest reported in literature. However, this process is much more complex than ozone generation. At high energy densities and high initial NO concentrations, the production of NO by the plasma becomes important due to the presence of nitrogen radicals that the plasma produces.
- Just like ozone production, the optimal settings for NO generation are long pulses and high voltages due to the high matching at these settings. However, unlike ozone generation, the polarity is less important.
- For ozone generation and NO removal, the rise time of the pulses has a significant influence on the process yields. A longer rise time decreases the dissipated energy by the plasma, but decreases the plasma volume even more significantly, resulting in a lower process yield.
- The results of the CO_2-conversion experiments show that the CO_2 plasma is significantly different from the plasma in synthetic air. Too few results are available for significant conclusions. If we compare our results with the results of other non-thermal plasmas, such as DBDs, then the main conclusion is that a nanosec-

ond pulsed transient plasma should not be used for CO_2 conversion due to the higher complexity of the technology and the lower yields.

9.4.1 Recommendations

- We showed that with the voltage amplitudes and pulse durations we used, we primarily have primary streamers (no secondary streamers were visible). If we want to fully understand the effect of the different streamer phases, longer pulses or higher voltages should be used to increase the secondary streamer phase. Higher applied voltages will be possible once the triple point causing the thick streamers is removed; then we can also compare the negative streamer plasma more directly with the positive streamer plasma.
- We have only shown some of the possible data that can be gathered with the ICCD-imaging setup, but an extensive amount of additional data can be gathered for more settings of the pulse source, allowing us to very precisely calculate the plasma volume for different pulse source settings. Combined with plasma-processing experiments, these results can lead to a better understanding of how the plasma volume influences the radical generation for different air-purification processes. Furthermore, coupled with a kinetic model to estimate different types of radicals, the results could be very insightful.
- The relevance of the pulse reflection that is reapplied to the reactor has to be further investigated. This pulse results in some energy dissipation by the plasma; thus, imaging and possibly time-resolved in-situ gas diagnostics would be required to understand the effect of this second pulse to the net result of the plasma process.

9.5 Outlook

We have accomplished much in the past years, building all the setups from scratch and gathering a significant amount of data (not all of which was shown in this thesis). Yet it feels like we have barely scratched the surface of the fascinating world of nanosecond pulsed transient plasmas. With the ICCD-imaging setup we still have a lot to explore, and if we could couple the imaging results with time-resolved and position-resolved electrical measurements with new electrical sensors in the reactor, we could gain incredible insights into the development of streamers. If we combine these measurements with the gas diagnostics of this thesis — or even with new diagnostics such as optical emission spectroscopy — we could develop a much deeper understanding of the electric fields in the streamer and the radicals that they produce. For all these investigations pulse parameters, reactor parameters, and plasma-processing conditions can be varied, creating endless possibilities for future work.

In parallel with experimental work, streamer modelling such as that performed at CWI (Centrum voor Wiskunde en Informatica) in Amsterdam is an invaluable tool to predict and/or verify experimental results. Coupled with the experimental results, this

modelling is the primary pathway to a deeper understanding of the discharge phase of the streamer plasma. At the same time, modelling of the reaction phase of the plasma would provide more insight into how the produced radicals result in the compounds we measure in experiments. Altogether, the future possibilities are endless.

During this project we collaborated with researchers from INP Greifswald, Germany (resulting in Appendix C and [72]), from Kumamoto University, Japan (resulting in Appendix A), from CWI in Amsterdam, and from the EPG (Elementary Processes in Gas Discharges) group and the PMP (Plasma and Materials Processing) group of the Applied Physics department of Eindhoven University of Technology. There have already been several requests from other researchers for the use of our nanosecond pulse technology, showing that more successful experimental collaborations lie ahead. Besides these experimental collaborations, we have now arrived at a point where streamer modelling becomes essential to take the next step in understanding what we observe in the laboratory. Therefore, we will use the close contacts we have at CWI to jointly explore the world of nanosecond pulsed transient plasmas.

A

Matching with a Plasma Reactor with a DC Bias Voltage

Abstract

   In this appendix we propose experiments which investigate the matching of a nanosecond pulse source to a corona plasma reactor which is aided by a high voltage on a tertiary electrode. The corona plasma reactor is a wire-cylinder reactor as is commonly used in pulsed power plasmas. A tertiary electrode is situated on a dielectric layer against the cylinder of the reactor. On this tertiary electrode we can apply a pulsed, RF or DC voltage to provide an additional plasma and bias voltage in the corona plasma reactor. The advantage of this method is that no compactly connected decoupling network is required to maintain the pulse shape of the primary high-voltage pulses. The pulse source that energises the main corona plasma is the nanosecond pulse source of the Kumamoto University, Japan. We show results of experiments with a DC voltage on the tertiary electrode. We varied the amplitude and polarity of the pulsed voltage, as well as the DC voltage and investigated their effect on the corona plasma with energy and ozone measurements. The results show that the matching to the reactor increases with increasing DC voltages. However, the matching effect decreases slightly at a higher repetition rate. The results also show that by applying a $\pm 15\,\mathrm{kV}$ DC bias voltage on the specially designed corona plasma reactor we can improve the initial pulse matching — even if we correct for the energy cost in the DC circuit — by a factor of around 1.25–2 depending on the voltage pulse amplitude, voltage polarity and on the repetition rate, which proves that the new corona plasma reactor with a tertiary electrode works well to improve matching. Furthermore,

- T. Huiskamp, N. Takamura, T. Namihira and A. J. M. Pemen, "Matching a Nanosecond Pulse Source to a Streamer Corona Plasma Reactor with a DC Bias," *Plasma Science, IEEE Transactions on*, vol. 43, no. 2, pp. 617–624, 2015.

ozone measurements confirmed that a better matching also results in a higher
ozone production, but in similar ozone production energy yields.

A.1   Introduction

In Chapter 6 we investigated which plasma reactor configuration yields the best energy
transfer ('matching') of the high voltage pulse from our nanosecond pulse source to the
plasma reactor. A very promising type of plasma reactor was the multiple-wire reactor,
which obtained very good matching results. In this appendix we introduce a new type
of promising plasma reactor: the plasma reactor with a DC bias. We developed this
plasma reactor during a research internship at the Kumamoto University in Kumamoto,
Japan.

In the introduction of Chapter 6 we referred to a number of different matching
methods and demonstrated some of these ourselves. These methods included vary-
ing the reactor length, reactor configuration, pulse amplitude, pulse polarity, pulse
duration, pulse rise time, pulse source output impedance and energy density volt-
age [29, 34, 117–120, 122–125]. However, another good way to provide better matching
is to superpose the pulse voltage on a DC bias [29, 117–119, 121, 125].

In this chapter we propose a new matching method by adding a tertiary electrode
on a dielectric layer in the corona plasma reactor. On this tertiary electrode we can
apply a pulsed, RF or DC voltage. The purpose of the pulsed and RF voltages is to
generate a (surface) dielectric barrier ((S)DBD) plasma on the tertiary electrode. This
(S)DBD plasma can improve the matching of the pulse source to the corona plasma
reactor in two ways.

First, the (S)DBD plasma can be generated at a high frequency to ensure that
the background ionisation of the gas in the corona plasma reactor is higher. A higher
background ionisation provides more free electrons for the streamers of the main plasma
to propagate, therefore changing the main plasma behavior [167].

Second, a secondary plasma on the surface of the outer wall of the corona plasma
reactor virtually decreases the outer diameter of the reactor. This decreases the trans-
mission line impedance Z_r of the reactor:

$$Z_r = \frac{1}{2\pi}\sqrt{\frac{\mu_r\mu_0}{\epsilon_r\epsilon_0}}\ln\frac{d_o}{d_i},\tag{A.1}$$

where μ_r and ϵ_r are the relative permeability and permittivity of the medium in the
reactor respectively (both 1 for air), μ_0 and ϵ_0 are the permeability and permittivity
of vacuum respectively and d_o and d_i are the outer and inner diameter of the reactor
respectively. A lower transmission line impedance improves the matching to the pulse
source, because the transmission line impedance of a corona plasma reactor is almost
always much higher than the output impedance of the source.

The purpose of a DC voltage on the tertiary electrode is to provide a DC bias to
the pulse voltage, because a DC bias has proven to be a very effective way to match a
pulse source to a corona plasma [29, 117–119, 125]. This DC voltage is superimposed on

the pulsed voltage and has some significant advantages. First, a DC bias increases the electric field in the plasma reactor and consequently results in a more intense discharge and therefore increases the matching. Second, this DC bias can generally be added at a low cost and therefore offers a cheap method to vary the plasma behaviour and last, the DC bias offers simple way to add energy to the plasma without the complexities of switching a high current and a high voltage. The downside to the DC-bias method is that the DC voltage has to be decoupled from the pulse voltage by a decoupling network, which can have an adverse effect on the properties of the pulse. When the DC voltage is applied to the tertiary electrode in the corona plasma reactor, this issue is overcome.

The result of the DC bias voltage will be an increased electric field in the plasma reactor which will result in a more intense plasma. Also, a DC corona can develop around the central wire, which can artificially increase d_i and will therefore decrease the impedance of the corona plasma reactor according to Eq. A.1 and increase the background ionisation in the corona plasma reactor.

In this chapter we focus on the experiments with a DC voltage on the tertiary electrode. We measure plasma energies to investigate if a better matching is provided by applying a DC voltage. Furthermore, we measure ozone production by the plasma to verify if a higher energy dissipation by the plasma also results in a higher plasma effectiveness.

In Section A.2 we present our experimental setup and procedure, followed by the results and discussion in Section A.3 and the conclusions in Section A.4.

A.2   Experimental setup and procedure

A.2.1   Nanosecond pulse source

The nanosecond pulse source we used for the experiments is described in [6,36]. It is a triaxial Blumlein configuration switched by a high-pressure SF_6 spark gap switch. A corona plasma reactor is connected directly to its output. Figure A.1 shows this setup.

The SF_6 spark gap is located on the left side of the figure. It switches the middle conductor of the Blumlein line to ground. This middle line is charged through the charging port with a charging circuit that will be described in Section A.2.3. When the spark gap switches a pulse propagates towards the output of the pulse source. This pulse has the same amplitude as the charging voltage and a pulse duration that is determined by the length of the middle conductor (5 ns in our case).

At the output of the pulse source a calibrated capacitive voltage divider (CVD) and a Bergoz CT-F1.0 current transformer measure the output voltage and current respectively. All waveforms were measured with a 2.5 GHz bandwidth oscilloscope (Tektronix DPO7254C) located in an EMI shielded room. Figure A.2 shows a typical voltage, current and energy measurement. In Fig. A.2c, E_{pulse} indicates the total energy dissipation in the plasma. This includes the energy deposited into the plasma by only the initial pulse $E_{1stpulse}$, but also by the subsequent reflections of the pulse. These reflections are a result of imperfect matching of the pulse source to the plasma.
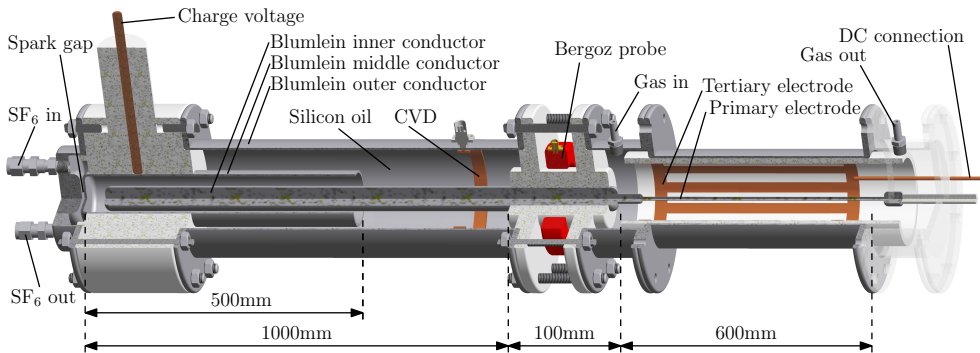
Figure A.1: Sketch of the 5 ns-pulse source with corona plasma reactor. Not to scale (for display purposes the length and thickness of various parts have been modified). The nanosecond pulse source is a triaxial Blumlein source. The SF$_6$ spark gap switches the middle conductor of the Blumlein line to ground. This middle line is charged through the charging port with a charging circuit. When the spark gap switches a pulse propagates towards the output of the pulse source. This pulse has the same amplitude as the charging voltage and a pulse duration that is determined by the length of the middle conductor.

The reflected pulse propagates back into the pulse source, where it will be reflected again to the corona reactor.

A.2.2 Corona reactor with DC bias

The nanosecond pulse source is connected to the corona plasma reactor as shown in Fig. A.1. Figure A.3 shows a cross-section drawing of this corona plasma reactor. The corona plasma reactor is a wire-cylinder reactor to which we added a dielectric layer on the cylinder wall. This layer consists of ceramic (Al$_2$O$_3$). On top of this layer we placed tertiary electrodes (copper strips) for the DC bias voltage. In future experiments we can also apply pulsed and RF-voltages to these electrodes to generate a secondary (S)DBD-plasma. The inner diameter of the cylinder electrode is 75 mm. The ceramic tube has a wall thickness of 5 mm and has an inner diameter of 65 mm. The length of the corona plasma reactor is 600 mm.

Figure A.4 shows the DC circuit that is used to connect to the tertiary electrodes. Resistor R limits the charging current of buffer capacitor C and also prevents any transients from the nanosecond pulse to damage the DC source. The buffer capacitor provides a stable DC voltage on the tertiary electrodes during plasma discharges. A P6015 voltage probe and a Bergoz CT-F0.5 current measure the associated voltage and current respectively.

The advantage of our DC-bias method is the way we add the DC voltage to the pulse source. A conventional method to superimpose the pulse voltage onto the DC voltage is by using a coupling capacitor to decouple the pulses from the DC voltage [18,25]. This is done by connecting a capacitor between the pulse source and the high-voltage wire
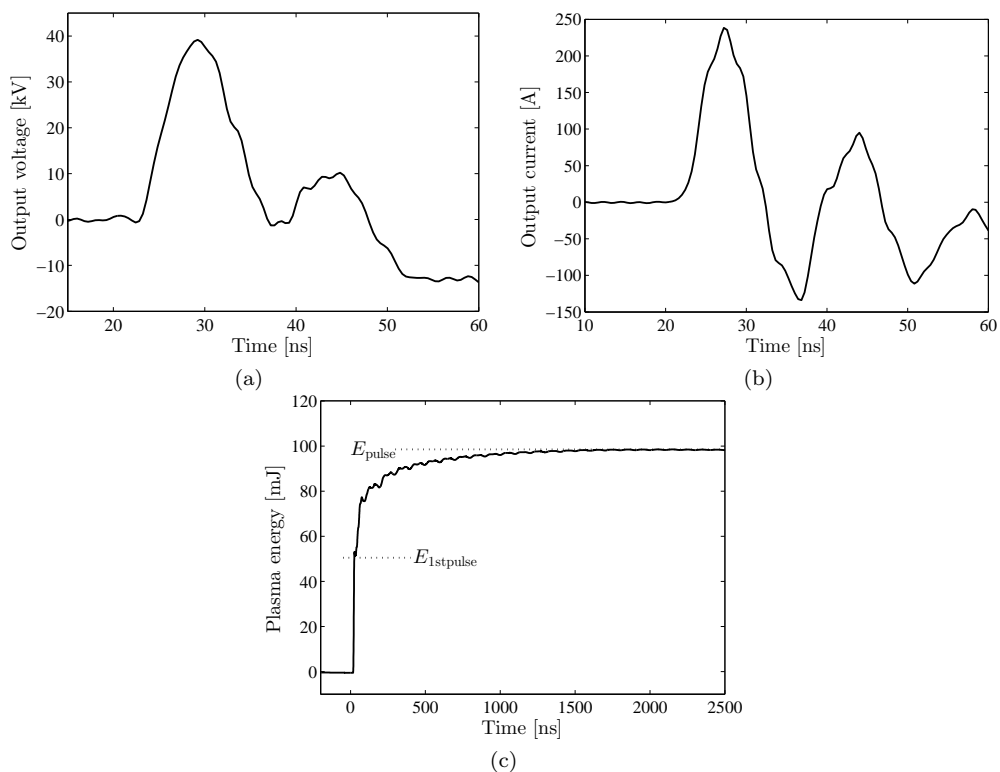
Figure A.2: Typical waveforms in the nanosecond pulse source for a pulse voltage of 40 kV and $V_{DC} = $ -5 kV. (a) Voltage. (b) Current. (c) Energy. E_{pulse} indicates the total energy dissipation in the plasma. This includes the energy deposited into the plasma by only the initial pulse $E_{1stpulse}$, but also by the subsequent reflections of the pulse. Note that the time scale for (c) is different from (a) and (b).

of the plasma reactor. With short pulses, this coupling capacitor has to be mounted very locally to avoid a deterioration of the pulse shape. Achieving the incorporation of a compactly connected capacitor is difficult. We avoid this difficulty by applying the DC bias voltage to the tertiary electrodes in the plasma reactor.

A.2.3 Charging circuit

Figure A.5 shows the charging circuit of the nanosecond pulse source. The high-voltage capacitors C_{HV} are charged in parallel by a 0–20 kV DC source with charging resistor R_{ch}. The voltage on the bottom capacitor is then reversed by thyratron switch S and inductor L_1. As a result, twice the charging voltage is applied to the primary winding of pulse transformer T and the high-voltage capacitors are discharged into the pulse forming line of the nanosecond pulse source. The Finemet core of the pulse transformer
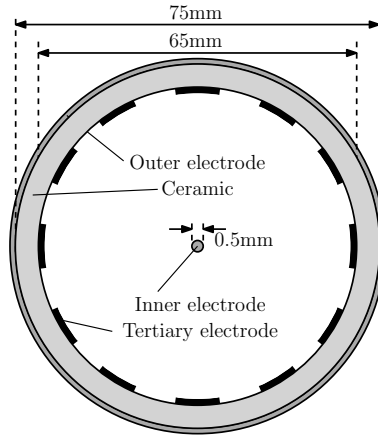
Figure A.3: Cross-section of the corona plasma reactor (not to scale). Tertiary electrodes are placed over a ceramic layer on the outer electrode. A DC bias is applied to these tertiary electrodes.
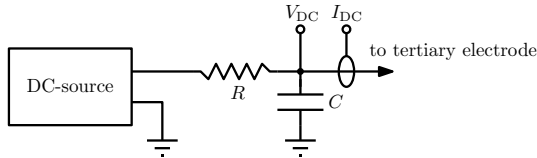

Figure A.4: The DC circuit. The output of this circuit is connected to the tertiary electrodes of the corona plasma reactor. Resistor R limits the charging current of buffer capacitor C and also prevents any transients from the nanosecond pulse to damage the DC source. The component values of this circuit are: $C = 8\,\text{nF}$ and $R = 1\,\text{M}\Omega$.

is pre-magnetised with an extra winding on the pulse transformer and a DC source with resistor R_{LV}. This allows for a bigger flux swing of the pulse transformer core without saturating.

A.2.4   Matching

We introduce four matching definitions to analyse the matching of the nanosecond pulse source to the corona plasma reactor: the total matching η_{tot}, the initial matching η_{i}, the corrected total matching $\widetilde{\eta}_{\text{tot}}$ and the corrected initial matching $\widetilde{\eta}_{\text{i}}$.

The total matching is the energy transfer efficiency of the total stored energy in the Blumlein line to the plasma and is calculated with

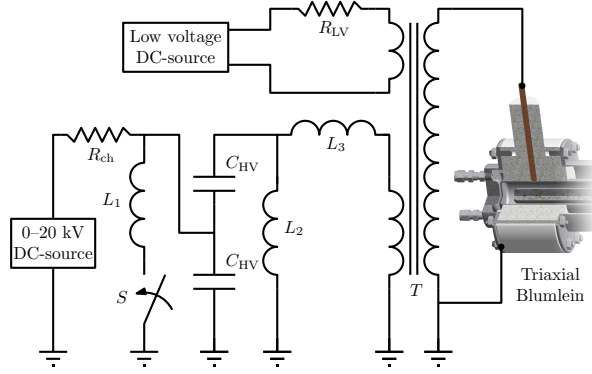$$\eta_{\text{tot}} = \frac{E_{\text{pulse}}}{E_{\text{Bl}}}, \tag{A.2}$$

Figure A.5: The circuit that charges the nanosecond pulse source. The high voltage capacitors are charged in parallel with a high-voltage DC source and discharged in series by voltage reversal with a thyratron (S). The capacitors are discharged into the pulse forming line of the Blumlein line via a pulse transformer. A DC reset current flows through an additional winding on the pulse transformer to reset the core after each pulse. The component values of this circuit are: $R_{ch} = 600\,\Omega$, $L_1 = 15\,\mu H$, $C_{HV} = 8\,nF$, $L_2 = 4.8\,mH$, $L_3 = 70\,\mu H$, $R_{LV} = 5\,\Omega$ and T is a 1:5 pulse transformer with a Finemet core.

where E_{Bl} is the total stored energy in the Blumlein line, which we calculate with

$$E_{Bl} = \frac{1}{2}C_{Bl}V_{pulse}^2, \tag{A.3}$$

where V_{pulse} is the amplitude to which the line is charged (the peak pulse amplitude) and C_{Bl} is the total capacitance of the Blumlein line, which we calculate with

$$C_{Bl} = \frac{2\pi\epsilon_0\epsilon_r L}{\ln\frac{d_2}{d_1}}, \tag{A.4}$$

where ϵ_r is the relative permittivity of the insulating silicon oil in the triaxial Blumlein pulse source, L is the total length of the Blumlein line and d_2/d_1 is the ratio of the outer and inner diameter of the Blumlein lines. With $\epsilon_r = 2.7$, $L = 0.913\,m$ and $d_2/d_1 = 2$, the total capacitance of the Blumlein line is 198 pF.

The initial matching is the energy transfer efficiency of the total stored energy in the Blumlein line to the plasma generated with the first pulse and is calculated with

$$\eta_i = \frac{E_{1stpulse}}{E_{Bl}}. \tag{A.5}$$

This matching definition is useful to understand how well the first applied pulse matches to the reactor, because in our own nanosecond plasma setup we insert a long SA24272 cable to act as a delay line between the nanosecond pulse source and the corona plasma

reactor. Any pulse reflections will be re-applied to the load more than 200 ns later [72]. Therefore, the initial matching of the pulse source to the plasma load is the most important goal of the study in this chapter.

Additionally we correct the total matching with the energy that is supplied by the DC circuit. We calculate the corrected matching with

$$\widetilde{\eta}_{\text{tot}} = \frac{E_{\text{pulse}}}{E_{\text{Bl}} + E_{\text{DC}}}, \tag{A.6}$$

where E_{DC} is the energy supplied by the DC circuit.

And finally, we correct η_i with E_{DC}:

$$\widetilde{\eta}_i = \frac{E_{\text{1stpulse}}}{E_{\text{Bl}} + E_{\text{DC}}}. \tag{A.7}$$

A.2.5 Ozone measurements

We used a UV/VIS spectrophotometer (V-550, JASCO Corporation, Japan) for absorbance measurements to determine ozone concentration in this chapter. The optical cell in which we measured the ozone concentration is situated in the exhaust of the plasma reactor. The ozone concentration was determined using

$$\log \frac{I_0}{I} = \frac{C_{\text{mol·L}^{-1}}}{\epsilon d}, \tag{A.8}$$

where I and I_0 are the light intensity in the presence and absence of ozone respectively, $C_{\text{mol·L}^{-1}}$ is the ozone concentration (in mol·L^{-1}), ϵ is the molar extinction coefficient (in L·mol^{-1}cm^{-1}) and d is the path length used in the measurements (in cm) [229]. We used $\epsilon = 3000$ L·mol^{-1}cm^{-1} at a wavelength of 254 nm and $d = 1$ cm in our measurements.

We calculated the ozone yield (in g·kWh^{-1}) in a similar way as we did in Eq. 6.12.

A.3 Results and discussion

A.3.1 Energy measurements

In most corona plasmas with a DC bias, the DC bias is applied to the central electrode and added directly to the pulsed voltage [29, 117–119, 125]. In doing so, the DC bias increases the applied electric field (and thus E/n) from the central electrode to the grounded wall in the reactor. In our case, we apply the DC bias to an electrode near the wall. Therefore, to increase the electric field in the corona reactor we apply a positive DC voltage to the tertiary electrode when we have a negative pulse voltage and vice-versa.

We measured the energy that the plasma dissipates for both negative and positive pulse voltages. Figure A.2 shows a typical energy measurement. We differentiate between two energies. First, the total plasma energy E_{pulse}, which is the total dissipated

power by the plasma due to the high-voltage pulse and its reflections. And second, the plasma energy due to the first pulse E_{1stpulse}. This last energy parameter is especially important because it indicates how well the pulse source matches to the corona reactor. Besides energy measurements in the nanosecond pulse source, we also measure the energy E_{DC} that is supplied by the DC circuit.

From the first reflection of the high-voltage pulse onward the gas in the corona reactor is highly ionised and therefore any extra applied high-voltage (due to the pulse reflections) will sustain or re-ignite the plasma [179]. In the nanosecond pulse source setup of this thesis we use the SA24272 cable between the nanosecond pulse source and the load. Any pulse reflections will be re-applied to the load more than 200 ns later [72]. Therefore, the initial matching of the pulse source to the plasma load is the most important goal of this work and E_{1stpulse} gives the most information..

Figures A.6 and A.7 show the results of the total energy measurements for positive and negative pulse voltages respectively at two different repetition rates of the pulse source f_{r}: 1 Hz and 100 Hz*. The error bars indicate the standard deviation on each measurement. At 100 Hz repetition rate arc discharges started to occur in some measurements. Therefore, we performed these measurements only up to 30 kV or 35 kV for those settings. We did all measurements with synthetic air (< 5 ppm H_2O content) in the corona plasma reactor with a flow of 1 L·min^{-1}.

From the results we can conclude that applying a DC bias to the tertiary electrode increases the total energy dissipated by the plasma from the nanosecond pulse, which indicates improved matching of the pulse source to the reactor. The energy increase becomes more pronounced when the DC voltage increases. This effect could be attributed to the higher electric field in the plasma reactor that a DC bias voltage will ensure. Also, a DC corona could develop on the central wire, which can artificially increase d_{i} and will therefore decrease the impedance of the corona plasma reactor according to Eq. A.1.

However, for higher repetition rates the matching effect of the DC bias reduces slightly. A possible explanation could be a shifting dominant source of background ionisation. The background ionisation of the gas in the corona plasma reactor will be increased if a DC corona plasma ignites at the wire electrode due to the applied DC bias. With this higher background ionisation the main plasma ignites more readily, resulting in a higher dissipated energy. For high repetition rates the background ionisation of the gas is further increased because there is more plasma [167]. Therefore any effect of a higher background ionisation due to the DC bias becomes less pronounced.

The improved plasma energies at higher applied DC voltages are accompanied by an energy cost in the DC circuit. Especially for high DC voltages E_{DC} increases significantly.

Figures A.8 and A.9 show the energy deposited by the first pulse for positive and negative pulse voltages respectively. It is apparent that E_{1stpulse} increases significantly

---

*We also performed all measurements at a repetition rate of 10 Hz. However, the results were all between the 1-Hz and 100-Hz measurements and did therefore not add much information to this appendix. They are included in [228].
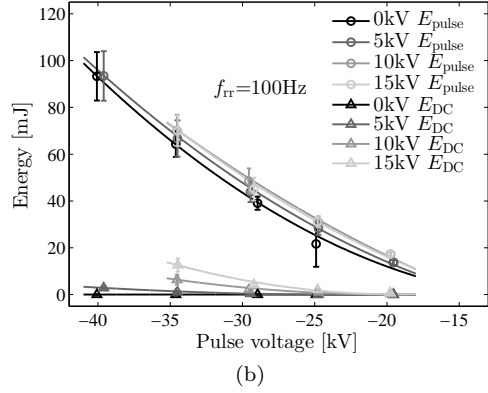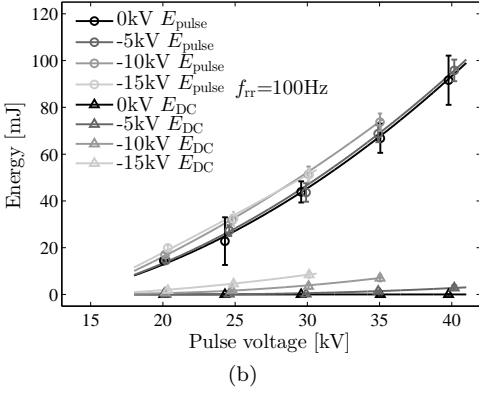
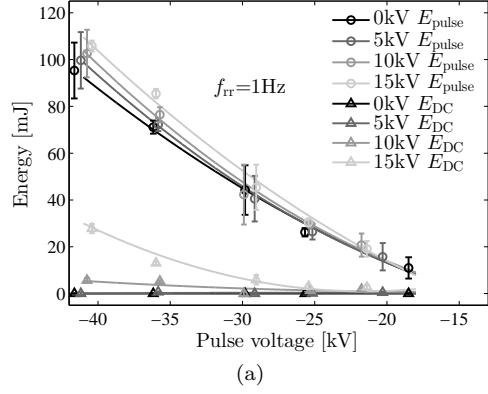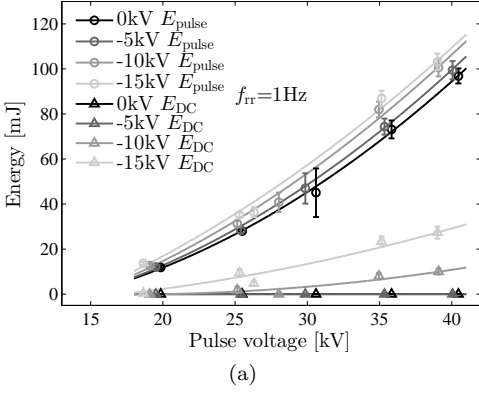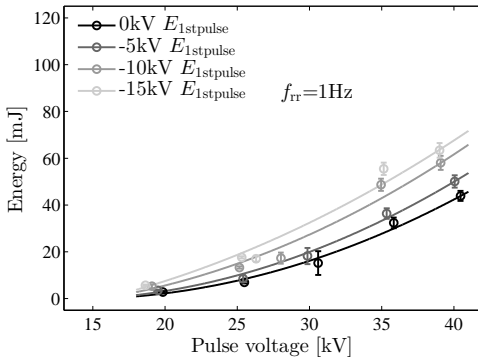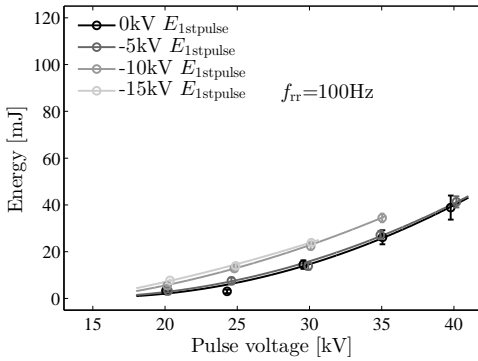Figure A.6: Energy measurements of the total dissipated plasma energy at positive pulse voltages at a repetition rate of (a) 1 Hz and (b) 100 Hz. E_{pulse} is the total energy that is dissipated by the plasma, while E_{DC} is the energy that is supplied by the high-voltage DC source. More energy is dissipated by the plasma when a higher DC bias is applied to the tertiary electrode at the cost of energy from the DC source.

Figure A.7: Energy measurements of the total dissipated plasma energy at negative pulse voltages at a repetition rate of (a) 1 Hz and (b) 100 Hz. E_{pulse} is the total energy that is dissipated by the plasma, while E_{DC} is the energy that is supplied by the high-voltage DC source. More energy is dissipated by the plasma when a higher DC bias is applied to the tertiary electrode at the cost of energy from the DC source.

when a DC bias is applied. When we compare Figs. A.6 and A.7 to Figs. A.8 and A.9 we can conclude that the main energy increases during the first pulse, which was the main goal of this work. When more energy is dissipated in the first pulse, the pulse reflection to the pulse source is lower, which explains why the energy increase with an applied DC voltage is lower for E_{pulse} than that it is for E_{1stpulse}. Now the energy increase in the main plasma (for the first pulse) is very similar to E_{DC}, even for higher DC voltages. Figure A.10 shows a good example of improved matching of the main
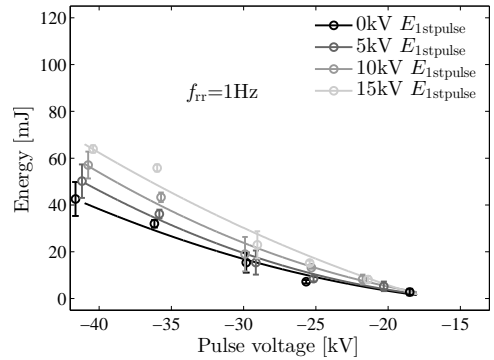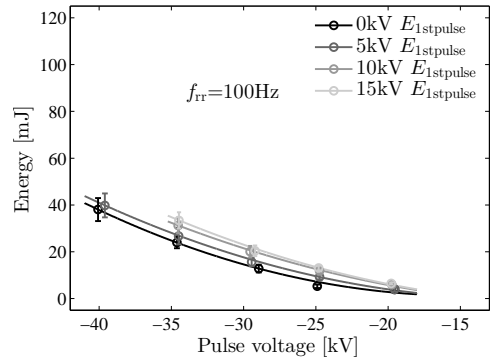
Figure A.8: Energy measurements of the energy dissipated by the plasma during the first pulse (denoted by $E_{1stpulse}$) at positive pulse voltages at a repetition rate of (a) 1 Hz and (b) 100 Hz. Comparing these results to Fig. A.6 we see that the main energy increase in E_{pulse} occurs during the first pulse.

Figure A.9: Energy measurements of the energy dissipated by the plasma during the first pulse (denoted by $E_{1stpulse}$) at negative pulse voltages at a repetition rate of (a) 1 Hz and (b) 100 Hz. Comparing these results to Fig. A.7 we see that the main energy increase in E_{pulse} occurs during the first pulse.

pulse when a DC bias is applied.

A.3.2   Matching

We introduced the matching definitions of Section A.2.4 to analyse the matching effects of the DC voltage in more detail. Figures A.11 and A.12 were generated with these definitions. There is now a clear effect of the DC voltage. For display purposes we only show the 0-kV and ±15-kV DC voltages, but the ±5-kV and ±10-kV show similar results which increase with the DC voltage. At a higher DC voltage the matching increases significantly and even when the matching is corrected for the energy from the
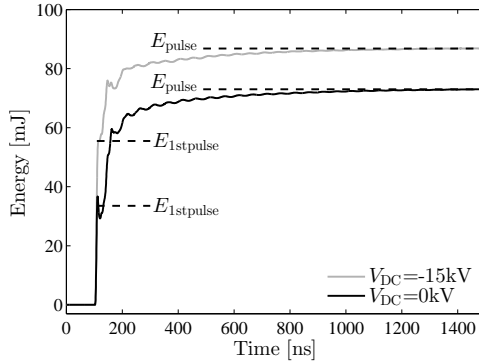
Figure A.10: Improved matching with a DC bias: by adding -15 kV on the tertiary electrode, the matching of the main pulse to the corona plasma reactor is increased. The pulse voltage is 35 kV and the repetition rate is 1 Hz in this example.

DC circuit the matching is still higher than the matching without a DC voltage. Only at a high repetition rate does the corrected matching eventually seem to be lower with a DC voltage for higher applied pulse voltages.

Another observation from the matching results is that the matching increases with the applied pulse voltage amplitude. This effect can be explained by the more intense plasma that is able to be generated at high voltages and is similar to what we observed in Chapter 6 and in literature [123–125, 133, 134]. We can also see that the matching is slightly less for the negative pulse voltages at 1-Hz repetition rate, which is expected when we consider that negative plasma ignites at a higher voltage [125, 134, 137]. At 100 Hz this effect is less pronounced, which can be attributed to a higher background ionisation, which enables plasma to ignite more easily. The effect that the matching is higher for positive voltages is consistent with the higher inception voltage associated with negative plasma and with findings in literature [125, 134, 137]. However, it is the opposite from what we found with our nanosecond pulse source and corona plasma reactor in Chapter 6, where we already commented on this unexpected phenomenon with the fast pulses. Therefore, the nanosecond pulse source that we use in the current chapter follows the more conventional results found in literature.

If we look at the results of the initial matching then the differences between the low repetition rate and the high repetition rate results with a DC bias is significant (the results of the total matching differ very little). This effect was already explained in the previous section and was attributed to the shift of the dominant form of background ionisation: the increased background ionisation due to the DC voltage becomes less than the increased background ionisation due to the higher repetition rate.

The results of the initial matching show that by applying a ±15 kV DC bias voltage on the specially designed corona plasma reactor we can improve the initial matching — even if we correct for the energy cost in the DC circuit — by a factor of around 1.25–2 depending on the voltage pulse amplitude, voltage polarity and on the repetition rate.
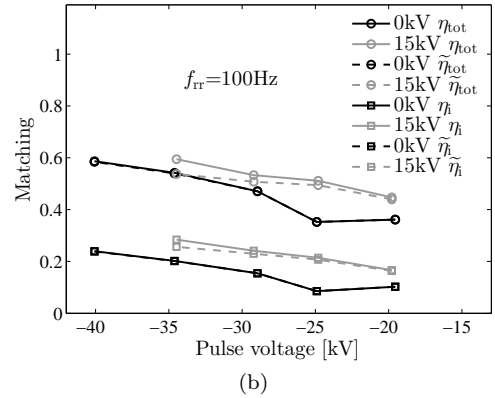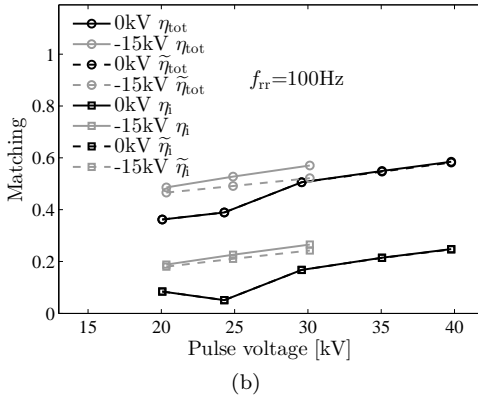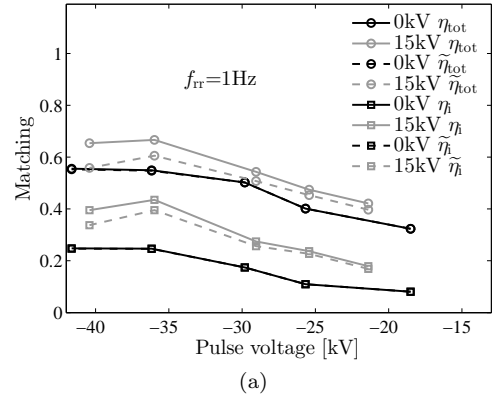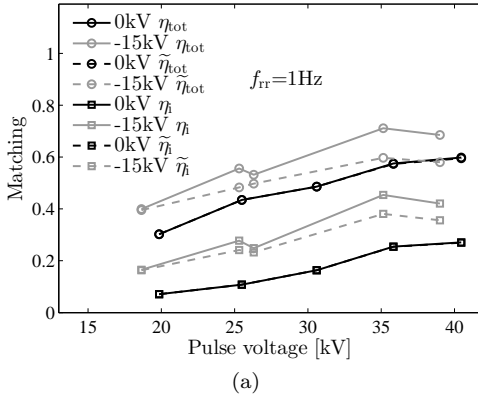
Figure A.11: Matching results for the energy measurements of Figs. A.6 and A.8 for positive voltages at a repetition rate of a) 1 Hz and b) 100 Hz. The results show increased matching when a -15 kV DC bias voltage is applied to the tertiary electrode, even when the energy from the DC circuit is taken into consideration. The effect decreases for high pulse voltages.

Figure A.12: Matching results for the energy measurements of Figs. A.7 and A.9 for negative voltages at a repetition rate of a) 1 Hz and b) 100 Hz. The results show increased matching when a 15 kV DC bias voltage is applied to the tertiary electrode, even when the energy from the DC circuit is taken into consideration. The effect decreases for high pulse voltages.

A.3.3 Ozone measurements

We measured ozone production in the corona plasma reactor to investigate if any increased plasma energy due to an applied DC voltage also results in an increased ozone production. The gas in the corona plasma reactor was again synthetic air with a flow of $1\,\mathrm{L\cdot min^{-1}}$. Due to the low sensitivity setting of the ozone measuring system, we only measured ozone at a repetition rate of 100 Hz.

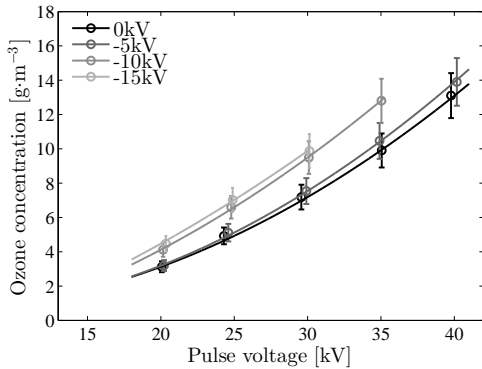Figures A.13 and A.14 show the results of the ozone measurements. From the

Figure A.13: Ozone measurements at positive pulse voltages at a repetition rate of 100 Hz. These results show that an increase in plasma energy (see Fig. A.6c) also increases the ozone production.
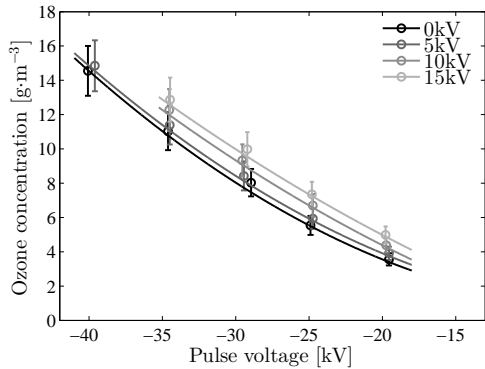
Figure A.14: Ozone measurements at negative pulse voltages at a repetition rate of 100 Hz. These results show that an increase in plasma energy (see Fig. A.7c) also increases the ozone production.

results we can conclude that the better matching of the pulse source also results in more ozone production. The ozone production is slightly higher for negative pulsed operation, but the difference with positive pulse operation is very small.

With the energy results of Figs. A.6b and A.7b and the ozone results of Figs. A.13 and A.14 we can calculate the ozone yield of the plasma. This yield is shown in Figs.A.15 and A.16 for positive and negative pulse voltages respectively. Figures A.15a and A.16a show the yield if we only take E_{pulse} into account. For positive pulse voltages the yield increases with increased DC voltages. For negative pulse voltages the yield with a DC voltage is below the yield without a DC voltage (except for $E_{\mathrm{DC}} = 15\,\mathrm{kV}$). Figures. A.15b and A.16b show the ozone yield when the DC energy E_{DC} is also included in the yield calculation. Now all yield results are similar when a DC voltage is used.
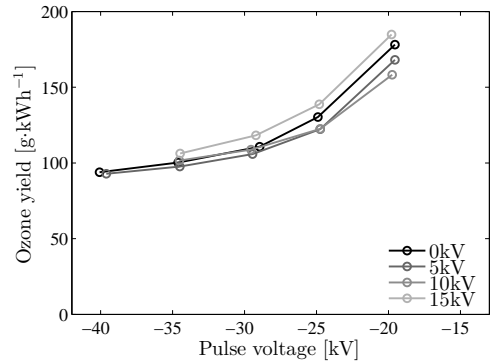
The yield results show that a DC bias has almost no effect on the ozone yield at a repetition rate of 100 Hz. The results might be different at lower repetition rates. Also, the ozone production is a cumulative effect of the plasma generated by the first pulse and all its reflections. Unfortunately, the ozone measurements are unable to distinguish between the ozone production during the first pulse and the ozone production during the reflections. Therefore, we have no information on what effect the increased matching for the first pulse has on the ozone production.

Another observation from the ozone yield results is that a negative corona plasma results in a higher ozone yield and that the ozone yield decreases for higher pulse voltages. This is consistent with for instance [5].
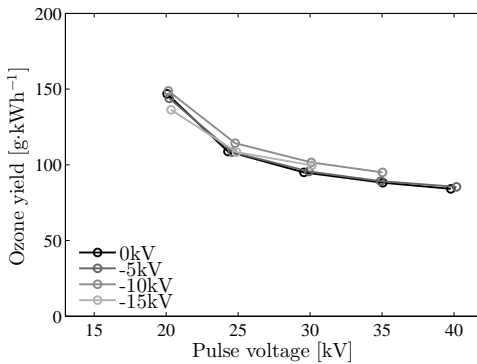
A final observation is that the ozone yields decrease with the applied voltage pulse amplitude. This can be explained by the destruction of ozone at high plasma energies (at the highest applied voltages at 100 Hz the energy density approaches $600\,\mathrm{J{\cdot}L^{-1}}$),
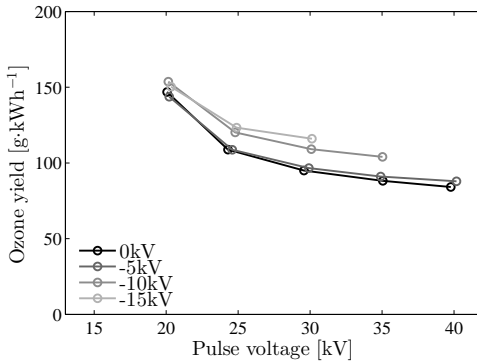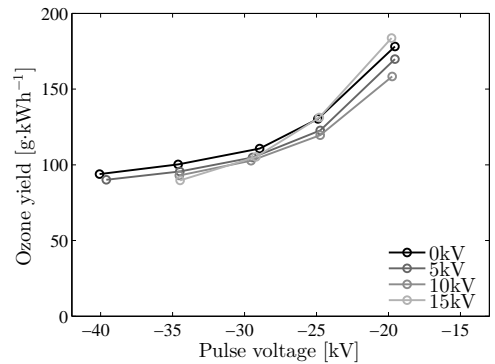
Figure A.15: The ozone yields at 100 Hz repetition rates for positive pulse voltages. a) Yield results when only E_{pulse} is used. b) Yield results where E_{DC} was added to E_{pulse} to calculate the yield. The results show that the result of the DC bias is a decrease in ozone yield.

Figure A.16: The ozone yields at 100 Hz repetition rates for negative pulse voltages. a) Yield results when only E_{pulse} is used. b) Yield results where E_{DC} was added to E_{pulse} to calculate the yield. The results show that the result of the DC bias is a decrease in ozone yield.

just as we saw in Section 6.6.

A.4 Conclusions

In this appendix we proposed experiments which investigate the matching of a nanosecond pulse source to a corona plasma reactor which is aided by a high voltage on a tertiary electrode. The corona plasma reactor is a wire cylinder reactor as is commonly used in pulsed power plasmas. A tertiary electrode is situated on a dielectric layer against the cylinder of the reactor. On this tertiary electrode we can apply pulsed, RF

or DC voltages to provide an additional plasma and bias voltage in the corona plasma reactor. The advantage of this method is that no compactly connected decoupling network is required to maintain the pulse shape of the primary high-voltage pulses. The pulse source that energised the main corona plasma was the nanosecond pulse source of the Kumamoto University, Japan.

We showed results of experiments with a DC voltage on the tertiary electrode which were performed during a leave to the Kumamoto University in Kumamoto, Japan. We varied the amplitude of the pulsed voltage, as well as the DC voltage and investigated their effect on the corona plasma with energy and ozone measurements. The results showed that the matching to the reactor increases with increasing DC voltages. However, the matching effect decreases slightly with higher repetition rates. This effect could be attributed to the minimised effect of increased background ionisation by the DC bias when compared to the increased background ionisation due to the higher repetition rate.

The most important aspect of the experiments in this chapter was the initial matching of the high-voltage pulse to the plasma reactor. This is the matching of the first pulse and does not include energy dissipated by reflections. This application of the first pulse most closely resembles the situation in which a long cable is inserted between the pulse source and the corona plasma reactor, which is our situation in this thesis. The results of the initial matching show that by applying a $\pm 15\,\text{kV}$ DC bias voltage on the specially designed corona plasma reactor we can improve the initial matching — even if we correct for the energy cost in the DC circuit — by a factor of around 1.25–2 depending on the voltage pulse amplitude, voltage polarity and on the repetition rate, which proves that the new corona plasma reactor with a tertiary electrode works well to improve matching.

Furthermore, ozone measurements confirmed that a better matching also results in a higher ozone production. However, the ozone production energy yield is not influenced by an applied DC bias.

A.5 Future work

Besides the experiment with the DC voltage on the tertiary electrode in the corona plasma reactor, of which we showed results in this appendix, we proposed two more experiments in the introduction: applying an RF source and a pulse source to the tertiary electrode. The main benefit of these experiments is that besides a bias voltage, now also a strong secondary (S)DBD plasma can be generated in the corona plasma reactor. This secondary plasma might aid the main plasma and provide better matching of the nanosecond pulse source to the corona reactor. It is our intention to show results of these experiments in future work and also apply the reactor with a tertiary high-voltage electrode to our own nanosecond pulse source.

B

Temperature and Pressure Effects on Positive Streamers in Air

Abstract

In this appendix we investigate temperature and pressure effects on the properties of a positive pulsed streamer plasma. We use a corona plasma setup in which we vary the temperature between 303–773 K at atmospheric pressure and the pressure between 37.9–100 kPa at room temperature to achieve the same neutral gas density and compare electrical and optical (ICCD imaging) measurements done in both experiments.

From the measurements we found that the dissipated plasma energy and the average streamer propagation velocity are both higher for the temperature experiments at the same neutral gas densities as in the pressure experiments. This suggests the existence of a specific temperature effect. A possible explanation for this effect is a higher streamer conductivity at high temperatures, as was previously found in literature.

B.1   Introduction

In Chapters 6 and Appendix A we investigated the energy transfer of a nanosecond pulse source to a corona plasma for a number of different pulse source parameters, plasma reactor parameters and process settings. In a separate study from the main contents of this thesis we also investigated how the energy transfer of a pulse source to the plasma depends on the reduced electric field E/n (where E is the applied electric

field and n is the gas density). This appendix presents the results of this separate study.

Besides the plasma energy we also present experimental results on how the temporal and spatial propagation of positive pulsed streamers in air depends on the reduced electric field. Streamers are generated in a wire-cylinder reactor at a constant voltage (so constant E). The density is changed by either varying the temperature T (303–773 K) at atmospheric pressure, or by varying the pressure p (37.9–100 kPa) at room temperature.

Previous studies on streamer development are mainly performed for various pressures [16,138,171,180]. In this appendix we us a corona plasma setup for which both the temperature and the pressure can be controlled. In this way it is possible to investigate the density effect on the plasma by changing one of both parameters without having to use literature values for comparison. In addition, previous studies into the temperature effect were focussed on a long streamer for leader research [231–233], whereas we study the temperature effect on a plasma that consists of multiple streamers as is commonly used in industrial applications.

With electrical diagnostics we study the energy the plasma dissipates under different experimental settings. For those same settings we look at streamer propagation and appearance with optical diagnostics (ICCD imaging).

This appendix consists of four sections. After this introduction section B.2 contains a description of our optical and electrical experimental setup. The results of the measurements and a discussion of these results is presented in section B.3 and in section B.4 we present our conclusions.

B.1.1 Gas density effects on positive streamers

It is known that the gas density has a strong influence on the development of streamers, because the mean free path between electron collisions is inversely proportional to the gas density. The mean free path determines how much energy an electron can gain as it is accelerated in an applied electric field before it collides with a background gas molecule. Sufficient energy gain is important to initiate and sustain a plasma. Therefore, streamer parameters (e.g. velocity, diameter, branching, etc.) are often displayed as functions of the reduced electric field E/n.

When looking at the effect of pressure, an extensive study by Briels [138] shows that the streamer velocity increases nearly linearly with the applied E/p ($\propto E/n$). In addition, streamers become thicker with decreasing pressure (so increasing E/p). Typical diameters range from 0.2 mm up to 3 mm. The smallest diameters are found when the applied voltage and/or rise-rate are reduced, i.e. when the applied E/p becomes smaller. Even thicker streamers (up to 1 cm diameter) have been reported for situations where very large voltage levels are applied [24].

In 1984 Aleksandrov *et al.* performed experiments on positive streamers in a 46.5 cm long gap for different temperatures [231]. They measured the conduction of a streamer channel created in this gap and the breakdown voltage of the gap for temperatures in the range of 294–900 K. They found that the breakdown voltage of the gap decreased

with increasing temperatures and that the conduction of the plasma channel increased such that the transferred charge through the streamer channel after reaching the cathode was 100 times higher at 900 K as compared to room temperature. In comparison, they only found a 5 times increase in transferred charge when they reduced the air density by decreasing the pressure at room temperature to a value corresponding to 900 K. They attributed the temperature effect to accelerating electron detachment from negative ions with increasing gas temperature.

Similar experiments were done in [232] where the electric field required for propagation of positive streamers in a gap was measured with varying temperatures. The results were compared with experiments in literature were the density was changed by varying the pressure [234]. In both cases the breakdown electric field decreased with reduced air density, but there appeared to be an added temperature effect on the streamer. However, in these experiments the temperature was only varied between 294 K and 421 K.

After these findings, Aleksandrov *et al.* used a 1.5D simulation to model the experiment as performed in 1984 [233]. They were able to reproduce the results of the experiment, but found that rather than accelerating electron detachment from negative ions as the reason for the temperature effect, the results could be explained by decomposition of cluster ions. These cluster ions (O_4^+ and N_4^+) were considered the dominant cause of electron loss because of their role in electron-ion recombination into O_2 and N_2 respectively. At higher temperatures the cluster ions can be decomposed and as a result the electron loss through electron-ion recombination is reduced severely, which explains the higher streamer conductivity in these conditions.

B.2 Experimental setup

B.2.1 High-temperature corona setup

The high-temperature corona setup that we used was first described in [66]. It is depicted in Figure B.1.

The setup consists of a stainless steel closed loop system with an integrated corona reactor. The corona reactor is a wire-cylinder configuration of 1.3 m long with a grounded cylinder of 160 mm in diameter and a high-voltage wire of 2 mm in diameter. A high-voltage pulse source (Section B.2.2) is connected to the wire electrode via a heat exchanger. The setup is traced with electrical heating elements and proper thermal insulation. This allows operation at gas temperatures in the range of 293–1073 K. By means of a vacuum pump the pressure in the setup can be adjusted between 10^2–10^5 Pa. A weight connected to the high-voltage wire and suspended above an insulator ensures the wire does not slacken at high temperatures.

B.2.2 Pulse source

The pulse source that we used is depicted in Figure B.2. Details on its origins and the resonant capacitor charger can be found in [25, 66, 235].
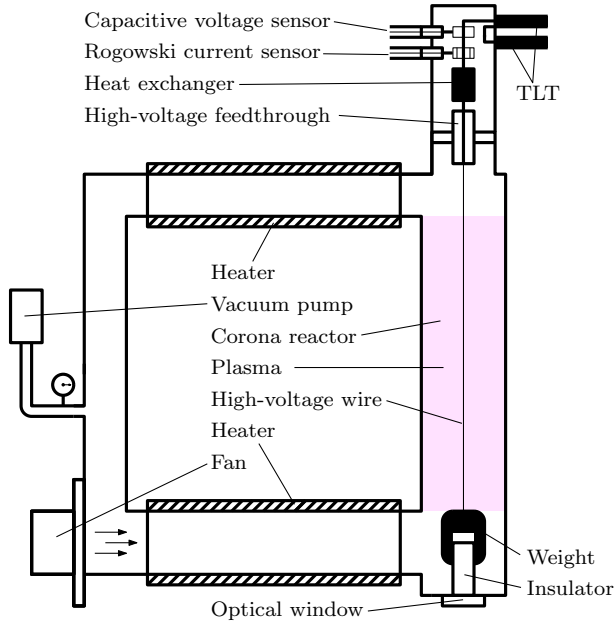
Figure B.1: The high-temperature corona setup (not to scale). It is a closed-loop gas system with a fan to circulate the air and was first described in [66]. With heaters and a vacuum pump we can control the temperature and the pressure in the setup. The corona reactor is energised through the TLT, at the top of the setup. Voltage and current sensors are also present at this position for plasma-energy measurements.

Figure B.2: The pulse source. A resonant capacitor charges the parallel connection of the high-voltage capacitor and the PFL. A discharge is triggered in the spark gap, after which the energy from the capacitor and the PFL is switched into two coaxial cables that form a transmission line transformer. These cables are connected in series at the output to double the voltage on the corona reactor.

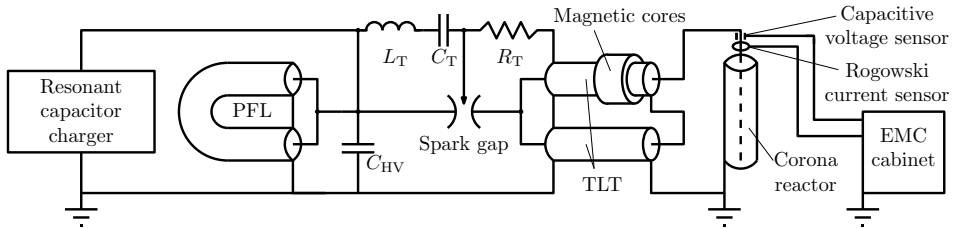A pulse forming line (PFL) is constructed from a 10 m long RG-218 coaxial cable with both ends connected in parallel. With this PFL the obtained output pulse would be a square pulse of 50 ns. However, to increase the energy per pulse and the peak output power a HV-capacitor C_{HV} of 700 pF was added. This also results in a slightly longer pulse (80 ns) and a more exponentially decaying waveform.

A transmission line transformer (TLT) is used to increase the output voltage. It consists of two 17 m long RG-218 coaxial cables connected in parallel at the spark gap side and connected in series at the corona reactor side. This makes the input and output impedances of the TLT 25 Ω and 100 Ω respectively. The voltage gain is around a factor 2. Ferrite cores are placed around the upper transmission line to increase the secondary mode impedance of the TLT.

The resonant capacitor charger charges C_{HV} and the PFL simultaneously in 20 µs. About 300–500 µs later the spark gap switch is triggered by the RLC-trigger network. This trigger network consists of R_T, C_T and L_T. When C_{HV} and the PFL are charged, the voltage on the trigger electrode initially follows the voltage on C_{HV}. After this charging period, the voltage on the trigger electrode decreases exponentially, thereby increasing the voltage difference between the first spark gap electrode and the trigger electrode, which eventually triggers the spark gap [236].

After triggering of the spark gap the PFL and C_{HV} discharge into the TLT which results in an output voltage on the corona reactor as shown in Figure B.3a. Figure B.3b shows the current in the corona reactor.

B.2.3 Electrical measurements

The voltage on the wire electrode of the corona reactor v_r and the corona reactor current i_r (which are the output voltage and output current of the pulse source respectively) as shown in Figures B.3a and B.3b are measured with D-I (Differentiating-Integrating) systems [32]. A capacitive voltage sensor and a single-turn Rogowski coil are situated above the HV-feedthrough of the corona reactor and are connected to passive integrators on the wall of an EMC cabinet [96]. In the EMC cabinet the output signals of the integrators are measured with a LeCroy WaveRunner 6 Zi 2 GHz 20 Gs·s^{-1} oscilloscope.

The power that is transferred to the corona reactor P_r is calculated from the measured reactor current and reactor voltage according to

$$P_r(t) = i_r(t)v_r(t). \tag{B.1}$$

The energy that is put into the corona reactor E_r is then calculated as

$$E_r(t) = \int_0^t P_r(\tau)\,d\tau. \tag{B.2}$$

And finally, the total energy that is dissipated by the plasma per pulse E_p is determined as

$$E_p = E_r(t_{end}), \tag{B.3}$$

where t_{end} indicates the end of a pulse period.
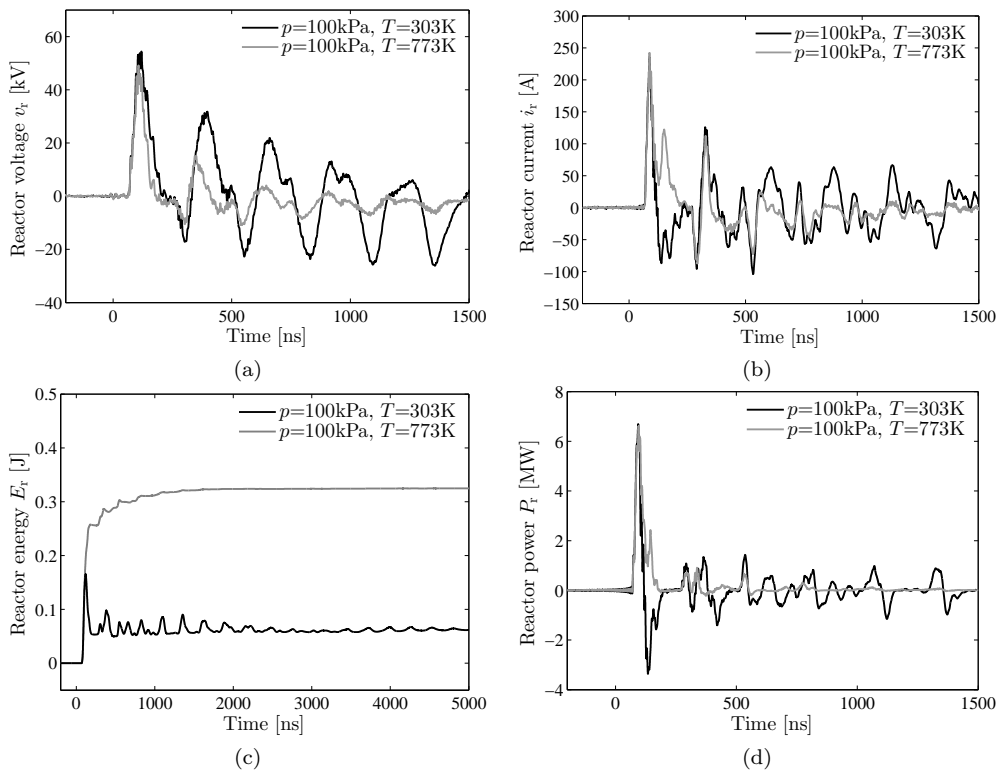
Figure B.3: Voltage (a), current (b), energy (c) and power (d) in the corona reactor for two different temperatures. At a higher temperature the corona current and consequently the reactor energy and the reactor power are higher.

The current $i_r(t)$, the voltage $v_r(t)$, the power $P_r(t)$ and the energy $E_r(t)$ are shown in Fig. B.3 for two different experimental settings.

B.2.4 Optical setup

To capture images of the corona plasma we used a 4 Picos-DIG ICCD camera from Stanford Computer Optics. It has a minimum exposure time of 200 ps and its CCD has a resolution of 780×580 pixels. We attached a Sigma 70–300 F4–5.6 DG MACRO lens to the camera and enclosed it in an EMC cabinet. Figure B.4 shows how it is positioned with respect to the corona reactor.

With the PC all camera data, such as the exposure time t_e, the Micro Channel Plate (MCP) gain and the time delay t_d can be programmed. A camera trigger circuit transforms the signal that is picked up with a capacitive sensor near the spark gap into a well defined trigger pulse for the camera whenever the spark gap switches. After

Figure B.4: The optical setup. An ICCD camera in a shielded EMC cabinet observes the plasma via a mirror through an optical window in the plasma reactor. The camera triggers on a signal taken from the spark gap and is controlled by a PC in a separate EMC cabinet.
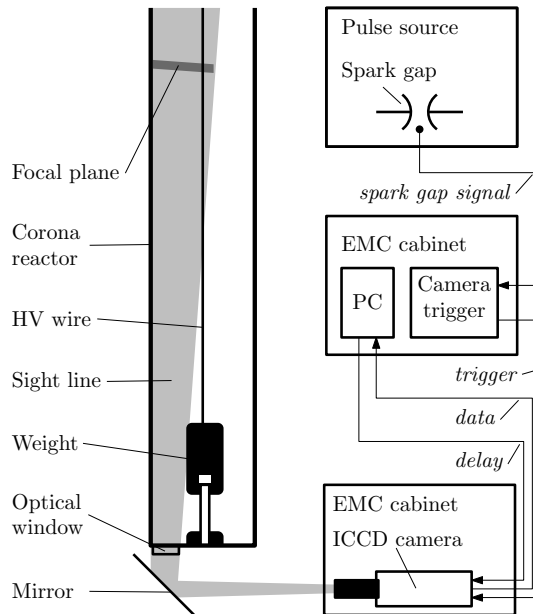
the programmed delay has passed the camera starts the exposure and captures an image. After the spark gap switches the HV-pulse is transmitted through the TLT to the corona reactor. The TLT length was chosen as 17 m because this allows for a 85 ns time period for the trigger signal to reach the camera and to compensate for the internal delay of the camera.

The corona reactor can be optically accessed through a window in the bottom of the corona reactor. To gain an unimpeded view of the plasma the optical path is slightly tilted from the corona reactor axis such that it can see past the weight that keeps the HV-wire straight and in the correct position. As a consequence, the focal plane is not entirely perpendicular to the reactor axis. However, at the used settings of the lens (200 mm F 8.0) the depth of field is still sufficient (7.5 mm) to sharply capture an entire streamer that crosses the gap. The relatively shallow depth of field also results in heavy blurring of the streamers that are present before and after the focal plane, which improves the visibility of the streamers in the focal plane.

Figure B.5 shows an image taken with the ICCD camera and how certain features of the setup can be recognised in the image.
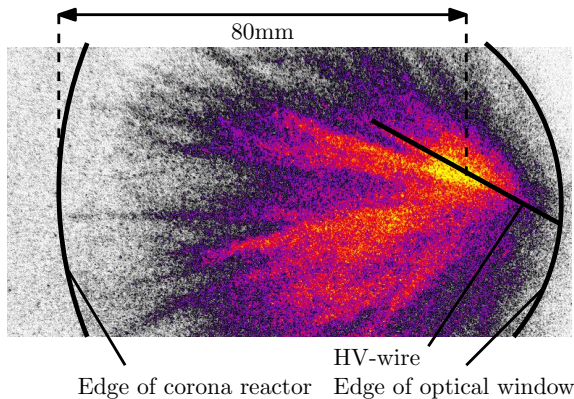
Figure B.5: An example image of the ICCD camera taken at $T = 373\,\mathrm{K}$, $p = 100\,\mathrm{kPa}$ and $t_\mathrm{e} = 100\,\mathrm{ns}$. Lines are drawn indicating the edge of the corona reactor, the edge of the optical port and the HV wire electrode.

B.3 Results and discussion

B.3.1 E/n variation by temperature and pressure

The ideal gas law states that the neutral gas density varies with the temperature and pressure according to

$$n = \frac{p}{k_\mathrm{B}T},$$ (B.4)

where k_B is the Boltzmann constant. According to [237] the use of the ideal gas law is justified for our experimental settings.

In the first set of experiments we varied T from $323\,\mathrm{K}$ ($50\,^\circ\mathrm{C}$) to $773\,\mathrm{K}$ ($500\,^\circ\mathrm{C}$) in steps of $50\,\mathrm{K}$, while keeping p at $100\,\mathrm{kPa}$ ($1000\,\mathrm{mbar}$). In the second set of experiments we varied p at room temperature to correspond to the same values of n as in the first set of experiments according to (B.4). We also included a measurement at room temperature at $100\,\mathrm{kPa}$. Room temperature was $303\,\mathrm{K}$ ($30\,^\circ\mathrm{C}$) for all experiments because of a slight heat-up of the system when it was operating. For all experiments the repetition rate of the pulse source was set at $15\,\mathrm{Hz}$.

Since the streamers initiate at the HV-wire the electric field value E that we used to calculate the reduced electric field E/n is chosen as the maximum electric field at the HV-wire. Therefore for each experiment E is calculated from

$$E = \frac{V_\mathrm{r}}{\ln(b/a)a}$$ (B.5)

where V_r is the peak voltage on the HV-wire, a is the radius of the HV-wire and b is the radius of the corona reactor. For all experiments V_r was constant.
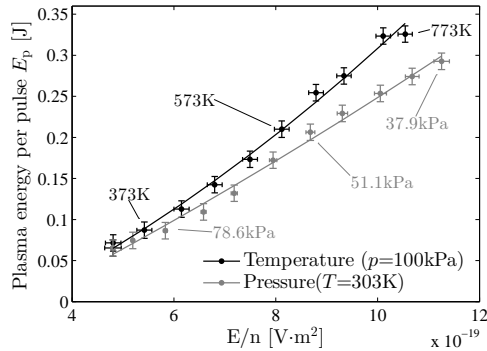
Figure B.6: Plasma energy as a function of E/n, where n was changed independently by temperature and by pressure. The results show an additional temperature effect which increases the plasma energy per pulse.

B.3.2 Plasma energy

For each experimental setting the plasma energy was measured as described in Section B.2.3. The results are displayed as a function of E/n in Figure B.6.

Each point in the figure is the mean of five measurements. The error bars in the y-direction represent the spread on the measurements. The error bars in the x-direction of the temperature measurements represent a measuring error of $\pm 10\,K$ and a ± 2 percent standard deviation on the measured voltage. The error bars in the x-direction of the pressure measurements represent a measuring error of $\pm 0.5\,kPa$ and a ± 2 percent standard deviation on the measured voltage.

As expected, the plasma energy increases as E/n increases. This can also be seen in Figures B.3a and B.3b; the reflections of the voltage and current pulses decrease for a higher temperature, which indicates that the impedance of the plasma is better matched to the output impedance of the TLT $(100\,\Omega)$ and consequently dissipates more energy.

Figure B.6 furthermore shows that a specific temperature effect exists that increases the plasma energy as compared to the pressure measurements. A possible explanation is to consider the streamers in our plasma as smaller versions of the long streamers in [231, 233]. In that case the results could be explained by a higher streamer conductivity at higher temperatures. If the streamers have a higher conductivity then the plasma impedance will be lower, which results in a better matching of the pulse source to the plasma and consequently a higher plasma energy.

The result that plasma energy increases with higher temperatures (lower values of n) is in agreement with results published in [126] $(T = 500\text{–}1000\,K)$ and [127] $(T = 123\text{–}293\,K)$.

B.3.3 Streamer velocity

Images were captured with the ICCD camera for each experimental setting. Long exposure images were captured with a 100 ns exposure time and the time delay set to just capture the inception of the streamers. For each experiment images were taken at an MCP gain setting to obtain the best exposed image.

Short exposure images were captured with a 3 ns exposure time. The short exposure images were taken with the same starting time delay as with the long exposure images and were then incremented in steps of 3 ns until a time delay of 100 ns was reached. The MCP gain setting was unique for each experimental setting, but constant throughout the series of short exposure images for each experimental setting.

During one HV-pulse one image was taken and all images were taken 20 times for averaging purposes. This resulted in a total of over 14 000 images.

Selected long exposure images are shown in Figures B.7 and B.8 (rotated 90 degrees when compared with the example image of Fig. B.5). They show that for low values of E/n a high number of branching streamers appear that do not cross the gap. Upon decreasing n the streamers start to cross the gap, become wider and branch less. These results are in agreement with for instance [16, 171, 180].

A selection of short exposure images with some accompanying reactor voltage waveforms are shown in Figure B.9. The images are cropped and rotated 90 degrees clockwise when compared with the example image of Fig. B.5.

From these images some observations can be made. For instance, at lower values of n the streamers cross the gap faster and the streamer heads are thicker, as was already observed in Figures B.7 and B.8. However, now we can also see that discharges start at an earlier time when n is low. This can be seen by looking at the images at 10 ns. Also, there appears to be a glow around the wire-electrode after the streamers bridge the gap for the images at $T \geq 573$ K and $P \leq 51.1$ kPa, which could indicate secondary streamer activity.

Average streamer propagation velocities were deduced from the short exposure images. When for an experimental setting 15 out of the 20 images of a 3 ns time-slot show a streamer reaching the ground electrode, the streamer is considered to have crossed the gap for that setting. For instance in Figure B.9 the image at 41 ns for the $p = 100$ kPa, $T = 773$ K setting shows a streamer reaching the ground electrode. If for example after 53 ns 12 images show a streamer crossing, but at 56 ns 18 images show a streamer crossing, then 54.5 ns will be the value used to calculate the propagation velocity. With this crossing time t_c and the gap distance as $b - a$ the average propagation velocity $\overline{v}$ is calculated as

$$\overline{v} = \frac{b - a}{t_c}. \tag{B.6}$$

Figure B.10 shows the propagation velocities for the temperature and pressure experiments as a function of E/n. The lowest two E/n values of both the temperature and the pressure experiments are not shown because there was no streamer crossing for those settings. The error bars in the y-direction represent a ± 2 ns jitter in the camera
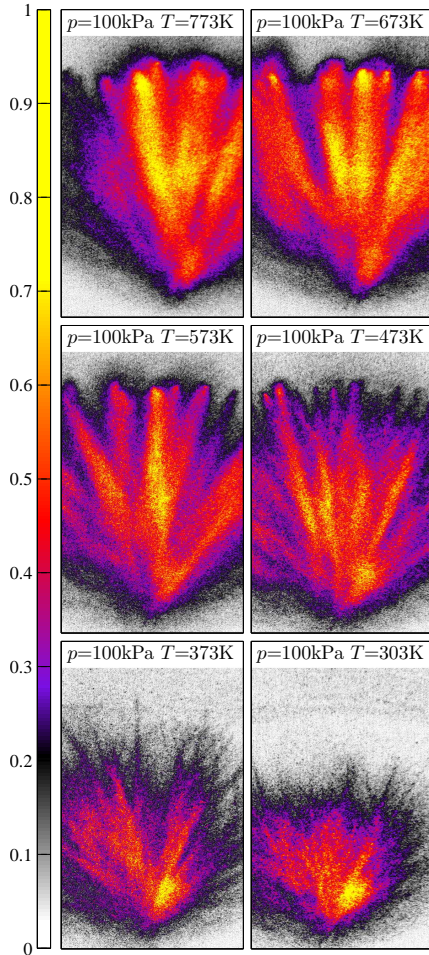
Figure B.7: Selected images from the 100 ns exposure images (with individual MCP gain) of the temperature experiments.
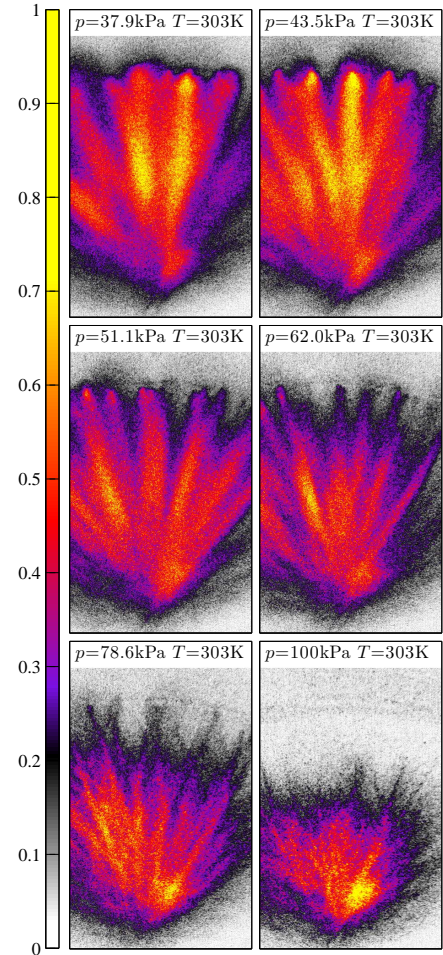
Figure B.8: Selected images from the 100 ns exposure images (with individual MCP gain) of the pressure experiments.

trigger system. The error bars in the x-direction are the same as for the plasma energy results of Section B.3.2.

The results of Figure B.10 again show an extra temperature effect on the streamer properties. The velocities are all in the order of 10^6 m·s^{-1}, which is in accordance with e.g. [16, 125, 134, 160, 168, 172]. A possible explanation of the temperature effect on the streamer velocity is to regard the streamer as a conductive channel. The applied voltage will drop partly over this channel, but the remainder is across the streamer head and the ground electrode. This results in an enhanced electric field at the streamer head when
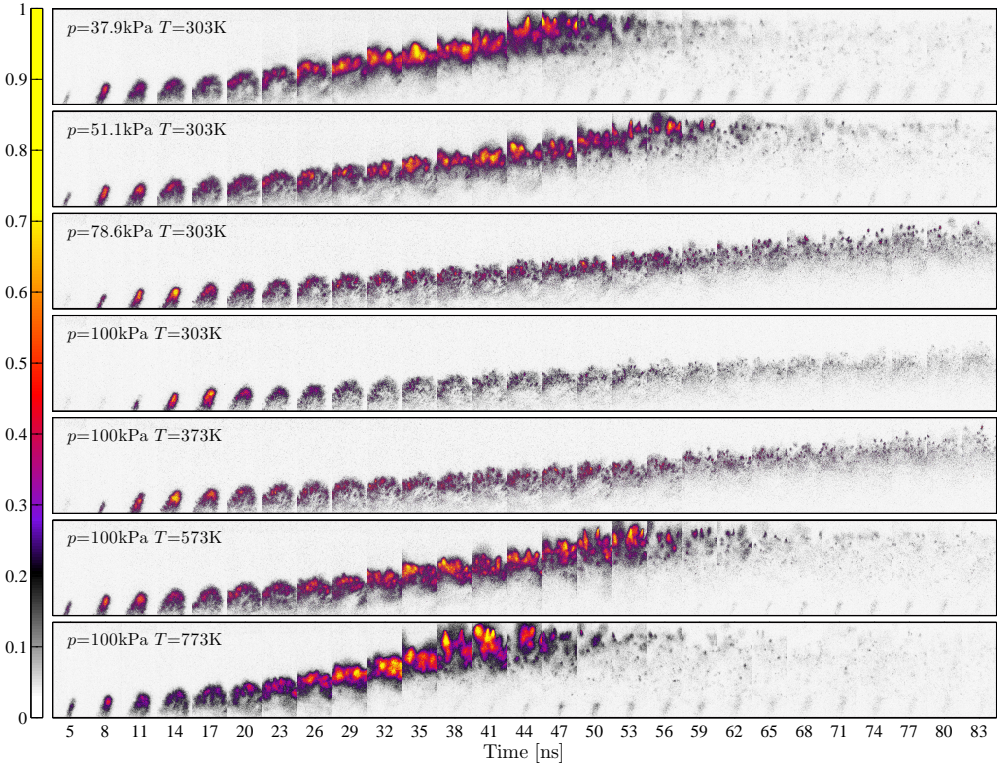
(a)
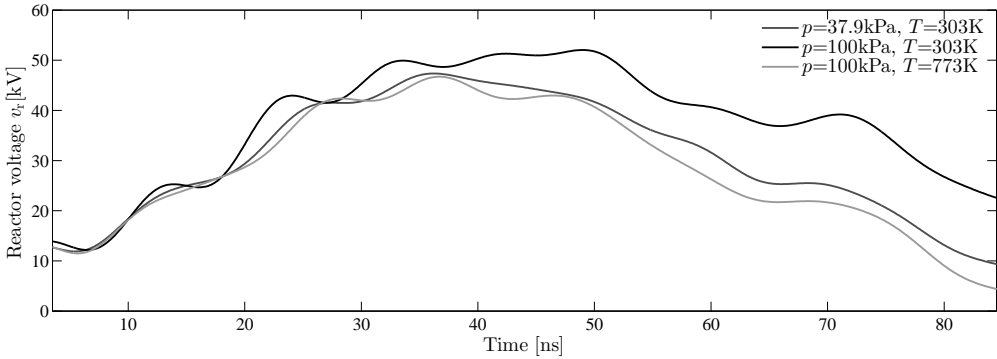
(b)

Figure B.9: Plasma development through time for different experimental settings (a) with accompanying voltage waveforms (b). In (a), each experimental setting has its own MCP gain setting of the camera for proper exposure at that experimental setting.
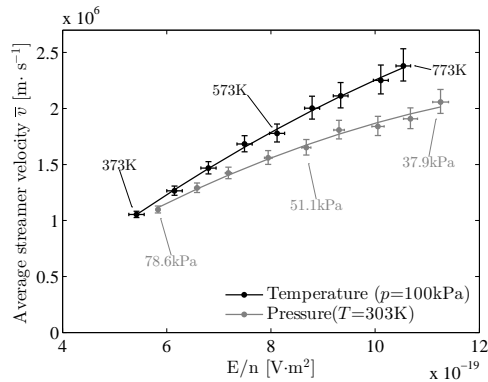
Figure B.10: Propagation velocities as a function of E/n, where n was changed independently by temperature and by pressure. The results show an additional temperature effect which increases the streamer propagation velocity.

it propagates through the gap. If we again assume a higher streamer conductivity at higher temperatures (Section B.3.2) then the voltage drop across the streamer channel is less for high temperatures as compared to low pressures. Therefore the electric field at the streamer head is higher and this results in a higher propagation velocity.

B.3.4   Streamer head position vs. time

The streamer head position as a function of time was determined for six experimental settings. The position was determined for all 20 images for each time slot of each experimental setting. The results are shown in Figures B.11 and B.12. The error bars in the y-direction represent the spread of the measurements and the error bars in the x-direction represents a ± 2 ns jitter in the camera trigger system.

From these results it appears that the streamers initially have a constant velocity and accelerate when they approach the ground electrode. This behaviour was also seen in [125, 164] and modelled in [145]. If we assume again that the applied voltage drops partly over the streamer channel then the electric field at the streamer head will increase as the streamer approaches the ground electrode. This would explain the acceleration towards the ground electrode. For both the $p = 78.6$ kPa, $T = 303$ K and $p = 100$ kPa, $T = 373$ K settings the acceleration towards the ground electrode is absent. This can be explained by looking at the voltage waveforms in Figure B.9; the voltage starts to drop when the streamer head is only halfway through the gap. This decreases the electric field near the streamer head.

B.3.5   The temperature effect

In the preceding experimental results it was shown that when experimental parameters are adjusted to vary E/n with temperature and pressure the temperature experiments
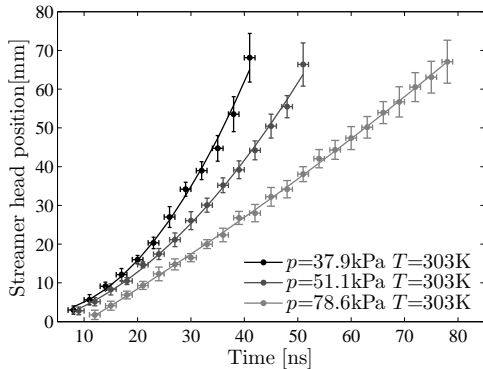
Figure B.11: Streamer head position as a function of time for the pressure experiments.
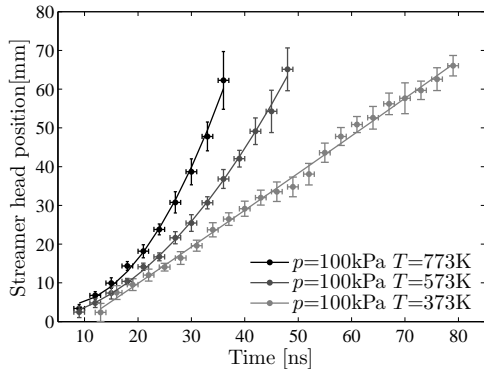
Figure B.12: Streamer head position as a function of time for the temperature experiments.

show higher values for both the dissipated plasma energy and the average streamer velocity. In both cases a possible explanation for this temperature effect was given by a higher streamer channel conductivity at high temperatures as compared to low pressures, which was measured and verified by a model for long streamers in literature [231, 233]. However, in our experiment we deal with a multitude of streamers in a large volume reactor, not a single long streamer, so it remains to be investigated whether the streamers in our setup also have a higher conductivity at higher temperatures. If they do, it offers a possible explanation for the temperature effect.

Another discrepancy between the experiments on a long streamer and our corona streamer plasma is that our plasma is generated by a repetitive high-voltage waveform and not single shot. Consequently, the background ionisation of the previous high voltage pulse influences the plasma created by a next high-voltage pulse [167]. This can be easily verified by running single shot experiments in our corona setup. If we get the same results as with the repetitive plasma it would give credence to the higher streamer channel conductivity explanation of the temperature effect.

Furthermore, modelling of the presented experiments might offer new insights into the temperature effect or offer a different explanation. Especially the temperature effect on the reaction rates of involved reactions could be an interesting starting point.

B.4 Conclusions

In this appendix we investigated temperature and pressure effects on the properties of a positive pulsed streamer plasma. A variation in temperature or pressure both influence the neutral gas density and therefore ultimately the streamer properties.

We used a corona plasma setup in which we varied the temperature between 303–773 K at atmospheric pressure and the pressure between 37.9–100 kPa at room tem-

perature to achieve the same neutral gas density and compared measurements done in both experiments. Where some studies report only on multiple streamer experiments by varying pressure and other studies only on multiple streamer experiments by varying the temperature, we were able to perform both experiments in the same setup and make direct comparisons.

We found with electrical measurements that the energy that was dissipated by the plasma was higher when the density was changed by a variation of temperature. With ICCD imaging we observed that in these experiments the average streamer velocity was higher as well. Both these results suggest the existence of a temperature effect.

A possible explanation for the temperature effect was given by literature findings where the streamer channel conductivity of a long streamer increased with high temperatures as compared to low pressures. A higher streamer channel conductivity would result in a lower plasma impedance and therefore in a higher dissipated plasma energy. Furthermore, if the streamer channel has a lower impedance a smaller fraction of the applied voltage will drop across the streamer channel and would therefore result in a higher electric field at the streamer head. A higher field at the streamer head would consequently increase the streamer propagation velocity.

Further experiments or modelling should be done to verify that the streamer conductivity also increases for a multiple streamer corona plasma as in our setup so that it might be presented as a valid explanation for the temperature effect. Modelling of the presented experiments might also offer new insights into the temperature effect or offer a different explanation.

C

Visualization of a Spark Discharge Driven By a High-Voltage Pulse with Sub-ns Rise-Time at Atmospheric Pressure

---

Abstract

A spark discharge generated by a 5-ns high-voltage pulse of 21 kV with a rise-time of 200 ps in a 1-mm gap between half-sphere steel electrodes was investigated in N_2-O_2 gas mixtures at atmospheric pressure. We compared short exposure and long exposure ICCD images of the discharge, as well as single shot images and accumulated images. At high repetition rates more discharge channels form due to higher background ionisation. The influence of the O_2 concentration between 0.1 and 10 vol% O_2 in N_2 is insignificant.

In Chapter 3 we presented the first 5-ns pulse source for plasma air purification purposes. This pulse source consists of a pulse forming line which is switched into a SA24272 cable by an oil spark gap. This delay cable enables the triggering of an ICCD camera. In this appendix we show the first plasma results that were obtained with this pulse source. We investigate the appearance of a spark discharge generated by the high-voltage pulse. Höft *et al.* used the same pulse source and setup to investigate the effect of reflections of the high-voltage pulse on a coaxial dielectric barrier plasma [72].

The plasma was generated in a Plexiglas discharge cell with half-sphere metal electrodes (indicated in Fig. C.1). The discharge cell was compactly connected to the SA24272 cable of the pulse source. We used a high-voltage pulse with an amplitude of $21\,(\pm 1)\,\mathrm{kV}$ to generate a plasma in the gap of 1 mm. Two different gas mixtures

---

The contents of this appendix have been published previously as [238]:

- T. Huiskamp, H. Höft, M. Kettlitz and A. J. M. Pemen, "Vizualisation of a Spark Discharge Driven by a High-Voltage Pulse With Sub-ns Rise-Time at Atmospheric Pressure," *Plasma Science, IEEE Transactions on*, vol. 42, no. 10, pp. 2414–2415, 2014.
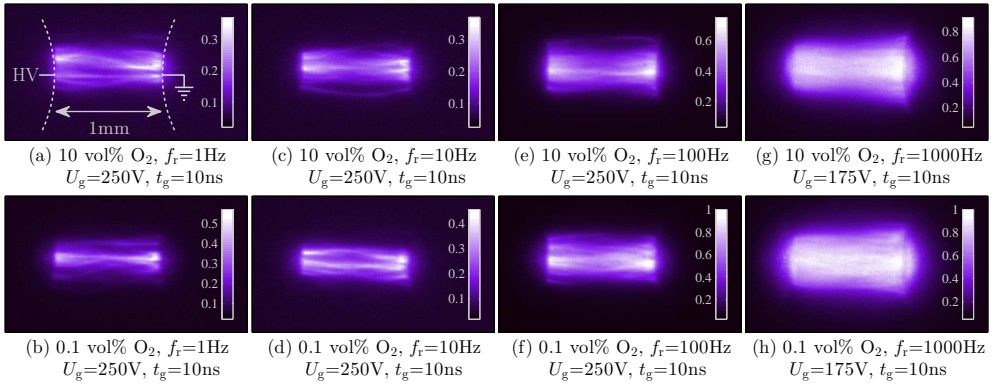
Figure C.1: Accumulated (20 images) short exposure ICCD images of a spark discharge for four different repetition rates at two different O_2 concentrations in N_2. The gap distance between the steel electrodes is 1 mm. The pulse voltage for all these images was $21\,(\pm 1)\,\text{kV}$. The camera settings for images (a) to (f) are identical and therefore all these images are normalised to the maximum of image (f). The camera settings for images (g) and (h) are also identical. Now the images are normalised to the maximum of image (h).

were used in the experiments: $0.1\,\text{vol}\%\ O_2$ in N_2 and $10\,\text{vol}\%\ O_2$ in N_2. Furthermore, we performed the experiments at four different repetition rates f_r: 1 Hz, 10 Hz, 100 Hz and 1 kHz.

We used the same Stanford Optics 4-Picos ICCD camera as in Chapter 7 with a microscope to record side-view images of the discharge. The image area is about $2 \times 3\,\text{mm}^2$ with a spatial resolution better than $10\,\mu\text{m}$. We took short exposure images with a gate time t_g of 10 ns and long exposure images with a gate time of $10\,\mu\text{s}$. The 10-ns images were timed to start at the rising of the voltage pulse and to record the discharge structure during the 5-ns high-voltage pulse. The $10\text{-}\mu\text{s}$ images capture the discharge emission during the high-voltage pulse and in the afterglow.

Figs. C.1 to C.3 show the results of the experiments. Fig. C.1 shows accumulated images with 10-ns gate for the two different gas mixtures at four repetition rates. Fig. C.2 shows the $10\text{-}\mu\text{s}$ images at the same experimental conditions of Fig. C.1. Only the gain U_g of the ICCD camera was changed to achieve properly exposed images. Finally, Fig. C.3 shows selected single shot images of the 10-ns and $10\text{-}\mu\text{s}$ images at a gas mixture of $10\,\text{vol}\%\ O_2$ in N_2.

The discharges appear as thin constricted channels, starting and ending in bright spots on the electrodes and some of them show branching (e.g. Fig. C.3d). More discharge channels are formed at higher repetition rates. This effect can be attributed to a higher level of background ionisation for higher pulse repetition rates. Furthermore there is no significant difference in the discharge structure (topology) between the two gas mixtures. This is likely because processes like electron attachment to oxygen play no dominant role because of the high electric field during breakdown [239].

From Fig. C.3 we can further observe that the discharge channels for the $10\text{-}\mu\text{s}$
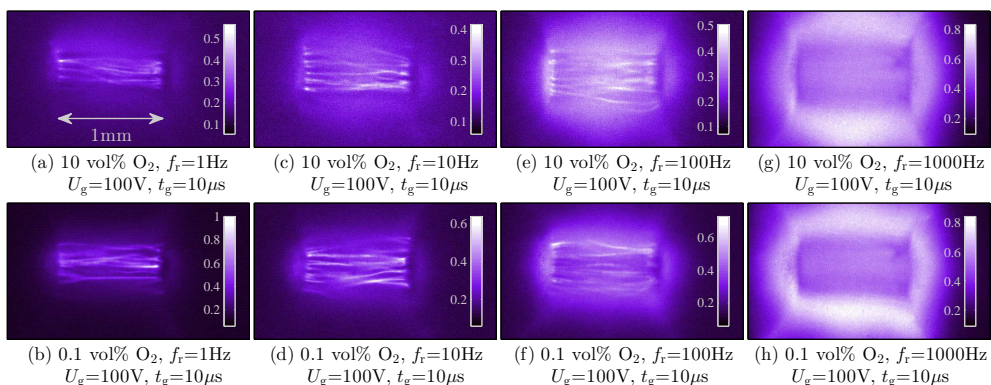
Figure C.2: Accumulated (20 images) long exposure images of the same discharges as in Fig. C.1. Now the camera settings are identical for all the images and therefore all images are normalised to the maximum of image (b)

(a) 10 vol% O_2, f_r=1Hz U_g=100V, t_g=10μs
(c) 10 vol% O_2, f_r=10Hz U_g=100V, t_g=10μs
(e) 10 vol% O_2, f_r=100Hz U_g=100V, t_g=10μs
(g) 10 vol% O_2, f_r=1000Hz U_g=100V, t_g=10μs

(b) 0.1 vol% O_2, f_r=1Hz U_g=100V, t_g=10μs
(d) 0.1 vol% O_2, f_r=10Hz U_g=100V, t_g=10μs
(f) 0.1 vol% O_2, f_r=100Hz U_g=100V, t_g=10μs
(h) 0.1 vol% O_2, f_r=1000Hz U_g=100V, t_g=10μs
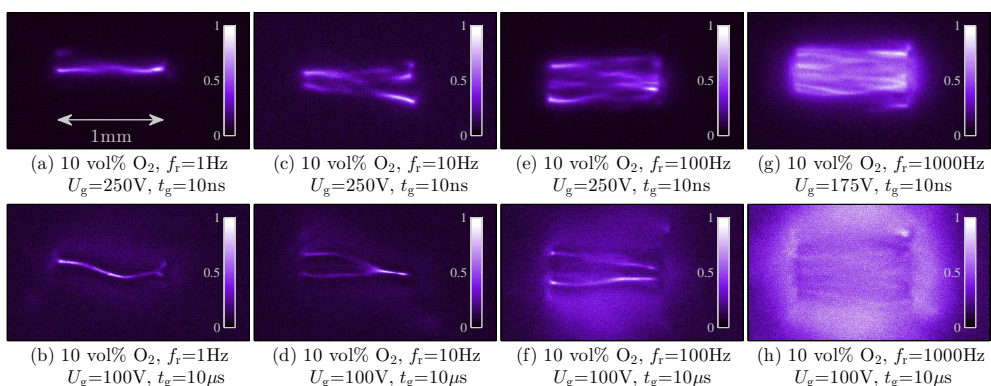
Figure C.3: Typical single shot long exposure images for different exposure times of the accumulated images of Figs. C.1 and C.2 for the highest oxygen concentration and various frequencies. The images are all normalised to the maximum of each image

(a) 10 vol% O_2, f_r=1Hz U_g=250V, t_g=10ns
(c) 10 vol% O_2, f_r=10Hz U_g=250V, t_g=10ns
(e) 10 vol% O_2, f_r=100Hz U_g=250V, t_g=10ns
(g) 10 vol% O_2, f_r=1000Hz U_g=175V, t_g=10ns

(b) 10 vol% O_2, f_r=1Hz U_g=100V, t_g=10μs
(d) 10 vol% O_2, f_r=10Hz U_g=100V, t_g=10μs
(f) 10 vol% O_2, f_r=100Hz U_g=100V, t_g=10μs
(h) 10 vol% O_2, f_r=1000Hz U_g=100V, t_g=10μs

images are thinner than for the 10-ns images (ca. 50 µm and 100 µm respectively). This constriction could be a result of the gas heating in the conducting channel like in an arc discharge [240].

Most striking is the glow-like discharge in a cylinder around the discharge channels that are much brighter than the channels themselves in the 10-µs images. This phenomenon is very pronounced at a repetition rate of 1 kHz. We have no explanation for this effect, but possibly gas heating effects and diffusion of excited species play an important role. An influence of metastable N_2 can be rejected because the effective lifetime of metastable N_2 in 10 vol% O_2 in N_2 is approximately 100 ns [241].

Bibliography

[1]   H.-H. Kim, "Nonthermal plasma processing for air-pollution control: A historical review, current issues, and future prospects," *Plasma Processes and Polymers*, vol. 1, no. 2, pp. 91–110, 2004.

[2]   U. Kogelschatz, "Dielectric-barrier discharges: their history, discharge physics, and industrial applications," *Plasma chemistry and plasma processing*, vol. 23, no. 1, pp. 1–46, 2003.

[3]   A. Fridman, A. Chirokov, and A. Gutsol, "Non-thermal atmospheric pressure discharges," *Journal of Physics D: Applied Physics*, vol. 38, no. 2, p. R1, 2005.

[4]   S. Samukawa, M. Hori, S. Rauf, K. Tachibana, P. Bruggeman, G. Kroesen, J. C. Whitehead, A. B. Murphy, A. F. Gutsol, S. Starikovskaia, U. Kortshagen, J. Boeuf, S. T. J, M. J. Kushner, U. Czarnetzki, and N. Mason, "The 2012 plasma roadmap," *Journal of Physics D: Applied Physics*, vol. 45, no. 25, p. 253001, 2012.

[5]   E. J. M. van Heesch, G. J. J. Winands, and A. J. M. Pemen, "Evaluation of pulsed streamer corona experiments to determine the O* radical yield," *Journal of Physics D: Applied Physics*, vol. 41, p. 234015, 2008.

[6]   T. Matsumoto, D. Wang, T. Namihira, and H. Akiyama, "Energy efficiency improvement of nitric oxide treatment using nanosecond pulsed discharge," *Plasma Science, IEEE Transactions on*, vol. 38, no. 10, pp. 2639–2643, 2010.

[7]   D. Wang, T. Namihira, and H. Akiyama, "Recent progress of nano-seconds pulsed discharge and its applications," *Journal of Advanced Oxidation Technologies*, vol. 14, no. 1, pp. 131–137, 2011.

[8]   T. Matsumoto, D. Wang, T. Namihira, and H. Akiyama, "Process performances of 2 ns pulsed discharge plasma," *Japanese Journal of Applied Physics*, vol. 50, no. 8, 2011.

[9]   M. Fujiwara, "Short-pulse discharge for simultaneous pursuit of energy and volume-efficient NO$_x$ removal," *Japanese journal of applied physics*, vol. 45, no. 2R, p. 948, 2006.

[10] T. Kakuta, I. Yagi, and K. Takaki, "Improvement of deoxidization efficiency of nitric monoxide by shortening pulse width of semiconductor opening switch pulse power generator," *Japanese Journal of Applied Physics*, vol. 54, no. 1S, p. 01AG02, 2015.

259

[11] R. Ono, Y. Nakagawa, and T. Oda, "Effect of pulse width on the production of radicals and excited species in a pulsed positive corona discharge," *Journal of Physics D: Applied Physics*, vol. 44, no. 48, p. 485201, 2011.

[12] T. Namihira, S. Tsukamoto, D. Wang, S. Katsuki, R. Hackam, H. Akiyama, Y. Uchida, and M. Koike, "Improvement of NO_x removal efficiency using short-width pulsed power," *Plasma Science, IEEE Transactions on*, vol. 28, no. 2, pp. 434–442, 2000.

[13] H. Raether, "Die entwicklung der elektronenlawine in den funkenkanal," *Zeitschrift für Physik*, vol. 112, no. 7-8, pp. 464–489, 1939.

[14] J. M. Meek, "A theory of spark discharge," *Physical Review*, vol. 57, no. 8, p. 722, 1940.

[15] G. Wormeester, S. Pancheshnyi, A. Luque, S. Nijdam, and U. Ebert, "Probing photo-ionization: simulations of positive streamers in varying N_2:O_2-mixtures," *Journal of Physics D: Applied Physics*, vol. 43, no. 50, p. 505201, 2010.

[16] S. Nijdam, F. M. J. H. Van De Wetering, R. Blanc, E. M. Van Veldhuizen, and U. Ebert, "Probing photo-ionization: experiments on positive streamers in pure gases and mixtures," *Journal of Physics D: Applied Physics*, vol. 43, no. 14, p. 145204, 2010.

[17] S. Nijdam, *Experimental investigations on the physics of streamers*. PhD thesis, Technische Universiteit Eindhoven, 2011.

[18] G. G. J. Winands, *Efficient Streamer Plasma Generation*. PhD thesis, Eindhoven University of Technology, 2007.

[19] F. J. C. M. Beckers, W. F. L. M. Hoeben, T. Huiskamp, A. J. M. Pemen, and E. J. M. van Heesch, "Pulsed corona demonstrator for semi-industrial scale air purification," *Plasma Science, IEEE Transactions on*, vol. 41, no. 10, pp. 2920–2925, 2013.

[20] F. J. C. M. Beckers, A. J. M. Pemen, and v. E. J. M. Heesch, "Streamer inception and propagation in a multiple wire-cylinder pulsed corona reactor," *Plasma Science, IEEE Transactions on*, vol. 42, no. 10, pp. 2404–2405, 2014.

[21] W. F. L. M. Hoeben, F. J. C. M. Beckers, A. J. M. Pemen, E. J. M. van Heesch, and W. L. Kling, "Oxidative degradation of toluene and limonene in air by pulsed corona technology," *Journal of Physics D: Applied Physics*, vol. 45, no. 5, p. 055202, 2012.

[22] P. Bruggeman and R. Brandenburg, "Atmospheric pressure discharge filaments and microplasmas: physics, chemistry and diagnostics," *Journal of Physics D: Applied Physics*, vol. 46, no. 46, p. 464001, 2013.

[23] Y. L. M. Creyghton, *Pulsed positive corona discharges : fundamental study and application to flue gas treatment*. PhD thesis, Eindhoven University of Technology, 1994.

[24] P. P. M. Blom, *High-Power Pulsed Corona*. PhD thesis, Eindhoven University of Technology, 1997.

[25] K. Yan, *Corona Plasma Generation*. PhD thesis, Eindhoven University of Technology, 2001.

[26] S. A. Nair, *Corona plasma for tar removal*. PhD thesis, Eindhoven University of Technology, 2004.

[27] F. J. C. M. Beckers, W. F. L. M. Hoeben, A. J. M. Pemen, and E. J. M. Van Heesch, "Low-level NO_x removal in ambient air by pulsed corona technology," *Journal of Physics D: Applied Physics*, vol. 46, no. 29, p. 295201, 2013.

[28] M. Simek and M. Clupek, "Efficiency of ozone production by pulsed positive corona discharge in synthetic air," *Journal of Physics D: Applied Physics*, vol. 35, no. 11, p. 1171, 2002.

[29] J. S. Clements, A. Mizuno, W. C. Finney, and R. H. Davis, "Combined removal of SO_2, NO_x, and fly ash from simulated flue gas using pulsed streamer corona," *Industry Applications, IEEE Transactions on*, vol. 25, no. 1, pp. 62–69, 1989.

[30] A. Pokryvailo, M. Wolf, Y. Yankelevich, S. Wald, L. R. Grabowski, E. M. van Veldhuizen, W. R. Rutgers, M. Reiser, B. Glocker, T. Eckhardt, P. Kempenaers, and A. Welleman, "High-power pulsed corona for treatment of pollutants in heterogeneous media," *Plasma Science, IEEE Transactions on*, vol. 34, no. 5, pp. 1731–1743, 2006.

[31] Y. S. Mok and S. W. Ham, "Conversion of NO to NO_2 in air by a pulsed corona discharge process," *Chemical engineering science*, vol. 53, no. 9, pp. 1667–1678, 1998.

[32] E. H. W. M. Smulders, B. E. J. M. Van Heesch, and S. S. V. B. van Paasen, "Pulsed power corona discharges for air pollution control," *Plasma Science, IEEE Transactions on*, vol. 26, pp. 1476–1484, Oct 1998.

[33] Y. S. Mok, H. W. Lee, and Y. J. Hyun, "Flue gas treatment using pulsed corona discharge generated by magnetic pulse compression modulator," *Journal of Electrostatics*, vol. 53, no. 3, pp. 195 – 208, 2001.

[34] Y. Wu, J. Li, N. Wang, and G. Li, "Industrial experiments on desulfurization of flue gases by pulsed corona induced plasma chemical process," *Journal of Electrostatics*, vol. 57, no. 3, pp. 233–241, 2003.

[35] Y.-H. Lee, W.-S. Jung, Y.-R. Choi, J.-S. Oh, S.-D. Jang, Y.-G. Son, M.-H. Cho, W. Namkung, D.-J. Koh, Y.-S. Mok, and J.-W. Chung, "Application of pulsed corona induced plasma chemical process to an industrial incinerator," *Environmental Science & amp; Technology*, vol. 37, no. 11, pp. 2563–2567, 2003.

[36] D. Wang, T. Matsumoto, T. Namihira, and H. Akiyama, "Development of higher yield ozonizer based on nano-seconds pulsed discharge," *Journal of Advanced Oxidation Technologies*, vol. 13, no. 1, pp. 71–78, 2010.

[37] T. Huiskamp, S. J. Voeten, E. J. M. van Heesch, and A. J. M. Pemen, "Design of a subnanosecond rise time, variable pulse duration, variable amplitude, repetitive, high-voltage pulse source," *Plasma Science, IEEE Transactions on*, vol. 42, no. 1, pp. 127–137, 2014.

[38] D. Wang, T. Namihira, and H. Akiyama, "Propagation of streamer heads during a 5-ns pulsed discharge," *Plasma Science, IEEE Transactions on*, vol. 39, pp. 2268–2269, Nov 2011.

[39] M. A. Malik, A. Ghaffar, and S. A. Malik, "Water purification by electrical discharges," *Plasma Sources Science and Technology*, vol. 10, no. 1, p. 82, 2001.

[40] T. Y. Tsong, "Electroporation of cell membranes.," *Biophysical journal*, vol. 60, no. 2, p. 297, 1991.

[41] J. Mankowski and M. Kristiansen, "A review of short pulse generator technology," *Plasma Science, IEEE Transactions on*, vol. 28, no. 1, pp. 102–108, 2000.

[42] W. S. Melville, "The use of saturable reactors as discharge devices for pulse generators," *Proceedings of the IEE-Part III: Radio and Communication Engineering*, vol. 98, no. 53, pp. 185–206, 1951.

[43] D. L. Birx, E. J. Lauer, L. L. Reginato, J. Schmidt, and M. Smith, "Basic principles governing the design of magnetic switches," tech. rep., California Univ., Livermore (USA). Lawrence Livermore Lab, 1980.

[44] P. W. Smith, *Transient electronics: Pulsed circuit technology.* J. Wiley, 2002.

[45] D. Zhang, Y. Zhou, J. Wang, and P. Yan, "A compact, high repetition-rate, nanosecond pulse generator based on magnetic pulse compression system," *Dielectrics and Electrical Insulation, IEEE Transactions on*, vol. 18, no. 4, pp. 1151–1157, 2011.

[46] I. Grekhov, "Pulse power generation in nano-and subnanosecond range by means of ionizing fronts in semiconductors: The state of the art and future prospects," *Plasma Science, IEEE Transactions on*, vol. 38, no. 5, pp. 1118–1123, 2010.

[47] V. M. Efanov, M. V. Efanov, A. V. Komashko, A. V. Kriklenko, P. M. Yarin, and S. V. Zazoulin, "High-voltage and high-PRF FID pulse generators," in *Ultra-Wideband, Short Pulse Electromagnetics 9*, pp. 301–305, Springer, 2010.

[48] A. B. J. M. Driessen, E. J. M. van Heesch, T. Huiskamp, F. J. C. M. Beckers, and A. J. M. Pemen, "Compact pulse topology for adjustable high-voltage pulse generation using a SOS diode," *Plasma Science, IEEE Transactions on*, vol. 42, pp. 3083–3088, Oct 2014.

[49] C. E. Baum, W. L. Baker, W. D. Prather, J. M. Lehr, J. P. O'Loughlin, D. V. Giri, I. D. Smith, R. Altes, J. Fockler, D. M. McLemore, M. D. Abdalla, and M. C. Skipper, "JOLT: a highly directive, very intensive, impulse-like radiator," *Proceedings of the IEEE*, vol. 92, pp. 1096 – 1109, July 2004.

[50] J. A. Gaudet, R. J. Barker, C. J. Buchenauer, C. Christodoulou, J. Dickens, M. A. Gundersen, R. P. Joshi, H. G. Krompholz, J. F. Kolb, A. Kuthi, M. Laroussi, A. Neuber, W. Nunnaly, E. Schamiloglu, K. H. Schoenbach, J. S. Tyo, and R. J. Vidmar, "Research issues in developing compact pulsed power for high peak power applications on mobile platforms," *Proceedings of the IEEE*, vol. 92, no. 7, pp. 1144–1165, 2004.

[51] P. Sarkar, S. W. Braidwood, I. R. Smith, B. M. Novac, R. A. Miller, and R. M. Craven, "A compact battery-powered half-megavolt transformer system for EMP generation," *Plasma Science, IEEE Transactions on*, vol. 34, no. 5, pp. 1832–1837, 2006.

[52] J. Kuffel, E. Kuffel, and W. S. Zaengl, *High voltage engineering fundamentals.* Newnes, 2000.

[53] "Eriks PTFE material datasheet." http://eriks.nl/datasheets/823//nl/downloads/industriele-kunststoffen/algemeen/staf-van-eriflon-ptfe-naturel/staf-van-eriflon-ptfe-naturel.pdf. Accessed: 01-08-2015.

[54] "Shell Diala S3 ZX-I Dried material datasheet." https://www.fmv.se/FTP/M7789-000183/datablad/M0746-067000_Shell_Diala_S3_ZX-I_Dried.pdf. Accessed: 01-08-2015.

[55] R. Curry, P. D. Champney, C. Eichenberger, J. Fockler, D. Morton, R. Sears, I. Smith, and R. Conrad, "The development and testing of subnanosecond-rise, kilohertz oil switches for the generation of high-frequency impulses," *Plasma Science, IEEE Transactions on*, vol. 20, no. 3, pp. 383–392, 1992.

[56] C. Yeckel and R. D. Curry, "Pulsed breakdown characterization of advanced liquid dielectrics for high-power high-pressure rep-rate oil switching," in *Pulsed Power Conference, 2009. PPC'09. IEEE*, pp. 860–865, IEEE, 2009.

262

[57] P. Norgard and R. D. Curry, "An in-depth investigation of the effect of oil pressure on the complete statistical performance of a high-pressure flowing oil switch," *Plasma Science, IEEE Transactions on*, vol. 38, no. 10, pp. 2539–2547, 2010.

[58] R. Pecquois, L. Pecastaing, M. Rivaletto, A. De Ferron, P. Pignolet, J. Martin, L. Caramelle, J. M. Duband, and R. Vezinet, "An oil peaking switch to drive a dipole antenna for wideband applications," in *Dielectric Liquids (ICDL), 2011 IEEE International Conference on*, pp. 1–4, IEEE, 2011.

[59] J. C. Martin, "Nanosecond pulse techniques," *Proceedings of the IEEE*, vol. 80, no. 6, pp. 934–945, 1992.

[60] S. Ramo, J. R. Whinnery, and T. Van Duzer, *Fields and waves in communication electronics*. John Wiley & Sons, 1993.

[61] N. Marcuvitz, *Waveguide handbook*, vol. 21. Inst of Engineering & Technology, 1951.

[62] R. L. Wigington and N. S. Nahman, "Transient analysis of coaxial cables considering skin effect," *Proceedings of the IRE*, vol. 45, no. 2, pp. 166–174, 1957.

[63] A. G. A. Lathouwers, "Ontwerp van een differentiërend-integrerend meetsysteem voor het meten van snelle transiënte spanningen in GIS," Master's thesis, Eindhoven University of Technology, 1988.

[64] M. A. van Houten, *Electromagnetic compatibility in high-voltage engineering*. PhD thesis, Eindhoven University of Technology, 1990.

[65] "Times Microwave LMR-1700." `http://www.timesmicrowave.com/documents/resources/LMR-1700.pdf`. Accessed: 01-08-2015.

[66] S. A. Nair, K. Yan, A. J. M. Pemen, G. J. J. Winands, F. M. Van Gompel, H. E. M. Van Leuken, E. J. M. Van Heesch, K. J. Ptasinski, and A. A. H. Drinkenburg, "A high-temperature pulsed corona plasma system for fuel gas cleaning," *Journal of electrostatics*, vol. 61, no. 2, pp. 117–127, 2004.

[67] "CST Microwave Studio." `https://www.cst.com/Products/CSTMWS`. Accessed: 01-08-2015.

[68] S. J. Voeten, *Matching High Voltage Pulsed Power Technologies*. PhD thesis, Eindhoven University of Technology, 2013.

[69] E. R. Schatz and E. M. Williams, "Pulse transients in exponential transmission lines," *Proceedings of the IRE*, vol. 38, no. 10, pp. 1208–1212, 1950.

[70] T. Huiskamp, F. J. C. M. Beckers, E. J. M. van Heesch, and A. J. M. Pemen, "First implementation of a subnanosecond rise time, variable pulse duration, variable amplitude, repetitive, high-voltage pulse source," *Plasma Science, IEEE Transactions on*, vol. 42, no. 3, pp. 859–867, 2014.

[71] T. Huiskamp, E. J. M. van Heesch, and A. J. M. Pemen, "Final implementation of a subnanosecond rise time, variable pulse duration, variable amplitude, repetitive, high-voltage pulse source," *Plasma Science, IEEE Transactions on*, vol. 43, no. 1, pp. 444–451, 2015.

[72] H. Höft, T. Huiskamp, M. Kettlitz, and A. J. M. Pemen, "Visualization of a coaxial dielectric barrier discharge driven by a sub-ns rising high-voltage pulse and its reflections," *Plasma Science, IEEE Transactions on*, 2014.

[73] J. Hendriks, S. B. van der Geer, and G. J. H. Brussaard, "Spark gap optimization by electrodynamic simulations," *Journal of Physics D: Applied Physics*, vol. 39, no. 2, p. 274, 2006.

[74] "LTspice IV." `http://www.linear.com/designtools/software/#LTspice`. Accessed: 01-08-2015.

[75] P. Norgard, R. D. Curry, and R. Sears, "Poly-α olefin synthetic oil: A new paradigm in repetitive high-pressure oil switches," *Plasma Science, IEEE Transactions on*, vol. 34, no. 5, pp. 1662–1669, 2006.

[76] R. A. Petr and T. R. Burkes, "Erosion of spark gap electrodes," *IEEE Transactions on Plasma Science*, vol. 8, pp. 149–153, 1980.

[77] A. E. Guile and B. Juttner, "Basic erosion processes of oxidized and clean metal cathodes by electric arcs," *Plasma Science, IEEE Transactions on*, vol. 8, no. 3, pp. 259–269, 1980.

[78] A. Donaldson, M. O. Hagler, M. Kristiansen, G. Jackson, and L. Hatfield, "Electrode erosion phenomena in a high-energy pulsed discharge," *Plasma Science, IEEE Transactions on*, vol. 12, no. 1, pp. 28–38, 1984.

[79] A. Donaldson, M. Kristiansen, A. Watson, K. Zinsmeyer, E. Kristiansen, and R. Dethlefsen, "Electrode erosion in high current, high energy transient arcs," *Magnetics, IEEE Transactions on*, vol. 22, no. 6, pp. 1441–1447, 1986.

[80] T. Bregel, W. Krauss-Vogt, R. Michal, and K. E. Saeger, "On the application of W/Cu materials in the fields of power engineering and plasma technology," *Components, Hybrids, and Manufacturing Technology, IEEE Transactions on*, vol. 14, no. 1, pp. 8–13, 1991.

[81] J. M. Koutsoubis and S. J. MacGregor, "Electrode erosion and lifetime performance of a high repetition rate, triggered, corona-stabilized switch in air," *Journal of Physics D: Applied Physics*, vol. 33, no. 9, p. 1093, 2000.

[82] N. Parkansky, L. Glikman, I. I. Beilis, B. Alterkop, R. L. Boxman, and D. Gindin, "W–C electrode erosion in a pulsed arc submerged in liquid," *Plasma Chemistry and Plasma Processing*, vol. 27, no. 6, pp. 789–797, 2007.

[83] J. Carlton, *Marine propellers and propulsion*. Butterworth-Heinemann, 2012.

[84] D. Affinito, A. Fisher, and E. Bar-Avraham, "Design and structure of an extended life high current sparkgap," *IEEE Transactions on Plasma Science*, vol. 7, p. 162, 1979.

[85] P. Norgard. Private communication, 2015.

[86] T. Huiskamp, F. J. C. M. Beckers, E. J. M. van Heesch, and A. J. M. Pemen, "A solid state, 0–120 kV, microsecond pulse charger for a nanosecond pulse source," *Plasma Science, IEEE Transactions on*, vol. 41, no. 12, pp. 3666–3674, 2013.

[87] B. M. Novac, M. Istenic, J. Luo, I. R. Smith, J. Brown, M. Hubbard, P. Appelgren, M. Elfsberg, T. Hurtig, C. Möller, A. Larsson, and S. E. Nyholm, "A 10-GW pulsed power supply for HPM sources," *Plasma Science, IEEE Transactions on*, vol. 34, no. 5, pp. 1814–1821, 2006.

[88] L. M. Redondo, H. Canacsinh, and J. F. Silva, "Generalized solid-state marx modulator topology," *Dielectrics and Electrical Insulation, IEEE Transactions on*, vol. 16, no. 4, pp. 1037–1042, 2009.

[89] L. M. Redondo and J. F. Silva, "Repetitive high-voltage solid-state marx modulator design for various load conditions," *Plasma Science, IEEE Transactions on*, vol. 37, no. 8, pp. 1632–1637, 2009.

[90] J.-W. Baek, D.-W. Yoo, G.-H. Rim, and J.-S. Lai, "Solid state marx generator using series-connected IGBTs," *Plasma Science, IEEE Transactions on*, vol. 33, no. 4, pp. 1198–1204, 2005.

[91] Y. Wu, K. Liu, J. Qiu, X. Liu, and H. Xiao, "Repetitive and high voltage marx generator using solid-state devices," *Dielectrics and Electrical Insulation, IEEE Transactions on*, vol. 14, no. 4, pp. 937–940, 2007.

[92] V. C. Valchev and A. Van den Bossche, *Inductors and transformers for power electronics*. CRC press, 2005.

[93] J. M. Williamson, D. D. Trump, P. Bletzinger, and B. N. Ganguly, "Comparison of high-voltage ac and pulsed operation of a surface dielectric barrier discharge," *Journal of Physics D: Applied Physics*, vol. 39, no. 20, p. 4400, 2006.

[94] H. Ayan, G. Fridman, A. F. Gutsol, V. N. Vasilets, A. Fridman, and G. Friedman, "Nanosecond-pulsed uniform dielectric-barrier discharge," *Plasma Science, IEEE Transactions on*, vol. 36, no. 2, pp. 504–508, 2008.

[95] H. Höft, M. Kettlitz, T. Hoder, K. Weltmann, and R. Brandenburg, "The influence of O_2 content on the spatio-temporal development of pulsed driven dielectric barrier discharges in O_2/N_2 gas mixtures," *Journal of Physics D: Applied Physics*, vol. 46, no. 9, p. 095202, 2013.

[96] E. J. M. van Heesch, J. N. A. M. van Rooij, R. G. Noij, and van der Laan P. C. T, "A new current and voltage measuring system; tests in a 150 kv and 400 kv GIS," in *Proc. 5th Int. Symp. on High Voltage Engineering*, vol. 3, p. 73.06, 1987.

[97] L. M. Redondo and J. F. Silva, "Flyback versus forward switching power supply topologies for unipolar pulsed-power applications," *Plasma Science, IEEE Transactions on*, vol. 37, no. 1, pp. 171–178, 2009.

[98] C. Waters, "Current transformers provide accurate, isolated measurements," *Power conversion & intelligent motion*, no. 12, 1986.

[99] J. Bergoz, "Current monitors for particle beams," *Nuclear Physics A*, vol. 525, pp. 595–600, 1991.

[100] P. Ripka, "Electric current sensors: a review," *Measurement Science and Technology*, vol. 21, no. 11, p. 112001, 2010.

[101] "North Star High Voltage." `http://www.highvoltageprobes.com/high-voltage-probes`. Accessed: 01-08-2015.

[102] W. Rogowski and W. Steinhaus, "Die messung der magnetischen spannung," *Electrical Engineering (Archiv fur Elektrotechnik)*, vol. 1, no. 4, pp. 141–150, 1912.

[103] D. G. Pellinen and P. W. Spence, "A nanosecond risetime megampere current monitor," *Review of Scientific Instruments*, vol. 42, no. 11, pp. 1699–1701, 1971.

[104] J. M. Anderson, "Wide frequency range current transformers," *Review of Scientific Instruments*, vol. 42, no. 7, pp. 915–926, 1971.

[105] A. P. J. van Deursen and V. Stelmashuk, "Inductive sensor for lightning current measurement, fitted in aircraft windowspart I: Analysis for a circular window," *IEEE Sensors Journal*, vol. 11, no. 1, p. 199, 2011.

[106] A. P. van Deursen, "Inductive sensor for lightning current measurement, fitted in aircraft windowspart II: Measurements on an A320 aircraft," *IEEE Sensors Journal*, vol. 11, no. 1, pp. 205–209, 2011.

[107] B. M. Novac, M. Ganciu, M. C. Enache, I. R. Smith, H. R. Stewardson, and V. V. Vadher, "A fast electro-optic high-voltage sensor," *Measurement Science and Technology*, vol. 6, no. 2, p. 241, 1995.

[108] R. D. Shah, R. J. Cliffe, B. M. Novac, I. R. Smith, and P. Senior, "An ultra-fast electro-optic probe for 500 kV pulsed voltage measurements," *Measurement Science and Technology*, vol. 13, no. 2, p. 226, 2002.

[109] A. Lorusso, V. Nassisi, and M. V. Siciliano, "Fast capacitive probe for electromagnetic pulse diagnostic," *Review of Scientific Instruments*, vol. 79, no. 6, pp. 064702–064702, 2008.

[110] T. C. Wagoner, W. A. Stygar, H. C. Ives, T. L. Gilliland, R. B. Spielman, M. F. Johnson, P. G. Reynolds, J. K. Moore, R. L. Mourning, D. L. Fehl, *et al.*, "Differential-output B-dot and D-dot monitors for current and voltage measurements on a 20-MA, 3-MV pulsed-power accelerator," *Physical Review Special Topics-Accelerators and Beams*, vol. 11, no. 10, p. 100401, 2008.

[111] C. Yao, Q. Xiao, Y. Mi, T. Yuan, C. Li, and W. Sima, "Contactless measurement of lightning current using self-integrating B-dot probe," *Dielectrics and Electrical Insulation, IEEE Transactions on*, vol. 18, no. 4, pp. 1323–1327, 2011.

[112] M. Raleigh and R. E. Pechacek, "Fast passive integrator," *Review of scientific instruments*, vol. 55, no. 12, pp. 2023–2026, 1984.

[113] V. Stelmashuk and A. P. J. van Deursen, "Passive integrator for ILDAS project," in *EMC Europe 2011 York*, pp. 37–40, IEEE, 2011.

[114] R. H. Huddlestone and S. L. Leonard, "Plasma diagnostic techniques," in *Plasma Diagnostic Techniques*, 1965.

[115] W. Stygar and G. Gerdin, "High frequency rogowski coil response characteristics," *Plasma Science, IEEE Transactions on*, vol. 10, no. 1, pp. 40–44, 1982.

[116] "MathWork Matlab." `http://www.mathworks.com/products/matlab/`. Accessed: 01-08-2015.

[117] E. M. Van Veldhuizen, W. R. Rutgers, and V. A. Bityurin, "Energy efficiency of NO removal by pulsed corona discharges," *Plasma Chemistry and Plasma Processing*, vol. 16, no. 2, pp. 227–247, 1996.

[118] K. Yan, H. Hui, M. Cui, J. Miao, X. Wu, C. Bao, and R. Li, "Corona induced non-thermal plasmas: fundamental study and industrial applications," *Journal of Electrostatics*, vol. 44, no. 1, pp. 17–39, 1998.

[119] H. Ma and Y. Qiu, "A study of ozone synthesis in coaxial cylinder pulse streamer corona discharge reactors," *Ozone Science & Engineering*, vol. 25, no. 2, pp. 127–135, 2003.

[120] V. Puchkarev and M. Gundersen, "Energy efficient plasma processing of gaseous emission using a short pulse discharge," *Applied physics letters*, vol. 71, no. 23, pp. 3364–3366, 1997.

[121] A. J. M. Pemen, I. V. Grekhov, E. J. M. van Heesch, K. Yan, S. A. Nair, and S. V. Korotkov, "Pulsed corona generation using a diode-based pulsed power generator," *Review of scientific instruments*, vol. 74, no. 10, pp. 4361–4365, 2003.

[122] J.-J. Ruan, W. Li, Y. Shi, Y. Nie, X. Wang, and T. en Tan, "Decomposition of simulated odors in municipal wastewater treatment plants by a wire-plate pulse corona reactor," *Chemosphere*, vol. 59, no. 3, pp. 327 – 333, 2005.

[123] T. M. P. Briels, J. Kos, E. M. van Veldhuizen, and U. Ebert, "Circuit dependence of the diameter of pulsed positive streamers in air," *Journal of Physics D: Applied Physics*, vol. 39, no. 24, p. 5201, 2006.

[124] T. Matsumoto, D. Wang, T. Namihira, and H. Akiyama, "Improvement of impedance matching between ns pulse generator and discharge reactor," in *Pulsed Power Conference, 2009 IET European*, pp. 1–4, IET, 2009.

[125] G. J. J. Winands, Z. Liu, E. J. M. van Heesch, A. J. M. Pemen, and K. Yan, "Matching a pulsed-power modulator to a streamer plasma reactor," *Plasma Science, IEEE Transactions on*, vol. 36, no. 1, pp. 243–252, 2008.

[126] D. Z. Pai, D. A. Lacoste, and C. O. Laux, "Transitions between corona, glow, and spark regimes of nanosecond repetitively pulsed discharges in air at atmospheric pressure," *Journal of applied physics*, vol. 107, no. 9, pp. 093303–093303, 2010.

[127] A. Mizuno, B. S. Rajanikanth, K. Shimizu, K. Kinoshita, K. Yanagihara, M. Okumoto, and S. Katsura, "Non-thermal plasma applications at very low temperature," *Combustion science and technology*, vol. 133, no. 1-3, pp. 49–63, 1998.

[128] S. Masuda, M. Sato, and T. Seki, "High-efficiency ozonizer using traveling wave pulse voltage," *Industry Applications, IEEE Transactions on*, no. 5, pp. 886–891, 1986.

[129] D. Braun, U. Kuchler, and G. Pietsch, "Behaviour of NO_x in air-fed ozonizers," *Pure and Applied Chemistry*, vol. 60, no. 5, pp. 741–746, 1988.

[130] B. Eliasson and U. Kogelschatz, "Modeling and applications of silent discharge plasmas," *Plasma Science, IEEE Transactions on*, vol. 19, no. 2, pp. 309–323, 1991.

[131] J. Kitayama and M. Kuzumoto, "Analysis of ozone generation from air in silent discharge," *Journal of Physics D: Applied Physics*, vol. 32, no. 23, p. 3032, 1999.

[132] W. J. M. Samaranayake, Y. Miyahara, T. Namihira, S. Katsuki, R. Hackam, and H. Akiyama, "Pulsed power production of ozone in O_2/N_2 in a coaxial reactor without dielectric layer," *Dielectrics and Electrical Insulation, IEEE Transactions on*, vol. 8, no. 5, pp. 826–831, 2001.

[133] K. Yan, E. J. M. Van Heesch, A. J. M. Pemen, and P. A. H. J. Huijbrechts, "From chemical kinetics to streamer corona reactor and voltage pulse generator," *Plasma chemistry and plasma processing*, vol. 21, no. 1, pp. 107–137, 2001.

[134] T. M. P. Briels, J. Kos, G. J. J. Winands, E. M. Van Veldhuizen, and U. Ebert, "Positive and negative streamers in ambient air: measuring diameter, velocity and dissipated energy," *Journal of Physics D: Applied Physics*, vol. 41, no. 23, p. 234004, 2008.

[135] T. Namihira, S. Tsukamoto, D. Wang, H. Hori, S. Katsuki, R. Hackam, H. Akiyama, M. Shimizu, and K. Yokoyama, "Influence of gas flow rate and reactor length on NO removal using pulsed power," *Plasma Science, IEEE Transactions on*, vol. 29, no. 4, pp. 592–598, 2001.

[136] N. Shimomura, M. Wakimoto, H. Togo, T. Namihira, and H. Akiyama, "Production of ozone using nanosecond short pulsed power," in *Pulsed Power Conference, 2003. Digest of Technical Papers. PPC-2003. 14th IEEE International*, vol. 2, pp. 1290–1293, IEEE, 2003.

[137] Y. P. Raizer, V. I. Kisin, and J. E. Allen, *Gas discharge physics*, vol. 1. Springer-Verlag Berlin, 1991.

[138] T. M. P. Briels, E. M. Van Veldhuizen, and U. Ebert, "Positive streamers in air and nitrogen of varying density: experiments on similarity laws," *Journal of Physics D: Applied Physics*, vol. 41, no. 23, p. 234008, 2008.

[139] T. M. P. Briels, E. M. v. Veldhuizen, and U. Ebert, "Time resolved measurements of streamer inception in air," *IEEE Transactions on Plasma Science*, vol. 36, no. 4, p. 908, 2008.

[140] S. Nijdam, K. Miermans, E. M. van Veldhuizen, and U. Ebert, "A peculiar streamer morphology created by a complex voltage pulse," *IEEE Transactions on Plasma Science*, vol. 39, no. 11, p. 2216, 2011.

[141] S. Chen, L. C. J. Heijmans, R. Zeng, S. Nijdam, and U. Ebert, "Nanosecond repetitively pulsed discharges in N_2–O_2 mixtures: inception cloud and streamer emergence," *Journal of Physics D: Applied Physics*, vol. 48, no. 17, p. 175201, 2015.

[142] P. O. Kochkin, C. V. Nguyen, A. P. J. Van Deursen, and U. Ebert, "Experimental study of hard x-rays emitted from metre-scale positive discharges in air," *Journal of Physics D: Applied Physics*, vol. 45, no. 42, p. 425202, 2012.

[143] P. O. Kochkin, A. P. J. van Deursen, and U. Ebert, "Experimental study of the spatio-temporal development of metre-scale negative discharge in air," *Journal of Physics D: Applied Physics*, vol. 47, no. 14, p. 145203, 2014.

[144] T. T. J. Clevis, S. Nijdam, and U. Ebert, "Inception and propagation of positive streamers in high-purity nitrogen: effects of the voltage rise rate," *Journal of Physics D: Applied Physics*, vol. 46, no. 4, p. 045202, 2013.

[145] A. Luque, V. Ratushnaya, and U. Ebert, "Positive and negative streamers in ambient air: modelling evolution and velocities," *Journal of Physics D: Applied Physics*, vol. 41, no. 23, p. 234005, 2008.

[146] D. Wang, M. Jikuya, S. Yoshida, T. Namihira, S. Katsuki, and H. Akiyama, "Positive- and negative-pulsed streamer discharges generated by a 100-ns pulsed-power in atmospheric air," *Plasma Science, IEEE Transactions on*, vol. 35, no. 4, pp. 1098–1103, 2007.

[147] L. M. Vasilyak, S. P. Vetchinin, and D. N. Polyakov, "Effect of the rise rate of nanosecond high-voltage pulses on the breakdown of air gaps," *Technical Physics Letters*, vol. 25, no. 9, pp. 749–751, 1999.

[148] J. Y. Won and P. F. Williams, "Experimental study of streamers in pure N_2 and N_2/O_2 mixtures and a 13 cm gap," *Journal of Physics D: Applied Physics*, vol. 35, no. 3, p. 205, 2002.

[149] K. Yoshinaga, S. Okada, D. Wang, T. Namihira, S. Katsuki, and H. Akiyama, "Effect of polarity and rise time of applied pulsed voltage on streamer discharge phenomena," *Acta Physica Polonica-Series A General Physics*, vol. 115, no. 6, p. 1050, 2009.

[150] Y. Teramoto, Y. Fukumoto, R. Ono, and T. Oda, "Streamer propagation of positive and negative pulsed corona discharges in air," *Plasma Science, IEEE Transactions on*, vol. 39, no. 11, pp. 2218–2219, 2011.

[151] G. J. J. Winands, Z. Liu, A. J. M. Pemen, E. J. M. Van Heesch, and K. Yan, "Analysis of streamer properties in air as function of pulse and reactor parameters by ICCD photography," *Journal of Physics D: Applied Physics*, vol. 41, no. 23, p. 234001, 2008.

[152] U. Ebert, W. van Saarloos, and C. Caroli, "Propagation and structure of planar streamer fronts," *Physical Review E*, vol. 55, no. 2, p. 1530, 1997.

[153] A. Komuro, R. Ono, and T. Oda, "Numerical simulation for production of O and N radicals in an atmospheric-pressure streamer discharge," *Journal of Physics D: Applied Physics*, vol. 45, no. 26, p. 265201, 2012.

[154] O. Eichwald, O. Ducasse, D. Dubois, A. Abahazem, N. Merbahi, M. Benhenni, and M. Yousfi, "Experimental analysis and modelling of positive streamer in air: towards an estimation of O and N radical production," *Journal of Physics D: Applied Physics*, vol. 41, no. 23, p. 234002, 2008.

[155] Y. L. M. Creyghton, E. M. Van Veldhuizen, and W. R. Rutgers, "Diagnostic techniques for atmospheric streamer discharges," *IEE Proceedings-Science, Measurement and Technology*, vol. 141, no. 2, pp. 141–147, 1994.

[156] D. Dubrovin, S. Nijdam, T. T. J. Clevis, L. C. J. Heijmans, U. Ebert, Y. Yair, and C. Price, "Positive streamers in air of varying density: experiments on the scaling of the excitation density," *Journal of Physics D: Applied Physics*, vol. 48, no. 5, p. 055205, 2015.

[157] R. Ono, C. Tobaru, Y. Teramoto, and T. Oda, "Laser-induced fluorescence of $N_2(A^3\Sigma_u^+)$ metastable in N_2 pulsed positive corona discharge," *Plasma Sources Science and Technology*, vol. 18, no. 2, p. 025006, 2009.

[158] S. V. Pancheshnyi, S. V. Sobakin, S. M. Starikovskaya, and A. Y. Starikovskii, "Discharge dynamics and the production of active particles in a cathode-directed streamer," *Plasma Physics Reports*, vol. 26, no. 12, pp. 1054–1065, 2000.

[159] G. V. Naidis, "Evaluation of $N_2(A^3\Sigma_u^+)$ density in nitrogen streamer discharges," *Plasma Sources Science and Technology*, vol. 19, no. 5, p. 055010, 2010.

[160] R. Ono and T. Oda, "Formation and structure of primary and secondary streamers in positive pulsed corona dischargeeffect of oxygen concentration and applied voltage," *Journal of Physics D: Applied Physics*, vol. 36, no. 16, p. 1952, 2003.

[161] E. Marode, "The mechanism of spark breakdown in air at atmospheric pressure between a positive point and a plane. I. Experimental: Nature of the streamer track," *Journal of Applied Physics*, vol. 46, no. 5, pp. 2005–2015, 1975.

[162] R. Ono and T. Oda, "Spatial distribution of ozone density in pulsed corona discharges observed by two-dimensional laser absorption method," *Journal of Physics D: Applied Physics*, vol. 37, no. 5, p. 730, 2004.

[163] A. Komuro, K. Takahashi, and A. Ando, "Numerical simulation for the production of chemically active species in primary and secondary streamers in atmospheric-pressure dry air," *Journal of Physics D: Applied Physics*, vol. 48, no. 21, p. 215203, 2015.

[164] L. Zhao, Z. Y. Luo, J. Y. Xuan, J. P. Jiang, X. Gao, and K. F. Cen, "Study of geometry structure on a wire–plate pulsed corona discharge reactor," *Plasma Science, IEEE Transactions on*, vol. 40, no. 3, pp. 802–810, 2012.

[165] A. V. Krasnochub, M. M. Nudnova, and A. Y. Starikovskii, "Cathode-directed streamer development in air at different pressures," in *43rd AIAA Aerospace Sciences Meeting and Exhibit, Reno, NV, AIAA Paper*, vol. 1196, p. 2005, 2005.

[166] E. M. Van Veldhuizen and W. R. Rutgers, "Pulsed positive corona streamer propagation and branching," *Journal of Physics D: Applied Physics*, vol. 35, no. 17, p. 2169, 2002.

[167] S. Nijdam, G. Wormeester, E. M. van Veldhuizen, and U. Ebert, "Probing background ionization: positive streamers with varying pulse repetition rate and with a radioactive admixture," *Journal of Physics D: Applied Physics*, vol. 44, no. 45, p. 455201, 2011.

[168] T. Namihira, D. Wang, S. Katsuki, R. Hackam, and H. Akiyama, "Propagation velocity of pulsed streamer discharges in atmospheric air," *Plasma Science, IEEE Transactions on*, vol. 31, no. 5, pp. 1091–1094, 2003.

[169] I. Yagi, S. Okada, T. Matsumoto, D. Wang, T. Namihira, and K. Takaki, "Streamer propagation of nanosecond pulse discharge with various rise times," *Plasma Science, IEEE Transactions on*, vol. 39, no. 11, pp. 2232–2233, 2011.

[170] A. Komuro, R. Ono, and T. Oda, "Effects of pulse voltage rise rate on velocity, diameter and radical production of an atmospheric-pressure streamer discharge," *Plasma Sources Science and Technology*, vol. 22, no. 4, p. 045002, 2013.

[171] S. Pancheshnyi, M. Nudnova, and A. Starikovskii, "Development of a cathode-directed streamer discharge in air at different pressures: experiment and comparison with direct numerical simulation," *Physical Review E*, vol. 71, no. 1, p. 016407, 2005.

[172] P. Tardiveau, E. Marode, and A. Agneray, "Tracking an individual streamer branch among others in a pulsed induced discharge," *Journal of Physics D: Applied Physics*, vol. 35, no. 21, p. 2823, 2002.

[173] R. McAdams, "Pulsed corona treatment of gases: system scaling and efficiency," *Plasma Sources Science and Technology*, vol. 16, no. 4, p. 703, 2007.

[174] A. Pokryvailo, Y. Yankelevich, N. Nissim, R. Baksht, and J. Ashkenazy, "Development of short pulsed corona on two-wire transmission line," *Plasma Science, IEEE Transactions on*, vol. 34, no. 1, pp. 104–114, 2006.

[175] E. J. M. van Heesch, M. H. P. Dagelinckx, F. M. van Gompel, and P. P. M. Blom, "Surge corona propagating along a transmission line," in *Proc. 9th Int. Symp. on High Voltage Engineering, 28 August–1 September 1995, Graz, Austria*, 1995.

[176] E. M. Van Veldhuizen and W. R. Rutgers, "Inception behaviour of pulsed positive corona in several gases," *Journal of Physics D: Applied Physics*, vol. 36, no. 21, p. 2692, 2003.

[177] T. Huiskamp, W. J. M. Brok, A. A. E. Stevens, E. J. M. van Heesch, and A. J. M. Pemen, "Maskless patterning by pulsed-power plasma printing," *Plasma Science, IEEE Transactions on*, vol. 40, no. 7, pp. 1913–1925, 2012.

[178] W. Sengers, "Streamer development and propagation through a coaxial reactor using a sub-nanosecond rise-time pulse source," Master's thesis, Eindhoven University of Technology, 2014.

[179] S. Nijdam, E. Takahashi, A. H. Markosyan, and U. Ebert, "Investigation of positive streamers by double-pulse experiments, effects of repetition rate and gas mixture," *Plasma Sources Science and Technology*, vol. 23, no. 2, p. 025008, 2014.

[180] T. M. P. Briels, E. M. van Veldhuizen, and U. Ebert, "Branching of positive discharge streamers in air at varying pressures," *Plasma Science, IEEE Transactions on*, vol. 33, no. 2, pp. 264–265, 2005.

[181] U. Ebert, C. Montijn, T. M. P. Briels, W. Hundsdorfer, B. Meulenbroek, A. Rocco, and E. M. Van Veldhuizen, "The multiscale nature of streamers," *Plasma Sources Science and Technology*, vol. 15, no. 2, p. S118, 2006.

[182] A. Luque, U. Ebert, and W. Hundsdorfer, "Interaction of streamer discharges in air and other oxygen-nitrogen mixtures," *Physical review letters*, vol. 101, no. 7, p. 075005, 2008.

[183] G. V. Naidis, "On streamer interaction in a pulsed positive corona discharge," *Journal of Physics D: Applied Physics*, vol. 29, no. 3, p. 779, 1996.

[184] J. Teunissen, A. Sun, and U. Ebert, "A time scale for electrical screening in pulsed gas discharges," *Journal of Physics D: Applied Physics*, vol. 47, no. 36, p. 365203, 2014.

[185] M. A. Malik and K. H. Schoenbach, "Nitric oxide conversion and ozone synthesis in a shielded sliding discharge reactor with positive and negative streamers," *Plasma Chemistry and Plasma Processing*, vol. 34, no. 1, pp. 93–109, 2014.

[186] M. A. Malik, J. F. Kolb, Y. Sun, and K. H. Schoenbach, "Comparative study of NO removal in surface-plasma and volume-plasma reactors based on pulsed corona discharges," *Journal of hazardous materials*, vol. 197, pp. 220–228, 2011.

[187] A. Mizuno, K. Shimizu, A. Chakrabarti, L. Dascalescu, and S. Furuta, "NO_x removal process using pulsed discharge plasma," *Industry Applications, IEEE Transactions on*, vol. 31, no. 5, pp. 957–962, 1995.

[188] X. Fei, L. Zhongyang, C. Wei, W. Peng, W. Bo, G. Xiang, F. Mengxiang, and C. Kefa, "Simultaneous oxidation of NO, SO_2 and Hg_0 from flue gas by pulsed corona discharge," *Journal of Environmental Sciences*, vol. 21, no. 3, pp. 328–332, 2009.

[189] K. Yan, R. Li, T. Zhu, H. Zhang, X. Hu, X. Jiang, H. Liang, R. Qiu, and Y. Wang, "A semi-wet technological process for flue gas desulfurization by corona discharges at an industrial scale," *Chemical Engineering Journal*, vol. 116, no. 2, pp. 139–147, 2006.

[190] A. M. Vandenbroucke, R. Morent, N. De Geyter, and C. Leys, "Non-thermal plasmas for non-catalytic and catalytic VOC abatement," *Journal of hazardous materials*, vol. 195, pp. 30–54, 2011.

[191] T. Yamamoto, K. Ramanathan, P. A. Lawless, D. S. Ensor, J. R. Newsome, N. Plaks, and G. H. Ramsey, "Control of volatile organic compounds by an AC energized ferroelectric pellet reactor and a pulsed corona reactor," *Industry Applications, IEEE Transactions on*, vol. 28, no. 3, pp. 528–534, 1992.

[192] C. M. Nunez, G. H. Ramsey, W. H. Ponder, J. H. Abbott, L. E. Hamel, and P. H. Kariher, "Corona destruction: an innovative control technology for VOCs and air toxics," *Air & Waste*, vol. 43, no. 2, pp. 242–247, 1993.

[193] N. Tippayawong and P. Inthasan, "Investigation of light tar cracking in a gliding arc plasma system," *International Journal of Chemical Reactor Engineering*, vol. 8, no. 1, 2010.

[194] G. J. J. Winands, K. Yan, A. J. M. Pemen, S. A. Nair, Z. Liu, and E. J. M. Van Heesch, "An industrial streamer corona plasma system for gas cleaning," *Plasma Science, IEEE Transactions on*, vol. 34, no. 5, pp. 2426–2433, 2006.

[195] M. Okubo, H. Kametaka, K. Yoshida, and T. Yamamoto, "Odor removal characteristics of barrier-type packed-bed nonthermal plasma reactor," *Japanese Journal of Applied Physics*, vol. 46, no. 8R, p. 5288, 2007.

[196] C. W. Park, J. H. Byeon, K. Y. Yoon, J. H. Park, and J. Hwang, "Simultaneous removal of odors, airborne particles, and bioaerosols in a municipal composting facility by dielectric barrier discharge," *Separation and Purification Technology*, vol. 77, no. 1, pp. 87–93, 2011.

271

[197] Y. Liang, Y. Wu, K. Sun, Q. Chen, F. Shen, J. Zhang, M. Yao, T. Zhu, and J. Fang, "Rapid inactivation of biological species in the air using atmospheric pressure nonthermal plasma," *Environmental science & technology*, vol. 46, no. 6, pp. 3360–3368, 2012.

[198] K. Kelly-Wintenberg, D. M. Sherman, P.-Y. Tsai, R. B. Gadri, F. Karakaya, Z. Chen, J. Reece Roth, and T. C. Montie, "Air filter sterilization using a one atmosphere uniform glow discharge plasma (the volfilter)," *Plasma Science, IEEE Transactions on*, vol. 28, no. 1, pp. 64–71, 2000.

[199] N. D. Vaze, M. J. Gallagher, S. Park, G. Fridman, V. N. Vasilets, A. F. Gutsol, S. Anandan, G. Friedman, and A. A. Fridman, "Inactivation of bacteria in flight by direct exposure to nonthermal plasma," *Plasma Science, IEEE Transactions on*, vol. 38, no. 11, pp. 3234–3240, 2010.

[200] G. Y. Park, S. J. Park, M. Y. Choi, I. G. Koo, J. H. Byun, J. W. Hong, J. Y. Sim, G. J. Collins, and J. K. Lee, "Atmospheric-pressure plasma sources for biomedical applications," *Plasma Sources Science and Technology*, vol. 21, no. 4, p. 043001, 2012.

[201] G. Centi, E. A. Quadrelli, and S. Perathoner, "Catalysis for CO_2 conversion: a key technology for rapid introduction of renewable energy in the value chain of chemical industries," *Energy & Environmental Science*, vol. 6, no. 6, pp. 1711–1731, 2013.

[202] A. Lebouvier, S. A. Iwarere, P. dArgenlieu, D. Ramjugernath, and L. Fulcheri, "Assessment of carbon dioxide dissociation as a new route for syngas production: a comparative review and potential of plasma-based technologies," *Energy & Fuels*, vol. 27, no. 5, pp. 2712–2722, 2013.

[203] J. A. Wojtowicz, "Ozone," *Kirk-Othmer encyclopedia of chemical technology*, 1996.

[204] G. Sathiamoorthy, S. Kalyana, W. C. Finney, R. J. Clark, and B. R. Locke, "Chemical reaction kinetics and reactor modeling of NO_x removal in a pulsed streamer corona discharge reactor," *Industrial & engineering chemistry research*, vol. 38, no. 5, pp. 1844–1855, 1999.

[205] T. Yamamoto, C.-L. Yang, M. R. Beltran, and Z. Kravets, "Plasma-assisted chemical process for no_x control," *Industry Applications, IEEE Transactions on*, vol. 36, no. 3, pp. 923–927, 2000.

[206] J. C. Whitehead, "Plasma catalysis: A solution for environmental problems," *Pure and Applied Chemistry*, vol. 82, no. 6, pp. 1329–1336, 2010.

[207] H. L. Chen, H. M. Lee, S. H. Chen, M. B. Chang, S. J. Yu, and S. N. Li, "Removal of volatile organic compounds by single-stage and two-stage plasma catalysis systems: a review of the performance enhancement mechanisms, current status, and suitable applications," *Environmental science & technology*, vol. 43, no. 7, pp. 2216–2227, 2009.

[208] V. R. Chirumamilla, W. F. L. M. Hoeben, F. J. C. M. Beckers, T. Huiskamp, and A. J. M. Pemen, "Experimental investigation on the effect of rise time on NO_x removal using a pulsed DBD with catalysts (*to be published*)," *Plasma chemistry and plasma processing*, 2015.

[209] Y. P. Butylkin, V. K. Zhivotov, E. G. Krasheninnikov, M. F. Krotov, V. D. Rusanov, Y. V. Tarasov, and A. A. Fridman, "Dissociation of CO_2 by a plasma-chemical process in a nonequilibrium microwave discharge," *Sov. Phys.-Tech. Phys.(Engl. Transl.);(United States)*, vol. 26, no. 5, 1981.

[210] A. A. Fridman and V. D. Rusanov, "Theoretical basis of non-equilibrium near atmospheric pressure plasma chemistry," *Pure and applied chemistry*, vol. 66, no. 6, pp. 1267–1278, 1994.

[211] F. Brehmer, S. Welzel, M. C. M. van de Sanden, and R. Engeln, "CO and byproduct formation during CO_2 reduction in dielectric barrier discharges," *Journal of Applied Physics*, vol. 116, no. 12, p. 123303, 2014.

[212] S. Paulussen, B. Verheyde, X. Tu, C. De Bie, T. Martens, D. Petrovic, A. Bogaerts, and B. Sels, "Conversion of carbon dioxide to value-added chemicals in atmospheric pressure dielectric barrier discharges," *Plasma Sources Science and Technology*, vol. 19, no. 3, p. 034015, 2010.

[213] B. Eliasson, W. Egli, and U. Kogelschatz, "Modelling of dielectric barrier discharge chemistry," *Pure and applied chemistry*, vol. 66, no. 6, pp. 1275–1286, 1994.

[214] L. M. Zhou, B. Xue, U. Kogelschatz, and B. Eliasson, "Nonequilibrium plasma reforming of greenhouse gases to synthesis gas," *Energy & fuels*, vol. 12, no. 6, pp. 1191–1199, 1998.

[215] S. Ponduri, C. A. Douat, and R. A. H. Engeln, "Relation between filament density and CO_2 dissociation in CO_2 dielectric barrier discharge *(will be updated before the thesis is printed)*," in *Proceedings of the 22nd Symposium on Plasma Chemistry (ISPC 22), 5-10 July 2015, Antwerp, Belgium*, 2015.

[216] C. A. Douat, S. Ponduri, and R. A. H. Engeln, "Effects of the addition of oxygen and nitrogen on the CO_2 dissociation in a CO_2 dielectric barrier discharge *(will be updated before the thesis is printed)*," in *Proceedings of the 22nd Symposium on Plasma Chemistry (ISPC 22), 5-10 July 2015, Antwerp, Belgium*, 2015.

[217] M. S. Bak, S.-K. Im, and M. Cappelli, "Nanosecond-pulsed discharge plasma splitting of carbon dioxide," *Plasma Science, IEEE Transactions on*, vol. 43, no. 4, pp. 1002–1007, 2015.

[218] Z. Liu, K. Yan, G. J. J. Winands, A. J. M. Pemen, E. J. M. Van Heesch, and D. B. Pawelek, "Multiple-gap spark gap switch," *Review of scientific instruments*, vol. 77, no. 7, pp. 073501–073501, 2006.

[219] P. R. Griffiths and J. A. De Haseth, *Fourier transform infrared spectrometry*, vol. 171. John Wiley & Sons, 2007.

[220] E. W. Lemmon, M. O. McLinden, D. G. Friend, P. J. Linstrom, and W. G. Mallard, "NIST chemistry WebBook, Nist standard reference database number 69," *National Institute of Standards and Technology, Gaithersburg*, 2011.

[221] I. C. Hisatsune, J. P. Devlin, and Y. Wada, "Vibrational spectrum and structure of N_2O_5," *Spectrochimica Acta*, vol. 18, no. 12, pp. 1641–1653, 1962.

[222] R. W. Lovejoy, C. Chackerian Jr, and R. W. Boese, "Integrated band intensities of gaseous N_2O_5," *Applied optics*, vol. 19, no. 5, pp. 744–748, 1980.

[223] C. A. Cantrell, J. A. Davidson, A. H. McDaniel, R. E. Shetter, and J. G. Calvert, "Infrared absorption cross sections for N_2O_5," *Chemical Physics Letters*, vol. 148, no. 4, pp. 358–363, 1988.

[224] G. Horvath, J. D. Skalnỳ, and N. J. Mason, "FTIR study of decomposition of carbon dioxide in DC corona discharges," *Journal of Physics D: Applied Physics*, vol. 41, no. 22, p. 225207, 2008.

[225] T. Nunnally, K. Gutsol, A. Rabinovich, A. Fridman, A. Gutsol, and A. Kemoun, "Dissociation of CO_2 in a low current gliding arc plasmatron," *Journal of Physics D: Applied Physics*, vol. 44, no. 27, p. 274009, 2011.

[226] S. Ponduri, *Understanding CO_2 containing non equilibrium plasmas: Modeling and Experiments.* PhD thesis, Eindhoven University of Technology, 2015.

[227] F. K. H. Brehmer, *Shining light on transient CO_2 plasma.* PhD thesis, Eindhoven University of Technology, 2015.

[228] T. Huiskamp, N. Takamura, T. Namihira, and A. J. M. Pemen, "Matching a nanosecond pulse source to a streamer corona plasma reactor with a DC bias," *Plasma Science, IEEE Transactions on*, vol. 43, no. 2, pp. 617–624, 2015.

[229] K. Rakness, G. Gordon, B. Langlais, W. Masschelein, N. Matsumoto, Y. Richard, C. M. Robson, and I. Somiya, "Guideline for measurement of ozone concentration in the process gas from an ozone generator," *Ozone Science & Engineering*, vol. 18, pp. 209–229, 1996.

[230] T. Huiskamp, A. J. M. Pemen, W. F. L. M. Hoeben, F. J. C. M. Beckers, and E. J. M. van Heesch, "Temperature and pressure effects on positive streamers in air," *Journal of Physics D: Applied Physics*, vol. 46, no. 16, pp. 165202–165210, 2013.

[231] D. S. Aleksandrov, E. M. Bazelyan, and B. I. Bekzhanov, "A positive long spark in heated air," *Izv. Akad. Nauk SSSR: Energ. Transp*, vol. 22-2, p. 120, 1984.

[232] N. L. Allen and A. Ghaffar, "The variation with temperature of positive streamer properties in air," *Journal of Physics D: Applied Physics*, vol. 28, p. 338, 1995.

[233] N. L. Aleksandrov and E. M. Bazelyan, "Temperature and density effects on the properties of a long positive streamer in air," *Journal of Physics D: Applied Physics*, vol. 29, no. 11, p. 2873, 1996.

[234] C. T. Phelps and R. F. Griffiths, "Dependence of positive corona streamer propagation on air pressure and water vapor content," *Journal of Applied Physics*, vol. 47, no. 7, pp. 2929–2934, 1976.

[235] G. J. J. Winands, K. Yan, S. A. Nair, A. J. M. Pemen, and E. J. M. Van Heesch, "Evaluation of corona plasma techniques for industrial applications: HPPS and DC/AC systems," *Plasma Processes and Polymers*, vol. 2, no. 3, pp. 232–237, 2005.

[236] K. Yan, E. J. M. Van Heesch, A. J. M. Pemen, P. Huijbrechts, and P. C. T. van der Laan, "A 10 kW high-voltage pulse generator for corona plasma generation," *Review of Scientific Instruments*, vol. 72, no. 5, pp. 2443–2447, 2001.

[237] G. J. Su, "Modified law of corresponding states for real gases.," *Industrial & Engineering Chemistry*, vol. 38, no. 8, pp. 803–806, 1946.

[238] T. Huiskamp, H. Höft, M. Kettlitz, and A. J. M. Pemen, "Visualization of a spark discharge driven by a high-voltage pulse with sub-ns rise-time at atmospheric pressure," *Plasma Science, IEEE Transactions on*, vol. 42, no. 10, pp. 2414–2415, 2014.

[239] K. H. Becker, U. Kogelschatz, K. H. Schoenbach, and R. J. Barker, *Non-equilibrium air plasmas at atmospheric pressure.* CRC press, 2004.

[240] E. M. Bazelyan and Y. P. Raizer, *Spark discharge.* CRC press, 1997.

[241] I. A. Kossyi, A. Y. Kostinsky, A. A. Matveyev, and V. P. Silakov, "Kinetic scheme of the non-equilibrium discharge in nitrogen-oxygen mixtures," *Plasma Sources Science and Technology*, vol. 1, no. 3, p. 207, 1992.

List of Publications

Journal publications

2012

T. Huiskamp, W. J. M. Brok, A. A. E. Stevens, E. J. M. van Heesch and A. J. M. Pemen, "Maskless Patterning by Pulsed Power Plasma Printing," *IEEE T. Plasma Sci.*, **40**, 1913 (2012).

2013

T. Huiskamp, F. J. C. M. Beckers, W. F. L. M. Hoeben, E. J. M. van Heesch and A. J. M. Pemen, "Temperature and pressure effects on positive streamers in air," *J. Phys. D: Appl. Phys.*, **46**, 165202 (2013).

F. J. C. M. Beckers, W. F. L. M. Hoeben, T. Huiskamp, A. J. M. Pemen and E. J. M. van Heesch, "Pulsed Corona Demonstrator for Semi-Industrial Scale Air Purification," *IEEE T. Plasma Sci.*, **41**, 2920 (2013).

T. Huiskamp, F. J. C. M. Beckers, E. J. M. van Heesch and A. J. M. Pemen, "A Solid State, 0–120 kV, Microsecond Pulse Charger for a Nanosecond Pulse Source," *IEEE T. Plasma Sci.*, **41**, 3666 (2013).

2014

T. Huiskamp, S. J. Voeten, E. J. M. van Heesch and A. J. M. Pemen, "Design of a Subnanosecond Rise Time, Variable Pulse Duration, Variable Amplitude, Repetitive, High-Voltage Pulse Source," *IEEE T. Plasma Sci.*, **42**, 127 (2014).

J. Zhang, E. J. M. van Heesch, F. J. C. M. Beckers, T. Huiskamp, and A. J. M. Pemen, "Breakdown Voltage and Recovery Rate Estimation of a Supercritical Nitrogen Plasma Switch," *IEEE T. Plasma Sci.*, **42**, 376 (2014).

T. Huiskamp, F. J. C. M. Beckers, E. J. M. van Heesch and A. J. M. Pemen, "First Implementation of a Subnanosecond Rise Time, Variable Pulse Duration, Variable

Amplitude, Repetitive, High-Voltage Pulse Source," *IEEE T. Plasma Sci.*, **42**, 859 (2014).

A. B. J. M. Driessen, E. J. M. van Heesch, T. Huiskamp, F. J. C. M. Beckers, and A. J. M. Pemen, "Compact Pulse Topology for Adjustable High-Voltage Pulse Generation Using a SOS Diode," *IEEE T. Plasma Sci.*, **42**, 3083 (2014).

H. Höft, T. Huiskamp, M. Kettlitz and A. J. M. Pemen, "Vizualisation of a Coaxial Dielectric Barrier Discharge Driven by a Sub-ns Rising High-Voltage Pulse and its Reflections," *IEEE T. Plasma Sci.*, **42**, 2336 (2014).

T. Huiskamp, H. Höft, M. Kettlitz and A. J. M. Pemen, "Vizualisation of a Spark Discharge Driven by a High-Voltage Pulse With Sub-ns Rise-Time at Atmospheric Pressure," *IEEE T. Plasma Sci.*, **42**, 2414 (2014).

2015

T. Huiskamp, E. J. M. van Heesch and A. J. M. Pemen, "Final Implementation of a Subnanosecond Rise Time, Variable Pulse Duration, Variable Amplitude, Repetitive, High-Voltage Pulse Source," *IEEE T. Plasma Sci.*, **43**, 444 (2015).

T. Huiskamp, N. Takamura, T. Namihira and A. J. M. Pemen, "Matching a Nanosecond Pulse Source to a Streamer Corona Plasma Reactor with a DC Bias," *IEEE T. Plasma Sci.*, **43**, 617 (2015).

T. Huiskamp, E. J. M. van Heesch and A. J. M. Pemen, "D-Dot and B-dot Sensors for Subnanosecond High-Voltage Pulse Measurements," *IEEE Sens. J.*, (2015), to be submitted.

T. Huiskamp, E. J. M. van Heesch and A. J. M. Pemen, "Matching a Subnanosecond Rise Time, Nanosecond High-Voltage Pulse Source to a Coaxial Corona Plasma Reactor," *J. Phys. D: Appl. Phys.*, (2015), to be submitted.

T. Huiskamp, W. Sengers, E. J. M. van Heesch and A. J. M. Pemen, "Time and Space Resolved ICCD Imaging of a Streamer Plasma in a Coaxial Reactor Generated by Subnanosecond Rise Time, Nanosecond High-Voltage Pulses," *Rev. Sci. Instrum.*, (2015), to be submitted.

T. Huiskamp, W. Sengers, E. J. M. van Heesch, U. Ebert, S. Nijdam, and A. J. M. Pemen, "Effect of Pulse Rise Time, Pulse Duration and Pulse Polarity on Streamers Generated by Subnanosecond Rise Time, Nanosecond High-Voltage Pulses in a Coaxial Corona Plasma Reactor," *J. Phys. D: Appl. Phys.*, (2015), to be submitted.

T. Huiskamp, W. F. L. M. Hoeben, F. J. C. M. Beckers, V. R. Chirumamilla, E. J. M. van Heesch and A. J. M. Pemen, "Energy Efficient Ozone Production and NO Removal with a Subnanosecond Rise Time, Nanosecond High-Voltage Pulse Source," *Plasma Chem. Plasma P.*, (2015), to be submitted.

Selected conference contributions

2011

T. Huiskamp, W. J. M. Brok and A. J. M. Pemen, "Pushing the Frontiers of Plasma Printing by Pulsed Power Technology," *IEEE Pulsed Power Symposium 2011*, 20 September 2011, Loughborough, UK.

2012

T. Huiskamp, E. J. M. van Heesch, W. F. L. M. Hoeben and A. J. M. Pemen, "Temperature and Pressure Effects on Positive Streamers in Air," 8th *International Symposium on Non-Thermal Plasma Pollution Control Technology and Sustainable Energy (ISNTP-8)*, 25–29 June 2012, Camaret, France.

T. Huiskamp, S. J. Voeten and A. J. M. Pemen, "Design of a Nanosecond Pulse Generator with CST Microwave Studio," 4th *Euro-Asian Pulsed Power Conference (EAPPC)*, 30 September–4 October 2012, Karlsruhe, Germany.

2013

T. Huiskamp, E. J. M. van Heesch and A. J. M. Pemen, "Evaluation of a 0–60 kV Oil-Switched Picosecond Rise Time 5 ns Pulse Generator," 19th *Pulsed Power Conference (PPC)*, 16–21 June 2013, San Francisco, USA.

T. Huiskamp, F. J. C. M. Beckers, E. J. M. van Heesch and A. J. M. Pemen, "A Solid State 0–120 kV Microsecond Pulse Charger for a Nanosecond Pulse Source," 19th *Pulsed Power Conference (PPC)*, 16–21 June 2013, San Francisco, USA.

2014

T. Huiskamp, E. J. M. van Heesch and A. J. M. Pemen, "Evaluation of a 0–50 kV Oil-Switched Picosecond Rise Time 0.5–10 ns Pulse Generator," *2014 IEEE International Power Modulator and High Voltage Conference (IPMHVC)*, 1–5 June 2014, Santa Fe, USA.

T. Huiskamp, E. J. M. van Heesch and A. J. M. Pemen, "Evaluation of a 0–50 kV Oil-Switched Picosecond Rise Time 0.5–10 ns Pulse Source," 5th *Euro-Asian Pulsed Power Conference (EAPPC)*, 8–12 September 2014, Kumamoto, Japan.

T. Huiskamp, N. Takamura, T. Namihira and A. J. M. Pemen, "Matching a Nanosecond Pulse Source to a Streamer Corona Plasma with a DC-Bias," 5th *Euro-Asian Pulsed Power Conference (EAPPC)*, 8–12 September 2014, Kumamoto, Japan (*awarded with an Excellent Student Award*).

2015

T. Huiskamp, E. J. M. van Heesch and A. J. M. Pemen, "Matching a (Sub)Nanosecond Pulse Source to a Coaxial Streamer Plasma Reactor," 20th *Pulsed Power Conference*

(PPC), 31 May–4 June 2015, Austin, USA.

T. Huiskamp, W. F. L. M. Hoeben, V. R. Chirumamilla, E. J. M. van Heesch and A. J. M. Pemen, "Air Purification with Subnanosecond Pulsed Streamer Plasma: High Yield Ozone Production, NO conversion and CO_2 Conversion," *20th Pulsed Power Conference (PPC)*, 31 May–4 June 2015, Austin, USA.

T. Huiskamp, A. A. E. Stevens and A. J. M. Pemen, "µPlasmaPrint Throughput Enhancement by Pulsed Power Technology," *20th Pulsed Power Conference (PPC)*, 31 May–4 June 2015, Austin, USA.

Acknowledgements

With only a couple of days left before I have to send the thesis to the printers, I finally get to write this part. People have been asking me for months "So now you're done, right?", and each time I had to explain that it was just another deadline, for the committee, for 'form 2', etcetera, but after next week I can finally tell them: "It is done." And that would not have been possible without the help of colleagues, friends and family.

First and foremost, I would like to express my gratitude to Guus Pemen, my co-promotor. Your continued support was instrumental in getting me into the PhD program in the first place, but also along the long road to where I am now. Thanks for letting me choose my own path, while being there at the right time to steer me in the right direction, or to suggest an alternative approach. Without your suggestion to switch on the high-temperature setup in my first year (which resulted in the whole building smelling of burned socks for a couple of days) I would've gone crazy with only the literature study to occupy me. Your support was also very important in landing me the Postdoc position. Let's see where it takes us.

I also would like to thank Wil Kling, my first promotor, who sadly passed away. Thanks for believing in me and my career at the university.

Ute, thanks for agreeing to be my second promotor after Wil passed. During the first years of my PhD, we were still a long way apart, but in the last year our worlds converged in streamers.

I am really grateful for the comments that I received from the members of my defense committee and the time that they spent on my thesis. Every one of you have you own expertise and together your comments really improved this thesis. Bucur, Luis and Bart, thanks for the pulsed power comments. Ute and Gerrit, thanks for the plasma feedback and finally, thanks to Bert and Guus for the all-round feedback. Besides the committee members, I would also like to thank Sander, who was brave enough to read a draft of Chapter 7 and Wilfred, who read Chapter 8 and provided me with very useful feedback and a host of new Scrabble words.

I really need to reserve one separate paragraph for Stefan. I've met a lot of interesting people during the last years: I've seen a man from a respected naval institute

Curriculum Vitae

Tom Huiskamp was born on 9 July 1985 in De Bilt. After finishing his secondary education (VWO) in 2003 at the Montessori Lyceum Herman Jordan in Zeist, he studied Electrical Engineering at Eindhoven University of Technology in Eindhoven. In early 2011 he graduated (cum laude) within the Electrical Energy Systems Group on applying pulsed power technology to InnoPhysics B.V.'s maskless plasma patterning technology. After staying on for a brief time at InnoPhysics B.V. to finalise the pulsed power technology for production machines, he started a PhD project at Eindhoven University of Technology of which the results are presented in this thesis.

During the PhD project, he visited other universities and institutions, most notably the Kumamoto University in Kumamoto, Japan in 2013, where he spent some time as a researcher. The result of this visit is presented in Appendix A of this thesis and was awarded with the Excellent Student Award at the 5$^{\text{th}}$ Euro-Asian Pulsed Power Conference in Kumamoto, Japan in 2014.

Since May 2015 he is employed at Eindhoven University of Technology as a postdoctoral researcher.